Studying chiral molecules with broadband microwave spectroscopy

Dissertation

zur Erlangung des Doktorgrades

an der Fakultät für Mathematik, Informatik und Naturwissenschaften

Fachbereich Chemie

der Universität Hamburg

vorgelegt von

Anna Krin

aus Hamburg

Hamburg
2019

Gutachter der Dissertation:

Prof. Dr. Melanie Schnell

Prof. Dr. Alf Mews

Gutachter der Disputation:

Prof. Dr. Gabriel Bester

Prof. Dr. Carmen Herrmann

Prof. Dr. Melanie Schnell

Datum der Disputation:

29.11.2019

"*Nature uses only the longest threads to weave her patterns, so each small piece of her fabric reveals the organization of the entire tapestry*"

Richard P. Feynman

Abstract

Natural essential oils are complex mixtures containing several compounds of structural similarity. They are well known for their wide range of applications in different areas, from medicine to cosmetics. One of the conventional methods for their quantitative analysis is gas chromatography (GC). Despite the numerous advantages of GC as an analytical tool, some aspects such as structure determination cannot be addressed with it. Another technique which is applicable to the volatile essential oil components is rotational spectroscopy. It is a powerful method for the structure determination not only of the respective compounds, but also of their different isomers and conformers. Rotational spectroscopy thus complements the information obtained with GC, which is necessary for a comprehensive study on the molecular systems of interest.

In the first part of this thesis, some of the main constituents of peppermint and thyme oils were analyzed with rotational spectroscopy. Structure determination of several oil components including menthol, thymol, linalool, and pulegone was performed. The internal dynamics of *trans*-thymol-B, linalool, pulegone, and menthyl acetate, resulting from the internal rotation of their methyl groups were studied. The conformational landscape of menthyl acetate was characterized both experimentally and computationally. All these key points help to better understand the functionality of the chemical substances discussed here, and their mode of interaction in our body. Additionally, a semi-quantitative analysis of thyme oil was performed. The results were compared to the GC study for benchmarking purposes, showing a good agreement.

Many of the essential oil constituents are chiral. Chirality is of utmost importance in the biological context. There is a high demand for reliable methods for a detailed characterization of chiral molecules. Recent developments in rotational spectroscopy have enabled the exploration of molecules in a chirality-sensitive way by applying the microwave three-wave mixing (M3WM) technique. The M3WM makes use of the advantages of rotational spectroscopy such as conformer selectivity and mixture compatibility. It was successfully applied in the scope of this thesis to differentiate between the enantiomers of some essential oil constituents. The M3WM was recently extended to allow coherent population transfer (CPT) of the enantiomers to rotational states of choice. This approach is discussed in the second part of the present work. It may pave the way for enantioseparation in future experiments. Finally, M3WM and CPT were combined in the experiment to manipulate the chiral conformers of a molecule, which has no stereogenic center (cyclohexylmethanol). Such a procedure significantly widens the range of molecular systems available for chiral analysis with rotational spectroscopy.

Zusammenfassung

Natürliche ätherische Öle sind komplexe Gemische, die mehrere strukturell ähnliche Komponenten beinhalten. Sie sind bekannt für ihr breites Anwendungsspektrum in verschiedenen Bereichen, von Medizin bis Kosmetik. Eine der konventionellen Methoden für deren quantitative Analyse ist die Gaschromatographie (GC). Trotz zahlreicher Vorteile der GC als eines analytischen Werkzeugs, können einige Aspekte wie z.B. Strukturbestimmung nicht damit erfasst werden. Eine andere Methode, die auf flüchtige Ölkomponenten anwendbar ist, ist die Rotationsspektroskopie. Dies ist eine leistungsfähige Methode, um nicht nur die Struktur der zu untersuchenden Komponenten, sondern auch die Strukturen ihrer Konformere und Isomere zu bestimmen. Somit ergänzt die Rotationsspektroskopie die mit GC gewonnene Information, was für eine umfassende Studie an dem zu untersuchenden Molekülsystem notwendig ist.

Im ersten Teil dieser Dissertation wurden einige der Hauptbestandteile von Pfefferminz- und Thymianöl mittels Rotationsspektroskopie analysiert. So wurde die Strukturbestimmung mehrerer Komponenten wie Menthol, Thymol, Linalool und Pulegon durchgeführt. Außerdem wurde die interne Dynamik von *trans*-Thymol-B, Linalool, Pulegon und auch Menthylacetat, die von der internen Rotation ihrer Methylgruppen hervorgerufen wird, erforscht. Die Konformationslandschaft von Menhylacetat wurde sowohl experimentell, als auch mittels quanten-chemischer Methoden charakterisiert. Alle diese Schlüsselaspekte tragen zu einem besseren Verständnis der Funktionalität der hier diskutierten Komponenten, sowie ihrer Wechselwirkung in unserem Körper bei. Zusätzlich wurde eine semiquantitative Analyse des Thymianöls, durchgeführt. Die Ergebnisse wurden für Benchmarking-Zwecke mit der GC-Analyse verglichen und zeigen eine gute Übereinstimmung.

Viele Komponenten ätherischer Öle sind chiral. Chiralität ist von herausragender Bedeutung im biologischen Zusammenhang. Deshalb besteht ein großer Bedarf nach zuverlässigen Methoden für eine detaillierte Charakterisierung chiraler Moleküle. Neuste Entwicklungen in der Rotationsspektroskopie ermöglichen es, sich mit den Molekülen unter Anwendung des Mikrowellen Drei-Wellen Mischens (M3WM) chiralitätssensitiv auseinanderzusetzen. Das M3WM macht sich die Vorteile der Rotationsspektroskopie wie Konformerenselektivität und ihre Anwendbarkeit auf komplexe Gemische zunutze. Sie wurde erfolgreich im Rahmen dieser Dissertation angewendet, um zwischen den Enantiomeren von molekularen Bestandteilen ätherischer Öle zu unterscheiden. Das M3WM wurde vor Kurzem erweitert, um einen kohärenten Populationstransfer (CPT) von Enantiomeren in ausgewählte Rotationsenergieniveaus zu ermöglichen. Dieser Ansatz ist im zweiten Teil der vorliegenden Arbeit diskutiert. Er könnte den Weg für eine Enantiomerentrennung in zukünftigen Experimenten ebnen.

Schlussendlich wurden M3WM und CPT kombiniert, um chirale Konformere eines Moleküls ohne stereogenes Zentrum (Chyclohexylmethanol) zu manipulieren. Dieser Vorgang erweitert erheblich das Sortiment an molekularen Systemen, die für die chirale Analyse mittels Rotationsspektroskopie verfügbar sind.

Publications

1. C. Pérez, A. L. Steber, A. Krin, and M. Schnell, State-Specific Enrichment of Chiral Conformers with Microwave Spectroscopy, *J. Phys. Chem. Lett.*, **2018**, *9*(16), 4539-4543.

2. P. Pinacho, A. Krin, C. Pérez, S. Zinn , J. C. López, S. Blanco, and M. Schnell, Microsolvated complexes of ibuprofen as revealed by high-resolution rotational spectroscopy, *Phys. Chem. Chem. Phys.*, **2018**, *20*, 15635-15640.

3. A. Krin, C. Pérez, P. Pinacho, M. M. Quesada-Moreno, J. J. López-González, J. R. Avilés-Moreno, S. Blanco, J. C. López, and M. Schnell, Structure Determination, Conformational Flexibility, Internal Dynamics, and Chiral Analysis of Pulegone and Its Complex with Water, *Chem. Eur. J.*, **2018**, *24*, 721.

4. C. Pérez, A. L. Steber, S. R. Domingos, A. Krin, D. Schmitz, and M. Schnell, Coherent Enantiomer-Selective Population Enrichment Using Tailored Microwave Fields, *Angew. Chem. Int. Ed.*, **2017**, *56*, 12512.

5. V. A. Shubert, D. Schmitz, C. Pérez, C. Medcraft, A. Krin, S. R. Domingos, D. Patterson, and Melanie Schnell, Chiral Analysis Using Broadband Rotational Spectroscopy, *J. Phys. Chem. Lett.*, **2016**, *7*(2), 341-350.

6. C. Pérez, A. Krin, A. L. Steber, J. C. López, Z. Kisiel, and Melanie Schnell, Wetting Camphor: Multi-Isotopic Substitution Identifies the Complementary Roles of Hydrogen Bonding and Dispersive Forces, *J. Phys. Chem. Lett.*, **2016**, *7*(1), 154-160.

7. D. Schmitz, V. A. Shubert, D. Patterson, A. Krin, and M. Schnell, Phase Dependence of Double-Resonance Experiments in Rotational Spectroscopy, *J. Phys. Chem. Lett.*, **2015**, *6*(8), 1493-1498 .

8. V. A. Shubert, D. Schmitz, C. Medcraft, A. Krin, D. Patterson, J. M. Doyle and M. Schnell, Rotational spectroscopy and three-wave mixing of 4-carvomenthenol: A technical guide to measuring chirality in the microwave regime, *J. Chem. Phys.*, **2015**, *142*, 214201.

Contents

1

Introduction

Outline

This thesis consists of two conceptually connected parts. The first part is devoted to the characterization of essential oil constituents with broadband rotational spectroscopy. Essential oils have a high biological and industrial value, owing to their applicability in various areas and the importance in our everyday life. This work focusses on two essential oils, peppermint oil and thyme oil. Rotationally resolved spectroscopy is a unique tool for a detailed characterization of such complex mixtures in the gas phase. Different chemical species and even their conformers can be unambiguously identified in the broadband spectra. As was mentioned in one of the first reviews about rotational spectroscopy, "once a molecule has been caught and fingerprinted by this method, it is forever recognizable"[1]. Moreover, the isotopic species of the component under study can be observed, often in natural abundance. This, in turn, allows its accurate structural determination. The results of the rotational spectroscopy analysis on peppermint and thyme oil constituents are discussed in Chapters 4-7.

Most of the oil compounds are chiral. The importance of chirality – or "handedness" – in biochemistry and pharmacology cannot be understated. Recent developments in broadband rotational spectroscopy have allowed for the characterization of molecules in a chirality-sensitive manner. The essential oil constituents are well-suited to benchmark the technique and to demonstrate its applicability in mixture analysis. These components are very volatile and can be thus easily brought into the gas phase. The differentiation between the "handedness" of some essential oil constituents is shown as a proof of principle in Chapters 4, 6, and 7. The experiments were performed both on pure samples of the components and directly in the oil.

In the second part of the thesis, some advances in the field of chiral analysis with rotational spectroscopy are presented. For instance, in Chapter 8 a new experimental approach is discussed, which can one days open the way towards chiral separation. Chiral analysis using broadband rotational spectroscopy, and the new developments in this field, belong to the main questions of the present thesis. For this reason, the aspect of chirality is explained in more details in the next section.

Chirality and chiral analysis

The phenomenon that two objects can exist as mirror images of each other is omnipresent not only on a microscopic- but also on a macroscopic scale. Thus, the spiral shells of gastropods, more commonly known as snails, can be coiled clockwise or counter-clockwise (Figure 1.1). In botany, a mirror image symmetry in the helical growth of several plants was reported[2]. A somewhat more intuitive example of a macroscopic structure with such mirror image symmetry are our hands. That is why it is not surprising that the term "chirality", which describes non-superimposable mirror image structures, originates from the word "$\chi\varepsilon\iota\rho$", a Greek term for "hand".

A definition of chirality was given by W. H. Thompson (Lord Kelvin) in 1893 at the Oxford University Junior Scientific Club[3] and is formulated as follows:

> *I call any geometrical figure, or group of points, 'chiral', and say that it has chirality if its image in a plane mirror, ideally realized, cannot be brought to coincide with itself.*[4]

Later, V. Prelog used an equivalent definition in his Nobel prize lecture in 1975:

> *An object is chiral if it cannot be brought into congruence with its mirror image by translation or rotation.*[5]

On a microscopic scale, chirality is also of utmost importance. Most of the biologically relevant molecules, the "building blocks of life", such as amino acids, carbohydrates, nucleic acids etc. are chiral. The two non-superimposable structures are called enantiomers. They belong to the group of stereoisomers. Stereoisomers have the same molecular formula and constitution but differ in spatial orientation of their atoms. Another group of molecules, which are also stereoisomers, but do not have mirror image symmetry, are called diastereomers.

Due to historical reasons, several nomenclatures for the description of the handedness (the absolute configuration) of enantiomers exist. One way to distinguish between enantiomers is by their interaction with linearly polarized light. This source of radiation is also chiral in the sense that it is composed of both left- and right-circularly polarized light. Once it passes through a chiral medium, one of the circularly polarized components is propagated slower than the other one, resulting in the rotation of the plane of the radiation[3]. By convention, the counter-clockwise direction of rotation corresponds to a negative value of the rotation angle α, while the clockwise rotation results in a positive value of α. The enantiomers are then designated as (+) or (−), depending on the sign of the rotation angle.

Another set of nomenclatures include the D/L, d/l, P/M and Δ/Λ descriptions. They will not be discussed in detail here. However, it should be pointed out that the D/L notation found in literature is nowadays used only for amino acids and sugars. In this case, D means *dextro*

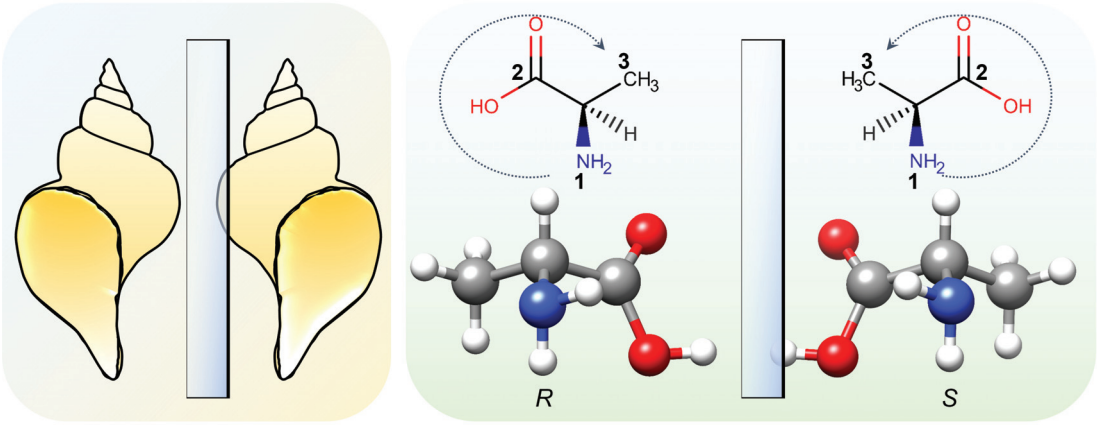

Figure 1.1: *Examples of a mirror-image symmetry on a macroscopic (left) and on a microscopic scale (right). The designation of the enantiomers of alanine as R and S in the image on the right is based on the Cahn-Ingold-Prelog (CIP)[6] nomenclature. The substituents are numbered according to their atomic number in the descending order.*

(Latin term for "right"), while L stands for *laevus* ("left"). Intriguingly, natural amino acids and sugars commonly exist only in one of the two enantiomeric forms. While amino acids are found in the L-form, sugars are present in the D-form. The reason behind this phenomenon, known as the homochirality of life, is since decades under debate and represents a hot research topic.

The most commonly used nomenclature, recommended by the International Union of Pure and Applied Chemistry (IUPAC), is the Cahn-Ingold-Prelog (CIP)[6] system. It describes a configuration of so-called chiral centers or of double bonds (E-, Z-stereoisomers) A chiral center is a tetrahedral carbon atom with four different substituents. According to the rules, a priority number has to be assigned to each of the four substituents, depending on their atomic number. If the numbering of the substituents occurs clockwise, the enantiomer is said to have an R-configuration (R for *rectus*), otherwise it is referred to as an S-enantiomer (S for *sinister*). An example for an assignment of the absolute configuration based on these rules is presented in Figure 1.1.

An equimolar mixture of enantiomers is called racemic (from Latin "bunch of grapes"). The term was first introduced by J. L. Gay-Lussac, who referred to the optically inactive form of tartaric acid as "the racemic acid"[7]. Later, L. Pasteur showed that the so-called racemic acid contained equal amounts of the two enantiomers of tartaric acid, which resulted in the establishment of the term for the description of any equimolar mixture of enantiomers.

If a mixture is not equimolar, the ratio of the enantiomers to each other is given by an enantiomeric excess (*ee*).

$$ee = \frac{[R] - [S]}{[R] + [S]}, \tag{1.1}$$

where $[R]$ and $[S]$ are the concentrations of the respective enantiomer.

Enantiomers possess identical physico-chemical properties, such as boiling and melting points, vapor pressure, solubility, diffusion constants etc. Without considering the small differences in energy due to parity violation, which are predicted to be about 10^{-14} J/mol[8], the two enantiomers have the same internal energies. Moreover, they have identical absorption spectra in UV, IR (Figure 1.3), or microwave frequency range. Mass spectra of enantiomers also show identical fragmentation. In the NMR, the differentiation between the enantiomers is possible, once chiral orientating media are used[9].

In spite of the same chemical and physical properties, the biological properties of enantiomers can be very different. This reflects in the first place in their different interactions with other chiral molecules. One of the examples in this context is our olfactory system. The receptors involved in our sense of smell are chiral. If they, for example, interact with the right-handed enantiomer of the monoterpene carvone, we perceive the odor as that of caraway, while the left-handed carvone smells like spearmint[10]. A similar example are the right- and left-handed enantiomers of limonene (orange vs. lemon odor)[11]. Also our sense of taste can be influenced by the absolute configuration of the enantiomers, interacting with the receptors of the gustatory system. Thus, while S-asparagine tastes bitter, its mirror image has a sweet taste[12].

Sometimes, one of the enantiomers can even have harmful, toxic effect, a fact which has to be considered in the development of new drugs containing chiral components. For instance, S-penicillamine is an antiarthritic drug, whereas R-penicillamine is highly toxic[12]. In pharmaceutical industries, 56% of the drugs currently in use are chiral products[13]. For this reason, there is a great demand on reliable methods for determining the absolute configuration and the purity (enantiomeric excess) of the enantiomers in mixtures.

In 1951, J. M. Bijvoet, a crystallographer at Utrecht University in the Netherlands, reported an X-ray crystal structure of sodium rubidium (+)-tartrate tetrahydrate[14]. This was the first example of the experimentally determined absolute configuration of an organic component[15]. In conventional X-ray crystallography, only the amplitude of the diffraction is measured, while no phase information is included. The Bijvoet method is based on the anomalous dispersion effects of heavy atoms, which can be measured very accurately[16]. This allows to extract the phase information and hence, to determine the absolute configuration of the component of interest. However, obtaining crystals can be challenging and sometimes even not possible. Another fact to consider is that the configuration observed in the solid state might not resemble the one in the liquid or in the gas phase. For this reason, a number of techniques such as optical rotatory dispersion (ORD)[17], circular dichroism (CD)[18], vibrational circular dichroism (VCD)[19], Raman optical activity (ROA)[20] and others were developed over the years for the liquid phase samples. A detailed discussion of them is beyond the scope of this chapter. Instead, only a brief overview with respect to their advantages and limitations will be given.

One of the oldest methods is polarimetry, which is used for the measurement of the enan-

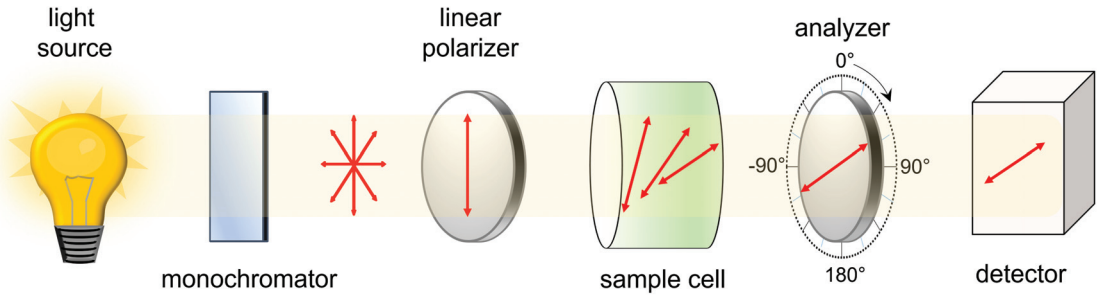

Figure 1.2: *Schematic representation of a set-up used in polarimetry for measuring optical activity of a chiral sample. By passing polychromatic light through an appropriate monochromator, a light source of a specific wavelength is obtained. Linearly polarized light is created in the next step using a linear polarizer. The polarizer and the analyzer are oriented perpendicular to each other, so no light reaches the detector. Once a sample cell containing chiral sample is placed between the polarizer and the analyzer, the polarization plane of the light passing through the sample cell is rotated.*

tiomeric optical activity. The principle behind it is the ability of enantiomers to rotate the plane of linearly polarized light, as mentioned above. The degree of rotation at a given temperature, concentration, and wavelength depends on the structure of a chiral molecule[21]. Achiral molecules do not show optical activity.

The concept of the instrumentation for measuring optical activity is simple. It is schematically presented in Figure 1.2. The instrument consists of a monochromator, a linear polarizer, an analyzer and a detector. To obtain a light source of a specific wavelength, polychromatic light is passed through an appropriate monochromator. Linearly polarized light is created in the next step using a linear polarizer. The polarizer is oriented perpendicular to the plane of the analyzer, so no light reaches the detector. Once a sample cell containing a chiral sample is placed between the polarizer, and the analyzer, the polarization of the light passing through the sample cell is rotated. The light can propagate to the detector. The angle by which the analyzer has to be rotated so that, again, no light can reach the detector is the measured optical rotation angle α.

For the sake of consistency and comparability, a parameter called the specific optical rotation is used for describing a chiral component. It is measured at 20 °C using a sodium lamp with the wavelength of 589.3 nm. Under such conditions, the specific optical rotation is designated as $[\alpha]_D^{20}$ and can be tabulated for different molecules.

Since the optical rotation of a chiral molecule in solute is dependent on the wavelength, the rotation angle α and the specific rotation $[\alpha]$ change as a function of wavelength[11]. This is the principle of the optical rotatory dispersion (ORD) measurements, where specific rotation is plotted as a function of wavelength at a given temperature. One distinguishes between positive and negative ORD plain curves depending on the value of optical rotation. This behavior is opposite for the two enantiomers. For complex biological systems such as proteins, ORD can be used to gain information on the three-dimensional structure[11].

However, the knowledge of specific rotation is not necessarily sufficient to determine the absolute configuration of a chiral molecule[11].

Using ORD for absolute configuration determination requires extensive quantum-mechanical calculations. Specific rotation is calculated at each wavelength of interest for an optimized geometry of a molecule under study. The signs of an ORD curve predicted in this way are compared to the ones of the experimentally obtained curve. If they match, then the absolute configuration of the calculated structure corresponds to the one of the molecules in the sample. Consequently, opposite signs for specific rotation mean opposite absolute configurations of the calculated and the experimental structures. If more than one conformer is present in the sample, the population-weighted sum of specific rotations at each of the given wavelengths should be used for a comparison with the experimental results. In addition to comparing signs, magnitudes of specific rotation have sometimes to be taken into account as well. This is necessary when a molecule of interest has several diastereomers. In such cases, the signs of the predicted ORD can agree with that of the experimentally measured ORD for more than one diastereomer[21]. Overall, an accurate computational prediction of ORD can be rather intense and time-consuming.

Another technique, circular dichroism (CD), makes use of the fact that enantiomers differently absorb right- (RCPL) and left- (LCPL) circularly polarized light. The difference in the molar extinction coefficients $\Delta\varepsilon$ of a given component for the LCPL vs. RCPL absorption, which determines the CD signal, can be written as[11]:

$$\Delta\varepsilon = \varepsilon_{LCPL} - \varepsilon_{RCPL}. \tag{1.2}$$

If the circularly polarized light is in the visible or in the ultraviolet wavelength range, electronic states of the molecule are involved in the CD spectroscopy. Molecules showing positive ORD plain curves also possess positive CD signals. In comparison to an ORD measurement, CD spectra have better resolution[11]. On the other hand, the CD signals are generally weaker than the signals produced by the ORD[11]. Another limitation of the electronic CD spectroscopy is that it cannot be applied to molecules lacking a chromophore.

Absorption of infrared light results in the excitation of molecular vibrational transitions. Techniques which take into account different vibrational states of the molecules are vibrational circular dichroism (VCD) and Raman optical activity (ROA). The measured VCD signal is the difference in the absorption of the LCPL and RCPL infrared light[19].

$$\Delta A = A_{LCPL} - A_{RCPL}. \tag{1.3}$$

This technique is of advantage for studying conformational characteristics even of big molecular systems such as proteins and nucleic acids. Using vibrational, instead of electronic, transitions allows to obtain more accurate structural information, since vibrational states are usually more numerous and better resolved than the electronic ones[22]. However, VCD has also some disadvantages compared to visible or ultraviolet CD. For instance, VCD signals

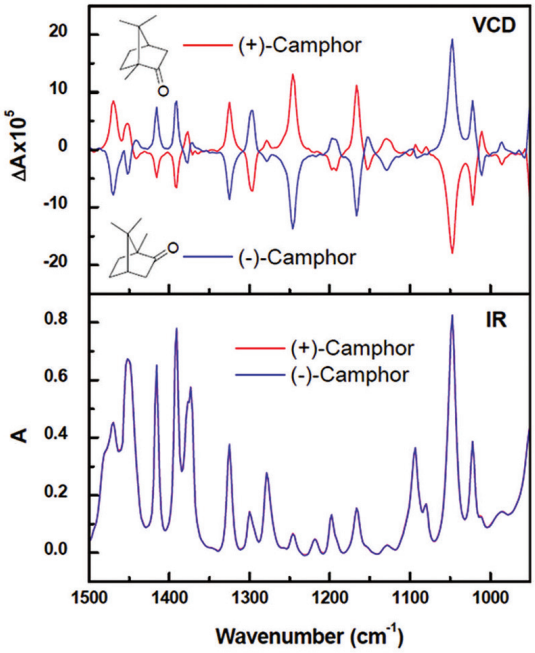

Figure 1.3: *Vibrational circular dichroism (VCD) (upper frame) and infrared (IR) (lower frame) spectra of (+)- and (–)-camphor[23]. The VCD spectra show opposite signs for the two enantiomers, which allows their differentiation. No differentiation between the enantiomers is possible based on their IR spectra. A: absorption, ΔA: difference in absorption of the left- and right- circularly polarized light.*

are much weaker, because the longer wavelengths, associated with the infrared region probe molecular chirality less efficiently than the shorter wavelengths of the visible region of electromagnetic spectrum[21]. Since the VCD-effect is so small, high-density samples are needed for the measurement. Additionally, CD spectra in the visible region have better signal-to-noise ratios than the VCD ones. This is due to the fact that detectors used for the visible region are significantly more sensitive than the ones which are in use for infrared spectral detection[21].

VCD measurements are performed mostly on liquid samples dissolved in inert solvents, because many of the chiral samples do not have enough vapor pressure for gas phase studies[21]. The sample has to be diluted to avoid sample aggregation and intermolecular hydrogen bonding which can make spectra interpretation very difficult[21]. The determination procedure of the absolute configuration is similar to that applied for an ORD measurement and also requires quantum-chemical calculations. Here the predicted signs of the vibrational bands in a VCD spectrum are compared to the experimentally observed ones. The different signs result from the differential absorption of LCPL and RCPL. The enantiomers of the same molecule have VCD spectra with opposite signs (e.g. camphor enantiomers, Figure 1.3). For several conformers present in the sample, a weighted average of their theoretical VCD spectra has to be considered. This average is built according to the Boltzmann-weighted population distribution of the conformers at the temperature used in the experiment. The experimental quantitative determination of conformational population is still challenging and belongs to

the topics which are not completely explored yet.

A specific kind of spectroscopy, which also addresses different vibrational states of a chiral molecule is Raman optical activity (ROA), based on the inelastic scattering of photons on a surface of matter (the Raman effect). The signal measured in ROA is the difference between the scattered intensities in RCPL and LCPL[11]:

$$ROA = I^{RCPL} - I^{LCPL}. \tag{1.4}$$

In contrast to VCD, water can be used as a solvent for ROA measurements, which allows to have conditions closer to the biological ones. Like VCD, ROA is applicable not only to small but also to very complex organic molecules such as carbohydrates, proteins and even intact viruses[24;25]. On the other hand, ROA is even less sensitive than VCD and requires larger sample amounts[22]. Since it also involves vibrational transitions, it provides more stereochemical information than CD spectroscopy in the visible or the ultraviolet frequency range[11]. It also allows the study of molecules, which lack a chromophore and are therefore inaccessible to visible or ultraviolet CD.

In ROA spectroscopy the absolute configuration determination is again based on a comparison between calculated and experimental spectra for all molecules of interest. However, the prediction of ROA spectra is more difficult than of VCD ones and requires calculation of electric dipole-electric dipole, electric dipole-magnetic dipole, and electric dipole-electric quadrupole polarizability tensors[21].

In summary, the major advantage of the techniques listed above is their applicability to a broad range of biologically relevant molecules, from small to very complex ones. For this reason, some of them, such as VCD, have become now methods of choice used in analytical labs and by pharmaceutical companies for absolute configuration determination. One of the disadvantages of the CD techniques is that they are based on weak effects, i.e. on higher order electric quadrupole and magnetic interaction terms[26]. Therefore, the obtained signals are rather weak, and high-density liquid samples are required. It should be also kept in mind that the produced signal is a weighted average over the conformers present in solution. In general, good predictions from quantum-chemical calculations are necessary for an interpretation of the observed results. Finally, the measurements are conducted mostly on liquid samples. The spectra show, therefore, peak broadening resulting from solvent effects[26].

To overcome this last drawback, several techniques for studying chiral samples in the gas phase were introduced recently. One of them is photoelectron circular dichroism (PECD). For a PECD measurement, a chiral sample is subjected to circularly polarized synchrotron radiation or femtosecond laser ionization[27;28]. The principle of PECD is manifested in an observed asymmetry of the photoelectron angular distribution with respect to the light propagation direction[26]. The sensitivity of this technique is higher compared to CD (on the order of 10%), because the observed effects are attributed to an electric dipole interaction[29]. PECD can be used for an accurate determination of the enantiopurity of a given sample[30].

In our lab, another powerful resonant technique for chiral-sensitive experiments in the gas phase was developed. It is called microwave three-wave mixing (M3WM) and is based on broadband rotational spectroscopy[31]. M3WM makes use of the advantages of rotational spectroscopy, namely high resolution and conformer selectivity. It provides additional information to that obtained with broadband rotational spectroscopy such as an unambiguous differentiation of the enantiomers, even in complex mixtures. The theoretical background for understanding this technique is given in Chapter 2, while instrumentation details for performing a M3WM experiment are provided in Chapter 3. It was applied to a range of chiral samples with the aim to determine their (*ee*) and the absolute configuration[32–34]. It was also used in the framework of this thesis for the chiral analysis of the essential oil constituents such as menthone, isomenthone (Chapter 4), pulegone (Chapter 6), and menthyl acetate (Chapter 7). An extension of M3WM by employing microwave five-pulse scheme for a coherent enantiomer-selective population enrichment in the rotational levels of choice[35] is described in Chapter 8. Finally, a state-specific enrichment of the conformers of cyclohexylmethanol, a molecule without stereogenic center[36], is presented in Chapter 9.

Bibliography

[1] E. B. Wilson. Microwave Spectroscopy in Chemistry. *Science*, 162(3849):59–66, 1968.

[2] J.-S. Wang, G. Wang, X.-Q. Feng, T. Kitamura, S.-W. Yu, and Q.-H. Qin. Hierarchical chirality transfer in the growth of Towel Gourd tendrils. *Sci. Rep.*, 3, 2013.

[3] J. Cronin and J. Reisse. Chirality and the Origin of Homochirality. In B. Barbier, M. Gargaud, C. de Duve, H. Martin, and J. Reisse, editors, *Lectures in Astrobiology*, pages 473–515. Springer Berlin Heidelberg, 12, 2005.

[4] W. Kelvin. The Molecular Tactics of a Crystal. Robert Boyle lecture. Clarendon Press, 1894.

[5] V. Prelog. Nobel Lecture. World Scientific Publishing Co, December 12, 1975.

[6] R. S. Cahn, C. Ingold, and V. Prelog. Spezifikation der molekularen Chiralität. *Angew. Chem.*, 78(8):413–447.

[7] A. Findlay. Use of the Name 'Racemic Acid'. *Nature*, 140(22), 1937.

[8] S. Mason and G. Tranter. The parity-violating energy difference between enantiomeric molecules. *Chem. Phys. Lett.*, 94(1):34 – 37, 1983.

[9] B. Luy. Distinction of Enantiomers by NMR Spectroscopy Using Chiral Orienting Media. *J. Indian Inst. Sci*, 90:119–132, 2010.

[10] J. C. Brookes, A. P. Horsfield, and A. M. Stoneham. Odour character differences for enantiomers correlate with molecular flexibility. *J. R. Soc. Interface*, 6(30):75–86, 2009.

[11] U. Meierhenrich. Amino Acids and the Asymmetry of Life: Caught in the Act of Formation. Advances in Astrobiology and Biogeophysics. Springer Berlin Heidelberg, 2008.

[12] M. Quack. Structure and Dynamics of Chiral Molecules. *Angew. Chem. Int. Ed.*, 28(5):571–586, 1989.

[13] L. Ai Nguyen, H. He, and C. Pham-Huy. Chiral Drugs: An Overview. *Int. J. Biomed. Sci.*, 2:85–100, 06 2006.

[14] B. E. Erickson. Sodium Rubidium (+)-Tartrate. X-ray crystallography nailed stereochemistry of organic compound. *C&EN*, 92(32), 2014.

[15] L. A. Nafie and R. K. Dukor. CHAPTER 15 - Vibrational optical activity in chiral analysis. In K. W. Busch and M. A. Busch, editors, *Chiral Analysis*, pages 505 – 544. Elsevier, Amsterdam, 2006.

[16] J. M. Bijvoet, A. F. Peerdeman, and A. J. Van Bommel. Determination of the Absolute Configuration of Optically Active Compounds by Means of X-Rays. *Nature*, 168:271–272, 08, 1951.

[17] C. Djerassi, H. Wolf, D. Lightner, E. Bunnenberg, K. Takeda, T. Komeno, and K. Kuriyama. Optical rotatory dispersion studies—LXXXIII; thiosteroids—IX: Optical rotatory dispersion and circular dichroism of episulfides and trithiocarbonates. *Tetrahedron*, 19(10):1547 – 1561, 1963.

[18] P. Crabbé. 3 - Optical Rotatory Dispersion and Circular Dichroism in Organic Chemistry. In F. C. Nachod and J. J. Zuckerman, editors, *Determination of Organic Structures by Physical Methods*, pages 133 – 205. Academic Press, 1971.

[19] L. A. Nafie, T. A. Keiderling, and P. J. Stephens. Vibrational circular dichroism. *J. Am. Chem. Soc.*, 98(10):2715–2723, 1976.

[20] L. D. Barron. Raman optical activity: a new probe of stereochemistry and magnetic structure. *Acc. Chem. Res.*, 13(3):90–96, 1980.

[21] P. L. Polavarapu. CHAPTER 14 - Determination of molecular stereochemistry using optical rotatory dispersion, vibrational circular dichroism and vibrational Raman optical activity. In K. W. Busch and M. A. Busch, editors, *Chiral Analysis*, pages 461 – 504. Elsevier, Amsterdam, 2006.

[22] T. Wu, X.-Z. You, and P. Bouř. Applications of chiroptical spectroscopy to coordination compounds. *Coord. Chem. Rev.*, 284:1 – 18, 2015.

[23] Y. He, B. Wang, R. Dukor, and L. Nafie. Determination of Absolute Configuration of Chiral Molecules Using Vibrational Optical Activity: A Review. *Appl. spectrosc.*, 65:699–723, 07 2011.

[24] L. D. Barron. *Molecular Light Scattering and Optical Activity*. Cambridge University Press, 2 edition, 2004.

[25] L. D. Barron. Compliments from Lord Kelvin. *Nature*, 446:505–506, 2007.

[26] D. Patterson and M. Schnell. New studies on molecular chirality in the gas phase: enantiomer differentiation and determination of enantiomeric excess. *Phys. Chem. Chem. Phys.*, 16:11114–11123, 2014.

[27] N. Böwering, T. Lischke, B. Schmidtke, N. Müller, T. Khalil, and U. Heinzmann. Asymmetry in Photoelectron Emission from Chiral Molecules Induced by Circularly Polarized Light. *Phys. Rev. Lett.*, 86:1187–1190, 2001.

[28] C. Lux, M. Wollenhaupt, T. Bolze, Q. Liang, J. Köhler, C. Sarpe, and T. Baumert. Circular Dichroism in the Photoelectron Angular Distributions of Camphor and Fenchone from Multiphoton Ionization with Femtosecond Laser Pulses. *Angew. Chem. Int. Ed.*, 51(20):5001–5005, 2012.

[29] I. Powis. Photoelectron circular dichroism of the randomly oriented chiral molecules glyceraldehyde and lactic acid. *J. Chem. Phys.*, 112(1):301–310, 2000.

[30] L. Nahon, L. Nag, G. A. Garcia, I. Myrgorodska, U. Meierhenrich, S. Beaulieu, V. Wanie, V. Blanchet, R. Géneaux, and I. Powis. Determination of accurate electron chiral asymmetries in fenchone and camphor in the VUV range: sensitivity to isomerism and enantiomeric purity. *Phys. Chem. Chem. Phys.*, 18:12696–12706, 2016.

[31] D. Patterson, M. Schnell, and J. M. Doyle. Enantiomer-specific detection of chiral molecules via microwave spectroscopy. *Nature*, 497:475–478, 2013.

[32] V. A. Shubert, D. Schmitz, C. Medcraft, A. Krin, D. Patterson, J. M. Doyle, and M. Schnell. Rotational spectroscopy and three-wave mixing of 4-carvomenthenol: A technical guide to measuring chirality in the microwave regime. *J. Chem. Phys.*, 142(21):214201, 2015.

[33] V. A. Shubert, D. Schmitz, and M. Schnell. Enantiomer-sensitive spectroscopy and mixture analysis of chiral molecules containing two stereogenic centers – Microwave three-wave mixing of menthone. *J. Mol. Spectrosc.*, 300:31 – 36, 2014.

[34] V. A. Shubert, D. Schmitz, D. Patterson, J. M. Doyle, and M. Schnell. Identifying Enantiomers in Mixtures of Chiral Molecules with Broadband Microwave Spectroscopy. *Angew. Chem. Int. Ed.*, 53(4):1152–1155.

[35] C. Pérez, A. L. Steber, S. R. Domingos, A. Krin, D. Schmitz, and M. Schnell. Coherent Enantiomer-Selective Population Enrichment Using Tailored Microwave Fields. *Angew. Chem. Int. Ed.*, 56(41):12512–12517, 2017.

[36] C. Pérez, A. L. Steber, A. Krin, and M. Schnell. State-Specific Enrichment of Chiral Conformers with Microwave Spectroscopy. *J. Phys. Chem. Lett.*, 9(16):4539–4543, 2018.

2

Theoretical background

2.1 Introduction

The main goal of molecular spectroscopy is to provide a detailed characterization of molecules and molecular complexes with respect to their structural and dynamical properties. Depending on the wavelength of the electromagnetic radiation interacting with the molecular system of interest, rotational, vibrational and electronic spectroscopy techniques were developed over the years. Rotational spectroscopy is the main focus of this work. Pure rotational spectra are observed predominantly in the frequency range from 1 GHz to 1 THz, from microwaves (or also centimeter waves) to submillimeter waves[1]. Some major aspects of the theory behind this technique will be summarized in this chapter.

Rotational spectroscopy is a useful analytical tool with a broad range of applications. It is well-known for its conformer-selectivity and exceptional accuracy in structure determination. Thus, information about bond lengths and angles in the molecule of interest can be obtained purely from experimental data without the necessity of high-level quantum chemical calculations. Nevertheless, computational methods typically aid the interpretation of complex broadband rotational spectra. Rotational spectroscopy also provides information about the inter- and intramolecular dynamics, and even the electronic structure. One of the research fields, where this technique became highly important, is astrochemistry. More than 200 molecules including ions and radicals could be identified in the interstellar space based on their rotational spectra. These molecules belong to the classes of hydrides, oxides, sulphides,

[1] This chapter is mainly based on the following literature:

- Handbook of High-resolution Spectroscopy, Quack, M. (editor), *John Wiley & Sons*, 1st edition, 2011
- Microwave Spectroscopy, Townes, C.H. and Schawlow, A.L., *Dover Publications*, 2012
- Molecular Quantum Mechanics, Atkins, P.W. and Friedman, R.S., *OUP Oxford*, 5th edition, 2011
- Molekülphysik und Quantenchemie: Einführung in die experimentellen und theoretischen Grundlagen, Haken, H. and Wolf, H.C., *Springer Berlin Heidelberg*, 5th edition, 2006

hydrocarbons, aldehydes, ketones, alcohols, amides[2] etc. The heaviest molecular component identified with rotational spectroscopy in the interstellar medium so far is the cyanopolyyne $HC_{11}N$[3].

The two major requirements for the applicability of this technique are that the molecule can be brought into the gas phase and that it has a permanent electric dipole moment. The later aspect is a gross selection rule of rotational spectroscopy. Other specific selection rules for different types of molecular rotors will be summarized in the following sections.

2.2 Energies of different molecular rotors

For the sake of simplicity, a case of a molecular rigid rotor will be introduced first. In a rigid rotor, atoms are thought to be connected by a fixed distance r, i.e., the effects resulting from vibrations or centrifugal distortions are ignored.

Based on their moments of inertia, molecules can be classified as linear, symmetric, spherical or asymmetric rotors or tops, which are depicted in Figure 2.1. To describe their rotational energy, three mutually orthogonal rotational axes a, b, and c and the moments of inertia I_a, I_b, and I_c for the rotation around these axes (principal moments of inertia) are required.

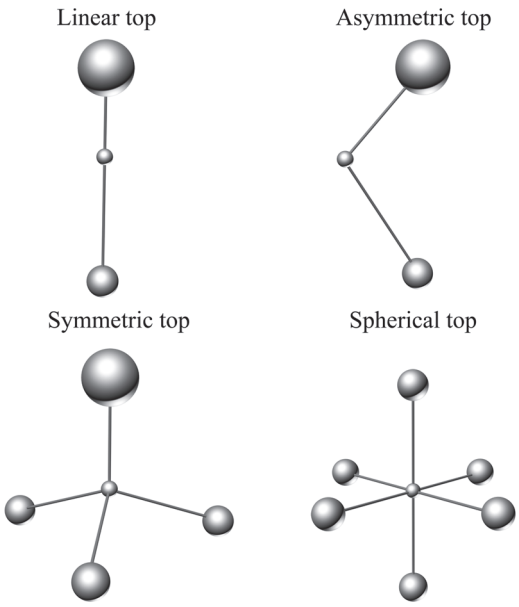

Figure 2.1: *Classification of different molecular rigid rotors depending on their moments of inertia around the three principal axes a, b and c. Linear top: I_a=0, I_b = I_c; asymmetric top: $I_a \neq I_b \neq I_c$; symmetric top: prolate tops (as the example depicted here) $I_a < I_b = I_c$, oblate tops $I_a = I_b < I_c$; spherical top: $I_a = I_b = I_c$.*

There are several possible ways to assign the molecular axes x, y, z to the principal axis system (a, b, c). These possible representations are summarized in Table 2.1.

Table 2.1: *Identification of the molecular-fixed coordinates x, y, z with the principal axes a, b, c. Superscripts r and l designate the right- and the left-handed coordinate systems respectively. Adapted from Ref. 1.*

Molecule-fixed coordinates	Representation					
	I^r	II^r	III^r	I^l	II^l	III^l
x	b	c	a	c	a	b
y	c	a	b	b	c	a
z	a	b	c	a	b	c

The rigid rotor rotational Hamiltonian is given as:

$$\hat{H} = \hbar^2\Big(\frac{\hat{J}_a^2}{2I_a} + \frac{\hat{J}_b^2}{2I_b} + \frac{\hat{J}_c^2}{2I_c}\Big), \tag{2.1}$$

where $\hat{J}$ is the dimensionless angular momentum operator.

In rotational spectroscopy, the Hamiltonian is commonly expressed using rotational constants A, B, C. By convention, $A \geq B \geq C$. The equation 2.1 can therefore be written as:

$$\hat{\mathcal{H}} = \frac{\hat{H}}{h} = A\hat{J}_a^2 + B\hat{J}_b^2 + C\hat{J}_c^2. \tag{2.2}$$

The rotational constants in MHz are obtained from the moments of inertia in the following way[1]:

$$A = \frac{h}{8\pi^2 I_a}, \qquad B = \frac{h}{8\pi^2 I_b}, \qquad C = \frac{h}{8\pi^2 I_c}. \tag{2.3}$$

Each component of the angular momentum $\hat{J}_a$, $\hat{J}_b$ and $\hat{J}_c$ commutes with the square of the total angular momentum $\hat{\boldsymbol{J}}^2$ (e.g. $[\hat{\boldsymbol{J}}^2, \hat{J}_a]$=0). Eigenvalues and matrix elements of angular momentum operators are derived from these commutation relations and with the help of the so-called ladder operators $\hat{J}_\pm = \hat{J}_x \pm i\hat{J}_y$ [1;4]. Using commutation relations $[\hat{\boldsymbol{J}}^2, \hat{J}_z]$=0 and $[\hat{\boldsymbol{J}}^2, \hat{J}_Z]$=0, the following matrix elements can be constructed[4]:

$$\langle JKM|\hat{\boldsymbol{J}}^2|JKM\rangle = J(J+1) \tag{2.4}$$

$$\langle JKM|\hat{J}_z|JKM\rangle = K \tag{2.5}$$

$$\langle JKM|\hat{J}_Z|JKM\rangle = M \tag{2.6}$$

with the quantum numbers J= 0,1,2...; K= -J, -J+1...,J; M = -J, -J+1...J[1].

The quantum number K is the projection of the angular momentum on the internal figure axis z of a molecule. The quantum number M measures the projection of the angular momentum on the laboratory-fixed Z-axis. Thus, wave functions $|JKM\rangle$ are simultaneous quantum numbers of the operators $\hat{\boldsymbol{J}}^2$, $\hat{J}_z$ and $\hat{J}_Z$[1].

In following, different cases of rigid rotors (see Figure 2.1) with respect to their rotational energies will be discussed.

2.2.1 Symmetric tops

Symmetric tops (Figure 2.1) have at least one C_3 (or higher order) symmetric axis. For this reason, two of their moments of inertia and subsequently their rotational constants are equal. They can be classified depending on the relative magnitudes of their rotational constants as

- Prolate tops, with $A > B$, $B = C$ (e.g. NH_3)
- Oblate tops, with $C < B$, $B = A$ (e.g. C_6H_6)

The Hamiltonian in the I^r representation for a prolate top is given as :

$$\hat{\mathcal{H}} = A\hat{J}_a^2 + B(\hat{J}_b^2 + \hat{J}_c^2) = B\hat{\boldsymbol{J}}^2 + (A-B)\hat{J}_z^2. \tag{2.7}$$

The energy eigenvalues are[1]:

$$\mathcal{E}(J,K,M) = BJ(J+1) + (A-B)K^2. \tag{2.8}$$

Consequently, for an oblate top with III^r representation the Hamiltonian can be written as:

$$\hat{\mathcal{H}} = B\hat{J}_a^2 + C(\hat{J}_b^2 + \hat{J}_c^2) = B\hat{\boldsymbol{J}}^2 + (C-B)\hat{J}_z^2 \tag{2.9}$$

with the eigenvalues[1]:

$$\mathcal{E}(J,K,M) = AJ(J+1) + (C-A)K^2. \tag{2.10}$$

The selection rules for the rotational transitions of a symmetric top are: $\Delta J = \pm 1$, $\Delta K = 0$, $\Delta M_J = 0, \pm 1$. Each energy level $\mathcal{E}(J,K \neq 0)$ is $2(2J+1)$ fold degenerate, because M can take $2J+1$ different values for a given value of J, and K can be either positive or negative[5].

2.2.2 Spherical tops

Examples of spherical rotors (Figure 2.1) include SF_6, CH_4, and other molecules, which belong to the tetrahedral, octahedral, and icosahedral point groups[5]. Here all three principal

moments of inertia are equal. The Hamiltonian can therefore be simply written as:

$$\hat{\mathcal{H}} = B\hat{\boldsymbol{J}}^2. \tag{2.11}$$

The eigenvalues are :

$$\mathcal{E}(J,K,M) = BJ(J+1). \tag{2.12}$$

The total degeneracy of the energy levels is $(2J+1)^2$. Note that due to symmetry, these molecules do not possess a permanent non-zero dipole moment, which could interact with the microwave radiation. For this reason, symmetric tops cannot be observed via pure absorption rotational spectroscopy. However, if such molecules are excited to degenerate vibrational states, it is possible to observe rotational transitions due to an effective dipole moment resulting from the vibrations[6].

2.2.3 Linear tops

In linear tops (Figure 2.1), the angular momentum vector is perpendicular to the molecular axis. The moments of inertia $I_a \ll I_b = I_c$. For most purposes, I_a can be taken to be zero. Here the rotational energy Hamiltonian in I^r is the same as in the spherical top

$$\hat{\mathcal{H}} = B\hat{\boldsymbol{J}}^2 \tag{2.13}$$

with the eigenvalues:

$$\mathcal{E}(J,K,M) = BJ(J+1). \tag{2.14}$$

In contrast to the spherical tops, where both J and M quantum numbers are needed for the description of motion, K=0 for the linear tops[5]. For this reason, the energy levels are $(2J+1)$-fold degenerate. The selection rules for the rotational transitions of a linear top are therefore:

$\Delta J = \pm 1$, $\Delta M_J = 0, \pm 1$.

From the equation 2.14 and the selection rules follows that the rotational transitions of a linear top have in the absence of centrifugal distortions the uniform spacing of $2B$ in the observed rotational spectrum[5].

2.2.4 Asymmetric tops

All molecules analyzed in the scope of this work belong to the class of asymmetric tops (Figure 2.1). In an asymmetric top all three principal moments of inertia are different ($I_a \neq$

$I_b \neq I_c$). One way to describe the energy levels of an asymmetric top is by examining how their behavior starts to deviate from the oblate and prolate symmetric tops as two limiting cases[6].

As mentioned in section 2.2.1, for a prolate symmetric top the rotational constant $B = C$, while for an oblate one $B = A$. The value of B varies between A and C in dependence of the degree of the molecular asymmetry. If there is a small difference between B and C, or B and A, the top is called near prolate or near oblate. The behavior of the energy levels with changing B is depicted schematically in Figure 2.2, where the left-hand side represents the limiting case of a prolate, while the right hand-side the case of an oblate symmetric top.

The previously introduced quantum numbers J, M and K are necessary for the description of an asymmetric top. Since there is no component of the angular momentum, which is constant along any direction in the rotating asymmetric molecule, the energy levels are specified by giving the values of K_a for a limiting prolate and K_c for a limiting oblate symmetric top. The notation $J_{K_aK_c}$ is given in Figure 2.2 and used throughout this manuscript.

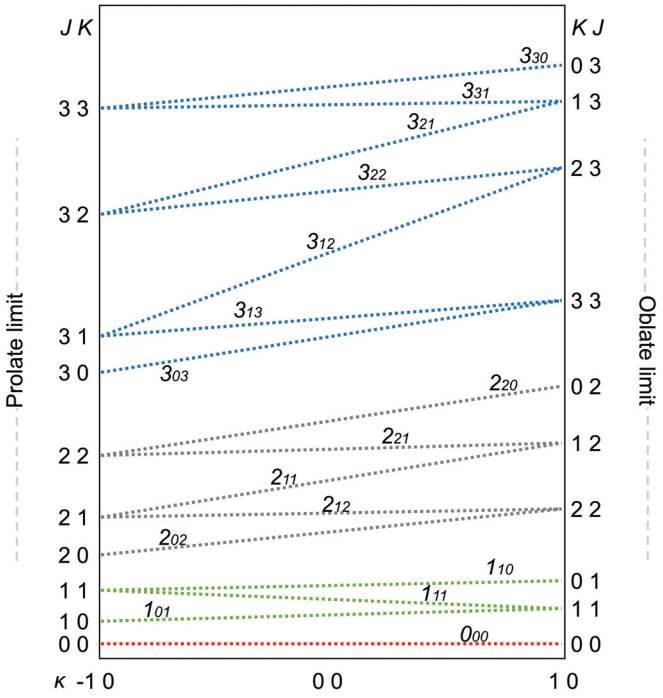

Figure 2.2: *The energy levels of the asymmetric top as a function of the Ray's parameter κ[7] for the two limiting cases of a prolate and an oblate symmetric top. The notation $J_{K_aK_c}$ is used. For a better visualisation, levels with different J values are depicted in different colors. Adapted from Ref. 1.*

The Ray's parameter κ is commonly used to indicate the degree of asymmetry[7]. It ranges from -1 (for the limiting case of a prolate symmetric rotor) to +1 (for the limiting case of an oblate symmetric rotor)

$$\kappa = \frac{2B - A - C}{A - C}. \tag{2.15}$$

From Figure 2.2 it can be seen that the levels with the same J do not cross. Due to the asymmetry, levels that are degenerate for symmetric top are split for $K \neq 0$. The amount of splitting is proportional to the molecular degree of asymmetry[6].

The Hamiltonian for an asymmetric top can be expressed in the form[1]:

$$\hat{\mathcal{H}} = \frac{1}{2}(A+C)\hat{\boldsymbol{J}}^2 + \frac{1}{2}(A-C)\hat{h}(\kappa) \tag{2.16}$$

with

$$\hat{h}(\kappa) = \hat{J}_a^2 + \kappa\hat{J}_b^2 - \hat{J}_c^2. \tag{2.17}$$

The eigenvalues of the asymmetric rotor are given as:

$$\mathcal{E}(J,K,M) = \frac{1}{2}(A+C)J(J+1) + \frac{1}{2}(A-C)E_J(\kappa). \tag{2.18}$$

Here $E_J(\kappa)$ is a numerical function, which needs to be evaluated for the particular case and the amount of symmetry[6]. The values for $E_J(\kappa)$ are tabulated. Alternatively, sophisticated approximation methods[8;9] were developed to evaluate $E_J(\kappa)$. Nowadays, $E_J(\kappa)$ can also be determined numerically.

The selection rules for an asymmetric top are more complicated than in the previously discussed cases. One of the reasons behind it is the increased number of separate levels[6]. Additionally, in an asymmetric molecule the dipole moment may lie in any arbitrary direction with respect to the principal axes of inertia. However, sometimes the dipole moment lies parallel to one of the principal axes a, b or c[6]. The selection rules emanate from the symmetry properties of the asymmetric-top wave functions. For the limiting case of a symmetric prolate rotor, the wave function is symmetric when K_a is even, and antisymmetric when K_a is odd. Consequently, for the limiting case of a symmetric oblate top, the wave function is even, when K_c is even, antisymmetric when K_c is odd[6]. The resulting selection rules for the rotational transitions in an asymmetric top are summarized in Table 2.2. The quantum numbers describing a transition between two rotational states are J, M, K_a, K_c for one state, and J', M', K_a', K_c' for the other one. If (K_a-K_a', K_c K_c') is (even, odd), the transition dipole matrix element is proportional to μ_a, if the difference is (odd, odd), its is proportional to μ_b, and if it is (odd, even), the transition dipole matrix element is proportional to μ_c (see Table 2.2)[10]. The transition is forbidden if (K_a-K_a', K_c K_c') is (even, even). If the dipole moment is not parallel to any principal axis, it may be resolved into its components along the principal axes.

The three types of transitions, a-, b- and c-type, commonly observed in rotational spectra emanate from these selection rules. If the dipole moment has non-zero components along all three principal axes, all types of rotational transitions consistent with the general selection rule $\Delta J = 0, \pm 1$ are allowed and can be observed depending on their intensity in the spectrum[6].

Table 2.2: *Selection rules for an asymmetric top. Here* $\Delta K_a = (K_a\text{-}K'_a)$, $\Delta K_c = (K_c\text{-}K'_c)$. *Adapted from Ref. 1 and Ref. 6.*

Type of transition	dipole	ΔK_a	ΔK_c
a	μ_a	$0, \pm 2, \ldots$	$\pm 1, \pm 3, \ldots$
b	μ_b	$\pm 1, \pm 3, \ldots$	$\pm 1, \pm 3, \ldots$
c	μ_c	$\pm 1, \pm 3, \ldots$	$0, \pm 2, \ldots$

2.2.5 Centrifugal distortion

So far, the rotational energy of the different molecular tops was given for the case of a rigid rotor. However, for higher J values this approximation cannot be applied, as the experimentally measured energies differ from the ones calculated for a rigid rotor. This is due to the fact that with increasing rotational excitation the molecule is stretched. Because of this centrifugal distortion, moments of inertia also increase, resulting in a decrease of the rotational constants[5;11]. That is why the rotational levels for higher J in a non-rigid rotor are less apart than it is predicted with a rigid rotor model (Figure 2.3).

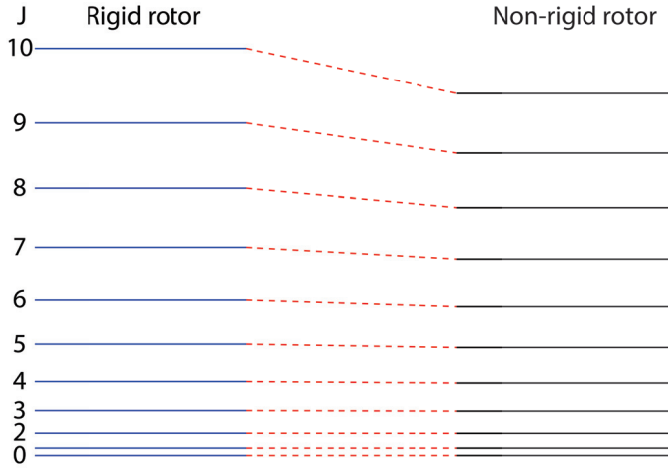

Figure 2.3: *Energy levels of a rigid rotor in comparison to a non-rigid one. The rotational levels for higher J are less apart than it is predicted for a rigid rotor, due to centrifugal distortion. For visualization purpose, the centrifugal distortion constant D is assumed to be* $10^{-3}B$. *Adapted from Ref. 11.*

Although the centrifugal distortion has to be considered in order to accurately determine the positions of rotational transitions, its effects still represent only a small fraction of the rotational energy which is accounted for mainly by the rigid rotor term. Therefore in many cases it can be treated as a perturbation of the rigid rotor Hamiltonian[12].

For a diatomic molecule, the more accurate description of rotational energy levels by considering centrifugal distortions is:

$$\mathcal{E}(J,K,M) = BJ(J+1) - DJ^2(J+1)^2, \tag{2.19}$$

where D is the centrifugal distortion constant.

$$D = \frac{\hbar^3}{4\pi kc\mu^2 R^6}, \tag{2.20}$$

with k being the force constant of the bond, and R the internuclear bond length in the rigid rotor[5]. Since D depends on the elastic force constant k for the atomic vibration around the bond, the study of centrifugal distortion can provide useful information for the elucidation of interatomic forces and bonding[12].

2.3 Determination of molecular structure

One of the main questions addressed with rotational spectroscopy is the molecular structure determination. A first idea about the molecular geometry can be obtained with quantum chemistry. If there is a good agreement between the calculated and the experimental rotational parameters, the calculated structure provides general information about the internal parameters such as bond lengths, bond angles and inter/intramolecular interactions of the molecules of interest. Calculations are often used to guide the assignment of the experimental data. The rotational spectroscopy on the other side allows to achieve an unprecedented accuracy in the experimental structural determination. The obtained results can be further used for benchmarking computational methods.

The principle behind structure determination with rotational spectroscopy is as follows. The rotational constants are inversely proportional to the moments of inertia and thus they carry important structural information. For a non-linear molecule with N atoms 3N–6 coordinates are required for its characterization in a Cartesian system. Thus, one set of constants obtained after the assignment of a rotational spectrum is not sufficient to determine all structural parameters of the respective molecule. These parameters can be obtained by determining the rotational constants of the parent molecule (the isotopically most abundant species) and of its isotopologues. Due to the high resolution and the sensitivity of rotational spectroscopy, isotopically substituted species can be observed in the spectrum in natural abundance. Since within the Born-Oppenheimer approximation the equilibrium structure r_e is independent of nuclear mass[1], the assignment of the isotopologues can be used for structure determination. The r_e structure gives the best comparability between experimental results and theory, because it is free of any vibrational effects (zero-point motions). However, in the structure measured with rotational spectroscopy zero-point motions are present.

Several methods were developed with the aim to compensate for zero-point motions and to obtain the results for the molecular structure close to the virtual r_e values. One of the established methods for an experimental structure determination is based on solving the so-called Kraitchman's equations[13]. The structure obtained with this approach is referred to as the r_s structure. The Cartesian coordinates of the substituted nuclei are determined from the principal planar moments of inertia[1].

The principal planar second moments of inertia P are defined as a linear combination of the measured moments of inertia I_a, I_b, I_c :

$$P_a = \frac{1}{2}(I_b + I_c - I_a). \tag{2.21}$$

The squares of the coordinates for a substituted nucleus can then be determined in the following way[13]:

$$r_{ia}^2 = \frac{1}{\mu}\frac{(P'_a - P_a)(P'_b - P_a)(P'_c - P_a)}{(P_b - P_a)(P_c - P_a)}, \tag{2.22}$$

where μ is the reduced mass dependent on the mass of the parent and of the isotopologue. P and P' are the planar second moments of inertia of the parent and of the isotopic species respectively.

This approach for the calculation of the coordinates has some limitations. First of all, for small values of r_{ia} ($r_{ia} \leqslant 0.1$ Å) the errors in $P'_a - P_a$ and $P'_a - P_b$ can be large, resulting in negative (imaginary) values for the coordinates[1]. Moreover, since only the squares of the coordinates are calculated, the sign of the coordinate is undetermined. Sometimes, it is taken from the calculated models of the respective parent, or determined according to chemical intuition.

The structure determination with Kraitchman's method can be applied only to mono-isotopically substituted species. An alternative approach for the experimental determination of molecular bond lengths and angles is to use a least-squares calculation, which is also based on the differences between the moments of inertia of the parent and of the isotopologues[14]. The structure determined with the non-linear least-squares procedure is called the effective structure r_0. In contrast to the r_s fit, this approach takes advantage of multiple substitution (if available). It does not fail for small nuclear coordinates[15]. However, the method is not solely based on experimental values. Structural parameters, which cannot be determined experimentally can be taken e.g., from r_s coordinates already known[15] or from the calculated structure.

The software STRFIT[14] was developed for the r_0 structure calculation. The fit requires a good estimation of the initial structural parameters. During the fitting process some of the structural parameters can be kept fixed at constant values (if e.g. the coordinates are already known). For some molecular systems discussed in this work, both r_s and r_0 structures were determined.

2.4 Internal rotation

Additionally to the overall molecular rotation, some molecules possess substituents, which can exhibit an internal rotation. Typical internal rotation groups are methyl tops. Internal rotation means that one or several tops of the molecule can rotate about a single bond relative

to the rest of the molecule (frame)[16]. Depending on the potential barrier of such motion and the mass of the moving group, splittings due to the internal dynamics can be observed in the spectra. This fine structure results from the interaction of the internal and the overall motions[12]. Thus, the internal rotation barrier can be determined directly from the rotational spectrum. The study of internal dynamics is of high chemical interest, since the barrier height depends on the molecular properties such as possible steric repulsion and the characters of the chemical bonds[16].

The internal rotation of two parts of a molecule relative to each other can be described by a torsional angle α (in the interval from α=0 to α=2π)[12]. During the internal rotation the potential energy changes as a function of α, depending on the molecular symmetry. The general form for a barrier V_N with N-fold symmetry can be given by a Fourier series expansion as[12]:

$$\left[-\frac{\hbar^2}{2I}\frac{d^2}{d\alpha^2} + V(\alpha) \right] \psi(\alpha) = E\psi(\alpha) \tag{2.23}$$

$$V(\alpha) = \frac{V_N}{2}(1 - \cos N\alpha) + \frac{V_{2N}}{2}(1 - \cos 2N\alpha) + ... \tag{2.24}$$

Commonly, only the first terms of this expansion are considered. For example, the approximation for a three-fold potential barrier:

$$V(\alpha) = \frac{V_3}{2}(1 - \cos 3\alpha) \tag{2.25}$$

gives good results for the most methyl tops. Such periodic potential is depicted in Figure 2.4. The frequency of torsional oscillation ν can be given based on the harmonic oscillator approximation for the torsional energy levels as:

$$\nu = \frac{3}{2\pi}\left(\frac{V_3}{2I_r}\right)^{1/2}, \tag{2.26}$$

where I_r is the reduced moment of inertia for the relative motion of the two groups[12]. This approximation is valid in the limit of an infinitely high barrier. In this case, each torsional state ν with an energy $h\nu(n+1/2)$ is three-fold degenerate. For a finite barrier, the quantum-mechanical tunnelling effect leads to a splitting of this three-fold degeneracy, depending on both height and width of the barrier into two levels: a doubly degenerate level labelled E and a nondegenerate level A (see Figure 2.4)[12]. The torsional sublevel spacing increases with energy[12].

If more than one top is involved in the internal rotation, the splitting scheme becomes more complex. For the case that communication between the two internally rotating tops can be neglected, they can be described with the local-mode theory. This means that the tops are treated independently, and their internal rotations are turned on successively[17]. An example

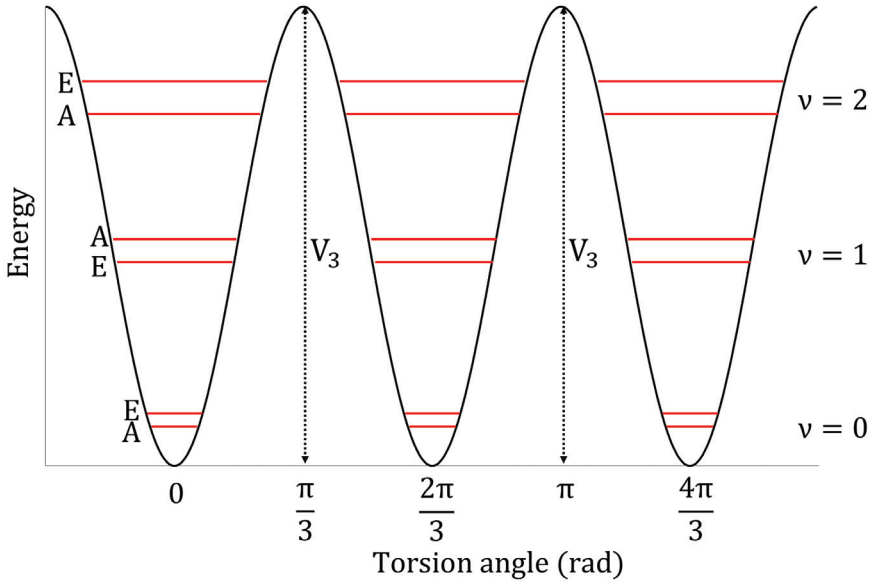

Figure 2.4: *Schematic representation of the potential function and the torsional energy levels. The levels are labelled with respective quantum numbers ν. The torsional sublevels A and E are denoted. The three-fold barriers V_3 are highlighted. Adapted from Ref. 12.*

of the coupling scheme for the two tops is given in Figure 2.5. The nomenclature adopted here is based on the one introduced in Ref. 17. Energy levels are labelled as AA, AE, EA and EE. The left-hand side of Figure 2.5 represents the case when no internal rotation is turned on. The next part shows a splitting resulting from the internal rotation of only one top. Each of these levels is further split into AA, AE, EA and EE components, once the second top is involved in the internal dynamics. This results in the four-energy pattern shown on the right-hand side (see also Ref. 16).

In case the two tops are non-equivalent and can by some mechanism (weakly) interact with each other, the EE energy level is further split into EE and EE* (right-hand side of Figure 2.5). If the top-top interaction splitting is small, a multiplet containing five components (AA, AE, EA, EE, EE*), given in Figure 2.5 will be observed experimentally. Some examples of molecular systems with two non-equivalent tops showing this characteristic pattern in their spectra are described in Chapters 5 and 6. Once the top-top interaction is much larger than either harmonic and/or tunnelling effects, the local mode theory is not a good approximation any more and the so-called normal-mode treatment has to be applied instead[16].

The experimental determination of the potential barrier height with rotational spectroscopy can provide useful insights into the interaction mechanisms governing molecular internal dynamics[16]. Several methods were developed for this purpose. One of them is the internal-axis method (IAM[18]). It uses a coordinate system in which the symmetry axis of the top is chosen as one of the coordinate axes, while the other two axes are kept fixed with respect to the frame[12]. This method can account for possible top-top couplings. The fitting program XIAM[19;20], which was also used in this work, is based on the internal-axis method.

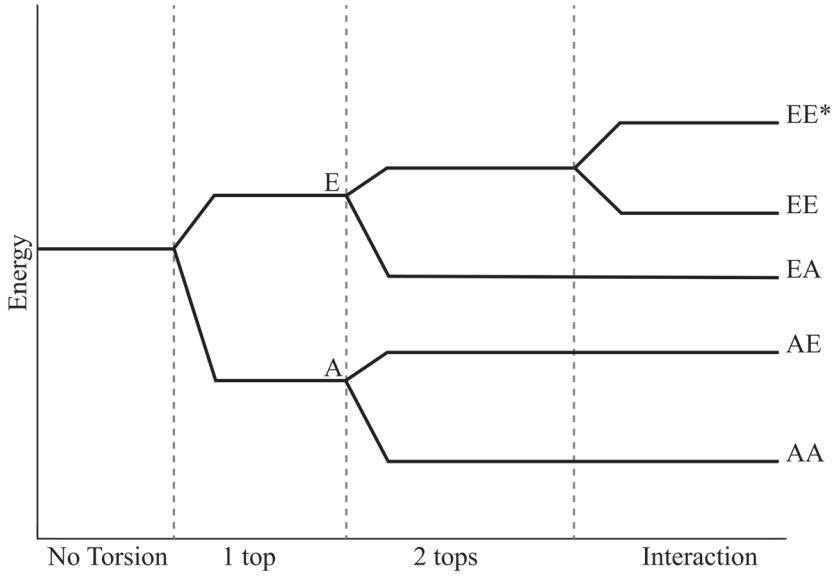

Figure 2.5: *Schematic torsional energy level diagram for the cases with no, one or two tops involved in the internal dynamics of a molecule. The last part represents the case when two tops are non-equivalent and can interact with each other.*

2.5 Microwave three-wave mixing

One of the main questions addressed in this thesis is chiral analysis of biologically relevant molecules and complex mixtures using rotational spectroscopy. The phenomenon of chirality is described in Chapter 1. For the sake of completeness, the terminology used throughout this section will be briefly summarized first.

A molecule that has one or several chiral centers can be present in the form of several optical stereoisomers, called enantiomers and diastereomers. While diastereomers can be distinguished with broadband rotational spectroscopy because of their unique fingerprint rotational spectra, this is not possible for enantiomers. This is due to the fact that the rotational constants of enantiomers are the same (without accounting for the predicted small energy differences due to parity violation). Recently, a coherent, non-linear, resonant technique based on rotational spectroscopy, was developed[21]. This chiral-sensitive method is called microwave three-wave mixing (M3WM). The M3WM is based on the fact that the scalar triple product of the dipole-moment components μ_a, μ_b and μ_c has an opposite sign for the two enantiomers. The main requirements are the same as for rotational spectroscopy: the sample needs to be polar and has to be brought into the gas phase. An additional condition for the M3WM applicability is that all three dipole moment components of the molecule of interest must be non-zero. A three-level system consistent of three rotational dipole-allowed transitions is required for the M3WM experiment. More details are given in Section 2.5.2. For a better conceptual understanding of the M3WM and its advanced application described in Section 2.5.3, a simplified case of a two-level system will be introduced first.

2.5.1 Two-level system

Many physical situations can be represented by an idealized two-level quantum system[22]. Here a two-level system with $|b\rangle$ being the upper, and $|a\rangle$ the lower level will be used. To describe the interaction of such a system with the resonant incident radiation, a density matrix formalism should be employed. The density operator (or more generally density matrix) is defined as:

$$\hat{\rho} = \sum_i p_i \left|\psi_i\right\rangle \left\langle\psi_i\right|, \tag{2.27}$$

where p_i is the probability to encounter the system in the state $|\psi_i\rangle$[22]. The evolution of the density matrix $\hat{\rho}$ for the isolated system in a pure state can be derived from the Liouville-von-Neumann equation:

$$\frac{\partial\hat{\rho}}{\partial t} = \frac{1}{i\hbar}[\hat{H},\hat{\rho}]. \tag{2.28}$$

For a two-level system, the evolution of the density matrix is given by the optical Bloch equations. The total Hamiltonian $\hat{H}$ is the sum of the atomic Hamiltonian $\hat{H_0}$= $\hbar\omega_0|b\rangle\langle b|$ (level $|a\rangle$ is taken to have zero energy) and the electric dipole Hamiltonian $\hat{H}_t$ = -$\hat{\mu}E_0\cos\omega t$[22]. This results in the following equations:

$$\begin{cases} \dfrac{\partial\rho_{aa}}{\partial t} = -i\Omega\cos\omega t(\rho_{ba}-\rho_{ab}) \\ \dfrac{\partial\rho_{bb}}{\partial t} = i\Omega\cos\omega t(\rho_{ba}-\rho_{ab}) \\ \dfrac{\partial\rho_{ab}}{\partial t} = i\omega_0\rho_{ab} - i\Omega\cos\omega t(\rho_{bb}-\rho_{aa}) \\ \dfrac{\partial\rho_{ba}}{\partial t} = -i\omega_0\rho_{ab} + i\Omega\cos\omega t(\rho_{bb}-\rho_{aa}), \end{cases} \tag{2.29}$$

where Ω is the Rabi frequency, which is defined as Ω= -$\mu_{ab}E_0/\hbar$. The term ω_0 is the resonance frequency $\omega_0 = {}^{(E_b-E_a)}/_{\hbar}$. In a quasi-resonant approximation, only one of the complex $\cos\omega t$ terms contributes appreciably to the evolution[22]. The equations 2.29 can be simplified in the following way:

$$\begin{cases} \dfrac{\partial\rho_{aa}}{\partial t} = -i\frac{\Omega}{2}\left(\rho_{ba}e^{i\omega t} - \rho_{ab}e^{-i\omega t}\right) \\ \dfrac{\partial\rho_{bb}}{\partial t} = i\frac{\Omega}{2}\left(\rho_{ba}e^{i\omega t} - \rho_{ab}e^{-i\omega t}\right) \\ \dfrac{\partial\rho_{ab}}{\partial t} = i\omega_0\rho_{ab} - i\frac{\Omega}{2}e^{i\omega t}\left(\rho_{bb}-\rho_{aa}\right) \\ \dfrac{\partial\rho_{ba}}{\partial t} = -i\omega_0\rho_{ba} + i\frac{\Omega}{2}e^{-i\omega t}\left(\rho_{bb}-\rho_{aa}\right) \end{cases} \tag{2.30}$$

The geometrical interpretation of the two-level system evolution is given by the Bloch vector $\mathbf{U}$, which lies inside a sphere with a radius $1/2$ (Bloch sphere)[22]. The elements u, v and w used for the projection of the Bloch vector $\mathbf{U}$ in coordinate system are:

$$u + iv = \rho_{ba} \tag{2.31}$$

$$w = \frac{1}{2}(\rho_{aa} - \rho_{bb}). \tag{2.32}$$

The Bloch sphere is depicted schematically in Figure 2.6 for the two states $|a\rangle$ and $|b\rangle$.

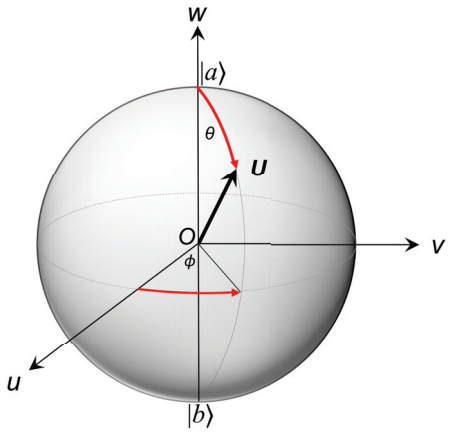

Figure 2.6: *Schematic representation of a Bloch sphere with a Bloch vector* $\boldsymbol{U}$*, which describes a two-level system with the two states* $|a\rangle$ *and* $|b\rangle$*. The projection of the Bloch vector on the w axis gives the population difference.* θ *and* φ *are spherical polar coordinates of* $\boldsymbol{U}$*. Adapted from Ref. 22.*

Once a resonant electromagnetic field is applied, the time evolution of the Bloch vector is given by the following expression:

$$\frac{d\boldsymbol{U}}{dt} = \boldsymbol{\Omega} \times \boldsymbol{U}, \tag{2.33}$$

where the vector $\boldsymbol{\Omega}$ has the elements $(\Omega, 0, 0)$. The Bloch vector precesses therefore around the vector $\boldsymbol{\Omega}$. If the initial state of a system at t_0 is $|a\rangle$, the Bloch vector describes a circle in the (v,w) plane, once an electromagnetic field is applied. If the applied electromagnetic field is removed after a period of time, the Bloch vector stops precessing and remains fixed at its final position[22]. In a specific case of a $\pi/2$ pulse the vector $\mathbf{U}$ comes to rest along the direction v, where the coherence is maximum and the difference between the populations of the two levels is zero[22].

2.5.2 M3WM cycles

In following, the principle behind the M3WM experiment will be described. As mentioned previously, a cycle of three rotational dipole-allowed transitions, which depend on the dipole moment components μ_a, μ_b and μ_c respectively, is needed for the M3WM experiment. By resonantly exciting two of the rotational transitions with orthogonally polarized microwave fields, a signal containing chiral information is recorded as a free induction decay (FID) in the

third mutually orthogonal direction. The angular frequencies of the three transitions a, b and c can be denoted as ω_{ab}, ω_{bc} and ω_{ac}. Two of the transitions are excited with orthogonally polarized microwave pulses with Rabi frequencies $\Omega_{ab} = E(\omega_{ab})\mu_{ab}/\hbar$ and $\Omega_{bc} = E(\omega_{bc})\mu_{bc}/\hbar$, where $E(\omega_{ab})$ and $E(\omega_{bc})$ are the amplitudes of the electric field oscillating at the respective angular frequencies[10]. The two excitation pulses are called "drive" and "twist", while the recorded signal is referred to as "listen". An example of such a cycle for a M3WM experiment is given in Figure 2.7. The procedure can be rationalized as a polarization-sensitive double-resonance experiment.

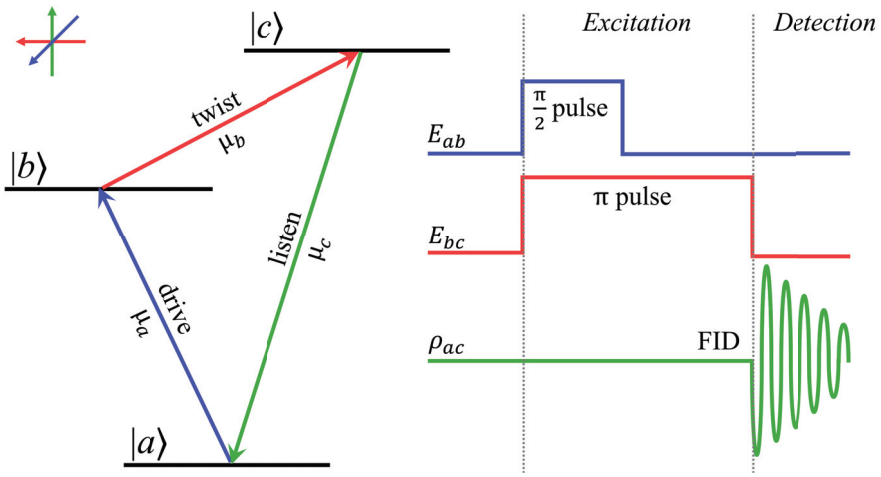

Figure 2.7: *An example of a M3WM cycle, consisting of three dipole-allowed rotational transitions, which depend on the dipole moment components μ_a, μ_b and μ_c, respectively. The orthogonal excitation pulses are called drive and twist. The drive pulse, which obeys the $\pi/2$ condition (see text), creates a coherence between the states $|a\rangle$ and $|b\rangle$. This coherence is then converted into a double coherence ρ_{ac} between the states $|a\rangle$ and $|c\rangle$ by the twist pulse under π condition. The M3WM signal ("listen") is recorded in the third mutually orthogonal direction as a free induction decay (FID). E_{ab} and E_{bc} are the electric fields for the excitation.*

The drive pulse creates a coherence between the states $|a\rangle$ and $|b\rangle$ and thus, a superposition between the two states. As follows from the discussion on the two-level system, the drive pulse has to fulfil a $\Theta_{ab} = \frac{\pi}{2}$ condition to achieve maximum coherence between the states $|a\rangle$ and $|b\rangle$. Here Θ is the "flip angle", which is related to the Rabi frequency Ω_{ab} in the following way: $\Theta_{ab} = \Omega_{ab}\Delta t$[10]. The achieved coherence is then transferred to a double-coherence between the states $|a\rangle$ and $|c\rangle$ by the twist pulse at a $\Theta_{bc} = \pi$ pulse condition (Figure 2.7). The obtained "listen" signal $S(t)$ can be expressed in the following form[23;24]:

$$S(t) \propto ee \cdot |\mu_a\mu_b\mu_c| \cdot \cos\left(2\pi\nu t + \frac{\pi}{2}\left(\frac{\mu_a\mu_b\mu_c}{|\mu_a\mu_b\mu_c|}\right)\right), \tag{2.34}$$

where ν is the frequency resonant to the "listen" transition, and t is the time interval between the start of the excitation and the detection. The phase of the recorded signal will exhibit a π shift, once the measurement is conducted on two enantiomers. This observation is due to

the sign difference of the scalar triple product of the dipole moment components as explained above. No net M3WM signal will be obtained, if the experiment is performed on a racemic sample (equal amount of both enantiomers, see Chapter 1). The amplitude of the signal is proportional to the enantiomeric excess (*ee*), the relative abundance of the two enantiomers in the sample (see equation 2.34). To determine the *ee* of the chiral sample of interest, the measured amplitude needs to be normalized with that of a sample with a known *ee*[10;23].

From equation 2.34 the absolute configuration ("handedness") of the enantiomers can be determined. However, it requires an accurate evaluation of the time interval t, which involves the characterization of the timing and the phase relations for the excitation pulses. An alternative approach for a more qualitative analysis involves a comparison between the phases of a sample with a known absolute configuration and of the one where the handedness has to be determined.

2.5.3 State-specific enantiomeric enrichment

The approach of M3WM presented here was recently extended to selectively transfer the enantiomers to the rotational levels of choice. This creates an enantiomeric enrichment in the particular rotational states. For this purpose, an additional microwave pulse (transfer pulse) on the frequency resonant to the listen transition is required. The difference in sign of the triple product of the dipole moment components affects the rotation of the Bloch vector[25]. As an example, suppose that in this particular case μ_a differs in sign for the two enantiomers, while μ_b and μ_c are the same. Further, we can assume that transition $|b\rangle \leftarrow |a\rangle$ depends on μ_a, $|c\rangle \leftarrow |b\rangle$ on μ_b, and $|a\rangle \leftarrow |c\rangle$ on μ_c. A scheme of a hypothetical three-level system is presented in Figure 2.8.

The $\pi/2$ drive pulse excites the transition $|b\rangle \leftarrow |a\rangle$. Due to the opposite signs of the Rabi frequency in this case, the Bloch vectors of the two enantiomers point in opposite directions[25]. The π twist pulse excites the $|c\rangle \leftarrow |b\rangle$ transition. Because the sign of μ_c is the same between the two enantiomers, the phase of the resulting FID shows a π-shift, which is normally exploited in a standard M3WM experiment described above.

Without the transfer pulse the FID would dephase on a rapid time scale (typically < 100 μs)[25]. By applying the $\pi/2$ transfer pulse, which is resonant with the transition $|a\rangle \leftarrow |c\rangle$, coherence will be transformed back into a population difference between the two enantiomers, located in two different rotational states $|a\rangle$ and $|c\rangle$. This creates a state-specific enantiomeric enrichment. The procedure is schematically summarized in Figure 2.8. By changing the phase of one of the three excitation pulses, the enantiomers can be selectively transferred to two different rotational levels of choice, producing an *ee* in the respective energy levels. This *ee* can be probed by a fourth rotational pulse, which shares the energy level with one of the two rotational states involved in the enantiomer-selective population enrichment.

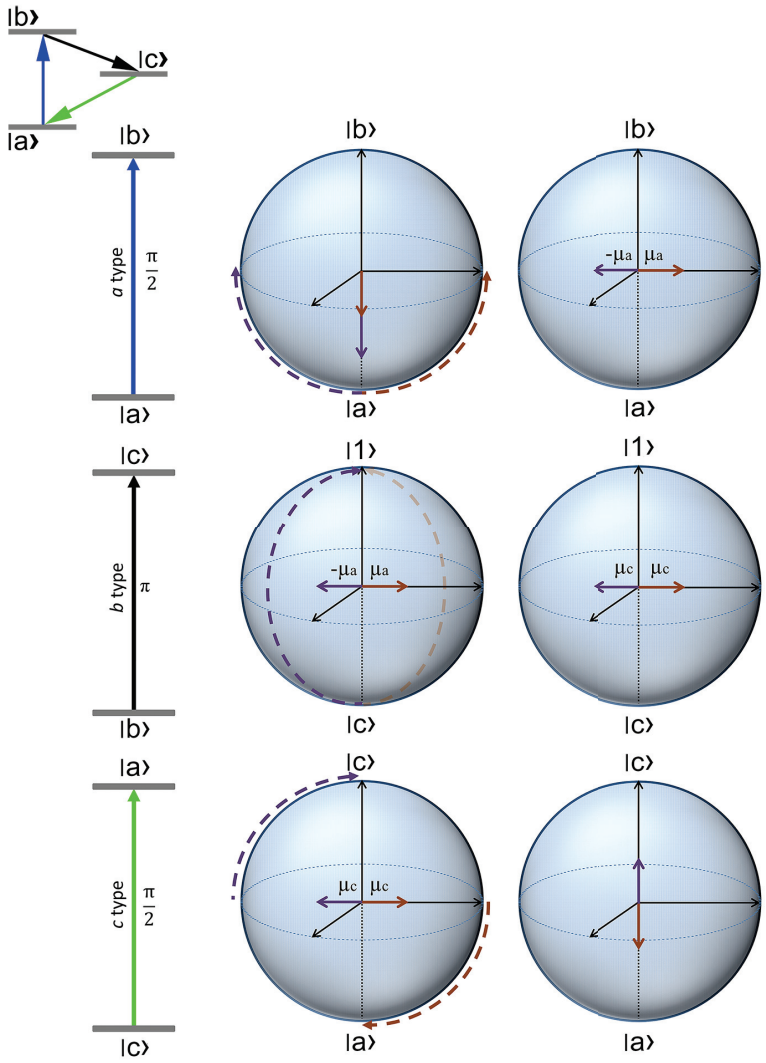

Figure 2.8: *State-specific enantiomeric enrichment can be achieved by applying three mutually orthogonal pulses as illustrated here in Bloch sphere representation. It is assumed that the two enantiomers differ in sign of μ_a. The $|b\rangle \leftarrow |a\rangle$ transition is driven by a $\pi/2$ pulse, which creates a coherence between the states $|a\rangle$ and $|b\rangle$. The superposition of these states is labelled as $|1\rangle$. This coherence is transformed into a double coherence between the states $|a\rangle$ and $|c\rangle$ by a π pulse, which excites the $|c\rangle \leftarrow |b\rangle$ transition. The phase of the resulting free induction decay (FID) differs in π for the two enantiomers, as is known from M3WM experiments. By applying another $\pi/2$ pulse, instead of recording the chiral signal, the coherence is converted back into a population difference for the two enantiomers, located in two different rotational states (modified after Ref. 25).*

There is an alternative way to describe this procedure. The standard M3WM can be considered as a so-called two-photon pathway, involving $|c\rangle \leftarrow |b\rangle \leftarrow |a\rangle$ transitions in this particular case. Consequently, the direct excitation of the "listen" transition $|a\rangle \leftarrow |c\rangle$ can be viewed as a one-photon process. The two competing events, the one- and the two-photon excitations, can interfere constructively or destructively depending on the relative phases between the

one- and the two-photon pathways. This interference can be used to determine the *ee* of the chiral sample, because the amplitude of the M3WM signal, corresponding to the two-photon process, is proportional to the *ee* (equation 2.34). The signal from the two-photon process is "probed" by the one-photon resulting in destructive interference. To determine the *ee*, the phase-dependent signal at the one-photon frequency is monitored. The larger the *ee*, the larger the signal intensity of the one-photon process should be to obtain maximal interference. Since the interference for probing the *ee* is destructive, the maximal interference between the two pathways leads to the minimal observed signal. In order to create state-specific enantiomeric enrichment, the one- and the two-photon processes should be applied simultaneously. This creates a three-photon pathway. The achieved enantiomeric enrichment is then probed by the forth pulse in the way explained above.

Both "standard" M3WM and enantiomer-selective population enrichment method were applied in the scope of this work and presented in more detail in the following chapters.

Bibliography

[1] A. Bauder. Fundamentals of Rotational Spectroscopy. In *Handbook of High-resolution Spectroscopy*, pages 58–111. American Cancer Society, 2011.

[2] P. Atkins and J. de Paula. *Physikalische Chemie*, volume v. 1. Wiley, 2006.

[3] M. B. Bell, P. A. Feldman, M. J. Travers, M. C. McCarthy, C. A. Gottlieb, and P. Thaddeus. Detection of $HC_{11}N$ in the Cold Dust Cloud TMC-1. *Astrophys. J. Lett.*, 483(1):L61, 1997.

[4] R. Zare. Angular momentum: understanding spatial aspects in chemistry and physics. Wiley, 1988.

[5] P. Atkins and R. Friedman. *Molecular Quantum Mechanics*. OUP Oxford, 5th edition, 2011.

[6] C. Townes and A. Schawlow. *Microwave Spectroscopy*. Dover books on physics. Dover Publications, 2012.

[7] B. S. Ray. Über die Eigenwerte des asymmetrischen Kreisels. *Z. Phys.*, 78(1):74–91, Jan, 1932.

[8] G. W. King. The Asymmetric Rotor. VI. Calculation of Higher Energy Levels by Means of the Correspondence Principle. *J. Chem. Phys.*, 15(11):820–830, 1947.

[9] S. Golden and J. K. Bragg. An Asymptotic Expression for the Energy Levels of the Asymmetric Rotor. III. Approximation for the Essentially Degenerate Levels of the Rigid Rotor. *J. Chem. Phys.*, 17(5):439–441, 1949.

[10] K. K. Lehmann. of chiral molecules. *J. Chem. Phys.*, 149(9):094201, 2018.

[11] H. Haken and H. Wolf. *Molekülphysik und Quantenchemie: Einführung in die experimentellen und theoretischen Grundlagen*. Springer-Lehrbuch. Springer Berlin Heidelberg, 5th edition, 2006.

[12] W. Gordy and R. Cook. *Microwave molecular spectra*. Techniques of chemistry. Wiley, 1984.

[13] J. Kraitchman. Determination of Molecular Structure from Microwave Spectroscopic Data. *Am. J. Phys.*, 21(1):17–24, 1953.

[14] Z. Kisiel. Least-squares mass-dependence molecular structures for selected weakly bound intermolecular clusters. *J. Mol. Spectrosc.*, 218(1):58 – 67, 2003.

[15] P. Nõsberger, A. Bauder, and H. H. Günthard. A versatile method for molecular structure determinations from ground state rotational constants. *Chem. Phys.*, 1(5):418 – 425, 1973.

[16] M. Schnell. Group Theory for High-resolution Spectroscopy of Nonrigid Molecules. In *Handbook of High-resolution Spectroscopy*, pages 607–630. American Cancer Society, 2011.

[17] N. Ohashi, J. T. Hougen, R. D. Suenram, F. J. Lovas, Y. Kawashima, M. Fujitake, and J. Pyka. Analysis and fit of the Fourier-transform microwave spectrum of the two-top molecule N-methylacetamide. *J. Mol. Spectrosc.*, 227(1):28 – 42, 2004.

[18] H. H. Nielsen. The Torsion Oscillator-Rotator in the Quantum Mechanics. *Phys. Rev.*, 40:445–456, May 1932.

[19] H. Hartwig and H. Dreizler. The Microwave Spectrum of trans-2,3-Dimethyloxirane in Torsional Excited States. *Z. Naturforsch.*, 51a:923–932, 1996.

[20] H. Hartwig. XIAM Manual, 1996. available at http://www.ifpan.edu.pl/ kisiel/introt/xiam/xiam-v25.txt.

[21] D. Patterson, M. Schnell, and J. M. Doyle. Enantiomer-specific detection of chiral molecules via microwave spectroscopy. *Nature*, 497(7450):475–477, 2013.

[22] G. Grynberg, A. Aspect, and C. Fabre. Introduction to Quantum Optics: From the Semi-classical Approach to Quantized Light. Cambridge University Press, 2010.

[23] V. A. Shubert, D. Schmitz, C. Medcraft, A. Krin, D. Patterson, J. M. Doyle, and M. Schnell. Rotational spectroscopy and three-wave mixing of 4-carvomenthenol: A technical guide to measuring chirality in the microwave regime. *J. Chem. Phys.*, 142(21):214201, 2015.

[24] V. A. Shubert, D. Schmitz, D. Patterson, J. M. Doyle, and M. Schnell. Identifying Enantiomers in Mixtures of Chiral Molecules with Broadband Microwave Spectroscopy. *Angew. Chem. Int. Ed.*, 53(4):1152–1155, 2014.

[25] D. W. Pratt and B. H. Pate. Chiral Imprinting in the Gas Phase. *Angew. Chem. Int. Ed.*, 56(51):16122–16124, 2017.

3

Experimental details

In the preceding chapter some major advantages of rotational spectroscopy as an analytical tool together with a brief theoretical background necessary for the understanding of its application were introduced. Here the main focus will be on the instrumental details of the spectrometer, which was used in the framework of this thesis. Some modifications of the general set-up, which are required for performing the microwave three-wave mixing (M3WM) experiments, will be discussed in this context. Additionally, the molecular beam technique called supersonic expansion, which we apply for cooling molecules down to their vibronic ground states, will be presented.

3.1 Chirped pulse Fourier transform microwave spectrometer

From a historical point of view, the development of the first Fabry-Pérot Fourier transform microwave (FTMW) spectrometer by T. J. Balle and W.H. Flygare in 1979[1;2] can be interpreted as a great advancement in rotational spectroscopy. In 1996, J.-U. Grabow et. al. achieved an impressive increase in the resolution of the spectrometer by using coaxially oriented beam resonator arrangement and incorporating a new design of the microwave assembly[3]. The spectrometer uses a cavity for the enhancement of the recorded signal and the reduction of the required excitation power. However, due to its narrow bandwidth (less than 1 MHz), the process of obtaining a spectrum, which spans a frequency range of several GHz, can be very time-consuming.

In 2008, B. H. Pate and co-workers introduced the chirped pulse technique for molecular excitation in the broadband Fourier transform spectroscopy[4]. Due to the usage of a chirped pulse with a linear frequency sweep to polarize a molecular sample, the time required for the measurement of a high-resolution rotational spectrum can be significantly reduced in comparison to a cavity spectrometer. This consequently results in the reduction of the sample consumption, which is another important benefit of the chirped pulse technique.

The intensity of the emitted molecular signal S is proportional to the transition frequency ω, the square of the dipole moment μ^2, the electric filed strength E_{pulse}, the population

difference between the two states involved in the transition ΔN_0, and the sweep rate α[4]:

$$S \propto \omega \cdot \mu^2 \cdot E_{pulse} \cdot \Delta N_0 \cdot \left(\frac{\pi}{\alpha}\right) \tag{3.1}$$

The chirped-pulse Fourier transform microwave spectrometer COMPACT (compact-passage acquired coherence technique) in Hamburg[5] (see Figure 3.1) used in this work, is, as the name indicates, based on the chirped pulse excitation.

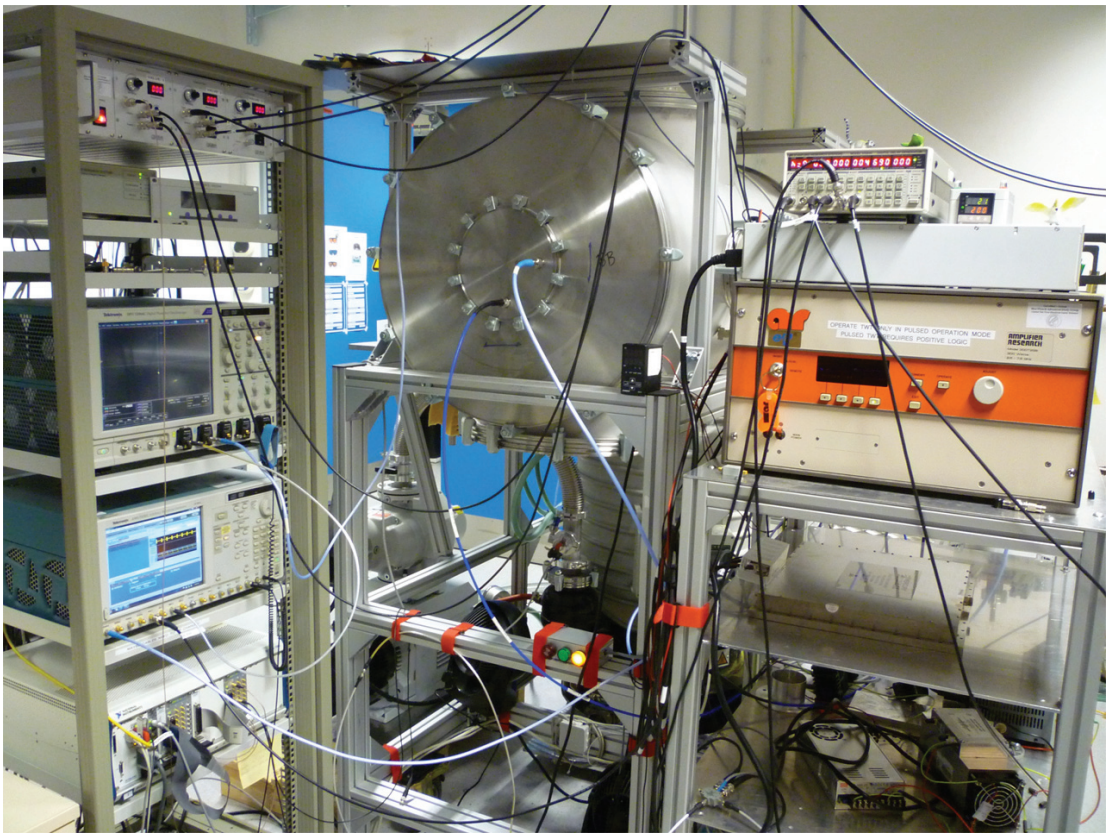

Figure 3.1: *The chirped-pulse Fourier transform microwave spectrometer COMPACT in Hamburg, which was used for the measurements in this thesis.*

The operation of the spectrometer can be divided in three parts as discussed in Ref. 4 (1) chirped microwave pulse generation; (2) excitation pulse and molecular beam interaction; (3) signal detection. In the following, the different parts of the COMPACT spectrometer will be presented.

3.1.1 Generation of the excitation pulse

The technical aspects and characteristics of the spectrometer were described previously by D. Schmitz and provided in Ref. 5 and Ref. 6. The spectrometer operates in the frequency range from 2-8.5 GHz, which was recently extended to 18 GHz. This frequency range is suitable for

the analysis of complex molecular systems. Such molecules have large moments of inertia and thus low rotational constant, leading to low transition frequencies. A scheme of the microwave circuit used in the spectrometer is given in Figure 3.2.

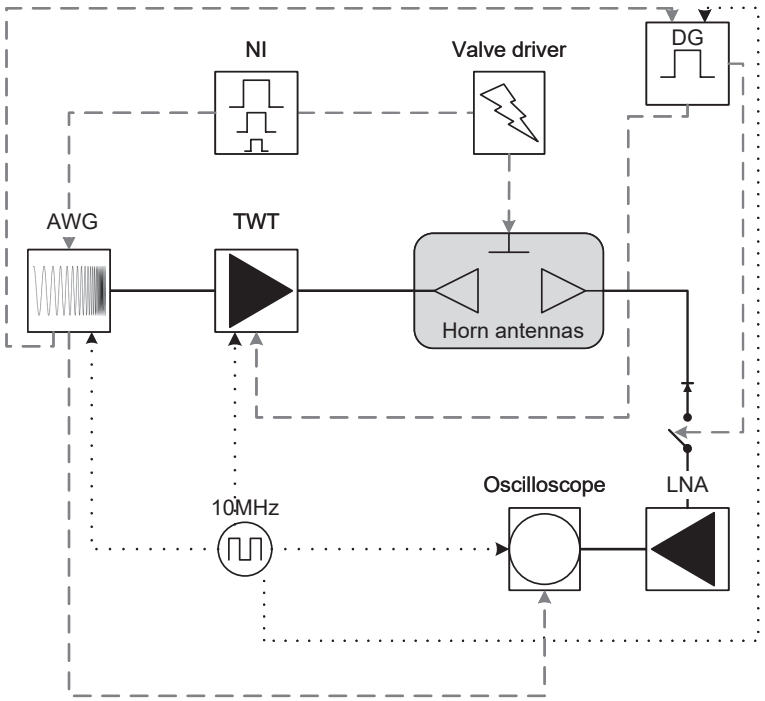

Figure 3.2: *Scheme of the high-frequency components of the spectrometer COMPACT in Hamburg. All frequency sources are phase-locked to a 10 MHz rubidium (Rb) frequency standard (dotted lines). The excitation pulse is produced by an arbitrary wave form generator (AWG), amplified via a travelling wave tube amplifier (TWT) and broadcast into the vacuum chamber using horn antennas. The molecular ensemble is supersonically expanded into the chamber through a pulsed valve. The valve driver is triggered by a National Instruments (NI) system. The obtained signal is amplified with a low-noise amplifier (LNA) and recorded using a 100 GS/s oscilloscope, which is triggered from one of the marker channels of AWG. The electronics on the detection side is protected using a high-power PIN-diode limiter and protection switch. The opening times of the protection switch and TWT are regulated via a delay generator (DG). Solid lines in the scheme represent connections between different instrumental parts using coaxial cables; dashed lines show schematically, how the triggering of the individual circuit parts is realized in the current set-up.*

The excitation chirp is generated on an arbitrary wave form generator (Tektronix AWG 7122C[7]), which can be operated in the dual-channel and in the interleaved mode. The operating rate of the AWG in the interleave mode is 24 GS/s with the Nyquist frequency range up to 12 GHz. Additionally, the AWG has two digital marker channels. One of them is used to trigger the data acquisition of the oscilloscope, when the obtained molecular signal is recorded. The other one provides a connection to a digital delay generator (Stanford Research Systems Model DG645[8]), which is introduced in the set-up for the timing control of the

experiment (more details are provided in Section 3.1.4). The duration of the chirp used in our broadband measurements is 4 μs. Such short sweep durations are required to polarize the sample on a time scale faster than the dephasing of the rotational signal (typically 10 μs)[4]. The generated excitation pulse is amplified with a travelling wave tube amplifier (TWT, Amplifier Research 300T2G8, 2.5-7.5 GHz) with minimum output power of 300 W[9].

3.1.2 Molecular sample polarization

After the excitation chirped pulse is generated and amplified with a TWT, it is broadcast into the vacuum chamber via a microwave horn antenna (Q-Par Angus WBHDP2-17# HGDual Polarised[10]). This antenna can support dual polarization. This aspect will be important for the M3WM experiments.

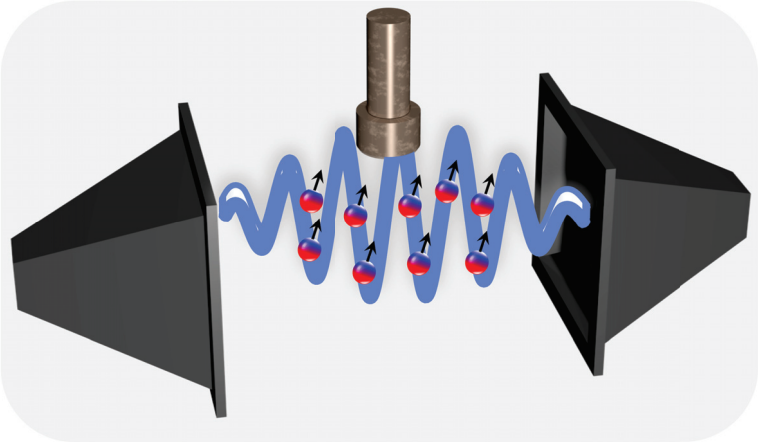

Figure 3.3: *When the molecules (red-blue spheres) resonantly interact with the microwave radiation, a macroscopic polarization is created. The black arrows schematically indicate the orientation of the molecular dipoles.*

Inside the chamber, an interaction between the chirped pulse and the molecular beam takes place. Prior to being introduced into the gas chamber, the sample needs to be brought into the gas phase. For this purpose, a heating system with a 1/8 DIN vertical temperature controller (CN710 series, Omega[11]) is used in the present set-up. This heating system allows an accurate temperature adjustment (heating up to 200 °C is possible) and reproducible experimental conditions. As the next step, the molecular sample is supersonically expanded into the chamber via a pulsed nozzle (Parker General Valve, Series 9[12]). The nozzle diameter is around 1 mm, and the applied backing pressure, which depends on the molecular system of interest, is typically 2-3 bar. The position of the valve is perpendicular to the propagation direction of the excitation pulse (see Figure 3.3). In the present set-up the valve can operate at a repetition rate of 9 Hz. One of the limiting factors for the repetition rate is the pumping speed of the vacuum system. The spectrometer is currently equipped with an oil diffusion pump (Leybold DIP 12000, pumping speed 12 000 l/s[13]) backed by a booster pump (Leybold RuVac WAU 251[14]) and a mechanical pump (Leybold D40B Trivac Vacuum Pump[15]). An

interaction between the molecules in the molecular beam and the excitation pulse creates a macroscopic polarization. This process is schematically presented in Figure 3.3.

3.1.3 Signal recording

A free induction decay (FID) of the molecular polarization created by an interaction between the molecular beam and the excitation chirp is received with a second Q-Par horn antenna (Q-Par Angus WBH 2-18-NHG[10]). The signal is amplified with a low-noise amplifier (LNA, AMF-7D-01001800-22-10P[16]) and recorded using a 100 GS/s digital oscilloscope (Tektronix DPO 72004C[17]). A PIN diode limiter (Advanced Control Components) followed by a PIN diode solid state switch (Advanced Technical Materials S1517D[18]) are introduced in the circuit. The purpose of the switch and of the diode limiter is to protect the LNA and the oscilloscope from a high-power excitation pulse.

The length of the recorded FID determines the resolution of the spectrum. The linewidth of the spectra measured on COMPACT with the present set-up is approximately 25 kHz. In order to reduce sample consumption and measurement time, several FIDs per gas pulse are recorded[19]. Typically, a sequence of eight FIDs is applied in our experiment. This is possible due to the fast frame mode of the digital oscilloscope. The excitation pulse generated with the AWG contains eight frames. In each of these frames the excitation pulse has a duration of 4 μs, while 40 μs are reserved for the recording of the FID. There is a time buffer of 0.5 μs between the excitation and the recording process. As mentioned above, the start of the data acquisition on the oscilloscope is triggered by the AWG. The acquired FID acquisitions are co-added and then subsequently averaged in the time domain[19].

Taking into account the repetition rate of 9 Hz for the operation of the valve, the effective repetition rate using the "fast frame" approach amounts to 72 Hz. This allows to acquire over 4 million acquisitions in a one-day measurement. This is often sufficient to observe even rare isotopologues such as ^{18}O and ^{15}N in natural abundance, since the signal-to-noise ratio (SNR) scales with the square root of the number of averages.

To obtain the recorded spectrum in the frequency instead of the time domain, a Fast Fourier transformation is made. Several time-domain filters such as Hamming, Kaiser Bessel and Gaussian are available to improve the base line resolution of the spectrum[4]. In our data analysis the Kaiser Bessel function is commonly used.

3.1.4 Triggering and time control of the experiment

All frequency sources used in the set-up described above are phase-locked to a rubidium (Rb) frequency standard (Stanford Research FS 725[20]) operating at 10 MHz. This ensures phase stability and reproducibility of the measurement. A rough scheme of the timing used in our experiment is given in Figure 3.4.

The start of the valve operation is triggered by the National Instruments PXI system (PXIe-1065[21]). The valve opening time in the present experiments is typically set to 450 μs, followed

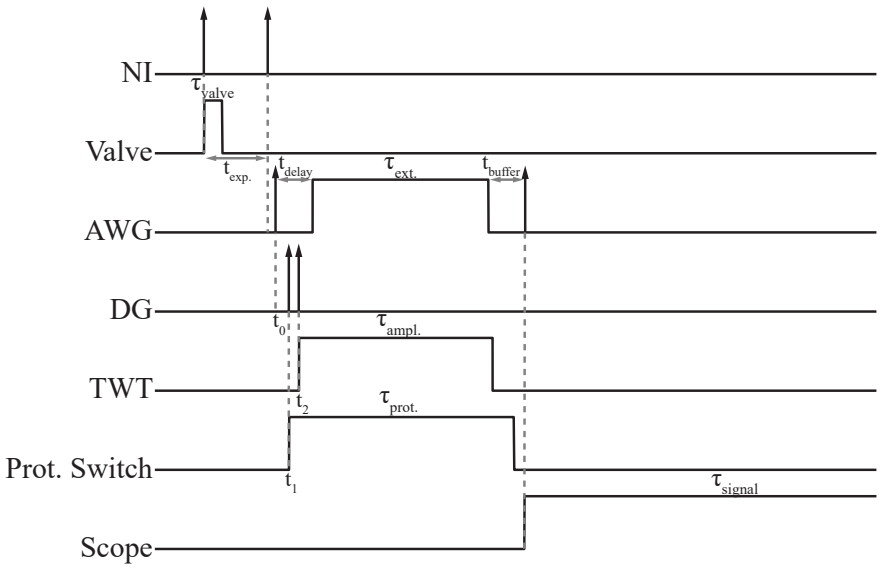

Figure 3.4: *Time scheme for a broadband experiment with the current set-up on the COMPACT spectrometer in Hamburg. Valve operation is triggered by the National Instruments (NI) system. Valve opening time used in our experiments is commonly $\tau_{valve} \approx 450\ \mu s$ followed by the period of expansion. Expansion time, $t_{exp.} \approx 1$ ms. Afterwards, an arbitrary wave form generator (AWG) is triggered by the NI. The AWG subsequently triggers the delay generator (DG) at $t_0 = 0.1\,\mu s$. The DG regulates opening times of the protection switch (Prot. Switch, $t_1 = t_0 + 880\,ns$, $\tau_{prot.} = 4.6\,\mu s$) and of the travelling wave tube amplifier (TWT, $t_2 = t_0 + 1200\,ns$, $\tau_{ampl.} = 4.2\,\mu s$) The duration of the excitation pulse generated on AWG is $\tau_{ext.} = 4\,\mu s$. Note that the timings provided here are typically used for the broadband measurement in our lab. The duration of the chirp and of the FID recording can be adjusted in accordance to the requirements of each individual experiment. To create an overlap between the generation of the chirp by the AWG and its amplification by the TWT, there is a delay for the excitation pulse, $t_{delay} = 1.5\,\mu s$ after the AWG has been triggered by the NI. The period of time between the excitation and the signal recording is $t_{buffer} = 0.5\,\mu s$; The signal is recorded for $40\,\mu s$ (τ_{signal}).*

by the period of expansion time t_{exp}=850 μs - 1 ms. After the expansion time, the AWG is triggered by the NI system. The AWG subsequently triggers a multi-channel digital pulse generator (DG) at $t_0 = 0.1\,\mu s$. The triggering occurs via one of the marker channels of AWG. The purpose of the DG is to control the timing of the electronic parts involved in the excitation. In the first step, it opens the PIN diode protection switch ($t_1 = t_0 + 850\,ns$), mentioned in Section 3.1.3. The switch is opened before and closed after the operation time of the TWT to protect the electronics on the detection side from the high power. There is a time delay for the excitation pulse, $t_{delay} = 1.5\,\mu s$ after the AWG has been triggered by the NI. This makes sure that the created chirp is amplified by the TWT. The TWT is activated ($t_2 = t_0 + 1200\,ns$) only for the time duration of the excitation pulse with a small time buffer before the excitation to take into account the ramp up time of the TWT. Finally, the oscilloscope is triggered via the second marker channel of the AWG for the data acquisition (t_{signal}). There is a short time delay of 0.5 μs between the excitation pulse and the signal

recording on the oscilloscope, which ensures that there is no interference between the emitted signal and the excitation pulse.

3.2 Modifications of the general set-up required for a M3WM experiment

The general set-up described above can be used for M3WM experiments with some minor modifications. All excitation pulses are generated on the same source (AWG 7122C, Section 3.1.1) to ensure their phase stability.

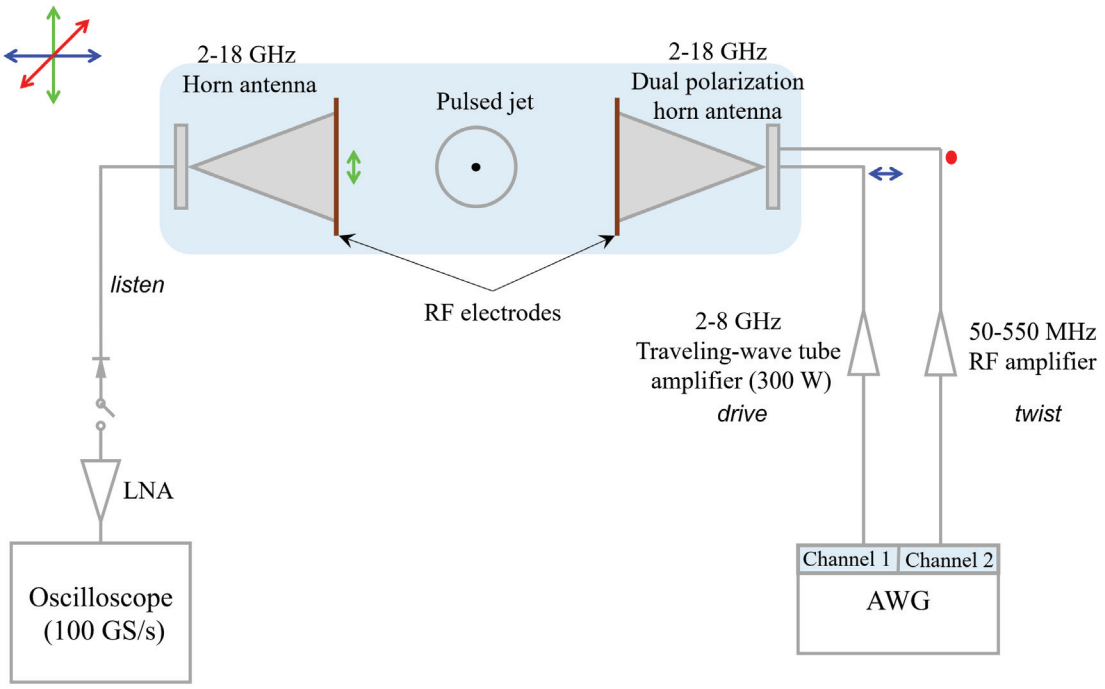

Figure 3.5: *Scheme of the set-up typically used for a M3WM experiment. Excitation pulses are generated on the same source to ensure phase stability and transmitted through the two channels of the AWG. Two amplification pathways are required: the MW pulse ("drive") is amplified using the TWT and broadcast through the dual polarization horn antenna. The RF pulse ("twist") is amplified with an RF amplifier and broadcast in the vacuum chamber using RF electrodes. The two excitation pulses are polarized orthogonally to each other as indicated by the colored arrows. The molecular signal is amplified with a low-noise amplifier (LNA) and recorded using a 100 GS/s oscilloscope.*

The two excitation pulses called drive and twist (Figure 3.5) are subsequently transmitted from the two different channels of the AWG (dual-channel mode of the AWG). The excitation pulses have to be broadcast orthogonally to each other. In our experiments, the drive pulse is typically in the microwave (MW), while the twist pulse is in the radio frequency (RF) range[22]. Two separate amplification pathways are required for this purpose. The drive pulse

is amplified with the TWT, while for the twist pulse an additional amplifier operating in the RF range (30-550 MHz KU PA 003055-100 A, RF Power Amplifier[23]) is necessary.

The MW drive pulse is broadcast into the vacuum chamber in horizontal polarization direction via a dual polarization Q-Par horn antenna. In the experiments reported previously, the single polarization horn antennas were used instead, which required the rotation of the receiving horn antenna relatively to the broadcast one[22]. An introduction of a dual-polarization horn antenna allows to broadcast the excitation pulse (drive) and to receive the MW signal (listen) in two orthogonal directions without the necessity of physically changing the relative orientations of the horns.

The amplified RF twist pulse is coupled to the stainless steel RF electrodes and broadcast in the third mutually orthogonal direction (perpendicular to drive and listen). No changes on the detection side are required.

Several molecular systems such as pulegone, menthone and isomenthone were studied in the framework of this thesis using the set-up presented in this section. Recently, we introduced an additional MW horn antenna (1-10 GHz) instead of the RF electrodes with the aim to widen the range of possible chiral systems under study and thus to increase the versatility of the instrument. This allowed to perform the M3WM based enantiomeric population enrichment experiment. The results are given in Chapter 8, where also some additional instrumentation details necessary for this particular experiment are provided. In general, if not stated otherwise, the set-up for the M3WM experiments reported in this thesis resembles the one depicted in Figure 3.5.

3.3 Supersonic expansion

The accuracy of spectroscopic measurements is in general limited by line broadening, which results mainly from Doppler motions, collisions and perturbations from neighboring molecules in the case of relatively dense media[24]. Most of these effects can be largely eliminated, once the measurement is conducted on a collision-free atomic or molecular beam. The low velocity distribution in such molecular ensembles leads to a narrow spectral line shape. Furthermore, the low rotational and vibrational temperatures of the beam limit the number of significantly populated energy levels of the molecular system. This in turn increases the signal intensity of the observed rotational transitions and also enormously simplifies the spectral interpretation.

One of the established techniques for producing cold molecular beam is the supersonic expansion, which is also used in our group. The flow is termed supersonic when the ratio between the mass flow velocity v and the speed of sound a, the so-called Mach number M ($M = v/a$), is greater than 1. The first seeded supersonic jet introduced by R. E. Smalley et. al.[25] in 1974 revolutionized the filed of high-resolution molecular spectroscopy. Once this unique technique was combined with FTMW spectrometer by T. J. Balle and W.H. Flygare[1], the applicability of rotational spectroscopy to larger molecules increased tremendously.

Another important development, which further promoted progress in the field of rotational spectroscopy, was the introduction of a pulsed valve by Gentry and Giese in 1978[26]. Pulsed beam sources offer several advantages in comparison to continuous ones, such as colder internal rotational states distributions, higher beam density and narrower velocity distribution[27]. As mentioned previously, a commercial pulsed valve (General Valve Series 9) is used for the supersonic expansion of the molecules in our set-up. This solenoid valve with a magnetically activated plunger allows to produce gas pulses of several hundreds of microseconds duration[27;28]. The equipment for obtaining supersonic free jet also includes a corresponding pumping system to establish low downstream pressures[29].

The principle behind the cooling effect of a supersonic beam can be explained as follows. The molecules can expand from a high-pressure region into vacuum through a small orifice in the nozzle reservoir[30]. The random molecular motion is converted into a direct mass flow once following requirements are fulfilled: 1) the reservoir pressure is by several orders of magnitude greater than the background pressure in the vacuum chamber, and 2) the mean free path between the collisions prior the expansion is much smaller than the orifice diameter[30].

The molecules under study can be seeded into a gas mixture containing noble gases, which have no vibrational or rotational modes and are therefore suitable carrier gases[30]. In the first step, the collisions with a carrier gas will accelerate the molecules of interest to the speed of the carrier gas. Once similar temperatures between polyatomic molecules and the career gas are established, only low energy collisions between them are possible, until the molecules are separated enough so that no collisions between them take place.

The velocity distribution in a supersonic jet is narrower and shifted to higher values in comparison to the velocity distribution in the reservoir prior to the expansion (see Figure 3.6). The narrow velocity distribution is caused by the cooling of the expanded gas. The shift to higher values results from an increase in the flow velocity. The terminal flow velocity $\langle v \rangle$ of the expanded jet can be determined in the following way:

$$\langle v \rangle = \sqrt{\frac{2R\gamma(T_0 - T_1)}{(\gamma - 1)N_A m}} \tag{3.2}$$

where T_0 is the temperature in a reservoir, T_1 the temperature of the expanded jet, N_A the Avogadro constant and m the particle mass. The term γ is defined as a ratio C_p/C_v, with C_p being the isobaric heat capacity and C_v the molar heat capacity at constant volume[31]. For an ideal gas γ =5/3. For the limiting case when $T_0 \gg T_1$ and considering γ for an ideal gas, the equation for the maximum terminal flow velocity $\langle v_{max} \rangle$ can be written as:

$$\langle v_{max} \rangle = \sqrt{\frac{5RT_0}{N_A m}} \tag{3.3}$$

The equation 3.3 is an approximation, which is valid only for an isentropic expansion of an ideal gas into vacuum[31].

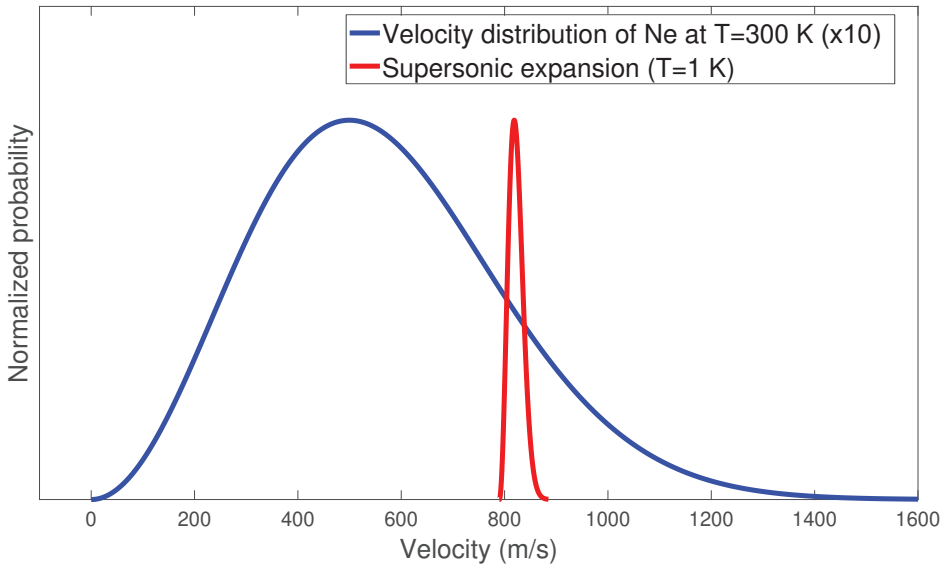

Figure 3.6: *Velocity distribution of neon (Ne) at a reservoir temperature of 300 K (blue curve), and in a supersonic molecular beam (red curve). The maximum velocity is shifted under the conditions of a supersonic expansion. All the curves are normalized to unity.*

The most probable velocity v_{mp} of a gas corresponding to the maximum value of its Maxwell-Boltzmann velocity distribution is $v_{mp} = \sqrt{(2RT/N_A m)}$. This means that after the expansion the mean flow velocity of the beam is virtually identical with the most probable velocity[31].

The main effect of the supersonic expansion is the cooling of the translational and of the internal degrees of freedom. The rate of equilibration between rotations and translations is relatively fast, resulting in an extensive rotational cooling of the molecules, before the collision-free region is reached[29]. The rate of vibration-rotation equilibrium is slower. Cooling of the rotational degrees of freedom is generally more efficient than that of vibrational ones, because of the small energy difference for the rotations. While rotational temperatures of the order of 0.1-10 K can be achieved in a supersonic jet expansion, vibrational temperatures are significantly higher, about 20-150 K[30]. However, since the energies of the most vibrational modes are large, thermal populations at the equilibrium reservoir temperatures are low, which minimizes the impact of incomplete vibrational cooling in the jet[30]. Additionally, the achieved vibrational temperatures can be influenced by the choice of a career gas. Heavier noble gases (Ar, Kr, Xe) provide more efficient vibrational cooling in comparison to He and Ne[30]. When, for instance, Ar is used as a career gas, less collisions are required to accelerate the seeded molecules and thus, larger number of collisions are available for cooling. This in turn can have a significant impact on the cooling of the vibrational degrees of freedom. On the other side, the achieved final rotational temperatures are higher in the case of Ar than by using He as a career gas[30].

Further important aspect is the cluster formation between the atoms of a carrier gas and the

seeded molecules. This process requires three-body collision and depends on the reservoir backing pressure and the orifice diameter D[30]. To reduce the number of possible cluster formations, one can decrease the backing pressure by increasing the diameter of the orifice. However, it should be bared in mind that the increase of the D will require a sufficient pumping speed for the maintenance of the low background pressure. The choice of a suitable carrier gas is thus a trade-off between the efficient vibrational cooling and the cluster formation. In our lab we commonly use Ne as a career gas.

In the future we intend to complement the application of the supersonic expansion by the usage of the buffer gas cooling to create cold molecular beams. The achieved forward velocity in a buffer gas cell is lower compared to the supersonic beam, while the flux is higher[32].

Bibliography

[1] T. J. Balle, E. J. Campbell, M. R. Keenan, and W. H. Flygare. A new method for observing the rotational spectra of weak molecular complexes: KrHCl. *J. Chem. Phys.*, 71(6):2723–2724, 1979.

[2] T. J. Balle and W. H. Flygare. Fabry–Perot cavity pulsed Fourier transform microwave spectrometer with a pulsed nozzle particle source. *Rev. Sci. Instrum.*, 52(1):33–45, 1981.

[3] J.-U. Grabow, W. Stahl, and H. Dreizler. A multioctave coaxially oriented beam-resonator arrangement Fourier-transform microwave spectrometer. *Rev. Sci. Instrum.*, 67(12):4072–4084, 1996.

[4] G. G. Brown, B. C. Dian, K. O. Douglass, S. M. Geyer, S. T. Shipman, and B. H. Pate. A broadband Fourier transform microwave spectrometer based on chirped pulse excitation. *Rev. Sci. Instrum.*, 79(5):053103, 2008.

[5] D. Schmitz, V. A. Shubert, T. Betz, and M. Schnell. Multi-resonance effects within a single chirp in broadband rotational spectroscopy:The rapid adiabatic passage regime for benzonitrile. *J. Mol. Spectrosc.*, 280:77–84, 2012.

[6] D. Schmitz. *Structural flexibility and chirality of polar molecules elucidated with broadband rotational spectroscopy*. PhD thesis, University of Hamburg, 2015.

[7] Arbitrary Waveform Generators AWG7000 Series Datasheet, 2016. https://www.tek.com/datasheet/arbitrary-waveform-generators-7.

[8] Digital Delay/Pulse Generator, Stanford Research Systems, DG645 Datasheet. https://www.thinksrs.com/downloads/pdfs/catalog/DG645c.pdf.

[9] Travelling wave tube amplifier, Amplifier Research 300T2G8, Datasheet. https://www.arworld.us/post/300T2G8.pdf.

[10] 2 - 18 GHz High Gain Horn Antenna, Q-par Angus Ltd., Datasheet. http://www1.isti.cnr.it/~salerno/Microonde/Horn_Antennas_Full.pdf.

[11] 1/8 DIN Vertical Temperature Controllers Datasheet. https://www.omega.com/temperature/pdf/CN710_SERIES.pdf.

[12] Miniature Solenoid Valves, Parker, Datasheet, 2016. http://www.parker.com/Literature/Precision%20Fluidics/Miniature%20Solenoid%20Valves/PulseValves.pdf.

[13] Stable High Vacuum Oil diffusion pumps, Oerlikon Leybold Vacuum, Datasheet, 2015. https://www.leyboldproducts.de/media/pdf/f2/1c/ec/PB_040020000_EN57d6efcd77c7e.pdf.

[14] RUVAC WAU 251 Oerlikon Leybold Vacuum, Datasheet. https://www.leyboldproducts.de/media/pdf/76/e1/56/TD_11721_EN595e995cb5e9f.pdf.

[15] D40B TRIVAC Vacuum Pump, Oerlikon Leybold Vacuum, Datasheet. https://www.ajvs.com/new/product_info.php?products_id=20305/.

[16] Low-noise amplifier AMF-7D-01001800-22-10P, L3 Narda-MITEQ, Datasheet. https://nardamiteq.com/viewmodel.php?model=AMF-7D-01001800-22-10P/.

[17] Digital and Mixed Signal Oscilloscopes, Tektronix, Datasheet. https://www.tek.com/datasheet/digital-and-mixed-signal-oscilloscopes.

[18] RF Switch - Pin Diode Solid State Switches. https://www.atmmicrowave.com/coaxial/rf-switch-pin-diode-switches/.

[19] C. Pérez, S. Lobsiger, N. A. Seifert, D. P. Zaleski, B. Temelso, G. C. Shields, Z. Kisiel, and B. H. Pate. Broadband Fourier transform rotational spectroscopy for structure determination: The water heptamer. *Chem. Phys. Lett.*, 571:1 – 15, 2013.

[20] Benchtop rubidium frequency standard, Stanford Research Systems, FS725 Datasheet. https://www.thinksrs.com/downloads/pdfs/catalog/FS725c.pdf.

[21] National Instruments NI PXIe-1065, User Manual and Specifications, 2017. http://www.ni.com/pdf/manuals/371990d.pdf.

[22] V. A. Shubert, D. Schmitz, C. Medcraft, A. Krin, D. Patterson, J. M. Doyle, and M. Schnell. Rotational spectroscopy and three-wave mixing of 4-carvomenthenol: A technical guide to measuring chirality in the microwave regime. *J. Chem. Phys.*, 142(21):214201, 2015.

[23] RF Power Amplifie KU PA 003055-100 A, Kuhne, Datasheet. https://www.kuhne-electronic.de/kuhne/en/shop/low-noise-amplifiers/KU+PA+BB+003055100+A++RF+Power+Amplifier/?action=shop_show_pdf_card&action_id=502&category_line_no=250000/.

[24] K. F. Smith and P. J. Unsworth. Molecular beam spectroscopy. *Sci. Progr.*, 53(209):45–59, 1965.

[25] R. E. Smalley, L. Wharton, and D. H. Levy. Molecular optical spectroscopy with supersonic beams and jets. *Acc. Chem. Res.*, 10(4):139–145, 1977.

[26] W. R. Gentry and C. F. Giese. Ten-microsecond pulsed molecular beam source and a fast ionization detector. *Rev. Sci. Instrum.*, 49(5):595–600, 1978.

[27] B. Yan, P. F. H. Claus, B. G. M. van Oorschot, L. Gerritsen, A. T. J. B. Eppink, S. Y. T. van de Meerakker, and D. H. Parker. A new high intensity and short-pulse molecular beam valve. *Rev. Sci. Instrum.*, 84(2):023102, 2013.

[28] L. Abad, D. Bermejo, V. J. Herrero, J. Santos, and I. Tanarro. Performance of a solenoid-driven pulsed molecular-beam source. *Rev. Sci. Instrum.*, 66(7):3826–3832, 1995.

[29] R. E. Smalley, L. Wharton, and D. H. Levy. Molecular optical spectroscopy with supersonic beams and jets. *Acc. Chem. Res.*, 10(4):139–145, 1977.

[30] M. V. Johnston. Supersonic jet expansions in analytical spectroscopy. *Trends Anal. Chem.*, 3(2):58 – 61, 1984.

[31] W. Christen, K. Rademann, and U. Even. Supersonic Beams at High Particle Densities: Model Description beyond the Ideal Gas Approximation. *J. Phys. Chem. A*, 114(42):11189–11201, 2010.

[32] N. R. Hutzler, H.-I. Lu, and J. M. Doyle. The Buffer Gas Beam: An Intense, Cold, and Slow Source for Atoms and Molecules. *Chem. Rev.*, 112(9):4803–4827, 2012.

Part I

Chiral components of essential oils

4

Structural and chiral analysis of the components in peppermint oil

4.1 Introduction

The application range of essential oils is as versatile as their composition. Pharmacology, medicine, food industry, or cosmetics are only a few fields, where they are widely used. Essential oils are complex multicomponent mixtures. Their main constituents belong to the group of terpenes, most of which reveal structural similarities.

Due to their great importance in our daily life, essential oils were studied extensively over the years, in order to, e.g. understand the way of their functionality in the human body, analyze dosage dependent side effects, identify and quantify major constituents, etc. One of the conventional techniques commonly applied for addressing this last question is gas chromatography (GC) coupled with mass spectrometry (GC-MS) or tandem mass spectroscopy (GC-MS-MS)[1–4]. A drawback of GC-MS techniques is that it can be difficult to recognize the retention time difference of structurally related components like the isomers of terpenes[5]. In addition, mass spectrometry can be ambiguous for structurally similar species[5]. Milestones on the way to an increase in separation efficiency were the developments of capillary and of multidimensional gas chromatography[5]. Also the introduction of chiral GC-MS, which enables the separation of enantiomeric compounds, contributed to a significant progress in the field of gas chromatographic techniques. However, the choice and preparation of suitable stationary phases can be laborious and time-consuming, which can be considered as one of the limitations of GC techniques in general. Additional methods for complex mixture analysis are often required to complement the information obtained with GC. One of the high-resolution spectroscopic techniques, which can be applied to disentangle the oil composition is a broadband rotational spectroscopy.

manuscript in preparation (experimental: 80%, data analysis: 70%)

A more detailed description of rotational spectroscopy is given in Chapter 2. For the purpose of this study, some of its major advantages should be emphasized. Due to its fingerprint character, rotational spectroscopy is highly suitable for analysis of complex mixtures containing similar components, as in the case of essential oils. It allows to identify different conformers[6] and isomers[7] of the same chemical component. Because of the difference in the distribution of atomic masses of the conformers, and therefore in their respective moments of inertia, conformers will have different sets of rotational constants and thus unique spectra. Moreover, because of the high sensitivity of rotational spectroscopy, isotopically substituted species can be observed in natural abundance, since the change in the molecular mass due to the isotopic substitution results in a different rotational spectrum of a species. The information obtained from the assignment of the isotopologues in the spectrum can be used for an accurate structure determination of the component of interest[8–10]. The structure information is of great importance for deeper insights into the functionality and interaction of the molecules. Additionally, by applying microwave three-wave mixing (M3WM)[11] (see also Chapter 2), the differentiation between the enantiomers of chiral essential oil components is possible.

The two main requirements for the applicability of this technique are that the molecules need to be polar and that they can be brought into the gas phase. The major constituents of essential oils are in general very volatile and possess permanent dipole moments, which renders them suitable for the study with rotational spectroscopy. Recently, another essential oil, namely buchu oil, was analyzed with this technique. In the scope of the study reported in Ref. 12 several terpenes present in this oil were identified and quantified. Also the enantiomeric excess (see Chapter 1) of one of its chiral components, menthone, was determined directly in the oil by applying M3WM[12].

In our lab two commercially available essential oils were studied with broadband rotational spectroscopy. These were peppermint (*Mentha* x *piperita L.*) and thyme (*Thymus vulgaris*) essential oils. In case of peppermint oil, spectra of two different samples were recorded. The analysis of one of them (sample I) regarding its chemical composition is reported in Ref. 13 and will not be discussed here. A detailed characterization of the other sample (sample II) will be presented in this chapter instead. The results for thyme oil will be summarized in Chapter 5.

Peppermint oil is well known for its soothing properties, and is often used in aroma therapy. In addition, it was shown to have antibacterial and antifungal activities,[14;15], and was tested as a therapy for irritable bowel syndrome symptoms[16–18], and as a treatment for some types of headache[19]. However, it is toxic, when applied in high dosage and may cause renal failure,[20] allergic reactions, nausea, and vomiting[21]. Apart from medicine and pharmacology, peppermint oil is also used in other fields, which include food industry (as e.g. flavor additives, in confectionery, or as food preservatives)[22], cosmetics (as e.g. fragrance in soaps, constituents of toothpastes, and mouthwashes)[23], and agriculture (as biopesticides)[24].

The main constituents of peppermint oil are menthol, menthone, eucalyptol, methyl acetate,

menthofuran, isomenthone, limonene, α-pinene, β-pinene, germacrene and pulegone[25;26]. Notably, since essential oils are natural products, individual samples can show high variations with respect to their composition. Several studies on peppermint oil using GC-MS were reported previously[26]. In one of the studies the most abundant menthone enantiomer in the oil was determined using achiral liquid chromatographic separation coupled with circular dichroism (CD) detection[27]. According to the reported results[27], (–)-menthone is present in the oil in almost enantiopure form.

In this chapter the rotational spectroscopy analysis of the peppermint oil sample not reported before (sample II) is given. Menthol is the most intense species in the recorded spectrum. Structure elucidation of its lowest energy conformer is reported. Additionally, another conformer of menthol is characterized for the first time in the context of this study. Conformational landscape of the menthol diastereomer, neomenthol, is analyzed using a computational approach. We also apply M3WM[11] to some chiral components of peppermint oil such as menthone and isomenthone in order to benchmark our technique with respect to the chiral analysis in mixtures and to demonstrate its capabilities.

4.2 Experimental and computational methods

The broadband spectrum of peppermint essential oil was measured with the CP-FTMW spectrometer COMPACT in Hamburg in the 2-8 GHz frequency range[28;29]. Instrumentation details are given in Chapter 3. No specific modifications were necessary in this case. The experimental set-up for the M3WM experiment also corresponds to the one described in Chapter 3. To increase the vapor pressure, the utilized oil sample was heated in a reservoir to 75°C, prior to being supersonically expanded into the vacuum chamber (neon as a carrier gas, 2 bars backing pressure).

To aid the assignment of additional menthol conformers, a separate broadband measurement on pure menthol was conducted. The menthol sample was purchased from Sigma-Aldrich and used without further purification. The applied experimental conditions correspond to the ones used in the previous rotational spectroscopy study on menthol[7] (3 bars backing pressure with neon as a carrier gas, 112°C heating temperature of the sample).

The spectra were assigned using an asymmetric rotor Hamiltonian in the I^r representation, as implemented in the PGOPHER[30] software. The structure of the lowest energy conformer of menthol was determined with the KRA[31] (based on the Kraitchman's equations[8]) and the STRFIT[32] (a non-linear least-squares procedure) programs. Conformational search for the lowest energy conformers of the other oil component, neomenthol, was performed with the aid of the Gaussian 09[33] software (see Section 4.5 for more details).

4.3 Broadband spectrum and identified components

In general, the line intensities in rotational spectra depend on numerous factors. In the weak-pulse limit of CP-FTMW spectroscopy they are proportional to the strength of the excitation field, the square of the transition dipole moment components, and the number of molecules interacting with the excitation field[28] (see Chapter 3). There are also some instrumental effects such as the frequency dependence of the amplifier (travelling wave tube, TWT, see Chapter 3) used for the enhancement of the excitation chirp. These effects can be corrected for by applying a specific instrument function. In the present study such corrections were not introduced as we are mainly focusing on the qualitative analysis of the sample.

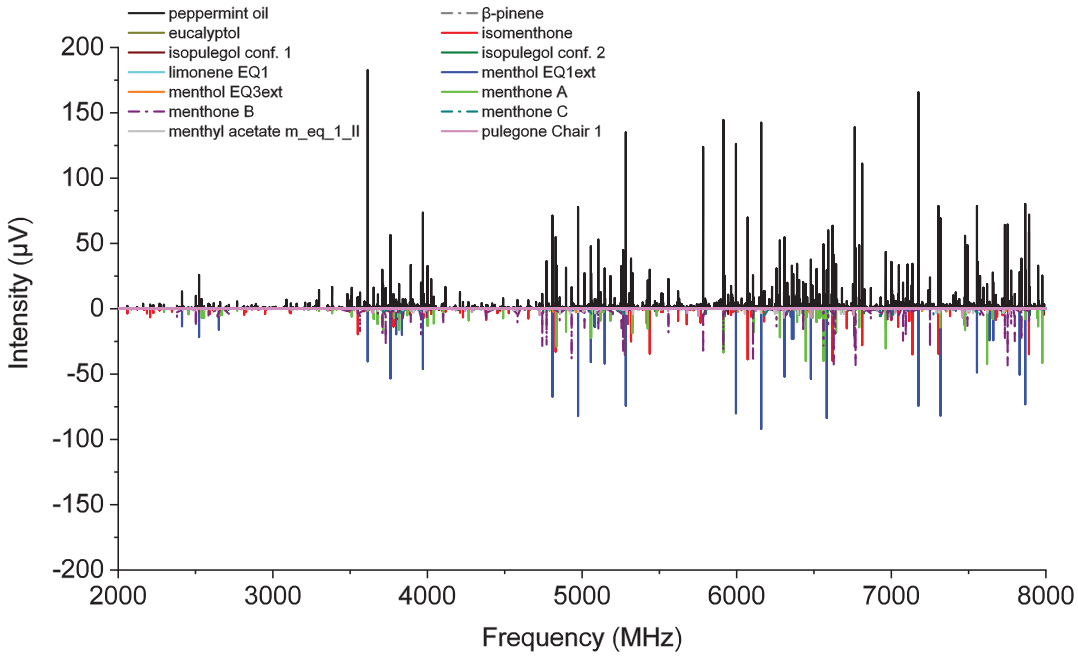

Figure 4.1: *The 2 - 8 GHz spectrum (4 million acquisitions, neon as a career gas) of peppermint oil. The black trace shows the experimental spectrum, while the lower traces represent simulations based on previously reported (see text) experimental rotational parameters for the main constituents of peppermint oil.*

Nine different terpenes were identified (see Table 4.1) in the present peppermint oil spectrum. Their schematic structures are visualized in Figure 4.2. Several components such as menthol, menthone, isomenthone[7], β-pinene[34], limonene[35], eucalyptol[36], pulegone[37] (see also Chapter 6), and isopulegol[38] were studied before with rotational spectroscopy. The nomenclature of their conformers used in this manuscript corresponds to the one introduced in the respective studies quoted here. The most intense lines in the spectrum belong to the lowest energy conformer of menthol EQ1ext[7] with a signal-to-noise ratio (SNR) of approximately 570:1 for the strongest transitions. All three conformers of menthone (A, B and C), and also one

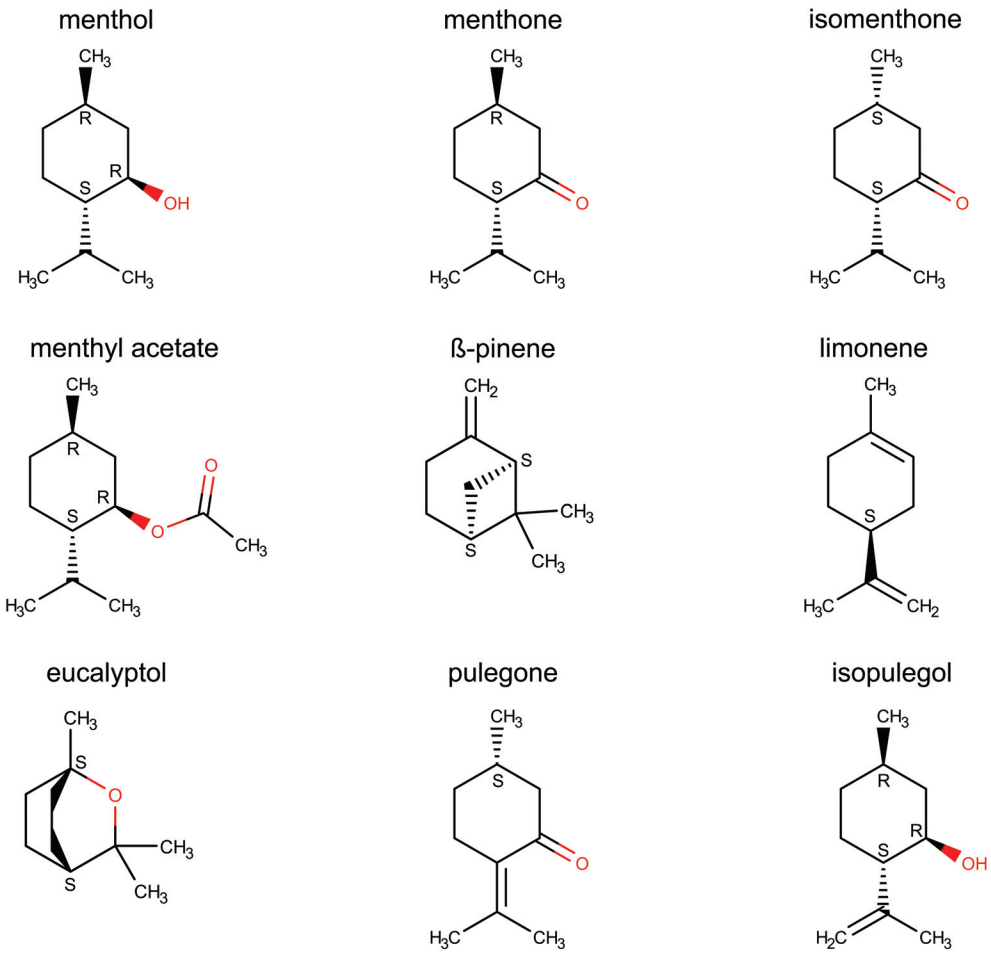

Figure 4.2: *Schematic structures of the different components present in peppermint oil (Mentha x piperita L.). The configuration of the chiral centers (R or S) is also given.*

conformer of isomenthone (eq-ax A)[7], could be assigned. Menthone B is the second strongest component in the spectrum with a SNR of roughly 360:1, followed by menthone A (SNR 300:1), isomenthone (SNR 250:1), and menthone C (SNR 130:1). Other components, which include eucalyptol, two conformers for isopulegol (1 and 2), limonene (EQ 1), β-pinene and one conformer of pulegone (Chair 1), show a similar SNR of roughly 20:1 for the strongest transitions.

According to the results of GC-MS[26], menthyl acetate is also present in the oil. This component was not analyzed previously with microwave spectroscopy. In order to determine its rotational parameters, additional studies on menthyl acetate were conducted using a commercially available sample. This approach allowed us to subsequently identify the lowest energy conformer of menthyl acetate (m_eq_1_II) in the peppermint oil spectrum with a SNR of 20:1. More details on the rotational spectroscopy analysis of menthyl acetate are provided in Chapter 7.

Table 4.1: *Experimental rotational constants and calculated (MP2 level of theory) magnitudes of the dipole moment components for the constituents found in the broadband spectrum of peppermint oil. Experimental values for the components in bold are reported for the first time in the context of this study.*

Component	Formula	A (MHz)	B (MHz)	C (MHz)	$\lvert\mu_a\rvert$ (D)	$\lvert\mu_b\rvert$ (D)	$\lvert\mu_c\rvert$ (D)	Ref.
Menthol (EQ1ext)	$C_{10}H_{20}O$	1779.79549(38)	692.62171(24)	573.34542(27)	1.4[a]	0.1	0.8	7
Menthol (EQ3ext)	$C_{10}H_{20}O$	1962.36595(77)	672.28085(29)	579.65418(31)	1.6[a]	0.03	0.8	–
Menthone A	$C_{10}H_{18}O$	1953.43379(43)	694.51551(19)	586.57758(19)	1.2[a]	2.5	0.5	7
Menthone B	$C_{10}H_{18}O$	2021.98637(36)	693.53686(16)	562.13636(16)	1.2[a]	2.2	1.2	7
Menthone C	$C_{10}H_{18}O$	2109.38469(65)	681.13604(27)	598.12413(25)	1.6[a]	2.0	1.2	7
Isomenthone	$C_{10}H_{18}O$	1535.27577(48)	812.92526(33)	671.43466(33)	0.6[a]	2.9	1.0	7
Menthyl acetate (m_eq_1_II)	$C_{10}H_{22}O_2$	687.63788(34)	577.21454(14)	357.20440(19)	0.5[a]	0.9	1.4	–
β-Pinene	$C_{10}H_{16}$	1901.889140(175)	1293.661042(80)	1150.831087(81)	0.5[a]	0.6	0.1	34
Limonene (EQ 1)	$C_{10}H_{16}$	3058.01643(149)	717.04590(76)	679.25973(75)	0.4[c]	0.4	0.4	35
Eucalyptol	$C_{10}H_{18}O$	1545.88790(43)	1080.467936	1038.933164	0.0[b]	1.6	0.0	36
Pulegone (Chair 1)	$C_{10}H_{16}O$	1909.05435(71)	739.06297(21)	578.14181(21)	0.7[a]	2.7	1.0	37
Isopulegol 1	$C_{10}H_{18}O$	1949.96485(299)	700.16883(113)	591.63903(111)	0.4	2.0	0.5	38
Isopulegol 2	$C_{10}H_{18}O$	1914.31605(195)	702.84904(119)	578.53932(124)	0.5	1.8	0.5	38

[a] 6-311++G(d,p)
[b] cc-pVTZ
[c] 6-311++G(2df,p)

After the identification of the main peppermint oil constituents and their conformers in the spectrum, several lines with a SNR of about 20:1 remained unassigned. Since menthol is the most abundant component of peppermint oil, it was assumed that also other conformers of this monoterpene should be present in the spectrum. A separate broadband measurement on pure menthol sample was performed for this purpose. This allowed to experimentally determine another menthol conformer (EQ3ext), which was subsequently identified in the peppermint oil spectrum (Section 4.4.2).

It is noticeable that eucalyptol was found to be the most intense species in the broadband spectrum of the other peppermint oil sample previously analyzed in our group (sample I, see Section 5.1)[13]. The spectra of the two samples were recorded under similar experimental conditions as described in Section 7.2. Since peppermint oil is a natural product, its composition can vary depending on several factors (e.g. geographical origin of the peppermint plant, way of cultivation and oil extraction, etc.). This variation in chemical composition results in different line intensities observed in the spectra due to the different number of molecules in the gas phase interacting with the excitation field[28].

4.4 Menthol

4.4.1 Structure of the lowest energy conformer of menthol

Menthol is observed to be the strongest component in the present spectrum (Figure 4.1). Since the SNR for the lowest energy conformer of menthol, EQ1ext, is 570:1, its singly substituted ^{13}C isotopologues could be observed in natural abundance (1.1%). Their rotational constants are provided in Table A.1. Together with the experimentally determined rotational parameters of the parent species, these were used to determine the substitution structure of EQ1ext (the so-called r_s structure) with the aid of the KRA program by solving Kraitchman's equations[8].

A comparison between the calculated (MP2/6-311++G(d,p)) and the experimental r_s substitution structure of EQ1ext is depicted in Figure 4.3, which shows a good agreement. The position of the oxygen atom in the hydroxyl group of EQ1ext could not be determined from the experimental data, because the SNR of the spectrum was not high enough (natural abundance of ^{18}O is 0.2%[39]).

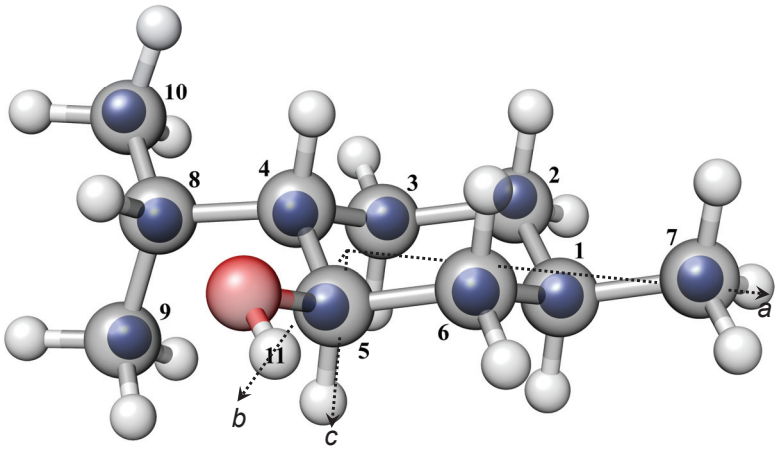

Figure 4.3: *Comparison between calculated (grey, MP2/6-311++G(d,p)) and experimental (blue spheres) Kraitchman substitution structure (r_s) of the lowest energy conformer of menthol, EQ1ext, determined from ^{13}C single isotopically substituted species in the broadband spectrum of peppermint oil. The carbon atom labelling is in accordance with the one used in Table A.1. Note that it does not correspond to the IUPAC nomenclature. The principal axes axes a, b and c are depicted.*

The approach based on the Kraitchman's equations can be regarded as a direct way for the structural determination. However, it bears some limitations. If an atom is located close to the principal axis, its coordinates cannot be determined with the Kraitchman's equations, resulting in imaginary numbers (see Chapter 2). Such coordinates have to be fixed to zero for the r_s structure. This is the case for the C3 (close to the *a*-axis), C4 (close to the *b*-axis), C5 (close to the *a*-axis), C8 (close to the *b*-axis), and C9 (close to the *b*-axis) atoms of EQ1ext (Figure 4.3). Significant deviations between the computationally predicted and

the experimental values are possible for the structural parameters including these atoms (highlighted in italics in Table A.2). This is, for instance, the case for the bond lengths r(C2 − C3), r(C3 − C4), r(C4 − C5), and r(C5 − C6) (see r_e structure in comparison to the r_s-fit, Table A.2).

An alternative approach for obtaining structural information is to fit the internal coordinates directly to the moments of inertia in a non-linear least-squares procedure[32] (the effective structure r_0). The r_0-fit allows to exploit the information from multi-isotopically substituted species. The structural parameters obtained both with r_s and r_0 fits are summarized in Table A.2. An overall better agreement between the theory and the experiment is achieved with the r_0 fit. Yet, it resulted in larger relative uncertainties for the angle ∠(C7 − C1 − C2) and the dihedral ∠(C6 − C5 − C4 − C3) in comparison to the r_s fit. Excluding these parameters from the r_0 fit by keeping them fixed to the ab initio values did not improve the standard deviation of the fit, which is 0.0024 uÅ^2.

4.4.2 Another conformer of menthol

A broadband spectrum (2-8 GHz) of pure menthol was recorded to aid the assignment of possible additional menthol conformers. This resulted in the experimental detection of another conformer, in following referred to as conformer 2. Based on its rotational parameters, it could be subsequently fitted in the peppermint oil spectrum (see Table A.3). The results of the final fits for the two menthol conformers in the peppermint oil spectrum are given in Table 4.2.

In the previously reported study[7], four conformers of menthol (in addition to the lowest energy EQ1ext) with zero-point corrected relative energies up to 5 kJ/mol were identified using quantum chemical calculations. The experimentally determined rotational constants of conformer 2 are close to two of them, namely EQ3int and EQ3ext. In order to make an assignment, a comparison of the experimental and the theoretical (MP2/6-311++G(d,p) level of theory) parameters was carried out (Table 4.2). Since EQ3int and EQ3ext differ only in the orientation of the hydroxyl group with respect to the cyclohexane ring, their rotational constants are very similar. It is noticeable that the rotational constant A of conformer 2 is closer to the one predicted for EQ3int. However, the zero-point corrected relative energy of EQ3ext is lower compared to EQ3int (see Table 4.2), meaning that EQ3ext should be the kinetically more stable conformer.

More reliable parameters for guiding the assignment are the calculated dipole moment components. In case of EQ3int all three dipole moment components μ_a, μ_b and μ_c are approximately 1 D. In contrast, μ_b of EQ3ext is predicted to be close to zero. Thus, for EQ3int all three types of rotational transitions are expected in the spectrum, while for EQ3ext only a- and c-type transitions should be observable. Indeed, only a- and c-type transitions were observed for conformer 2, allowing an assignment of this component to EQ3ext.

According to the calculations given in Ref. 7, the interconversion barrier between EQ1ext and EQ3ext is approximately 10 kJ/mol. This means that both conformers should be present in

Table 4.2: *Comparison between theoretical parameters for EQ1ext, EQ3ext, and EQ3int (MP2/6-311++G(d,p) level of theory) and experimental ones (EQ1ext and conformer 2). The calculated parameters were taken from Ref. 7, while the experimental ones belong to the species identified in the peppermint oil spectrum. Note that for the assignment of conformer 2, rotational parameters determined in a separate broadband measurement on pure menthol were used as a starting point for the final fit. Here it is also specified, if the respective type of rotational transitions was observed (y) in peppermint oil spectrum or not (n).*

Parameter	Experimental		MP2 [a]		
	EQ1ext	Conformer 2	EQ1ext[b]	EQ3ext[b]	EQ3int[b]
A | MHz	1779.79328(39)	1962.34911(98)	1795	1975	1960
B | MHz	692.62118(29)	672.27902(57)	699.7	674.7	674.1
C | MHz	573.34522(33)	579.65735(55)	574.5	582.7	581.5
ΔJ | kHz	0.0168(45)	0.0159(86)			
μ_a | D[c]	*y*	*y*	1.4	1.6	1.1
μ_b | D	*n*	*n*	-0.1	-0.03	-1.0
μ_c | D	*y*	*y*	0.8	0.8	-0.9
ΔE kJ/mol [d]			0	3.0	5.0
σ [e] | kHz	8.2	8.6			
N [f]	81	35			

[a] $6-311++G(d,p)$
[b] Parameters taken from Ref 7
[c] $D \approx 3.3356 * 10^{-30} C \cdot m$
[d] Zero-point corrected relative energy
[e] RMS deviation of the fit
[f] Number of fitted transitions

the cold jet, which is in agreement with our experimental result. The intensity ratio between EQ1ext and EQ3ext in the present broadband spectrum of peppermint oil is about 30:1.

4.5 Theoretical study of neomenthol

Menthol is a chiral molecule and has three stereogenic centers (Figure 4.2) that give rise to eight stereoisomers or four enantiomeric pairs. In contrast to the enantiomers, which have an opposite configuration at all their stereogenic centers, only some of the stereogenic centers of the diastereomers differ in their absolute configuration. The four diastereomers of menthol are called menthol, isomenthol, neomenthol, and neoisomenthol. Their respective structures are depicted in Figure 4.4. Of the four diastereomers, only menthol and neomenthol should be present in peppermint oil[40].

A conformational analysis was performed to determine the energetically most stable conformers of neomenthol, which could be present in our spectrum. Since the core structure of neomenthol is a cyclohexane ring, its substituents (methyl-, hydroxyl-, and isopropyl groups) can be located either in the equatorial or in the axial positions (Figure 4.5).

The energetically most preferred arrangement is when the methyl group and the bulky isopropyl group are positioned equatorially. The hydroxyl group is then orientated axially. Consequently, another structural arrangement implies isopropyl and methyl groups in axial orientations, while the hydroxyl group is located in equatorial position.

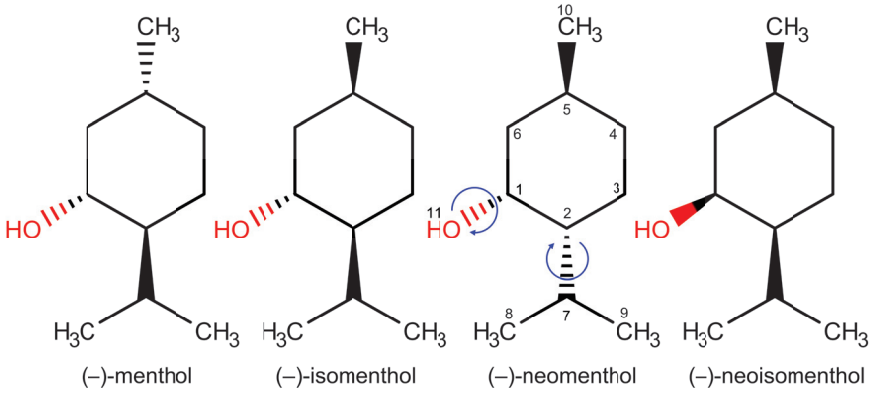

Figure 4.4: *Schematic representation of the four diastereomers of menthol: menthol, isomenthol, neomenthol, and neoisomenthol. In case of neomenthol, the arrows indicate the bonds, which were rotated to obtain a potential energy surface (PES) scan for the possible neomenthol conformers; the atom labelling corresponds to the IUPAC nomenclature.*

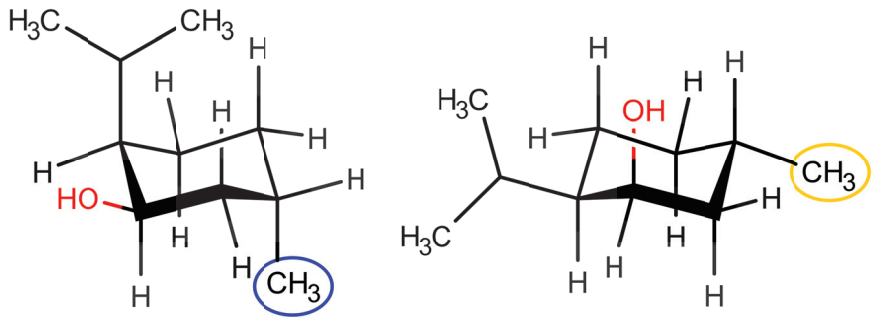

Figure 4.5: *Two possibilities for the arrangement of the neomenthol substituents (methyl-, hydroxyl-, and isopropyl groups) in either equatorial or axial positions with respect to the cyclohexane core structure. The highlighted methyl group shows how these positions can be interchanged by the ring flipping.*

In order to find the lowest energy conformers with such geometries, a potential energy surface (PES) scan using the Gaussian 09 program package[33] was performed. Two dihedral angles involving the isopropyl group (C8–C7–C2–C3) and the hydroxyl group (H11–O–C1–C6) were scanned in steps of 10 ° at the B3LYP/6-311g level of theory (see Figure 4.4 for labelling). The results are depicted in Figure 4.8. The minima in the PES were subsequently optimized at the B3LYP level of theory with Grimme's empirical dispersion correction[41]. They are shown in Figures 4.6 and 4.7. The respective calculated parameters are summarized in Table 4.3.

Table 4.3: *Calculated (B3LYP-D3/6-311++G(d,p)) rotational parameters for the (–)-enantiomers of the equatorial, eq1-eq8, and the axial, ax1-ax6, conformers of neomenthol. The axial and equatorial conformers (with respect to the orientation of the isopropyl and methyl groups) presented here correspond to the minima in the PES (see Figure 4.8 a) and b)). The zero-point corrected relative energy is given.*

	A (MHz)	B (MHz)	C (MHz)	μ_a	μ_b	μ_c	ΔE (kJ/mol)
Conformer eq1	2002.62	677.67	570.54	-0.9	-0.6	0.8	0
Conformer eq2	1994.80	676.29	569.66	1.4	0.6	0.7	0.1
Conformer eq3	1977.30	677.76	568.37	-0.8	1.5	0.3	1.4
Conformer eq4	1965.14	674.95	598.12	-1.1	-0.4	1.0	3.1
Conformer eq5	2069.11	665.05	614.02	-0.9	-0.8	0.8	3.6
Conformer eq6	1941.82	676.25	594.46	-0.9	1.5	0.1	5.2
Conformer eq7	2048.58	663.05	612.31	-0.9	1.4	0.6	5.4
Conformer eq8	1955.89	669.62	598.14	1.3	0.4	0.8	5.6
Conformer ax1	1537.56	855.39	645.36	0.2	-1.1	1.0	18.3
Conformer ax2	1592.67	850.31	641.76	1.9	-0.2	-0.3	19.1
Conformer ax3	1598.55	841.52	637.63	0.4	-1.5	-1.0	21.6
Conformer ax4	1574.91	820.76	685.24	-1.6	0.2	-0.1	24.3
Conformer ax5	1565.50	821.87	684.77	0.04	0.8	1.2	24.6
Conformer ax6	1557.14	820.59	683.62	-0.1	1.5	-1.0	25.3

The equatorial (with respect to the orientation of the isopropyl and the methyl groups) conformers eq1-eq8 are, as expected, significantly lower in energy than the axial (ax1-ax6) ones (see Table 4.3). One of the reasons behind this observation is the steric hindrance of the isopropyl group in the axial position, and the repulsive forces due to its proximity to the hydrogens of the cyclohexane (see Figure 4.7).

Since the zero-point corrected relative energy difference between the three lowest conformers eq1-eq3 is small (around 1 kJ/mol), they were analyzed in more detail. They differ only in the orientation of the hydroxyl group with respect to the cyclohexane ring (Figure 4.6). The conformers eq1 and eq2 are close in energy, with ΔE = 0.1 kJ/mol, while eq3 is about 1.4 kJ/mol higher in energy than conformer eq1. Notably, these energy differences lie within the accuracy of calculation. To calculate the interconversion barrier between eq1, eq2, and eq3, an additional scan by changing the dihedral angle of the hydroxyl group (H11–O–C1–C6) was performed. The barrier between the conformers eq1 and eq2, and eq2 and eq3 was determined to be approximately 4 kJ/mol (Figure 4.9) or about 330 cm^{-1}. Since Ne was used as a carrier gas, the relaxation of the eq1, eq2, and eq3 conformers into each other would be less effective than by using heavier inert gases (Ar, Kr). According to literature, no relaxation is expected, if the conformational interconversion barrier is greater than 350 cm^{-1}, or roughly 4.2 kJ/mol[42].

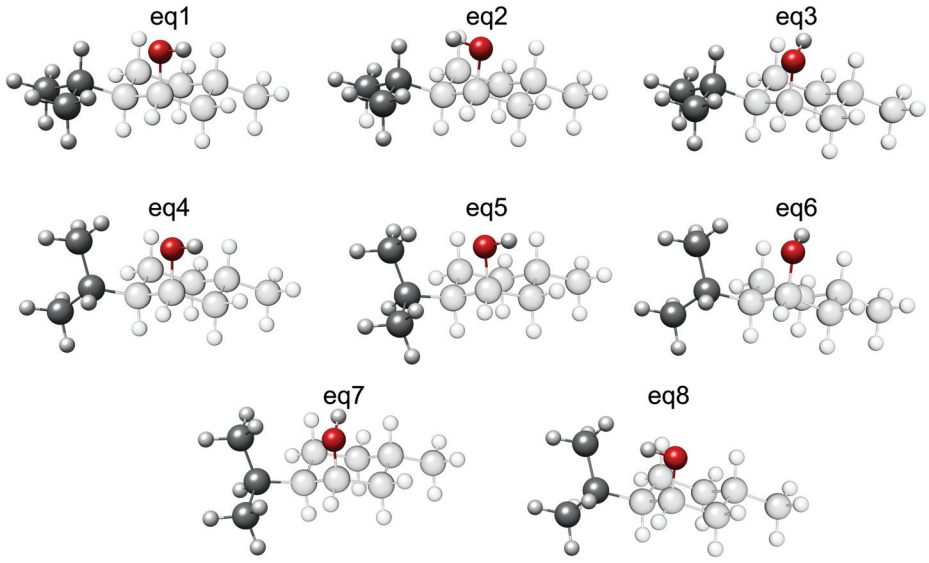

Figure 4.6: *Lowest energy structures obtained from a potential energy surface (PES, see Figure 4.8 a)) scan for the equatorial (with respect to the orientation of the isopropyl and methyl groups) conformers of neomenthol. Structures were optimized at B3LYP-D3/6-311++G(d,p) level of theory. The difference in the orientation of the substituents of the respective conformers is highlighted, while the rest of the molecule is transparent.*

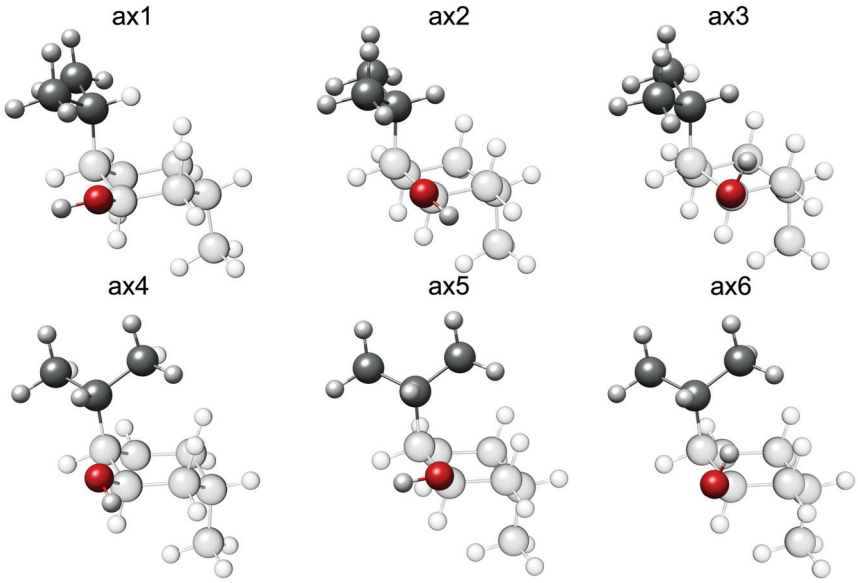

Figure 4.7: *Lowest energy structures obtained from potential energy surface (PES, see Figure 4.8 b)) scan for the axial (with respect to the orientation of isopropyl and methyl groups) conformers of neomenthol. Structures were optimized at B3LYP-D3/6-311++G(d,p) level of theory. The difference in the orientation of the substituents of the respective conformers is highlighted, while the rest of the molecule is transparent.*

This empirical cut-off value is close to the predicted interconversion barriers of eq1, eq2 and eq3. Thus, the relaxation of the respective conformers into each other cannot be ruled out. This aspect could not be explored experimentally, since none of the neomenthol conformers could be assigned in the present peppermint oil spectrum, probably due to a low concentration of neomenthol in the sample. While menthol is expected to be the major component, neomenthol is mostly considered as an impurity[40].

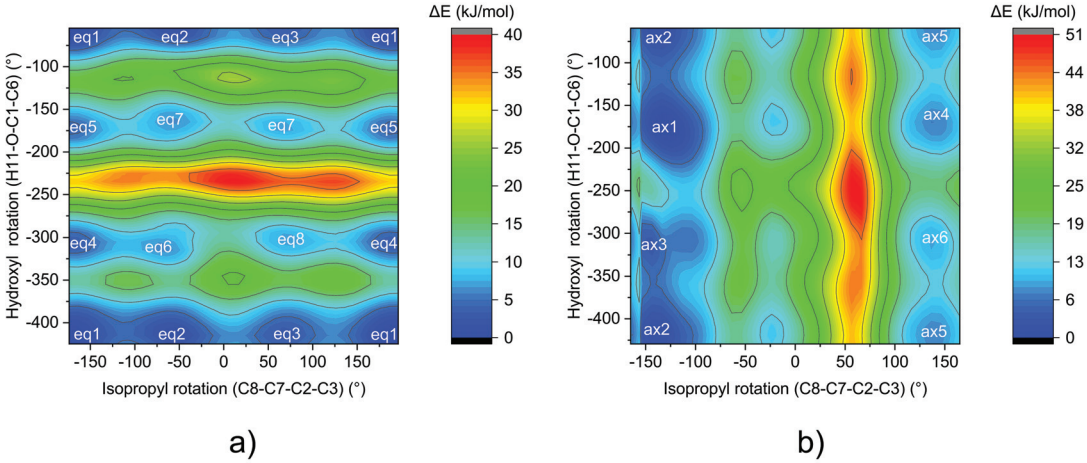

Figure 4.8: *Potential energy landscape of neomenthol as a function of the isopropyl (C8–C7–C2–C3) and the hydroxyl (H11–O–C1–C6) dihedral angles, which were scanned in steps of 10 °. a) Scan for the lowest energy neomenthol conformers with isopropyl and methyl groups in equatorial position. b) Scan for the lowest energy neomenthol conformers with isopropyl and methyl groups in axial position. The respective minima are highlighted (eq=equatorial, ax=axial). Calculations were performed at the B3LYP/6-311G level of theory.*

4.6 M3WM in peppermint oil

Most of the peppermint oil components are chiral and can be expected to occur enantio-enriched. It was reported before[43] that (–)-menthone, (+)-isomenthone, (–)-menthol, and (–)-menthyl acetate are the dominating enantiomers of the respective species in peppermint oil. M3WM was applied in this study on several chiral constituents of the oil with the aim to determine their enantiomer in excess, and to benchmark the technique by comparing the obtained results with the ones from the literature.

One of the requirements for a successful M3WM experiment is the presence of three non-zero dipole moment components (see Chapter 2). This is normally true for molecules with C_1 symmetry. However, due to some specific geometric arrangements, one of the dipole moment components can become close to zero. This is the case for EQ1ext, the most intense conformer of menthol (see Section 4.4), where μ_b is close to zero (Table 4.2).

The next strongest component is menthone with its three conformers (A, B and C), and its diastereomer isomenthone. M3WM was successfully applied on menthone A and isomenthone

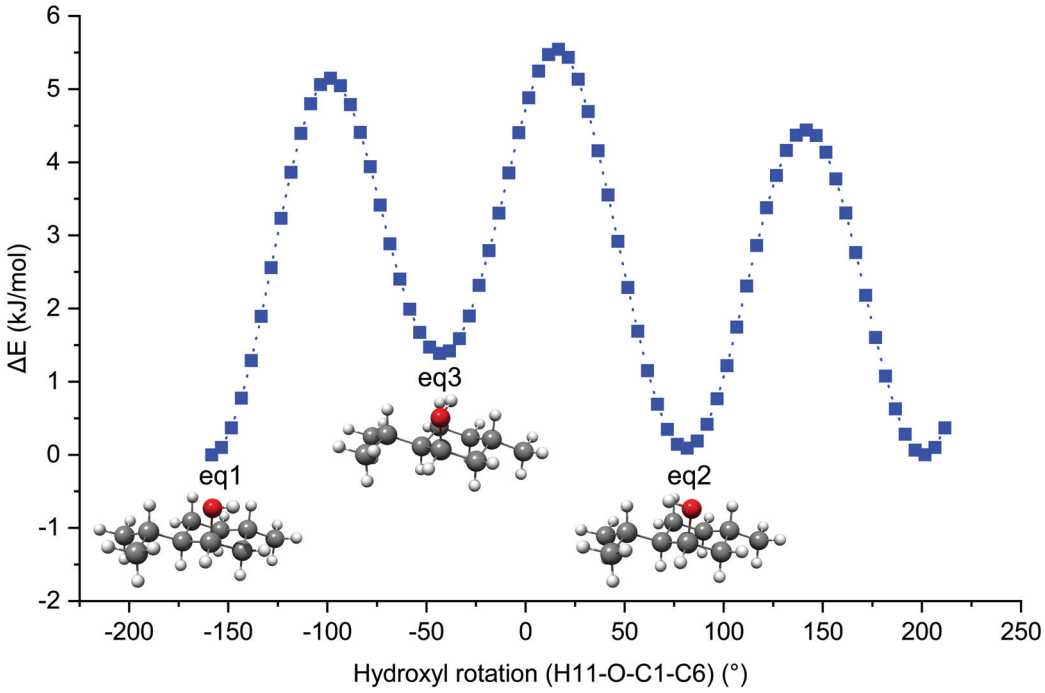

Figure 4.9: *Interconversion barrier between the three lowest energy conformers (eq1-eq3) of neomenthol as obtained by scanning the dihedral angle involving the hydroxyl group (H11–O–C1–C6). Calculations were carried out at the B3LYP-D3BJ/6-311++G(d,p) level of theory.*

eq-ax A before[44;45]. The experiment on these molecular systems was repeated directly in peppermint oil in the scope of the present work. The respective M3WM cycles together with the used pulse durations for drive and twist are depicted in Figure 4.10. The obtained "listen" signal at 3713.18 MHZ (frequency domain) for menthone A contained in the oil is shown in Figure 4.12.

To determine the excess enantiomer of menthone in peppermint oil, a commercially available nearly enantiopure sample ((–)-menthone, 90% purity) was purchased as a reference. The phase behavior of the M3WM signal of enantiopure (–)-menthone and of menthone in the oil was compared. The time domain FIDs of the listen transitions for the two samples are in phase, meaning that (–)-menthone should indeed be the dominant enantiomer in the oil, as was reported before[43] (Figure 4.11).

The M3WM experiment with isomenthone eq-ax A in the oil was also successful (see Figure 4.12). Currently, there is no commercially available enantio-enriched isomenthone sample, meaning that a similar analysis of the enantiomeric composition as with menthone A could not be performed for isomenthone. M3WM experiments with other chiral components in the oil such as menthyl acetate and pulegone were also tried, but remained unsuccessful. This is probably due to the low intensity of these components in the present peppermint oil spectrum. Instead, the M3WM experiments were conducted on pure pulegone (Chapter 6) and menthyl acetate (Chapter 7) to determine the suitable cycles for future studies. Since

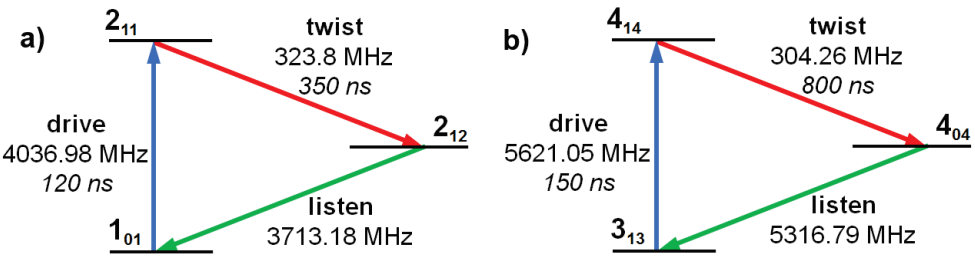

Figure 4.10: *Three-wave mixing cycles including pulse durations used for the M3WM experiment on a) menthone A and b) isomenthone eq-ax A.*

the percentage of the respective components can vary between the samples, the idea would be to repeat the experiment using different samples of *Mentha x piperita L.* This allows to obtain a more detailed and comprehensive chiral analysis of this natural product and to test the advantages and limitations of M3WM.

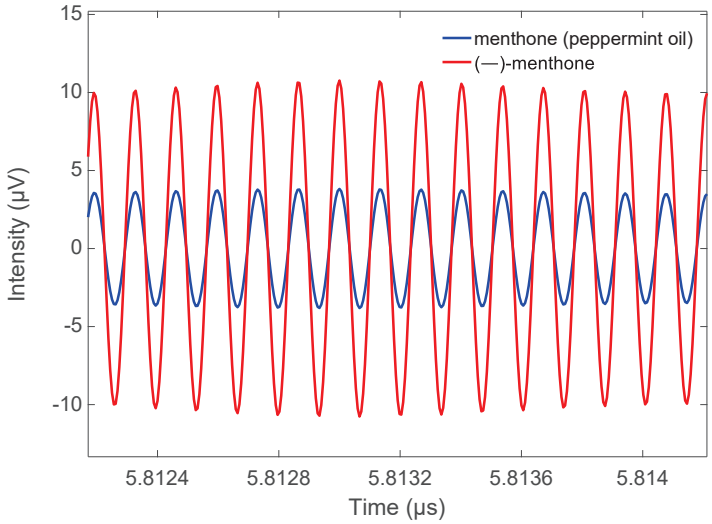

Figure 4.11: *Comparison of the time-domain M3WM signals (free induction decay, FID) for the listen transition at 3713.18 MHZ for menthone A in peppermint oil (blue) and enantio-enriched commercially available sample of (–)-menthone (red).*

4.7 Summary

In summary, we could identify nine different terpenes with their respective conformers in the peppermint oil broadband spectrum. The strongest component is here the lowest energy conformer of menthol, EQ1ext, for which the structure could be determined experimentally. Menthol is known to inhibit our nicotinic acetylcholine receptors[46]. It also activates the so-called TRPM receptors (subfamily M, member 8), which are responsible for the cold sensation[47]. The experimental structure determination of the lowest energy conformer of menthol can therefore be of interest for further exploration of these biochemical pathways.

However, it should be bared in mind that the most stable conformer in the gas phase does not necessarily represent the lowest energy one in aqueous solution.

Another menthol conformer, EQ3ext, present in the spectrum is reported for the first time. Menthol has a high commercial value. The cheapest way of its production from an industrial point of view is a hydrogenation of (−)-menthone. The by-product of this synthesis is (+)-neomenthol[48]. This component is also present by the enzymatic production of menthol, which takes place during the maturation process of different *Mentha* species[49]. It was expected that neomenthol is present in the oil sample analyzed here. For this reason, an extensive conformational analysis of neomenthol was performed. Although this component could not be observed experimentally, the obtained computational results might be useful for future studies.

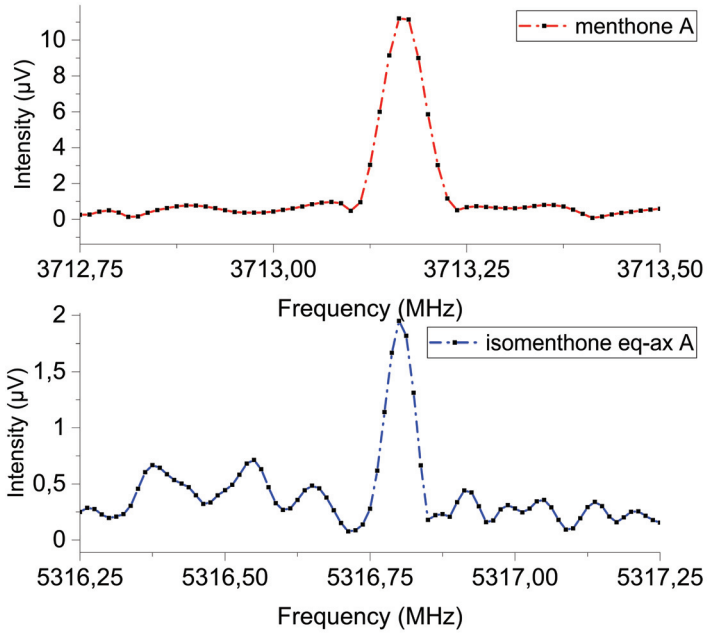

Figure 4.12: *M3WM signal as obtained for the "listen" transition of menthone A at 3713.18 MHz and of isomenthone eq-ax A at 5316.79 MHz (60.000 averages each).*

The lowest energy conformer of menthyl acetate m_eq_1_II was identified in the present spectrum. As in the case of EQ3ext, a separate measurement on pure sample was conducted to aid the assignment. More details regarding menthyl acetate are given in Chapter 7.

M3WM was performed on menthone and isomenthone, showing that this technique is applicable to complex chiral samples such as commercially available peppermint oil. The next step is to extend the range of the chiral components analyzed directly in the oil with the M3WM by using different peppermint oil samples, where such components as e.g. menthyl acetate are present in higher amounts. This would allow to benchmark the technique and to explore its capability.

Bibliography

[1] A. Cazaussus, R. Pes, N. Sellier, and J. C. Tabet. GC-MS and GC-MS-MS analysis of a complex essential oil. *Chromatographia*, 25(10):865–869, 1988.

[2] D. J. Daferera, B. N. Ziogas, and M. G. Polissiou. GC-MS Analysis of Essential Oils from Some Greek Aromatic Plants and Their Fungitoxicity on Penicillium digitatum. *J. Agric. Food Chem.*, 48(6):2576–2581, 2000.

[3] A. R. Bilia, G. Flamini, V. Taglioli, I. Morelli, and F. F. Vincieri. GC–MS analysis of essential oil of some commercial Fennel teas. *Food Chem.*, 76(3):307 – 310, 2002.

[4] J. Li, J. Liu, H. Lan, M. Zheng, and T. Rong. GC-MS analysis of the chemical constituents of the essential oil from the leaves of yacon *(Smallanthus sonchifolia). Front. Agric. China*, 3(1):40, 2009.

[5] P. J. Marriott, R. Shellie, and C. Cornwell. Gas chromatographic technologies for the analysis of essential oils. *J. Chromatogr. A*, 936(1):1 – 22, 2001.

[6] S. R. Domingos, C. Pérez, C. Medcraft, P. Pinacho, and M. Schnell. Flexibility unleashed in acyclic monoterpenes: conformational space of citronellal revealed by broadband rotational spectroscopy. *Phys. Chem. Chem. Phys.*, 18:16682–16689, 2016.

[7] D. Schmitz, V. A. Shubert, T. Betz, and M. Schnell. Exploring the conformational landscape of menthol, menthone, and isomenthone: a microwave study. *Front. Chem.*, 3:15, 2015.

[8] J. Kraitchman. Determination of Molecular Structure from Microwave Spectroscopic Data. *Am. J. Phys.*, 21(1):17–24, 1953.

[9] C. Pérez, S. Lobsiger, N. A. Seifert, D. P. Zaleski, B. Temelso, G. C. Shields, Z. Kisiel, and B. H. Pate. Broadband Fourier transform rotational spectroscopy for structure determination: The water heptamer. *Chem. Phys. Lett.*, 571:1 – 15, 2013.

[10] S. Zinn, T. Betz, C. Medcraft, and M. Schnell. Structure determination of trans-cinnamaldehyde by broadband microwave spectroscopy. *Phys. Chem. Chem. Phys.*, 17:16080–16085, 2015.

[11] D. Patterson, M. Schnell, and J. M. Doyle. Enantiomer-specific detection of chiral molecules via microwave spectroscopy. *Nature*, 497:475–478, 2013.

[12] B. H. Pate, L. Evangelisti, W. Caminati, Y. Xu, J. Thomas, D. Patterson, C. Pérez, and M. Schnell. Chapter 17 - Quantitative Chiral Analysis by Molecular Rotational Spectroscopy. In P. L. Polavarapu, editor, *Chiral Analysis (Second Edition)*, pages 679 – 729. Elsevier, 2018.

[13] S. R. Domingos, C. Pérez, and M. Schnell. Sensing Chirality with Rotational Spectroscopy. *Annu. Rev. Phys. Chem.*, 69(1):499–519, 2018.

[14] M. Moghaddam, M. Pourbaige, H. K. Tabar, N. Farhadi, and S. M. A. Hosseini. Composition and Antifungal Activity of Peppermint (Mentha piperita) Essential Oil from Iran. *J. Essent. Oil Bear. Pl.*, 16(4):506–512, 2013.

[15] A. Sivropoulou, S. Kokkini, T. Lanaras, and M. Arsenakis. Antimicrobial activity of mint essential oils. *J. Agric. Food Chem.*, 43(9):2384–2388, 1995.

[16] B. D. Cash, M. S. Epstein, and S. M. Shah. A Novel Delivery System of Peppermint Oil Is an Effective Therapy for Irritable Bowel Syndrome Symptoms. *Dig. Dis. Sci.*, 61(2):560–571, 2016.

[17] R. Khanna, J. K. Macdonald, and B. G. Levesque. Peppermint oil for the treatment of irritable bowel syndrome: a systematic review and meta-analysis. *J. Clin. Gastroenterol.*, 48(6):505–512, 2014.

[18] S. L. Haber and S. Y. El-Ibiary. Peppermint oil for treatment of irritable bowel syndrome. *Am. J. Health Sys. Pharm.*, 73(2):22–31, 2016.

[19] H. Göbel, A. Heinze, K. Heinze-Kuhn, A. Göbel, and C. Göbel. Oleum menthae piperitae (Pfefferminzöl) in der Akuttherapie des Kopfschmerzes vom Spannungstyp. *Der Schmerz*, 30(3):295–310, 2016.

[20] V. Schulz, R. Hänsel, and V. E. Tyler. *Rational Phytotherapy. A Physicians' Guide to Herbal Medicine.* Springer, 2001.

[21] M. Pittler and E. Ernst. Peppermint oil for irritable bowel syndrome: a critical review and metaanalysis. *Am. J. Gastroenterol*, 93(7):1131–135, 1998.

[22] V. R. Preedy. *Essential Oils in Food Preservation, Flavor and Safety.* Elsevier Science Inc., 2015.

[23] A. Sarkic and I. Stappen. Essential Oils and Their Single Compounds in Cosmetics—A Critical Review.

Cosmetics, 5(1), 2018.

[24] A. K. Tripathi, S. Upadhyay, M. Bhuyan, and P. R. Bhattacharya. A review of essential oils as biopesticide in insect-pest management. *J. Pharmacognosy Phytother.*, 1, 08 2009.

[25] J. Rohloff. Monoterpene Composition of Essential Oil from Peppermint (Mentha × piperita L.) with Regard to Leaf Position Using Solid-Phase Microextraction and Gas Chromatography/Mass Spectrometry Analysis. *J. Agric. Food Chem.*, 47(9):3782–3786, 1999.

[26] M. A. Hawrył, K. Skalicka-Woźniak, R. Świeboda, M. Niemiec, K. Stępak, M. Waksmundzka-Hajnos, A. Hawrył, and G. Szymczak. GC-MS fingerprints of mint essential oils. *Open Chem.*, 13, 01 2015.

[27] M. Zougagh, P. Aranda, G. Castañeda, and A. Ríos. Supercritical fluid extraction—Achiral liquid chromatography with circular dichroism detection for the determination of menthone enantiomers in natural peppermint oil samples. *Talanta*, 79(2):284 – 288, 2009.

[28] G. G. Brown, B. C. Dian, K. O. Douglass, S. M. Geyer, S. T. Shipman, and B. H. Pate. A broadband Fourier transform microwave spectrometer based on chirped pulse excitation. *Rev. Sci. Instrum.*, 79(5):053103, 2008.

[29] D. Schmitz, V. A. Shubert, T. Betz, and M. Schnell. Multi-resonance effects within a single chirp in broadband rotational spectroscopy: The rapid adiabatic passage regime for benzonitrile. *J. Mol. Spectrosc.*, 280:77–84, 2012.

[30] C. M. Western. PGOPHER: A program for simulating rotational, vibrational and electronic spectra. *J. Quant. Spectrosc. Ra.*, 186:221 – 242, 2017.

[31] Z. Kisiel. Assignment and Analysis of Complex Rotational Spectra. In J. Demaison, K. Sarka, and E. A. Cohen, editors, *Spectroscopy from Space*, volume 20, pages 91–106. Springer, Dordrecht, 2001.

[32] Z. Kisiel. Least-squares mass-dependence molecular structures for selected weakly bound intermolecular clusters. *J. Mol. Spectrosc.*, 218(1):58 – 67, 2003.

[33] M. J. Frisch, G. W. Trucks, H. B. Schlegel, G. E. Scuseria, M. A. Robb, J. R. Cheeseman, G. Scalmani, V. Barone, B. Mennucci, G. A. Petersson, H. Nakatsuji, M. Caricato, X. Li, H. P. Hratchian, A. F. Izmaylov, J. Bloino, G. Zheng, J. L. Sonnenberg, M. Hada, M. Ehara, K. Toyota, R. Fukuda, J. Hasegawa, M. Ishida, T. Nakajima, Y. Honda, O. Kitao, H. Nakai, T. Vreven, J. A. Montgomery, J. E. Peralta, F. Ogliaro, M. Bearpark, J. J. Heyd, E. Brothers, K. N. Kudin, V. N. Staroverov, R. Kobayashi, J. Normand, K. Raghavachari, A. Rendell, J. C. Burant, S. S. Iyengar, J. Tomasi, M. Cossi, N. Rega, J. M. Millam, M. Klene, J. E. Knox, J. B. Cross, V. Bakken, C. Adamo, J. Jaramillo, R. Gomperts, R. E. Stratmann, O. Yazyev, A. J. Austin, R. Cammi, C. Pomelli, J. W. Ochterski, R. L. Martin, K. Morokuma, V. G. Zakrzewski, G. A. Voth, P. Salvador, J. J. Dannenberg, S. Dapprich, A. D. Daniels, O. Farkas, J. B. Foresman, J. V. Ortiz, J. Cioslowski, and D. J. Fox. Gaussian 09, 2009.

[34] E. M. Neeman, J.-R. Avilés-Moreno, and T. R. Huet. The quasi-unchanged gas-phase molecular structures of the atmospheric aerosol precursor β-pinene and its oxidation product nopinone. *Phys. Chem. Chem. Phys.*, 19:13819–13827, 2017.

[35] J. R. A. Moreno, T. R. Huet, and J. J. L. González. Conformational relaxation of S-(+)-carvone and R-(+)-limonene studied by microwave Fourier transform spectroscopy and quantum chemical calculations. *Struct. Chem.*, 24(4):1163–1170, Aug 2013.

[36] C. Medcraft and M. Schnell. A Comparative Study of Two Bicyclic Ethers, Eucalyptol and 1,4-Cineole, by Broadband Rotational Spectroscopy. *Z. Phys. Chem.*, 230, 01 2015.

[37] A. Krin, P. C., P. Pinacho, M. M. Quesada-Moreno, J. J. López-González, J. R. Avilés-Moreno, S. Blanco, J. C. López, and M. Schnell. Structure Determination, Conformational Flexibility, Internal Dynamics, and Chiral Analysis of Pulegone and Its Complex with Water. *Chem. Eur. J*, 24(3):721–729.

[38] J. L. Neill, B. H. Pate, L. Evangelisti, N. Seifert, and L. Spada. Chiral Analysis in Complex Sample Mixtures by Fourier Transform Molecular Rotational Resonance Spectroscopy. Seattle, Washington, USA, 2015. CPAC Spring Meeting.

[39] T. B. Coplen, J. K. Böhlke, P. De Biévre, T. Ding, N. E. Holden, J. A. Hopple, H. R. Krouse, A. Lamberty, H. S. Peiser, K. Revesz, S. E. Rieder, K. J. R. Rosman, E. Roth, P. D. P. Taylor, R. D. Vocke, and Y. K. Xiao. Isotope-abundance variations of selected elements (IUPAC Technical Report). *Pure Appl. Chem.*, 74(10):1987–2017, 2002.

[40] M. Albrecht, J. Will, and M. A. Suhm. Chirality Recognition in Menthol and Neomenthol: Preference for Homoconfigurational Aggregation. *Angew. Chem. Int. Ed.*, 49(35):6203–6206.

[41] S. Grimme, J. Antony, S. Ehrlich, and H. Krieg. A consistent and accurate ab initio parametrization of density functional dispersion correction (DFT-D) for the 94 elements H-Pu. *J. Chem. Phys.*, 132(15):154104, 2010.

[42] R. S. Ruoff, T. D. Klots, T. Emilsson, and H. S. Gutowsky. Relaxation of conformers and isomers in seeded supersonic jets of inert gases. *J. Chem. Phys.*, 93(5):3142–3150, 1990.

[43] R. C. Menary and S. M. Garland. Authenticating Essential Oil Flavours and Fragrances. Rural Industries Research and Development Corporation, 1999.

[44] V. A. Shubert, D. Schmitz, and M. Schnell. Enantiomer-sensitive spectroscopy and mixture analysis of chiral molecules containing two stereogenic centers – Microwave three-wave mixing of menthone. *J. Mol. Spectrosc.*, 300:31 – 36, 2014.

[45] D. Schmitz, V. A. Shubert, D. Patterson, A. Krin, and M. Schnell. Phase Dependence of Double-Resonance Experiments in Rotational Spectroscopy. *J. Phys. Chem. Lett.*, 6(8):1493–1498, 2015.

[46] A. Ashoor, J. C. Nordman, D. Veltri, K.-H. S. Yang, L. Al Kury, Y. Shuba, M. Mahgoub, F. C. Howarth, B. Sadek, A. Shehu, N. Kabbani, and M. Oz. Menthol Binding and Inhibition of α7-Nicotinic Acetylcholine Receptors. *PLOS ONE*, 8(7):1–12, 07 2013.

[47] B. Schäfer. Menthol. *Chem. unserer Zeit*, 47(3):174–182, 2013.

[48] D. Manuale, C. Betti, A. J. Marchi, J. Yori, and E. Romeo. Synthesis of liquid menthol by hydrogenation of dementholized peppermint oil over Ni catalysts. *Quím. Nova*, 33:1231–1234, 12 2009.

[49] H. S. Toogood, A. N. Cheallaigh, S. Tait, D. J. Mansell, A. Jervis, A. Lygidakis, L. Humphreys, E. Takano, J. M. Gardiner, and N. S. Scrutton. Enzymatic Menthol Production: One-Pot Approach Using Engineered Escherichia coli. *ACS Synth. Biol.*, 4(10):1112–1123, 2015.

5

Rotational spectroscopy study of two chemotypes of thyme oil

5.1 Introduction

In the previous chapter we focused on the characterization of peppermint essential oil with broadband rotational spectroscopy. Here the rotational spectroscopy analysis of another essential oil, thyme oil (*Thymus vulgaris*), will be presented. The advantages of applying rotational spectroscopy for a detailed analysis of complex mixtures such as essential oils are summarized in Chapter 4.

Thyme oil has been studied before with gas chromatography technique coupled with mass spectroscopy (GC-MS)[1]. According to the results reported in Ref. 1, its main constituents are thymol, carvacrol, 1,8-cineole, linalool, borneol, α-pinene, 4-carvomenthenol, and camphor. The applications of thyme oil are very versatile. It was tested as potential antifungal oleogel[2] and shows antiseptic, antispasmodic, antimicrobial, antioxidative, and calming effects[3]. It was reported to strengthen memory and concentration[3] and used as a treatment of several diseases and indispositions, from common cold and skin conditions to hangovers and even depression[3]. Like peppermint oil, thyme oil is also widely used in food[4] and cosmetics[5] industry. To our knowledge, no studies on this essential oil using rotational spectroscopy were reported so far.

Thyme oil can be present in different chemotypes, depending on geographical region, climate, and other local conditions, with linalool, borneol, geraniol, sabinene hydrate, thymol, and carvacrol as their most abundant components respectively[6]. We analyzed two samples of thyme oil from Spain with two different chemotypes, containing either thymol or linalool. In the following, they will be referred to as thyme oil I (with thymol as the most abundant components) and thyme oil II (with linalool as the main compound). The aim of the study was to explore the chemical composition of thyme oil I and II and to elucidate the structures

manuscript in preparation (experimental: 60%, data analysis: 60%)

of their major constituents. The relative abundance of the different oil components was determined in a semi-quantitative way and compared to the results of the GC-MS analysis provided by the supplier. The experimental structure of the lowest energy conformer of thymol in thyme oil I could be determined based on the rotational constants of its ^{13}C isotopologues. Additionally, internal rotation of the other thymol conformer (the second lowest one) was analyzed. The signal-to-noise ratio (SNR) of linalool, the main component of thyme oil II, was not sufficient for obtaining such an information directly from the oil broadband spectrum. For this reason, a separate measurement on pure linalool sample was conducted to gain insights into its structure and internal dynamics.

5.2 Experimental techniques

The oil samples ("Thyme Thymol Organic" and "Thyme Linalool Organic", natural products, extracted using steam distillation) were purchased from Florihana and used without further purification. They were heated in a reservoir close to the orifice to 100° C and supersonically expanded into the vacuum chamber using neon as a carrier gas (3 bars backing pressure). The broadband spectra were measured on the chirped-pulse Fourier transform microwave (CP-FTMW) spectrometer COMPACT in the 2-8 GHz frequency range[7;8]. Further details regarding the experimental set-up are given in Chapter 3.

A separate broadband spectrum of one of the thyme oil constituents, linalool ((R)-(–)-linalool, Sigma Aldrich, 95% enantio-enriched), was recorded in the 2-18 GHz frequency range (neon as a carrier gas, 2.5 bar backing pressure). To increase the vapor pressure the sample was heated to 75° C. The experimental set-up corresponds to the one described in Chapter 3 with minor differences. For instance, a 40 W solid-state amplifier (6-18 GHz operation range) was used for the amplification of the excitation chirp in the 8-18 GHz frequency range instead of the travelling-wave tube (TWT) amplifier, which is only specified for 2-8 GHz.

The rotational transitions were assigned to an asymmetric rigid rotor Hamiltonian with the aid of the PGOPHER[9] and JB95[10] program packages. Refined fits were obtained with the non-linear least-squares fit program SPFIT developed by Pickett[11].

The experimental structures of some of the thyme oils constituents were determined using the KRA[12] and the STRFIT[13] programs. Additionally, the internal dynamics of the most stable conformer of linalool and the second lowest conformer of thymol was analyzed with the program XIAM[14] based on the extended internal-axis method of Woods[15].

5.3 Computational methods

The conformational landscape of linalool was explored computationally. Possible structures of its conformers with an energy cut-off of 20 kJ/mol were first obtained using a molecular mechanics approach with the SYBYL force field as implemented in the SPARTAN software[16].

This conformational search resulted in sixty non-redundant conformers, which were further re-optimized at the B3LYP-D3 dispersion-corrected density functional with the 6-311++G(d,p) basis set. Several energetically most stable conformers with zero-point corrected relative energies up to 10 kJ/mol were re-optimized using second-order perturbation theory (MP2) with the 6-311++G(d,p) basis set. All conformers were tested to be true minima by performing frequency calculations.

5.4 Broadband spectra of thyme oil

The recorded 2-8 GHz thyme oil I spectrum is very dense and contains several terpenes, which were studied previously with rotational spectroscopy, such as thymol[17], carvacrol[17], camphor[18], 4-carvomenthenol[19], and linalool[20]. Their structures are schematically displayed in Figure 5.1. The broadband spectrum together with some enlarged sections (zoom-ins) are given Figure 5.2.

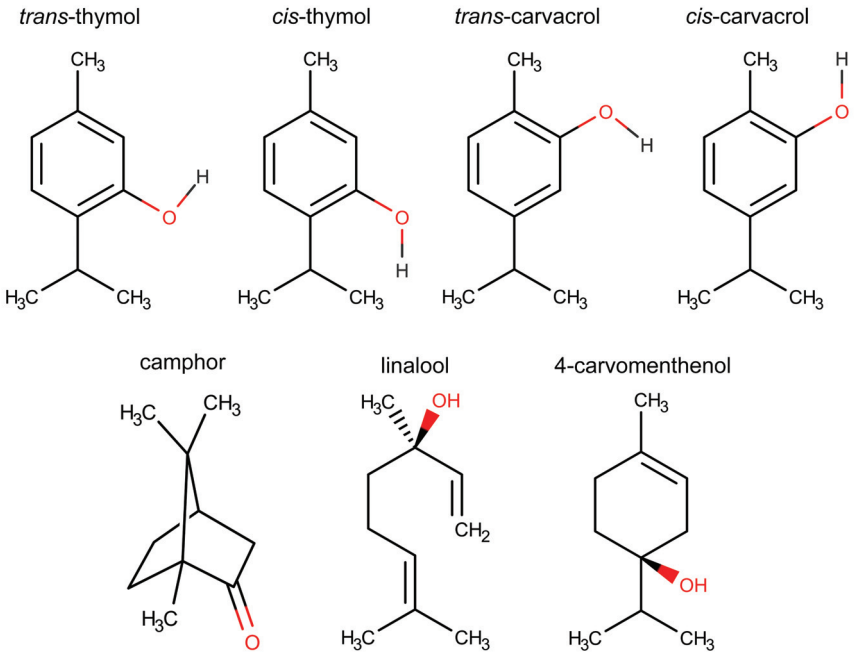

Figure 5.1: *Schematic structures of the different components present in thyme oil I.*

According to the information provided by the supplier, also other chemical components should be present in thyme oil I. A closer examination of corresponding GC data revealed that these compounds are expected to have low concentration in the oil sample characterized by Florihana (limonene, 0.57%; α-pinene, 1.65%; α-thujene, 1.43%[21]), or they are essentially non-polar (*para*-cymene, dipole moment 0.1 D according to the MP2/6-311++G(d,p) calculation). This explains, why they were not observed in our recorded broadband spectrum. An important aspect to consider is that the GC study carried out by the supplier is not a specific

analysis of our sample batch. Thus, variations in sample compositions characterized in our lab and studied by Floriaha can be expected, meaning that certain components listed above might not be present in the oil sample used in our experiment.

The nomenclature for the conformers of thymol, carvacrol, and carvomenthenol was adopted from Ref. 17 and Ref. 19 respectively. The most intense lines in the spectrum belong to the energetically most stable conformer of thymol, *trans*-thymol-A[17], with the SNR of roughly 600:1.

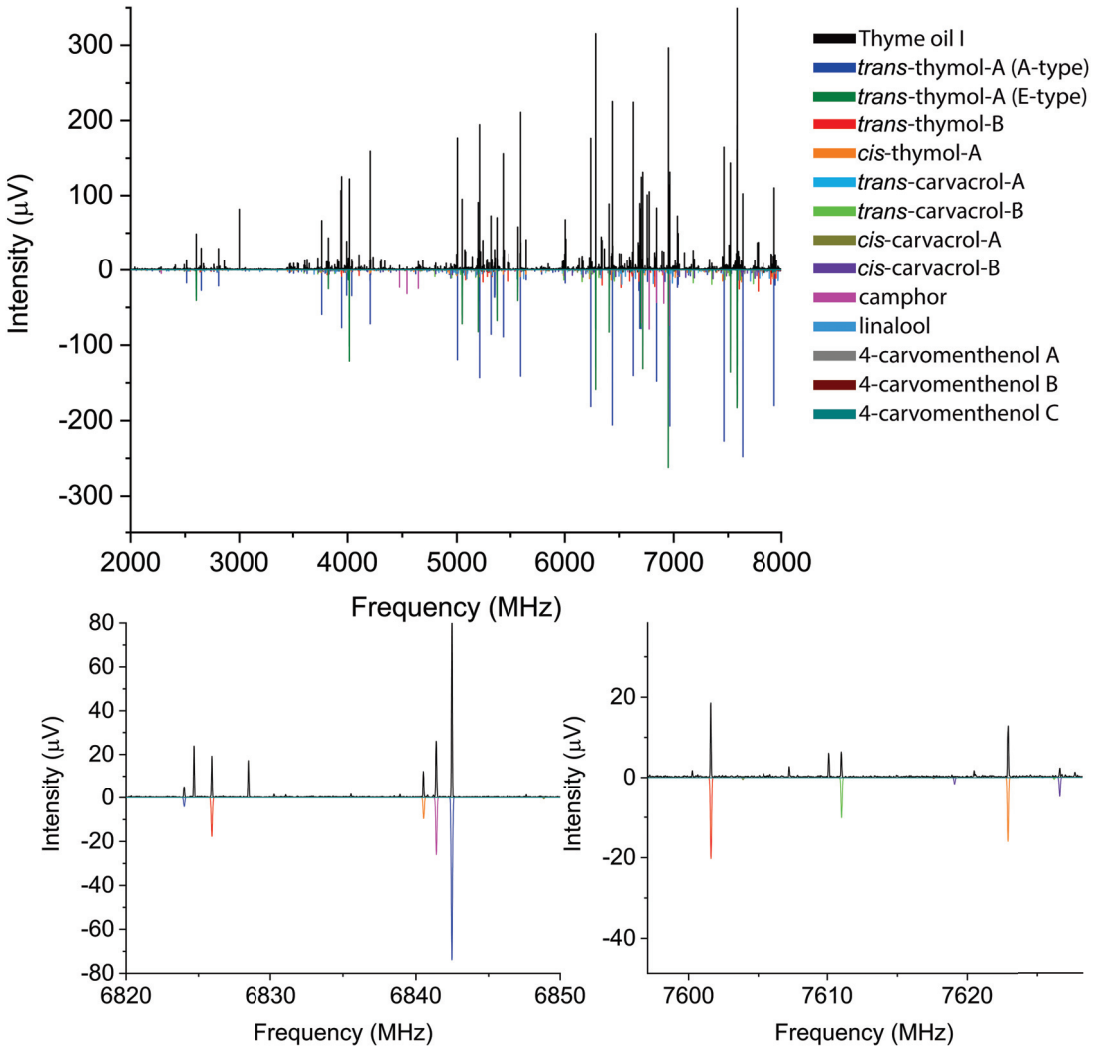

Figure 5.2: *The 2 - 8 GHz spectrum (3.5 million acquisitions, neon as a carrier gas) of thyme oil I (containing thymol as the most abundant component). The black trace is the experimental spectrum, while the lower traces represent simulations based on previously reported (see text) rotational parameters for the main constituents of the oil.*

The next strongest component in the spectrum is camphor with a SNR of 200:1 for the most intense transitions. The second lowest energy conformer of thymol, *trans*-thymol-B, shows a

Table 5.1: *Experimental rotational constants and calculated magnitudes of the dipole moment components for the thyme oil I components.*

Component	Formula	A (MHz)	B (MHz)	C (MHz)	$\lvert\mu_a\rvert$ (D)	$\lvert\mu_b\rvert$ (D)	$\lvert\mu_c\rvert$ (D)	Ref.
trans-thymol-A	$C_{10}H_{14}O$	2034.068(71)	739.18202(35)	591.51673(30)	1.43[a]	0.53	0.07	17
trans-thymol-B	$C_{10}H_{14}O$	2261.070(62)	708.92030(45)	611.86246(50)	1.50[a]	0.72	0.04	17
cis-thymol-A	$C_{10}H_{14}O$	2048.642(32)	739.25463(50)	590.31448(44)	1.15[a]	1.11	0.14	17
trans-carvacrol-A	$C_{10}H_{14}O$	2283.1750(15)	642.240345(30)	564.09631(25)	1.28[a]	0.81	0.00	17
trans-carvacrol-B	$C_{10}H_{14}O$	2159.0853(25)	670.84871(51)	577.52683(41)	1.42[a]	0.45	0.00	17
cis-carvacrol-A	$C_{10}H_{14}O$	2274.0616(37)	643.77212(46)	564.76557(38)	0.77[a]	1.30	0.00	17
cis-carvacrol-B	$C_{10}H_{14}O$	2152.8772(44)	672.34073(50)	578.22275(42)	1.05[a]	1.14	0.00	17
camphor	$C_{10}H_{16}O$	1446.968977(72)	1183.367110(47)	1097.101031(33)	2.74[b]	0.66	0.08	18
linalool	$C_{10}H_{18}O$	1646.74020(46)	682.19862(16)	618.75100(20)	1.12[a]	0.04	1.87	20
4-carvomenthenol A	$C_{10}H_{18}O$	2370.3204(13)	683.17421(30)	606.39955(24)	1.39[a]	0.30	1.01	19
4-carvomenthenol B	$C_{10}H_{18}O$	2255.1848(23)	673.70463(35)	646.54551(32)	1.23[a]	0.82	0.91	19
4-carvomenthenol C	$C_{10}H_{18}O$	2236.4047(12)	674.83599(26)	647.30427(19)	1.15[a]	0.29	1.20	19

[a] MP2/6-311++G(d,p)
[b] MP2/6-31G(d,p)

SNR of 60:1, followed by *cis*-thymol-A (SNR roughly 40:1) and the two conformers of carvacrol, *trans*-carvacrol-B (30:1), and *trans*-carvacrol-A (25:1). Other compounds identified in the present spectrum include *cis*-carvacrol-A, *cis*-carvacrol-B, linalool, and three conformers of 4-carvomenthenol A, B, and C. These oil constituents are rather weak with a SNR of about 5:1. Overall, five terpenes with their respective isomeric and conformational forms were observed in the spectrum of thyme oil I. The determined components and their previously reported rotational parameters are listed in Table 5.1.

The other chemotype, thyme oil II contains linalool as the major constituent. Linalool is also present in thyme oil I, but it is less abundant there (5.4% according to GC data[21;22], see also Table 5.3), resulting in lower peak intensities in the rotational spectrum and, subsequently, in lower SNR. While the SNR of linalool is only around 5:1 in thyme oil I, it is approximately 120:1 in thyme oil II for the strongest lines. Excerpts of the broadband spectrum are given in Figure 5.3.

Some constituents of thyme oil II such as thymol, camphor, and 4-carvomenthenol are also present in both spectra, but with different intensities. For instance, the SNR of 4-carvomenthenol A in thyme oil II is around 150:1. The difference in the amount of 4-carvomenthenol between thyme oil I and II (1% vs 14%[21;22], see Table 5.3) is reflected in different intensities of 4-carvomenthenol conformers in the two broadband spectra.

Note that in thyme oil II 4-carvomenthenol A is expected to be less abundant than linalool.

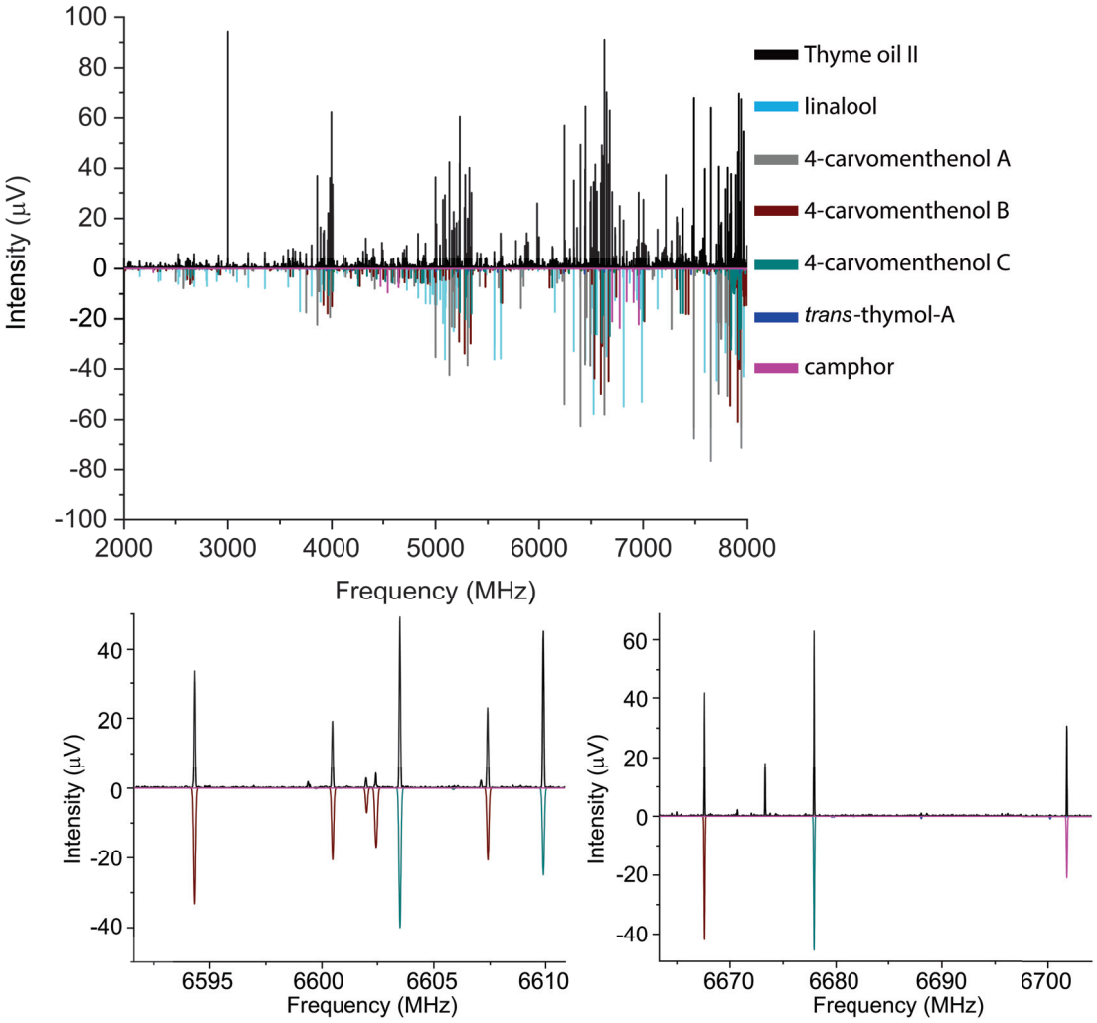

Figure 5.3: *The 2 - 8 GHz spectrum (2 million acquisitions, neon as a carrier gas) of thyme oil II (containing linalool as the most abundant component). The black trace corresponds to the experimental spectrum, while the lower traces represent simulations based on previously reported rotational parameters for the main constituents of the oil (see text).*

Intriguingly, it shows higher intensity and therefore higher SNR than linalool for the strongest transitions (150:1 vs 120:1). Although, according to the prediction (MP2/6-311G(d,p)), the strongest dipole moment component of linalool is μ_c, its most intense lines in the recorded spectrum are predominantly a-type. A comparison of the rotational parameters listed in Table 5.1 reveals that the μ_a of 4-carvomenthenol A is higher than of linalool (1.39 D vs. 1.12 D). Since the line intensity is proportional to the square of the dipole moment, the intensity of 4-carvomenthenol for the a-type transitions is expected to be about 1.5 higher than of linalool, which is in consistence with the experimental observation.

Another conformer of carvomenthenol, 4-carvomenthenol C, has roughly the same SNR of 115:1 as linalool, followed by 4-carvomenthenol B (SNR 76:1), and camphor with a SNR of about 50:1. Only one conformer of thymol, *trans*-thymol-A, was identified in the spectrum

of thyme oil II with a SNR of approximately 5:1, while none of the conformers of carvacrol could be observed. Notably, carvacrol should be present in the sample, but in low relative abundance (about 0.19%[22]), according to the data provided by the supplier. This also applies to some other thyme oil II constituents, such as e.g. α- and β,-pinene, α-thujene, eucalyptol with a relative abundance of around 2%, as stated by the supplier[22]. Since the intensity of rotational lines is proportional to the number of molecules interacting with the excitation field[7], the low relative amounts of the respective components in mixture can result in low measured rotational line intensities (depending on the dipole moment components). The obtained low SNR might be insufficient for an accurate assignment of the molecular species of interest. Additionally, as already emphasized, differences in the relative composition of the sample analyzed by the supplier and utilized in our experiment are possible. This might explain the fact that carvacrol, α-, and β-pinene, and other compounds mentioned above could not be identified in our thyme oil II spectrum.

In total, the spectrum of thyme oil II is less intense and less dense, compared to the one of thyme oil I, which could be to some extent because of the differences in the valve performance between the experiments. Note that while the measured absolute intensities can differ due to such experimental effects, the observed relative intensity pattern is more reliable and reproducible. Four terpenes (linalool, carvomenthenol, camphor and thymol) with their six different conformers in total were identified in thyme oil II.

Several constituents of thyme oil I and II show characteristic splittings in the recorded spectra resulting from the internal rotation of their respective methyl tops. For some of the components, these internal dynamics were analyzed previously. This is for instance true for the lowest energy conformer of thymol, *trans*-thymol-A[17]. Thymol features three methyl groups, two of them being attached to an sp^3-(isopropyl group) and one to an sp^2-hybridized C-atom (Figure 5.1). The internal rotation barrier in latter case should be low enough to give rise to observable fine structure in the recorded spectrum. Indeed, in the previous broadband study on thymol[17] a splitting pattern showing doublets with A and E states (see Chapter 2) was observed. Based on their reported frequencies[17], the splittings of *trans*-thymol-A could be also assigned in the present thyme oil I spectrum. They are labelled as A- and E-type in Figure 5.2. No splittings were observed due to the internal rotation of the other two methyl tops, which is expected because of their calculated high rotation barrier[17].

The internal rotation barrier of the second lowest energy conformer of thymol, *trans*-thymol-B, was not determined experimentally in the previous study. Because of the sufficient SNR (60:1) of this conformer in thyme oil I, such an analysis was possible in the present work. The results are summarized in Section 5.7.

Other components, the internal dynamics of which was characterized before, both experimentally and computationally, are *trans*-carvacrol-A, *trans*-carvacrol-B[17], and linalool[20]. The previously reported internal rotation analysis of linalool is revisited here and discussed in Section 5.8.2. Further components, *cis*-carvacrol-A, *cis*-carvacrol-B, *cis*-thymol-A, *cis*-thymol-B, should feature low internal rotation barriers for some of their methyl tops, accord-

ing to the reported calculated results[17]. No experimental results with respect to the internal dynamics of these species were reported so far. Their SNR in the present spectra was also not high enough to obtain such an information.

5.5 Analysis of the oil composition

A semi-quantitative analysis of thyme oils I and II was performed based on the calculated dipole moment components and the observed line intensities of the oil constituents. For the sake of comparability, only a-type transitions ($|4_{04}\rangle \leftarrow |3_{03}\rangle$, $|4_{14}\rangle \leftarrow |3_{13}\rangle$, $|4_{13}\rangle \leftarrow |3_{12}\rangle$) in the frequency range 5-6 GHz were considered. The calculated μ_a dipole moment components are the strongest for most of the thyme oil constituents with the exceptions of *trans*-carvacrol A, *trans*-carvacrol-B, and linalool (see Table 5.1). The chosen frequency range corresponds to the optimal operation range of our TWT amplifier. As mentioned in Section 5.4, some compounds show splittings in the spectra due their methyl top internal rotation. In such cases, a sum of the intensities of the corresponding internal rotation components was taken into account.

The measured rotational line intensities were divided by the square of the respective μ_a. The obtained values were averaged and normalized to the most abundant species in the spectrum. As a last step, the results for the different conformers belonging to the same oil constituent were combined and compared to the GC analysis data provided by the supplier[21;22] (Tables 5.2 and 5.3).

Table 5.2: *The ratios between the measured intensities (int) of the a-type transitions in the frequency range 5-6 GHz and the squares of the calculated μ_a dipole moment components for the different conformers present in thyme oils I and II. The obtained values were normalized with respect to the most abundant species (trans-thymol-A (thyme oil I) and the lowest energy conformer of linalool (thyme oil II), highlighted in bold). The relative abundance (%) of the respective conformers is given. Less compounds were observed in thyme oil II in comparison to thyme oil I.*

Conformer	Thyme oil I		Thyme oil II	
	Normalized int/μ_a^2	%	Normalized int/μ_a^2	%
***trans*-thymol-A**	**1.00 ± 0.20**	61.7	0.04 ± 0.01	1.6
trans-thymol-B	0.12 ± 0.02	7.4	–	–
cis-thymol-A	0.19 ± 0.04	11.7	–	–
trans-carvacrol-A	0.05 ± 0.01	3.1	–	–
trans-carvacrol-B	0.03 ± 0.007	1.9	–	–
cis-carvacrol-A	0.07 ± 0.02	4.3	–	–
cis-carvacrol-B	0.04 ± 0.01	2.5	–	–
linalool	0.03 ± 0.01	1.9	**1.00 ± 0.20**	40.5
4-carvomenthenol A	0.008 ± 0.004	0.6	0.40 ± 0.08	16.2
4-carvomenthenol B	0.007 ± 0.005	0.6	0.26 ± 0.06	10.5
4-carvomenthenol C	0.02 ± 0.006	1.0	0.73 ± 0.15	29.6
camphor	0.05 ± 0.006	3.1	0.04 ± 0.02	1.6

In Table 5.2 errors of the normalized intensity values were calculated in accordance with the

general error propagation formula[23]. The calculation was performed based on the following considerations. The analysis described here relies on the predicted dipole moment components. Depending on the molecular system, the difference between the calculated and the experimental dipole moment components can be in the order of 6-9%, as shown in Ref 24. The error of 10% used in our calculation is therefore a reasonable estimation. Another point to account for, is the uncertainty in the measured line intensity, which is related to the noise level. Here we estimate this error to be about $1\,\mu$V, which is twice our noise level in the present measurement. In principle, we also have to take into account the frequency dependence of the TWT amplifier and of the other instrumental parts, such as the horn antennas used to broadcast the microwave radiation into the interaction zone of the spectrometer. As explained in Chapter 4, such effects can be corrected for by using the corresponding instrumental functions, which were not applied in the present analysis.

According to the Table 5.2, the most abundant species in the recorded spectra are *trans*-thymol-A (thyme oil I) and the lowest energy conformer of linalool (thyme oil II). The errors obtained for the normalized intensity values are up to 20%, mainly owing to the high uncertainty in the calculated dipole moment components. Higher accuracy in future studies can thus be achieved by using experimental instead of calculated dipole moment components, since the uncertainties in the experimental dipole moments determined using Stark effect measurements are expected to be below 1%[18].

It is evident from Table 5.2 that the two chemotypes of thyme oil have significant differences in their relative composition. While some of the components are present in high amount for one of the chemotypes, their amount can be as low as 0.5-2% in the oil sample with the other chemotype. This is for instance the case for linalool, the conformers of 4-carvomenthenol, and *trans*-thymol A. Note that the determined relative ratio of 4-carvomenthenol C in thyme oil II is higher than of 4-carvomenthenol A, while its SNR in the spectrum is lower. This is attributable to the fact that the calculated μ_a^2 value of 4-carvomenthenol C is lower than of 4-carvomenthenol A (see Table 5.1), resulting in larger normalized intensity values for 4-carvomenthenol C.

A comparison between the results obtained with the GC and the rotational broadband spectroscopy is given in Table 5.3, showing a reasonable agreement with some exceptions. According to the GC analysis , linalool is the second most abundant thyme oil I constituent of the compounds discussed in the scope of the present work (see Section 5.4). This disagrees with our result, according to which linalool seems to be the least abundant component of the five terpenes identified in the spectrum. Another discrepancy between our results and the GS analysis is the determined relative ratio of 4-carvomenthenol in thyme oil II, which is in our analysis higher than of linalool (see Table 5.3).

One of the factor, which might be responsible for the accounted discrepancies between our results and the GC data is the presence of other conformers not accounted for in our study. In principle, the population of a flexible molecule can be distributed over several conformers, as in the case of thymol, carvacrol, or carvomenthenol. Only one conformer of linalool was

Table 5.3: *Comparison between the gas chromatographic (GC) data provided by the supplier and our analysis. In our work the ratios of different components were obtained by summarizing the results given in Table 5.2 for the individual conformers and normalizing them with respect to the most abundant component: thymol (thyme oil I) and linalool (thyme oil II). GC results (percentage) are provided only for the molecular species relevant in the present analysis. Compounds, which were reported by supplier but not assigned in our spectra were omitted.*

	Thyme oil I				Thyme oil II			
	Our work		GC		Our work		GC	
Component	Normalized int/μ_a^2	Relative ratio	Percentage[21] %	Relative ratio	Normalized int/μ_a^2	Relative ratio	Percentage[22] %	Relative ratio
Thymol	80.9	1.00	34.7	1.00	1.6	0.04	0.3	0.01
Carvacrol	11.7	0.15	3.5	0.10	–	–	–	–
Linalool	1.9	0.02	5.4	0.16	40.5	1.00	30.4	1.00
4-Carvomenthenol	2.5	0.03	1.0	0.03	56.3	1.39	14.1	0.46
Camphor	3.0	0.04	2.6	0.07	1.6	0.04	0.8	0.03

identified in our spectrum. The presence of another less populated conformer could lead to an incorrect estimated abundance of linalool.

There can also be a slightly different oil composition of the samples studied in our lab and tested by the supplier, since the data provided by the Florihana company is not a specific analysis of our sample badge. Variations in the composition are thus possible, as reiterated in the previous section. For a better comparison, a specific GC analysis of the oil samples utilized in our experiment is advisable. Such an analysis was not carried out, as the study presented here has solely an illustrative purpose, to show the advantages and limitations of rotational spectroscopy as an analytical tool for the characterization of essential oils.

5.6 Structure of *trans*-thymol-A

In Section 5.4 it was pointed out that *trans*-thymol A is the lowest energy conformer of thymol and the strongest molecular species in the thyme oil I spectrum. Its SNR (600:1) was sufficient for the experimental structure elucidation. This information was not reported in the previous rotational spectroscopy study on thymol[17]. The experimentally obtained rotational parameters used for the determination of the atomic coordinates are given in Table B.1.

The procedure for the structural determination was here analogue to the one described in Chapter 4 for the menthol conformer EQ1ext. As a first step, the r_s structure based on the Kraitchman's approach[25] was determined. A comparison between the calculated (MP2/6-311++G(d,p)) and the experimental r_s structure is given in Figure 5.4, which shows a good agreement. However, some of the C-atoms of *trans*-thymol-A are located close to the principal axes. These include C1 (close to the *b*-axis), C3 (close to the *a*-axis), C5 (close to the *b*-axis), C7 (close to the *a*-axis) and C10 (close to the *a*-axis).

While the atomic coordinates of C1, C3, and C10 could be determined experimentally, some of

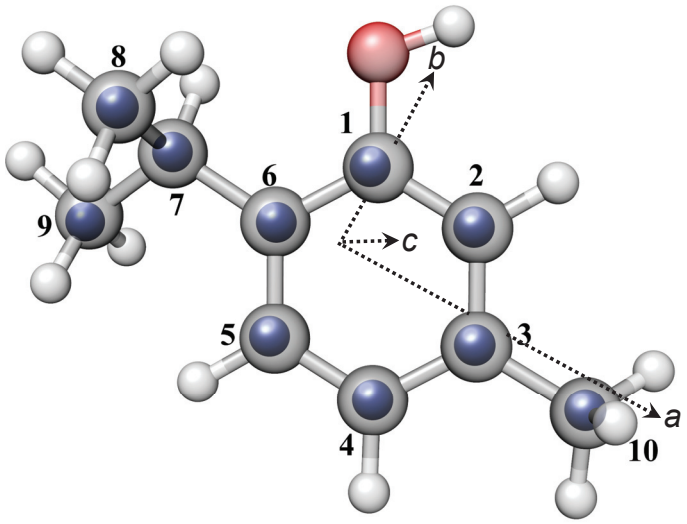

Figure 5.4: *Comparison between calculated (grey, MP2/6-311++G(d,p)) and experimental (blue spheres) Kraitchman substitution structure (r_s) of the lowest energy conformer of thymol, trans-thymol-A, determined from ^{13}C single isotopically substituted species in the broadband spectrum of thyme oil I. Note that the carbon atom labelling does not correspond to the IUPAC nomenclature. The principal axes a, b and c are depicted.*

the coordinates of C5 (along a and c) and C7 (along b) had to be set to zero. Otherwise, their values result in imaginary numbers, when solving the Kraitchman's equations. Structural parameters involving C5 and C7 are highlighted in italics in Table B.2. For some of them, there is a discrepancy between the calculated (r_e) and the experimental values. A better agreement between the theory and the experiment for some of these parameters was achieved by performing a non-linear least-squares r_0 (Table B.2). In contrast to r_s, this approach allows to exploit multi- instead of single isotopically substituted species. A brief theoretical overview of the two methods for the structure determination is provided in Chapter 2.

The SNRs of the other thyme oil I constituents were not high enough for their experimental structure determination except for camphor, where the structure was already published before[18].

5.7 Internal rotation of *trans*-thymol-B

Thymol conformers were analyzed extensively in the previous rotational spectroscopy study on this monoterpenoid[17]. While the internal rotation barrier of its lowest energy conformer *trans*-thymol-A was determined experimentally, no experimental results on the internal dynamics of *trans*-thymol-B were reported so far. Instead, the internal rotation of *trans*-thymol-B was characterized computationally[17]. Only the A states of this molecular species were assigned in the previous broadband spectrum of thymol. Due to its sufficiently high SNR in our thyme oil I spectrum (60:1), internal rotation analysis of *trans*-thymol-B was possible

directly in the recorded oil spectrum.

It was already mentioned in Section 5.4 that the observed rotational line splittings of thymol result from the internal rotation of its methyl top, which is attached to an sp^2-hybridized C-atom (Figure 5.1). Since only one top is involved in the internal rotation, the splitting pattern of *trans*-thymol-B consists of doublets, analogous to *trans*-thymol-A. The internal rotation barriers of the remaining two tops are predicted to be high (about 13.7 kJ/mol[17]) to have an impact on the spectrum in a measurable way.

Table 5.4: *Molecular parameters of trans-thymol-B obtained with XIAM. A comparison with the previously reported[17] computationally determined parameters is provided.*

	XIAM	MP2[d]
A | MHz	2233.7813(13)	2229.72
B | MHz	708.86585(33)	708.94
C | MHz	611.86109(28)	611.43
D_{pi2J} | kHz	7.71(13)	
F_0 | GHz	[160.1][b]	160.1
V_3 | kJ/mol[a]	0.300330(17)	0.261[e]
$\measuredangle(i,a)$ | °[c]	8.14910(50)	8.8
$\measuredangle(i,b)$ | °	81.85120(60)	81.2
$\measuredangle(i,c)$ | °	89.931(84)	88.9
N_{lines}	41	
σ | kHz	6.95	

[a] Internal rotation barrier
[b] The value was kept fixed.
[c] Calculated angles between the internal rotor axis of the methyl group and the principal axes of inertia
[d] 6-311++G(d,p)
[e] B3LYP/6-311++G(d,p)

The internal rotation analysis of *trans*-thymol-B was performed with the aid of the program XIAM. The A states reported in the previous study 17 were used as a starting point for the fit. In total, we assigned 41 distinct lines (A- and E- states) with a standard deviation of 6.95 kHz using XIAM. The line list is given in Table B.3. The experimental and the calculated[17] parameters are summarized in Table 5.4. The predicted V_3 rotation barrier of *trans*-thymol-B is 0.261 kJ/mol (B3LYP/6-311++G(d,p)), and therefore close to our experimentally determined value of 0.300330(17) kJ/mol. This experimental result is also consistent with the one obtained for *trans*-thymol-A (0.3699(11) kJ/mol[17]). The last aspect is not surprising, since the two conformers differ only in the orientation of the isopropyl group[17].

5.8 Structure and internal rotation of linalool

Linalool is the major constituent of thyme oil II. It shows a high degree of structural flexibility as a consequence of the presence of many C-C single bonds (molecular formula $(CH_3)_2C{=}CH(CH_2)_2C(CH_3)(OH)CH{=}CH_2$), which can give rise to different conformers. It was studied before theoretically[26] and experimentally using vibrational[27] and rotational spectroscopy[20]. In this later study several conformers of linalool with relative energies up to 13 kJ/mol were optimized based on ab initio (MP2) and density-functional theory (B3LYP) calculations. Only the lowest energy conformer was identified in the measured rotational spectrum (9-15.25 GHz)[20]. The calculations were redone in the scope of the analysis presented here as described in more detail in Section 5.2.

Within the accuracy of calculations, the results are in agreement with the ones obtained by Nguyen et al.[20]. The zero-point corrected relative energy difference between the first and the second lowest energy conformers was reported to be 4.8 kJ/mol[20], while in our study it was determined to be around 5.3 kJ/mol (MP2/6-311++G(d,p)). Based on the calculations, linalool assumes a folded conformation stabilized through an intramolecular interaction between its OH group and one of the double bonds ($O-H...\pi$ interactions, Figure 5.5). It is remarkable that no other conformer with relative zero-point corrected energies below 5 kJ/mol was identified for this acyclic, structurally flexible monoterpene so far.

Because the SNR of linalool in thyme oil II was only approximately 120:1, a separate broadband spectrum in the frequency range 2-18 GHz for the commercially available linalool sample with a SNR of about 360:1 was recorded instead. The experimental conditions for the linalool broadband measurement correspond to the ones described in Section 7.2. The extension of the recorded frequency range allowed to assign more rotational lines to the lowest energy conformer of linalool and to experimentally determine its structure. Moreover, additional information on the internal dynamics of this conformer, which was not provided in the previous study[20], could be obtained. A second conformer of linalool was not observed in our experimental spectrum, probably because of its low population in the molecular jet. The estimated Boltzmann population ratio for the two conformers at the pre-expansion conditions (100 °C) is about 5:1, considering their relative energy difference of 5.3 kJ/mol. This further confirms the lack of additional conformers below 5 kJ/mol in agreement with the calculations.

5.8.1 Structure of linalool

The strongest lines in the recorded broadband spectrum (2-18 GHz) of linalool belong to its energetically lowest conformer, which was analyzed before[20]. Since the SNR in the broadband spectrum of linalool was sufficient for assigning single substituted ^{13}C isotopologues, an experimental r_s structure of its lowest energy conformer could be obtained with the program KRA. The respective rotational parameters for the ^{13}C isotopologues used for the r_s fit are given in Table B.4.

Comparison between calculated (r_e, MP2/6-311++G(d,p)) and experimental r_s structures is presented in Figure 5.5, showing a good agreement. It is noticeable that C7 atom of linalool is located close to the principal axis *a*. For this reason, its coordinates along the *b* and the *c* axes had to be kept to zero, to avoid the appearance of imaginary numbers by solving the Kraitchman's equations. The same is also true for the coordinate of C10 along the *c*-axis, since C10 lies in the *ab*-plane (Figure 5.5). As discussed in Section 5.6, a significant discrepancy between the predicted (r_e structure) and the experimentally determined structural parameters involving these atoms (highlighted in italics in Table B.5) is possible. This is the case for the bond lengths r(C6 – C7) and r(C7 – C9) (Table B.5).

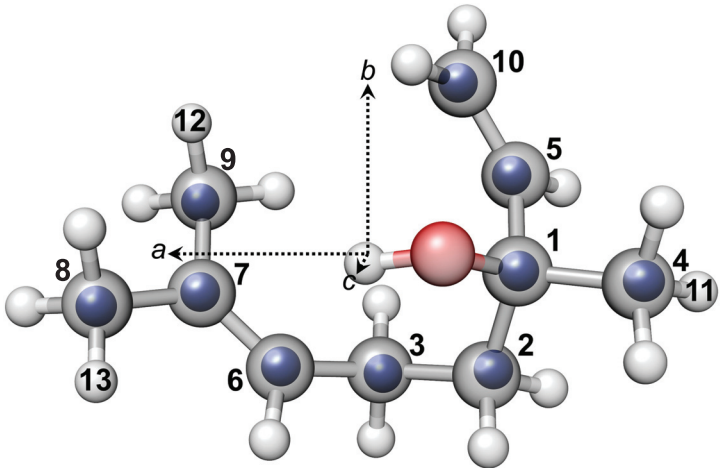

Figure 5.5: *Comparison between calculated (grey, MP2/6-311++G(d,p)) and experimental (blue spheres) Kraitchman substitution (r_s) structure of the lowest energy conformer of linalool[20], determined from ^{13}C single isotopically substituted species in the broadband spectrum of linalool. The applied carbon atom labelling corresponds to the one used in Table B.4.*

Analogous to *trans*-thymol-A, the effective r_0 structure of linalool was determined in addition to r_s. In total, 18 parameters were obtained for the lowest energy conformer of linalool with this approach. As evident from Table B.5, the agreement between the theory and the experimental results is better, once the r_0 fit is performed. Additional structural parameters for the internal coordinates involving O1 such as e.g. r(C1 – O1), ∠(C2 – C1 – O1), ∠(C4 – C1 – O1) etc. could be included in the present r_0 fit, although the isotopically substituted species containing ^{18}O were not observed experimentally.

5.8.2 Internal rotation of linalool

Linalool has three methyl tops (top 1 containing C4, top 2 containing C8, and top 3 containing C9, see Figure 5.5), the internal rotation tunnelling motions of which could give rise to splittings in the spectrum. Rotational energy barriers of all three methyl tops were calculated in the previous study[20] and reported to be 1327 cm^{-1} (around 16 kJ/mol), 324 cm^{-1} (around 4 kJ/mol), and 776 cm^{-1} (around 9 kJ/mol) for methyl tops 1, 2, and 3, respectively at the

MP2/6-311++G(d,p) level of theory. The barrier for methyl top 2 could be determined experimentally using programs XIAM[28] (400.20(64) cm^{-1}) and BELGI-C_1[29] (399.4(17) cm^{-1})[20]. Only a few multiplets due to the rotation of top 3 with the splittings in the order of 10 kHz were observed in the previous spectrum. Because of that, no experimental V_3 barrier of top 3 was reported. We analyzed the internal dynamics of linalool in our study with the aim to experimentally determine the V_3 barrier of top 3. The theoretical values for the barrier heights of tops 2 and 3 were recalculated at the B3LYP-D3/6-311++G(d,p) level of theory and found to be in consistency with the ones provided by Nguyen et al.

Top 1 is attached to an sp^3-hybridized C-atom, and as already discussed for thymol in Section 5.4, the internal rotation barrier for such a methyl group is expected to be high (more than 12 kJ/mol), which is in agreement with the calculated value[20]. Since the barrier is high, no line splittings were observed in the spectrum resulting from the rotation of top 1. Tops 2 and 3 are, however, both attached to the same sp^2-hybridized C-atom. A similar arrangement is present in the other monoterpene, pulegone. For pulegone a multiplet consisting of AA/AE, EA, EE, EE* states was observed[30] (see also Chapter 6). The AA and AE states could not be resolved in the pulegone spectrum, since their frequency differences were less than the experimental resolution. Characteristic multiplet structures due to the internal rotation of the two inequivalent tops as discussed in Ref. 30 were also evident in the present broadband spectrum of linalool (see Figure 5.6) for some of its transitions with K_a values equal to 3. This is a clear indication that despite the rather high barrier, internal motions of both top 2 and top 3 are observed experimentally. The respective internal rotation barriers were determined using the program XIAM. The results are summarized in Table 5.5.

According to our experimental analysis, the V_3 barrier of top 3 is 9.2581(74) kJ/mol. The predicted (B3LYP-D3/6-311++G(d,p)) value of 9.1 kJ/mol is in a good agreement with this result. The V_3 barrier of top 2 was determined simultaneously in the scope of the present analysis. The obtained value of 4.7707(95) or 398.81(80) cm^{-1} is consistent with the XIAM analysis reported by Nguyen et al. Other experimental parameters, such as angles between the internal rotor axis of methyl top 2 and the principal axes also match the ones from the previous study (Table 5.6).

Overall, we assigned and fitted 384 lines using XIAM with a standard deviation of 10.8 kHz (see Table B.6). Note that to obtain such a standard deviation the angles between the internal rotor axis of methyl top 3 and the principal axes of inertia had to be kept fixed to the calculated (MP2/6-311++G(d,p)) values. This could be due to the fact that while V_3 barrier of top 2 depends on the well resolved EA, EE and EE* states, the barrier of top 3 is more dependent on the AA and AE states. A comparison between experimental and calculated (using XIAM) frequencies for some transitions is presented in Figure 5.6. In most cases AA and AE states could not be resolved in the spectrum (as in our study on pulegone, Chapter 6), because the predicted frequency difference was less than 15 kHz. Only 18 distinct rotational transitions corresponding to the AA and AE states could be assigned.

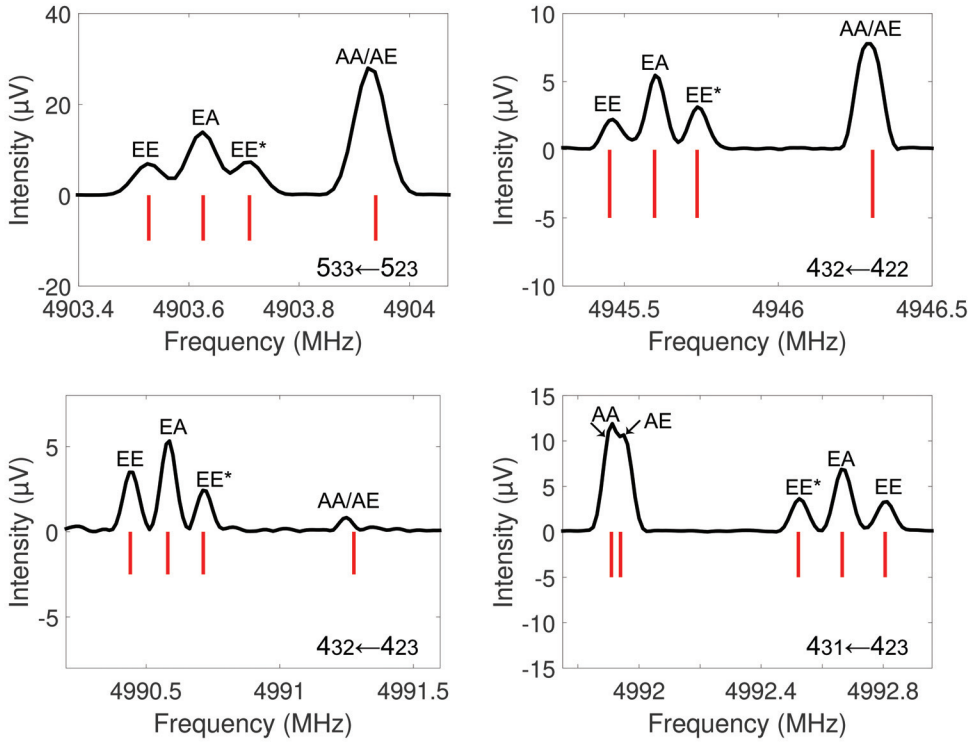

Figure 5.6: *Examples of the observed multiplet structure in the broadband spectrum of linalool due to the internal rotation of two methyl groups, top 2 (containing C8) and top 3 (containing C9) for several rotational transitions. The upper traces (black) are the experimental spectra. The lower (red) traces are stick spectra (not taking into account specific intensity distributions) based on the simulations of the fitted molecular constants for linalool, using XIAM. The labelling of the rotational transitions follows the J_{K_aKc} scheme.*

5.9 Summary and Outlook

The chemical composition of thyme oil I and II was analyzed in the scope of this study. According to our results, *trans*-thymol A is the most abundant conformer in thyme oil I, while the lowest energy conformer of linalool prevails in thyme oil II. The oil samples also differ in the relative abundance of the other oil constituents. In general, the semi-quantitative analysis of the samples using rotational spectroscopy agrees well with the GC data provided by the supplier. Nevertheless, the results can still be improved by using experimentally determined dipole moments (if available) and accounting for the instrumental effects of the used set-up components. This later aspect would also allow to include a larger subset of rotational transitions into the analysis. Furthermore, since the oil constituents have different boiling points, their intensities in the spectrum might differ depending on the chosen experimental conditions. In upcoming experiments several thyme oil spectra using a broad temperature range should be recorded to test this influence on the calculated abundance of the respective components.

The structure of the lowest energy conformer of thymol, *trans*-thymol-A was determined from the assignment of its monosubstituted ^{13}C isotopologues (in natural abundance) in the broadband spectrum of thyme oil I. Additionally, internal dynamics of another thymol conformer, *trans*-thymol-B, was characterized directly in the oil. The information on the experimental internal rotation barrier of this component was not reported in the previous rotational spectroscopy study on thymol[17].

Table 5.5: *Molecular parameters of linalool obtained with XIAM and quantum chemical calculations. A comparison with the previously reported XIAM results on methyl top 2 is provided.*

	XIAM	MP2[d]	Previous work[20]
A | MHz	1646.73610(25)	1637.70	1646.74020(46)
B | MHz	682.19743(15)	700.36	682.19862(16)
C | MHz	618.75028(19)	635.51	618.75100(20)
Δ_J | kHz	0.09988(75)	0.11	0.11550(54)
Δ_{JK} | kHz	0.4012(35)	0.44	0.3843(36)
Δ_K | kHz	−0.2846(58)	−0.29	
δ_J | kHz	−0.02134(92)	0.005	0.00735(32)
δ_K | kHz			0.234(20)
methyl top 2			
V_3 | kJ/mol[a]	4.7707(95)	4.3[e]	
V_3 | cm^{-1} [a]	398.81(80)	359.5[e]	400.20(64)
I_α | u Å^2	3.1586[b]		
$\measuredangle(i,a)$ | °[c]	85.126(49)	86.40	85.04(10)
$\measuredangle(i,b)$ | °	25.63(65)	29.08	30.01(39)
$\measuredangle(i,c)$ | °	64.90(65)	61.19	60.49(38)
methyl top 3			
V_3 | kJ/mol[a]	9.2581(74)	9.1[e]	
V_3 | cm^{-1} [a]	773.92(62)	760.7[e]	
I_α | u Å^2	3.1586[b]		
$\measuredangle(i,a)$ | °[c]	[47.88][b]	47.88	
$\measuredangle(i,b)$ | °	[82.97][b]	82.97	
$\measuredangle(i,c)$ | °	[42.98][b]	42.98	
N_{lines}	384		83
σ | kHz	10.8		4.6

[a] Internal rotation barrier

[b] The value was kept fixed.

[c] Calculated angles between the internal rotor axis of the methyl group and the principal axes of inertia

[d] 6-311++G(d,p)

[e] B3LYP-D3/6-311++G(d,p)

When the SNR of a particular component is not high enough, such information can still be retrieved with the help of a separate measurement, conducted on a pure sample of the component of interest. This approach was applied here for linalool. With the aid of a separately recorded broadband spectrum of linalool, the structure of its lowest energy conformer, which is also present in the thyme oil, could be determined. Furthermore, its internal dynamics could be analyzed, providing additional information to the one obtained in the previous rotational spectroscopy study on linalool[20].

Another interesting aspect is also a chiral analysis of thyme oil with the M3WM technique. The M3WM experiments on the pure samples of some of its components such as carvomenthenol B and C were carried out previously in our group[19]. The next step is therefore a M3WM experiment on 4-carvomenthenol directly in thyme oil II, where it is present in high abundance based on our results. Together with the chiral analysis of peppermint oil (Chapter 4), this would allow to explore in greater depth the applicability and capability of the M3WM technique.

Bibliography

[1] A.-B. Cutillas, A. Carrasco, R. Martinez-Gutierrez, V. Tomas, and J. Tudela. Thyme essential oils from Spain: Aromatic profile ascertained by GC–MS, and their antioxidant, anti-lipoxygenase and antimicrobial activities. *J. Food. Drug. Anal.*, 26(2):529 – 544, 2018.

[2] G. Kasparaviciene, Z. Kalveniene, A. Pavilonis, R. Marksiene, J. Dauksiene, and J. Bernatoniene. Formulation and Characterization of Potential Antifungal Oleogel with Essential Oil of Thyme. *Evid. Based Complement Alternat. Med.*, 2018, 2018.

[3] S. Bahare, M. A. Prakash, S. Ila, S.-R. Mehdi, C. M. del Mar, S.-C. Antonio, F. Hannane, N. N. Nasri, K. Farzad, and S.-R. Javad. Thymol, thyme, and other plant sources: Health and potential uses. *Phytother. Res.*, 2018.

[4] T. El-Obeid, H. M. Yehia, H. Sakkas, L. Lambrianidi, M. I. Tsiraki, and I. N. Savvaidis. Shelf-life of smoked eel fillets treated with chitosan or thyme oil. *Int. J. Biol. Macromol.*, 114:578 – 583, 2018.

[5] A. Sarkic and I. Stappen. Essential Oils and Their Single Compounds in Cosmetics—A Critical Review. *Cosmetics*, 5(1), 2018.

[6] P. Satyal, B. L. Murray, R. Mcfeeters, and W. Setzer. Essential Oil Characterization of Thymus vulgaris from Various Geographical Locations. *Foods*, 5:70, 10 2016.

[7] G. G. Brown, B. C. Dian, K. O. Douglass, S. M. Geyer, S. T. Shipman, and B. H. Pate. A broadband Fourier transform microwave spectrometer based on chirped pulse excitation. *Rev. Sci. Instrum.*, 79(5):053103, 2008.

[8] D. Schmitz, V. A. Shubert, T. Betz, and M. Schnell. Multi-resonance effects within a single chirp in broadband rotational spectroscopy: The rapid adiabatic passage regime for benzonitrile. *J. Mol. Spectrosc.*, 280:77–84, 2012.

[9] C. M. Western. PGOPHER: A program for simulating rotational, vibrational and electronic spectra. *J. Quant. Spectrosc. Ra.*, 186:221 – 242, 2017.

[10] D. Plusquellic. JB95. available at http://www.nist.gov/pml/electromagnetics/grp05/jb95.cfm.

[11] H. M. Pickett. The Fitting and Prediction of Vibration-Rotation Spectra with Spin Interactions. *J. Mol. Spectrosc.*, 148:371–377, 1991.

[12] Z. Kisiel. Assignment and Analysis of Complex Rotational Spectra. In J. Demaison, K. Sarka, and E. A. Cohen, editors, *Spectroscopy from Space*, volume 20, pages 91–106. Springer, Dordrecht, 2001.

[13] Z. Kisiel. Least-squares mass-dependence molecular structures for selected weakly bound intermolecular clusters. *J. Mol. Spectrosc.*, 218(1):58 – 67, 2003.

[14] H. Hartwig. XIAM Manual, 1996. available at http://www.ifpan.edu.pl/ kisiel/introt/xiam/xiam-v25.txt.

[15] R. Woods. A general program for the calculation of internal rotation splittings in microwave spectroscopy. *J. Mol. Spectrosc.*, 21(1):4 – 24, 1966.

[16] L. Lafayette, G. Sauter, L. Vu, and B. Meade. Spartan Performance and Flexibility: An HPC-Cloud Chimera, OpenStack Summit, Barcelona, October 27, 2009.

[17] D. Schmitz, V. A. Shubert, B. M. Giuliano, and M. Schnell. The broadband microwave spectra of the monoterpenoids thymol and carvacrol: Conformational landscape and internal dynamics. *J. Chem. Phys.*, 141(3):034304, 2014.

[18] Z. Kisiel, O. Desyatnyk, E. Białkowska-Jaworska, and L. Pszczółkowski. The structure and electric dipole moment of camphor determined by rotational spectroscopy. *Phys. Chem. Chem. Phys.*, 5(5):820–826, 2003.

[19] V. A. Shubert, D. Schmitz, C. Medcraft, A. Krin, D. Patterson, J. M. Doyle, and M. Schnell. Rotational spectroscopy and three-wave mixing of 4-carvomenthenol: A technical guide to measuring chirality in the microwave regime. *J. Chem. Phys.*, 142(21):214201, 2015.

[20] H. V. L. Nguyen, H. Mouhib, S. Klahm, W. Stahl, and I. Kleiner. A touch of lavender: gas-phase structure and dynamics of the monoterpene linalool validated by microwave spectroscopy. *Phys. Chem. Chem. Phys.*, 15:10012–10018, 2013.

[21] Chromatography sheet records of Thymus Vulgaris Thymoliferum, 2011. https://www.florihana.com/images/boutique/product_files/chromatographies/FLE091/FLE091B221217ES.pdf/.

[22] Chromatography sheet records of Thymus Vulgaris Linaoliferum, 2011. https://www.florihana.com/images/boutique/product_files/chromatographies/FLE093/FLE093L280818ES.pdf/.

[23] I. Farrance and R. Frenkel. Uncertainty of Measurement: A Review of the Rules for Calculating Uncertainty Components through Functional Relationships. *Clin. Biochem. Rev.*, 33:49–75, 05 2012.

[24] A. L. Hickey and C. N. Rowley. Benchmarking Quantum Chemical Methods for the Calculation of Molecular Dipole Moments and Polarizabilities. *J. Phys. Chem. A*, 118(20):3678–3687, 2014.

[25] J. Kraitchman. Determination of Molecular Structure from Microwave Spectroscopic Data. *Am. J. Phys.*, 21(1):17–24, 1953.

[26] S. Ting-Li, W. Yu-Dong, Z. Chen-Xi, S. Xiao-Min, and H. Jing-Tian. Theoretical Study on the Reaction Mechanism of the Linalool with Ozone in Atmosphere. *Acta Chimica. Sinica*, 69(17):1965–1972, 2011.

[27] M. Sandasi, G. Kamatou, C. Gavaghan, M. Baranska, and A. Viljoen. A quality control method for geranium oil based on vibrational spectroscopy and chemometric data analysis. *Vib. Spectrosc.*, 57(2):242 – 247, 2011.

[28] H. Hartwig and H. Dreizler. The Microwave Spectrum of trans-2,3-Dimethyloxirane in Torsional Excited States. *Z. Naturforsch.*, 51a:923–932, 1996.

[29] M. Tudorie, I. Kleiner, J. Hougen, S. Melandri, L. Sutikdja, and W. Stahl. A fitting program for molecules with two inequivalent methyl tops and a plane of symmetry at equilibrium: Application to new microwave and millimeter-wave measurements of methyl acetate. *J. Mol. Spectrosc.*, 269(2):211 – 225, 2011.

[30] A. Krin, P. C., P. Pinacho, M. M. Quesada-Moreno, J. J. López-González, J. R. Avilés-Moreno, S. Blanco, J. C. López, and M. Schnell. Structure Determination, Conformational Flexibility, Internal Dynamics, and Chiral Analysis of Pulegone and Its Complex with Water. *Chem. Eur. J*, 24(3):721–729.

6

Structure determination, internal dynamics, and chiral analysis of pulegone and its complex with water

6.1 Introduction

In the previous chapters, a detailed analysis of some of the major constituents of different essential oils using rotational spectroscopy was presented. The results of these studies illustrate the power of microwave spectroscopy as an analytical tool. Due to the fingerprint character of this technique, conformers of structurally similar components can be identified. In addition, by applying the microwave three-wave mixing (M3WM) technique, which is described in Chapter 2, enantiomers of the chiral compounds can be addressed individually in a chirality-sensitive manner, as was shown for menthone and isomenthone (see Chapter 4).

This chapter continues the discussion on the components of essential oils studied with rotational spectroscopy. Here we focus on the monoterpene pulegone (2-isopropylidene-5-methylcyclohexanone). This component has not been characterized previously with rotational spectroscopy, despite its broad range of applications in food, fragrance, and the pharmaceutical industry[1]. It is a chiral molecule and, as for many other chiral components, its enantiomers show different biological activity. In general, some dosage-dependent side effects by oral intake of pulegone are known, which can lead to hepatic and renal failure, gastritis, and in severe cases even to death[2]. Intriguingly, its (S)-enantiomer has been reported to have much lower toxicity in humans[3]. It is also notable that the (R)-enantiomeric form is more commonly found in essential oils[2].

This chapter is based on the following publication:

A. Krin, C. Pérez, P. Pinacho, M. M. Quesada-Moreno, J. J. López-González, J. R. Avilés-Moreno, S. Blanco, J. C. López, M. Schnell, *Chem. Eur. J.* **2018**, *24*, 721. (experimental: 60%, data analysis: 50%; writing up: 70%)

Pulegone was analyzed before in the liquid phase, mainly using infrared (IR) spectroscopy and vibrational circular dichroism (VCD). In one of the experimental studies, the near-IR-VCD spectrum of pulegone, among other terpenes, was measured[4]. Also, the solvent effects in IR and VCD spectroscopy were explored both experimentally and computationally on the example of pulegone[5;6]. Another VCD-study was devoted to the investigation of chirality transfer (also known as "induced chirality") on the example of pulegone upon complexation with an achiral solvent $CDCl_3$[7]. According to the results, the transfer of chirality yields the so-called non-robust normal modes observed in VCD spectra, for which the signs cannot be predicted reliably with standard Density Functional Theory (DFT) calculations[7] (more details regarding VCD are provided in Chapter 1). In the scope of the recent IR-Raman-VCD study on pulegone in the mid-IR region (4000-150 cm^{-1})[5], two energetically stable conformers of pulegone were determined computationally, but only the energetically lowest one was reported to be observed experimentally.

Pulegone is present in peppermint (*Mentha piperita L.*, up to 5%[8]) and pennyroyal (*Mentha pulegium*, 85-97%[8]) essential oils. However, the signal-to-noise ratio (SNR) in our recorded peppermint broadband spectrum (20:1) was not sufficient for the direct characterization of pulegone in the oil (see Chapter 4). For this reason, a separate broadband measurement on pulegone was performed, which allowed a subsequent extensive analysis regarding its structure, internal dynamics and interaction with water. This later aspect is of particular interest with respect to possible structural changes of this biologically relevant molecule due to (micro)solvation. As was shown in other studies, rotational spectroscopy is highly suitable for the characterization of microsolvated complexes and the dominant intermolecular forces involved in the formation of such complexes in the gas phase[9;10]. The conformational landscape of pulegone was explored both computationally and experimentally, complementing the previously reported results[5].

6.2 Experimental techniques

The broadband spectrum of pulegone was measured on the chirped-pulse Fourier transform microwave (CP-FTMW) spectrometer COMPACT[11;12] in the frequency range from 2-8 GHz (1.5 million acquisitions). A detailed description of the set-up can be found in Chapter 3. No specific changes to the standard set-up were implemented for the study presented here.

The sample was purchased enantioenriched ((R)-(+)- and (S)-(–)pulegone, 97% chemical purity) and used without further purification. Pulegone is liquid at room temperature. In order to bring it into the gas phase, the sample was heated to 80 °C in a reservoir close to the valve orifice to increase the vapor pressure, and then supersonically expanded into a vacuum chamber using neon (2 bar backing pressure) as a carrier gas.

A separate broadband measurement was conducted for the pulegone-water clusters (2 million acquisitions), where an external reservoir of water was applied. The measured rotational spectra were assigned with the aid of the JB95[13] and the PGOPHER[14] program packages.

The fits were subsequently refined in the I^r representation with the SPFIT[15] program. Structural analysis of the energetically lowest conformer of pulegone was carried out using the KRA software package[16;17]. An additional approach for the structure determination included the non-linear least-squares procedure, as implemented in the STRFIT program[18]. For the characterization of the internal dynamics of pulegone, the program XIAM[19] was used, which can handle up to three symmetric internal rotors, such as methyl groups. The analysis of the pulegone enantiomers was also performed with M3WM. No changes to the instrumental set-up described in Chapter 3 were required for the M3WM experiments.

6.3 Computational methods

The structures and rotational parameters for the most stable conformers of pulegone were first calculated at the M06-2X/6-311++G(d,p) level of theory, using Gaussian 09[20]. These obtained structures were subsequently re-optimized at the MP2/6-311++G(d,p) level of theory, which had previously shown a good agreement with experimental results for the other molecular systems similar to pulegone, such as menthone[21]. Several pulegone-water clusters were calculated at the M06-2X/6-311++G(d,p) and B3LYP-D3BJ/6-311++G(d,p) (accounting for the dispersion) levels of theory. All obtained structures were tested to be true minima of the potential energy surface by checking for imaginary frequencies from vibrational frequency calculations.

6.4 Results and Discussion

6.4.1 The pulegone monomer

6.4.1.1 Theoretical analysis of the pulegone conformers

Pulegone is a chiral molecule with one chiral center. It is presented in Figures 6.1 and 6.2, where the chiral center is marked with an asterisk. The core structure of pulegone is composed of a cyclohexanone ring with two functional groups: a methyl and an isopropylidene groups (see Figure 6.1). Different conformational arrangements are possible for pulegone, since the cyclohexanone ring can take on either the chair or the energetically less preferable twist-boat configuration. Thus, the methyl group, attached to the chiral center, can be orientated either equatorially or axially with respect to the cyclohexanone ring.

Several stable conformers of pulegone, featuring these possible structural differences, were identified computationally. They are presented in Figure 6.1 with their respective relative zero-point corrected energies. Note that also the enantiomeric forms are depicted for the two energetically lowest conformers, Chair 1 and Chair 2 (see Figure 6.1). In this way, the actual difference between these conformers, which is the orientation of the methyl group, can be better visualized.

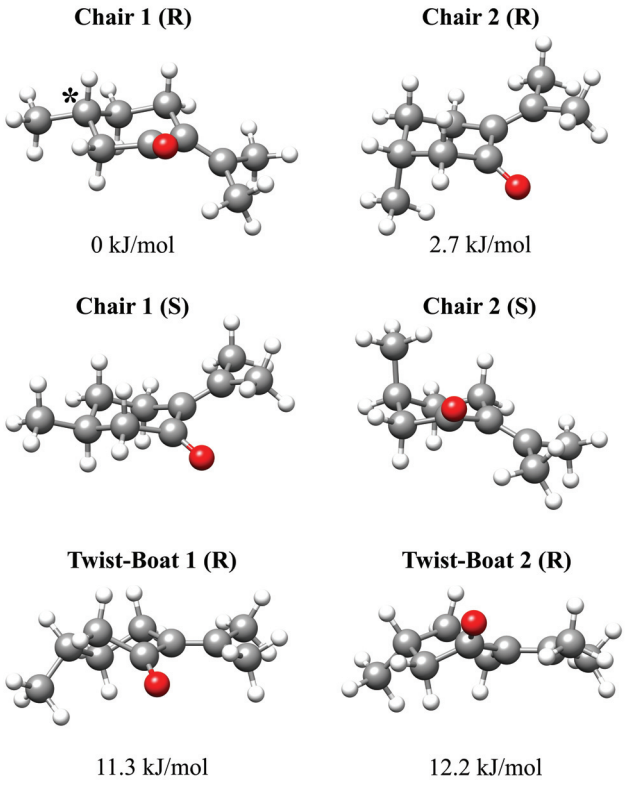

Figure 6.1: *Structures of the four pulegone conformers, optimized at the MP2/6-311++G(d,p) level of theory, together with their calculated relative energies. For Chairs 1 and 2, both enantiomers are shown, while for the Twist-Boats 1 and 2 only the R enantiomers are given. The stereogenic center is marked with an asterisk on the example of Chair 1.*

In the case of the energetically lowest conformer Chair 1, the methyl group is orientated, as expected, equatorially, which is in general the more preferable position for bulky substituents. In Chair 2, the methyl group is arranged axially. Due to this difference, the energy of Chair 2 is 2.7 kJ/mol higher relative to Chair 1 (see Figure 6.1). The interconversion from Chair 1 into Chair 2 and vice versa can occur only through ring flipping. Since it is known that the barrier for such an interconversion is about 40 kJ/mol for an unsubstituted cyclohexane ring, a large barrier height is also expected for the interconversion of Chair 1 and Chair 2 into each other. Although the interconversion might occur at room temperature, such a process is not expected to take place under the cold conditions of the molecular jet. For this reason, both conformers are expected to be kinetically stabilized in the jet and thus to be observed experimentally in the rotational broadband spectrum.

The other conformers of pulegone, which were determined computationally, are Twist-Boat 1 and Twist-Boat 2. Due to the twist-boat configuration of the cyclohexanone ring, these conformers are much higher in energy in comparison to Chair 1 (11.3 kJ/mol and 12.2 kJ/mol respectively). Conformers with such high relative energies are not expected to be significantly

populated to be observed experimentally.

The relative Gibbs energies, calculated at the pre-expansion conditions (80 °C) allowed us to estimate the relative population ratio of the conformers in the supersonic jet. Based on the results from ab initio calculations (MP2/6-311++G(d,p) level of theory), the relative population for Chair 1/Chair 2/Twist-Boat 1/Twist-Boat 2 is expected to be 1/0.25/0.02/0.01. This calculation is in agreement with the previous theoretical study on pulegone[5]. There, only two conformers of pulegone, EQ-1 (corresponds to Chair 1 here) and Ax-1 (corresponds to Twist-Boat 1) were computed, while there is no discussion on Chair 2. The expected population for Ax-1 was estimated to be 1.5%, similar to our result mentioned above.

The calculated rotational parameters for the four conformers are given in Table 6.1. Note that while Chair 1 and Chair 2 differ clearly in their rotational parameters, the difference is only about 18 MHz for Twist-Boat 1 and Twist-Boat 2.

6.4.1.2 Broadband spectrum of pulegone

In this section, the experimental results for the pulegone conformers observed in the molecular jet will be presented and compared to the calculated ones. The experimental rotational spectrum of pulegone is moderately dense. The strongest lines correspond to b-type transitions. Two species could be identified in the spectrum. Their experimental rotational parameters are given in Table 6.1. For both observed species, characteristic multiplets due to internal rotation were observed. An excerpt of the broadband spectrum is presented in Figure 6.2.

The experimentally observed component with the higher intensity has a SNR of 800:1. By comparing its rotational constants to the calculated ones (MP2/6-311++G(d,p) level of theory, see Table 6.1) it is noticeable that the experimental B and C constants are close to the ones calculated for Chair 1. The A constant differs by approximately 24 MHz or about 1.2% from the predicted value. The Ray's asymmetry parameter κ[22] (see also Chapter 2), which takes into account the relative ratios between the rotational constants, can also be helpful for the assignment. Here, the calculated κ is -0.75 for Chair 1 and -0.76 for the experimentally observed component with the higher intensity. This leads to the conclusion that the strongest component in the spectrum corresponds to the calculated Chair 1 conformer. Following the same argumentation, the less intense component (SNR 30:1) could be assigned to Chair 2. Here, the calculated rotational constants were closer to the experimentally observed ones than for Chair 1.

The agreement between the predicted dipole moment components and the observed rotational transitions is another criterion which can guide the assignment. The μ_b component is the largest for all the calculated structures, while μ_a and μ_c are significantly smaller. Indeed, the most intense lines in the spectrum were of b-type. Only a few a- and c-types could be assigned for Chair 1 and 2 with much lower intensity than the b-type transitions. Another aspect, which can further support the conformational assignment, are molecular structural parameters (e.g. angles) determined by the analysis of internal rotation, as described in more detail in Section 6.4.1.4.

Table 6.1: *Comparison of experimental and calculated molecular parameters (MP2/6-311++G(d,p) level of theory) for pulegone. The fits reported here include only AA states due to internal rotation (see text for nomenclature). The observed rotational transitions are given using the following nomenclature: P branch ΔJ=-1, Q branch ΔJ=0, R branch ΔJ=+1; a, b, and c correspond to the respective type of the rotational transitions.*

Parameter	Experimental		MP2*			
	Chair 1	Chair 2	Chair 1	Chair 2	Twist-Boat 1	Twist-Boat 2
A | MHz	1909.05435(71)**	1820.46706(90)	1885.42	1817.17	1974.04	1966.07
B | MHz	739.06297(21)	816.91977(53)	734.76	822.31	764.90	746.45
C | MHz	578.14181(21)	635.95024(53)	584.11	640.85	606.24	588.09
Δ_J | kHz	0. 0302(24)	0.0318(35)				
Δ_{JK} | kHz	-0.273(10)	0.0597(67)				
Δ_K | kHz	1.079(48)	-0.136(30)				
κ	-0.76	-0.69	-0.75	-0.69	-0.77	-0.77
μ_a | D$^\diamond$	^aR	^aR	0.7	0.4	-0.1	0.5
μ_b | D	^bR, ^bQ	^bR, ^bQ	-2.7	-2.7	-2.8	-2.7
μ_c | D	^cR, ^cQ	^cR, ^cQ	-1.0	-1.1	0.9	0.8
ΔE | kJ/mol			0	2.7	11.3	12.2
σ † | kHz	7.53	10.6				
N ‡	97	38				

* $6-311++G(d,p)$
** Standard error in parenthesis in units of the last digit
$^\diamond$ $D \approx 3.3356 * 10^{-30} C \cdot m$
† RMS deviation of the fit
‡ Number of fitted transitions

Overall, there is a good agreement between the experimental observations and the theory. First of all, as expected, only the two energetically most preferable conformers, Chair 1 and Chair 2, were assigned in the spectrum, while Twist-Boat 1 and Twist-Boat 2 were not observed despite an intense search. Chair 1 is significantly more intense than Chair 2 (higher SNR), which is also expected, since according to the calculated Gibbs energy (see Section 6.4.1.1), it should be more populated in the molecular jet.

6.4.1.3 Substitution structure

The SNR of Chair 1 was sufficient to observe and assign singly substituted ^{13}C- and ^{18}O-isotopologues in natural abundance. The experimentally determined rotational constants of the isotopologues are presented in Table C.1. More than 20 transitions could be assigned for the ^{13}C-species. Only a few lines were observed for ^{18}O due to its low abundance of 0.27%.

As a first step, these results were used for the r_s structure determination based on the Kraitchman's approach (Chapter 2), which is presented in Figure 6.3. The carbon atom C2 lies in the *ab* plane, while C3 and C5 are located close to the principal axes. The experimentally

determined and calculated atomic positions are summarized in Table C.2. While there is a big difference between the calculated (MP2/6-311++ G(d,p)) and the experimental (r_s) positions for the C3 atom, there is a good agreement for C2 and C5. Note that the atomic labelling used here does not correspond to the IUPAC nomenclature, but was adopted from the previous pulegone study[5].

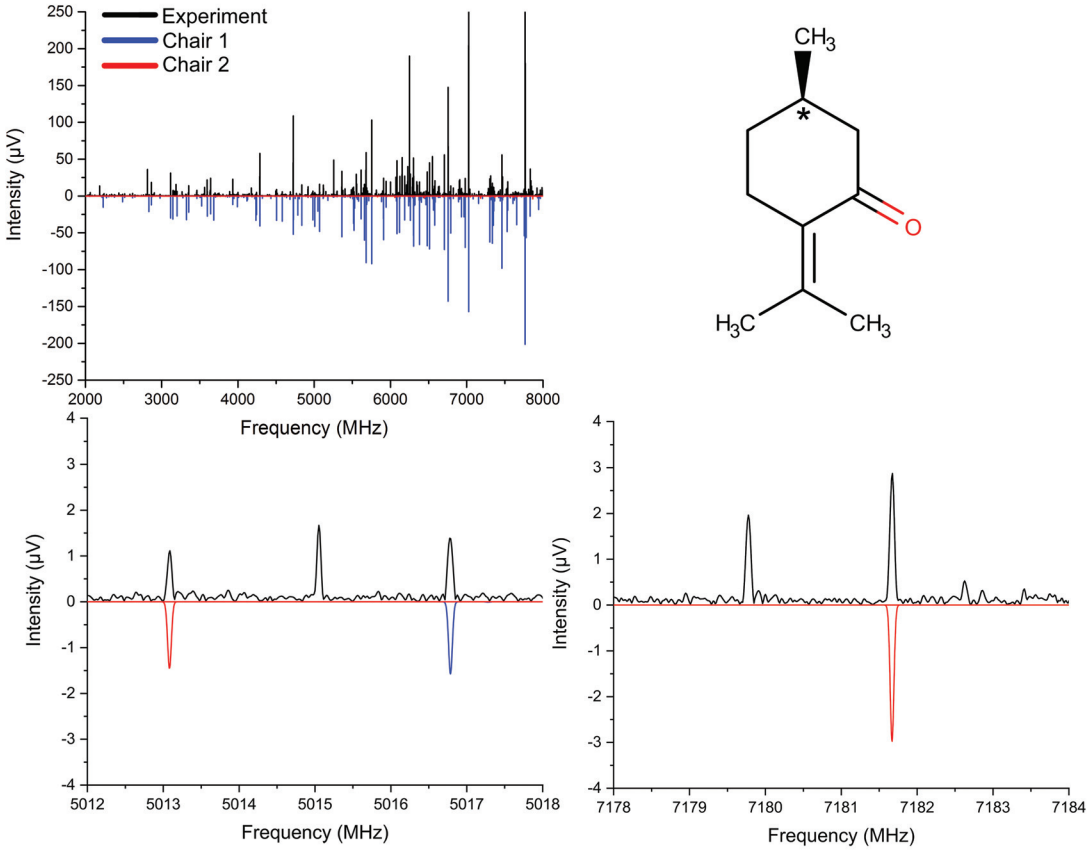

Figure 6.2: *Portions of the 2 - 8 GHz spectrum (1.5 million acquisitions, neon as a career gas) of pulegone. The black trace shows the experimental spectrum, while the lower traces represent simulations based on experimentally fitted rotational parameters for Chair 1 and Chair 2. A schematic structure of R-(+)-pulegone is presented on the right. The chiral center is marked with an asterisk.*

Next, the effective ground structure r_0 of Chair 1 was obtained (see Chapter 2). A comparison between the r_s and the r_0 structures is given in Figure 6.3. Here, the underlying structure (grey for carbon, red for oxygen) represents the results from the r_0-fit, while the determined r_s atom positions are depicted as blue spheres. The respective structural parameters from the results of the r_s and r_0 fits are listed in Table C.3. Overall, there is a good agreement between calculated and experimental parameters.

Since the SNR for Chair 2 was only 30:1 in the present spectrum, no experimental structure determination could be done.

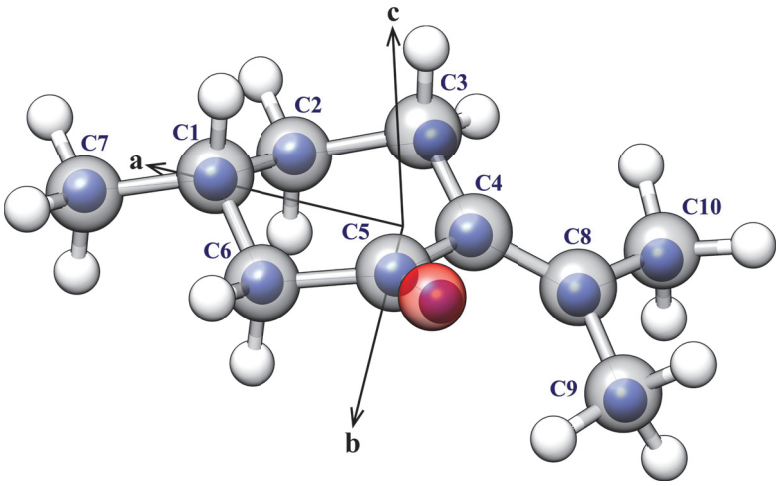

Figure 6.3: *Experimental structures for Chair 1: r_0- (underlying structure, grey for carbon and red for oxygen) and r_s-substitution structure (blue spheres). The principal axis system is also indicated.*

6.4.1.4 Internal rotation

Internal rotation of methyl groups can result in characteristic line splitting in rotational broadband spectra, if the internal rotation barrier is low enough (Chapter 2). Pulegone has three methyl groups (see Figure 6.2). In the following, they will be referred to as top 1 (containing C10), top 2 (containing C9), and top 3 (containing C7 and being attached to the chiral center of the molecule, C1, see Figure 6.1 for labelling). For the tops which are attached to the same sp^2-hybridized carbon atom C8, namely top 1 and top 2, a low internal rotation barrier is expected. Indeed, according to the calculations the barriers are 2.2 and 5.7 kJ/mol for tops 1 and 2, respectively (B3LYP/ 6–311G level of theory). Top 3 is attached to an sp^3-hybridized C-atom. It is known from previous studies on similar molecules[23;24] that the barrier for the internal rotation of such a methyl group should be significantly higher. The calculated barrier for top 3 is 12 kJ/mol (B3LYP/6–311G level of theory), which is too high to give rise to observable line splitting for the frequency resolution of approximately 25 kHz of the COMPACT spectrometer.

Numerous line splittings into multiplets were observed in the present spectrum for Chair 1 and Chair 2. Examples of such fine structure are presented in Figures 6.4 (Chair 1) and 6.5 (Chair 2). The observed multiplets have components spanning several MHz and clearly indicate the presence of two internally rotated tops. They were analyzed and fitted using program XIAM (see Section 6.2). The results for the internal dynamics of Chair 1 will be discussed first.

Due to the internal rotation of two inequivalent methyl tops, splitting into five lines is expected. These are labelled as AA, AE, EA, EE and EE*. A coupling scheme for the splitting is given in Figure 6.6. In the first step, 97 lines for the AA states were fitted to a rigid-rotor Hamiltonian with a standard deviation of 7.53 kHz (see Table 6.1). This fit was subsequently

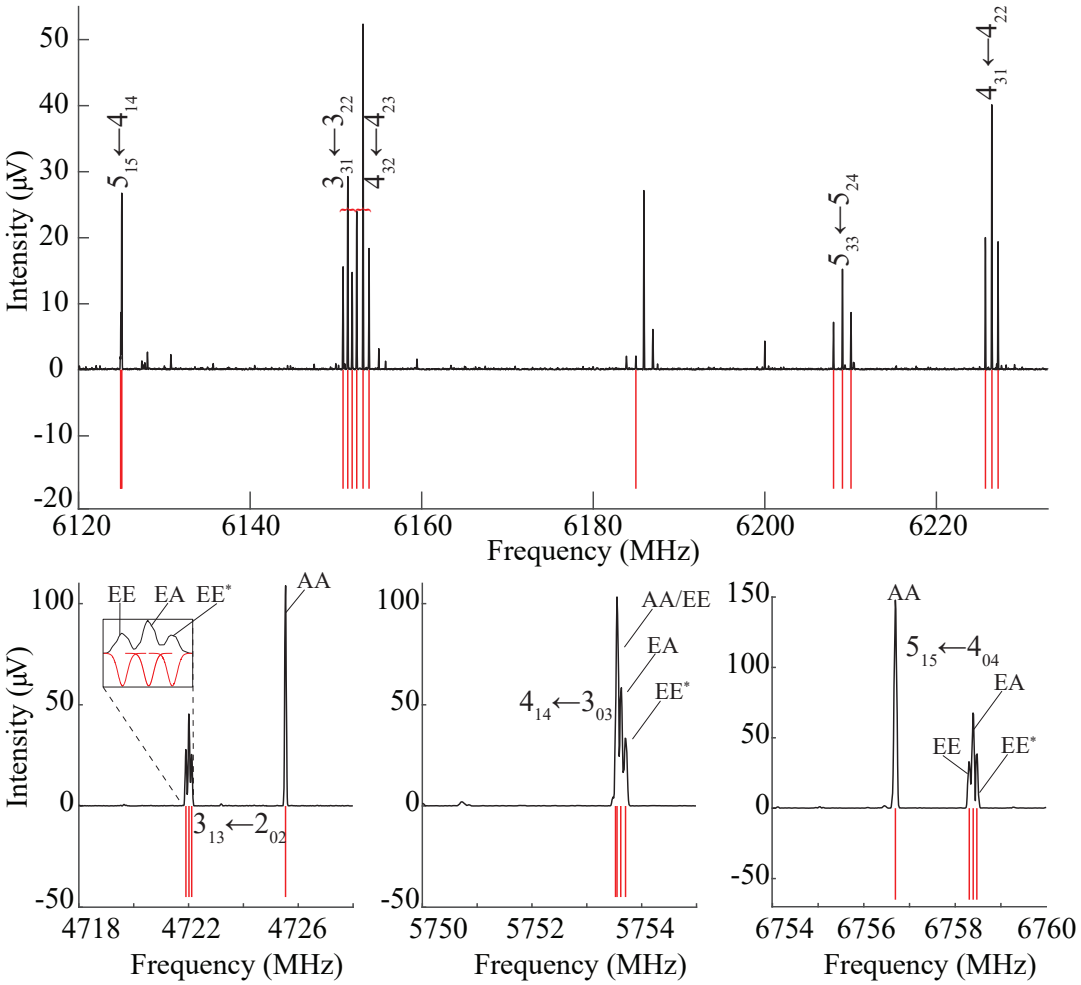

Figure 6.4: *Parts of the broadband rotational spectrum to illustrate the characteristic multiplet structure due to internal dynamics. In all parts, the upper traces (black) are the experimentally obtained spectra. The lower (red) traces are stick spectra (not taking into account specific intensity distributions) based on simulations using the fitted molecular constants for Chair 1.*

used to predict frequencies for the strongest b-type transitions of the other internal rotation components of Chair 1. This prediction was performed using XIAM based on the calculated values for the internal rotation barriers. In a step-by-step procedure, a total of 234 lines were assigned and fitted with a standard deviation of 9.09 kHz (Table C.4). The internal rotations of the methyl tops of Chair 1 are hindered by only low barriers of 1.961911(46) kJ/mol for top 1, which is pointing away from the carbonyl group,and 6.3617(12) kJ/mol for top 2, which interacts with the carbonyl group, resulting in the higher barrier. These values are close to the calculated ones. The results for the experimentally determined and calculated rotational barriers are summarized in Table 6.2.

The assignment was more challenging for Chair 2, due to its lower SNR in the spectrum. The previously determined experimental values for V_3 of Chair 1 were used for the prediction of

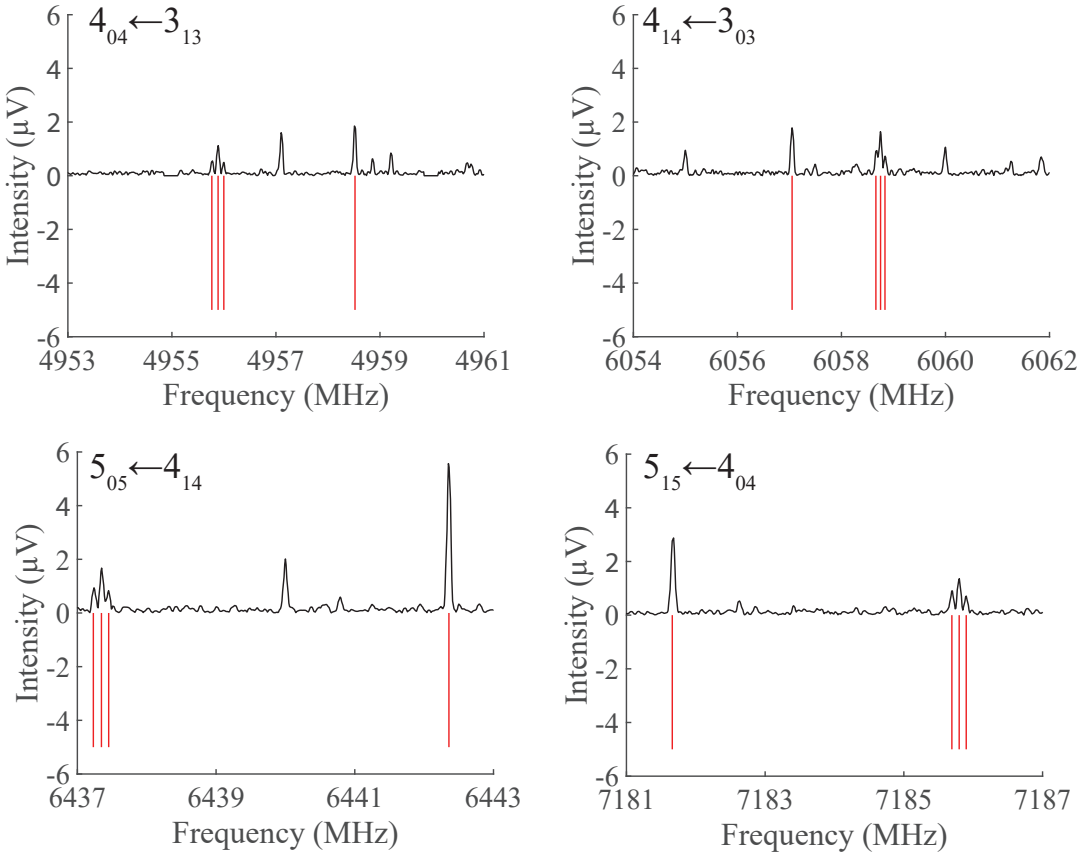

Figure 6.5: *Parts of the pulegone broadband rotational spectrum. The four sections are zoom-ins of individual rotational transitions to illustrate the multiplet structure due to internal dynamics. In all parts, the upper traces (black) are the experimentally obtained spectrum. The lower (red) traces are stick spectra (not taking into account specific intensity distributions) based on simulations using the fitted molecular constants for Chair 2 and employing the program XIAM.*

the internal rotation components for Chair 2. Overall, 50 lines could be assigned and fitted for Chair 2 with a standard deviation of 6.94 kHz (see Table 6.2 and Table C.5). As expected, the experimentally determined V_3 barriers of Chair 2 are close to the ones of Chair 1 and are 1.96094(74) kJ/mol and 6.705(44) kJ/mol for top 1 and 2 respectively (see Table 6.2). Note that due to higher intensity, more lines could be assigned for Chair 1, which allowed to determine the internal rotation barriers with higher accuracy. AA and AE states could not be resolved in our spectrum, since according to the calculations, their frequency difference is less than 20 kHz and, thus, beyond the resolution of our spectrometer. That is why the V_3 barrier of top 1 is better determined than of top 2 for both Chair 1 and Chair 2. The V_3 barrier of top 1 depends more strongly on the EA, EE, and EE* splittings, which are well resolved in the spectrum (see Figure 6.4 and 6.5).

It is interesting to compare the obtained experimental results for the internal dynamics of pulegone to another molecule with similar structural features, namely acetone. Like pulegone,

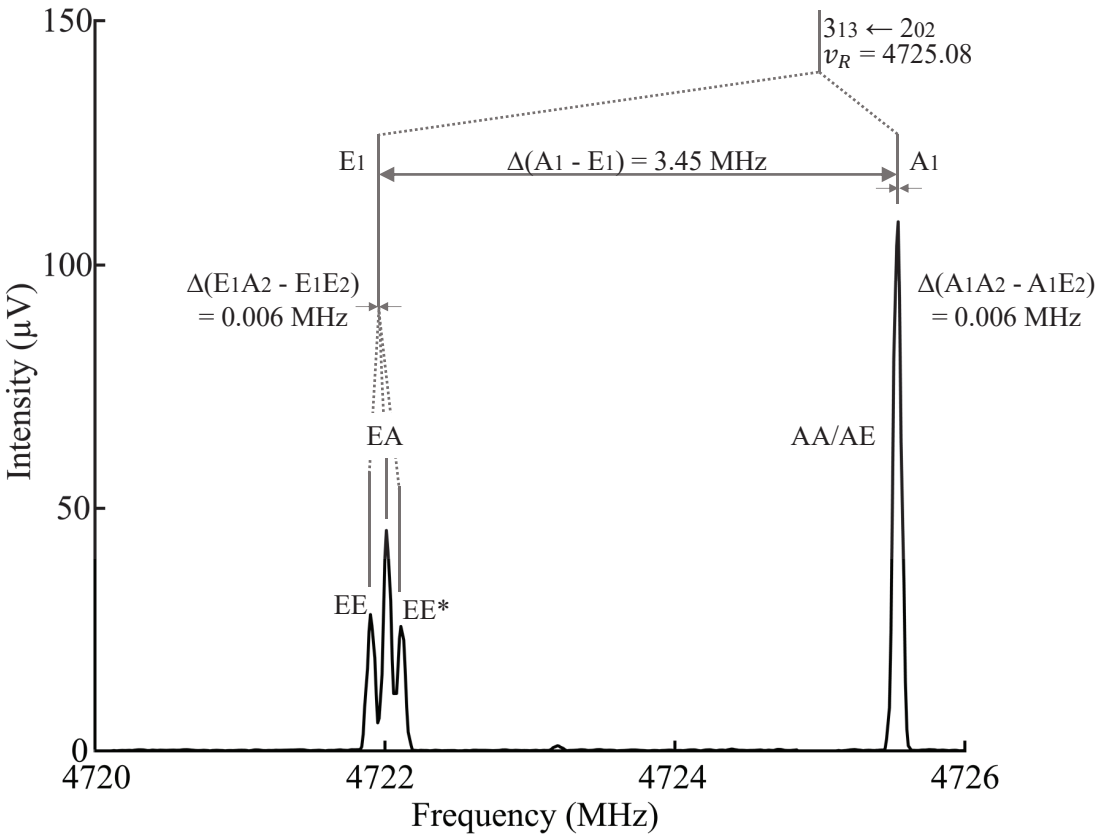

Figure 6.6: *Coupling scheme for the $3_{13} \leftarrow 2_{02}$ rotational transition of Chair 1. v_R refers to the hypothetical unperturbed transition. Top 1 (V_3 = 1.961911(46) kJ/mol) splits this transition into A_1 and E_1 components, which are predicted to be 3.45 MHz apart. Top 2 (V_3 = 6.3617(12) kJ/mol) further splits each of those components, resulting in four components (0.006 MHz apart). They are labelled A_1A_2 (AA), A_1E_2 (AE), E_1A_2 (EA) and E_1E_2. Note that top-top interaction splits also the E_1E_2 component into a doublet labelled EE and EE*. In summary, the interaction between top 1 and top 2 splits all rotational transitions into five components labelled AA, AE, EA, EE and EE*, but AA and AE splittings could not be resolved with our instrument.*

acetone has two methyl tops attached to an sp^2-hybridized C-atom. However, in the case of acetone, the two tops are equivalent, contrary to pulegone, where the two tops have different chemical environments (e.g. top 2 is located close to a carbonyl oxygen). This results in different splitting patterns for the two molecules. While for acetone the internal motion gives rise to quartets[25], a more complex pattern is observed for pulegone, as was described above. The experimental V_3 for acetone is 3.18327(59) kJ/mol[25], which is an intermediate value for the top 1 and top 2 barriers of pulegone, closer to the experimentally determined barrier of top 1 in pulegone. This could be due to the fact that top 1 is not affected by any interactions with neighbouring groups, similar to the methyl tops of acetone.

From the fit of the different internal components of Chair 1 and Chair 2, other parameters such as angles formed by the internal rotation axes of methyl tops 1 and 2 with the principal inertial

Table 6.2: *Comparison of experimental and calculated molecular parameters for pulegone (see Figure 6.1 for the labelling of the conformers). The experimental parameters of Chair 1 and 2 were determined by fitting the internal rotation of methyl tops 1 and 2 (containing C10 and C9, respectively (Figure 6.3)) with XIAM. The observed rotational transitions are given using the following nomenclature: P branch $\triangle J = -1$, Q branch $\triangle J = 0$, R branch $\triangle J = +1$; a, b, and c correspond to the respective type of the rotational transitions.*

	Experimental		**MP2/6-311++G(d,p)**			
Parameter	Chair 1	Chair 2	Chair 1	Chair 2	Twist-Boat 1	Twist-Boat 2
A | MHz	1908.49282 (69)	1819.9074 (12)	1885.42	1817.17	1974.04	1966.07
B | MHz	738.85952(24)	816.68532 (59)	734.76	822.31	764.90	746.45
C | MHz	578.14126(23)	635.94683 (29)	584.11	640.85	606.24	588.09
Δ_J | kHz	0.0330 (25)	0.0414 (23)	0.04	0.03	0.05	0.02
Δ_{JK} | kHz	-0.281 (11)	0.0786 (58)	-0.32	0.12	-0.22	-0.05
Δ_K | kHz	1.231 (57)	-0.033 (25)	1.25	-0.02	0.86	0.48
δ_J | kHz	0.00195 (72)	–	-0.001	0.005	0.01	0.001
δ_K | kHz	–	-0.0067 (12)	0.06	0.003	0.01	0.03
κ	-0.76	-0.69	-0.75	-0.69	-0.77	-0.77
V_3 (1) | kJ/mol	1.961911(46)	1.96094 (74)	2.2[‡]	2.2[‡]	-	-
V_3 (2) | kJ/mol	6.3617(12)	6.705(44)	5.7[‡]	5.7[‡]	-	-
$\measuredangle\delta$ (1) | rad	2.141735 (43)	2.17298 (73)	2.1	2.17	-	-
$\measuredangle\delta$ (2) | rad	[2.13][§]	0.970(25)	2.13	0.99	-	-
$\measuredangle\varepsilon$ (1) | rad	3.15223(54)	3.01264(19)	3.12	2.95	-	-
$\measuredangle\varepsilon$ (2) | rad	0.507(26)	2.880(24)	0.56	2.78	-	-
D_{pi2J} [*] (1) | MHz	-0.02207 (35)	-0.0521 (62)	-	-	-	-
D_{pi2K} [*] (1) | MHz	0.2705 (12)	-	-	-	-	-
D_{pi2K} [*] (2) | MHz	0.167 (86)	-	-	-	-	-
D_{pi2-} [*] (1) | MHz	-0.02643 (20)	-0.0545 (90)	-	-	-	-
ΔE | kJ/mol			0	2.7	11.3	12.2
σ [◇] | kHz	9.09	6.94				
N [†]	234	50				

[*] Empirical internal rotation (overall rotation distortion operator).
[◇] RMS deviation of the fit
[†] Number of fitted transitions
[‡] B3LYP/6-311G level of theory
[§] fixed to the calculated value

axes can be derived. They are presented in Table 6.2. These parameters can further support the assignment of the species observed in the spectrum. For instance, in the case of pulegone, the angle $\epsilon(2)$, which is defined as the angle between the principal axis b and the projection of the internal rotation axis in the principal axis system[26], is significantly different for Chairs 1 and 2 (0.507(26) rad Chair 1, 2.880(24) rad Chair 2). The calculated (MP2/6-311++G(d,p)) values for $\epsilon(2)$ for Chair 1 and Chair 2 are in agreement with the experimentally determined ones, which corroborates the previous assignment of these conformers.

6.4.1.5 Enantiomer differentiation using M3WM

The two enantiomers of pulegone exhibit different physiological effects in the human body, with the S-(−)-pulegone being less toxic than its enantiomeric counterpart. Also the abundance of these enantiomers in natural essential oils is very different. According to the previous reports, S-(−)-pulegone is rarely found in essential oils[2].

Since all three dipole moment components of pulegone are non-zero (see Table 6.1), its enantiomers can be characterized by using the M3WM technique. As shown in Chapter 4, this technique can be applied to such complex mixtures as essential oils. It allows to determine the excess enantiomer of the molecule of interest present in the oil. One possibility is to use an enantiopure sample of the respective component as a reference. The M3WM experiment is then performed both on the oil and on the reference sample. By comparing the phases of the recorded M3WM signals the excess enantiomer in the oil is determined. This procedure is demonstrated in Chapter 4 on the example of (−)-menthone. Prior to the final M3WM experiment in the oil, possible M3WM-cycles consisting of a-, b-, and c-type rotational transitions have to be determined from the assigned broadband spectrum. In this section the results of such preparatory experiment on enantio-enriched samples (R-(+)- and S-(−)-enantomers) of pulegone are summarized.

Both conformers of pulegone, Chair 1 and Chair 2, have three non-zero dipole moment components, which is one of the requirements for the M3WM. However, the observed rotational line intensity of Chair 1 is significantly higher in the spectrum. For this reason, the M3WM experiment was performed on Chair 1. Two M3WM cycles were determined for this pulegone conformer. They are depicted in Figure 6.7. The transitions in these cycles involve only the states with AA symmetry with respect to the internal dynamics. Cycle 1 consists only of Q-branch transitions, which obey the ΔJ=0 selection rule (Figure 6.7).

In order to determine the optimal pulse duration of the excitation pulses ("drive" and "twist"), nutation curves were measured for the two cycles. In this procedure, the signal amplitude of the respective rotational transition is recorded as a function of pulse duration. The drive pulse should fulfil $\pi/2$ Rabi conditions for the maximal coherence between the two rotational states involved. For the twist pulse the π Rabi condition should be met (Chapter 2). In the case of cycle 1, the determined optimal drive pulse duration ($5_{24} \leftarrow 5_{14}$ transition at 2620.09 MHz) was 50 ns. For the twist ($5_{23} \leftarrow 5_{24}$ at 497.09 MHz) the duration necessary to achieve the π condition was 1600 ns. The optimal drive pulse duration for cycle 2 ($5_{05} \leftarrow 4_{14}$ at 5680.25 MHz) was the same as for cycle 1 (50 ns), while the twist pulse ($5_{15} \leftarrow 5_{05}$ at 444.79 MH) was significantly shorter (300 ns). The obtained nutation curves for the drive transitions of both cycles are presented in Figure 6.8.

The molecular M3WM response (listen: $5_{14} \leftarrow 5_{23}$ at 3117.18 MHz for cycle 1, and $4_{14} \leftarrow 5_{15}$ at 6125.06 MHz for cycle 2) was recorded in the form of a free induction decay (FID). The experiment was performed with two pulegone enantiomers "back-to-back", and a comparison of the phases for the recorded signals was carried out (Figure 6.7). A clear π phase shift is observed, as expected, for the two enantiomers due to the opposite sign in the scalar triple

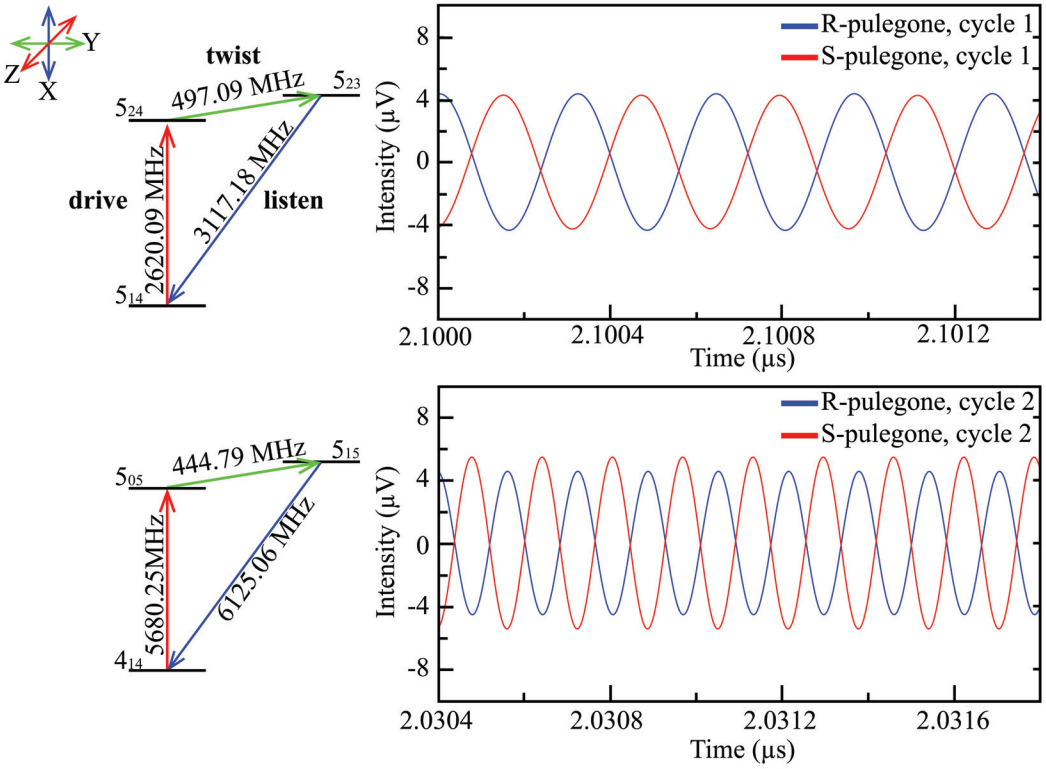

Figure 6.7: *Two M3WM cycles for the pulegone conformer Chair 1. The nomenclature for labelling the respective rotational states is $J_{K_aK_c}$. The linearly polarized MW pulse (drive, defined to be along the Z axis in the laboratory space) and radio frequency (RF) pulse (twist, defined along the Y axis) are the two orthogonal excitation pulses. The molecular M3WM response (listen) in the form of a free induction decay (FID) is recorded in the X direction.*

product of their dipole-moment components (see equation 2.34, Chapter 2). The results can be used for the subsequent analysis of pulegone in mixtures (such as e.g. essential oils) to determine its respective excess enantiomer.

6.4.2 The pulegone-water complex

According to the literature, pulegone is largely insoluble in water[27]. To overcome this drawback, several strategies such as supramolecular incapsulation, have been developed[28]. Microsolvated clusters involving a few water molecules can be formed under the supersonic conditions of the molecular jet. The experimental observation of pulegone-water clusters in the gas phase can provide a better understanding of their intermolecular interactions. Such interactions can occur only via the polar carbonyl group (keto-group) of pulegone, which can act as hydrogen bond acceptor (see Figures 6.1 and 6.2).

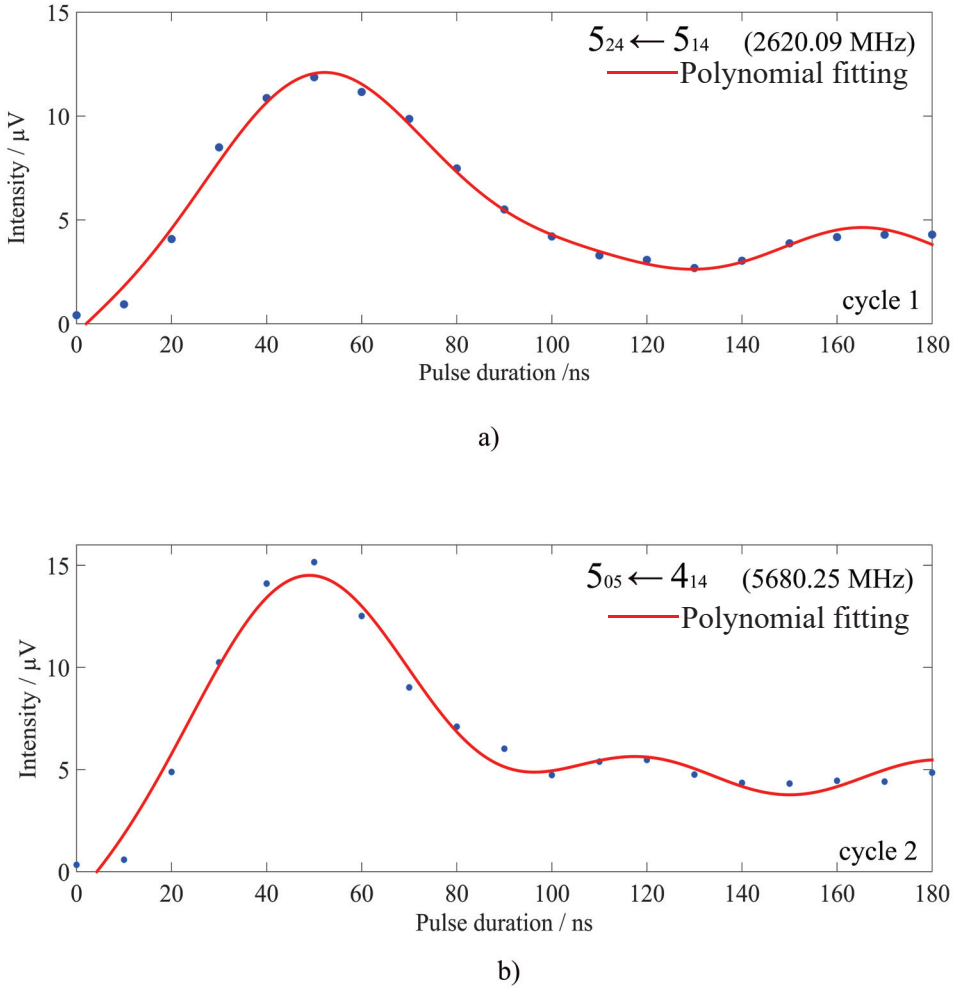

Figure 6.8: *Nutation curves for the drive transitions of the two M3WM cycles to determine the optimal pulse durations ($\pi/2$ conditions) by direct excitation of (a) the c-type transition $5_{24} \leftarrow 5_{14}$ at 2620.09 MHz (cycle 1) and (b) the b-type transition $5_{05} \leftarrow 4_{14}$ at 5680.25 MHz (cycle 2). In both cases, maximum amplitudes for the drive signal are observed for the pulse durations around 50 ns.*

Structures of several clusters including the kinetically most stable conformer of pulegone, Chair 1, and one water molecule were calculated at the M06-2X/6-311++G(d,p) and B3LYP-D3BJ/6-311++G(d,p) levels of theory. The energetically lowest ones are given in Figure 6.9 with the calculated distances between the two molecules. The obtained clusters are labelled as Chair 1-water a and Chair 1-water b. The calculated (B3LYP-D3BJ/6-311++G(d,p)) energy difference for these two clusters is 2 kJ/mol, with Chair 1-water a being energetically more preferable.

As expected, in both clusters the interaction between Chair 1 and water occurs via strong hydrogen bond interactions (calculated distances are around 1.9 Å for both clusters). Secondary long-range (dispersion) interactions of the oxygen of water with the C-H groups of

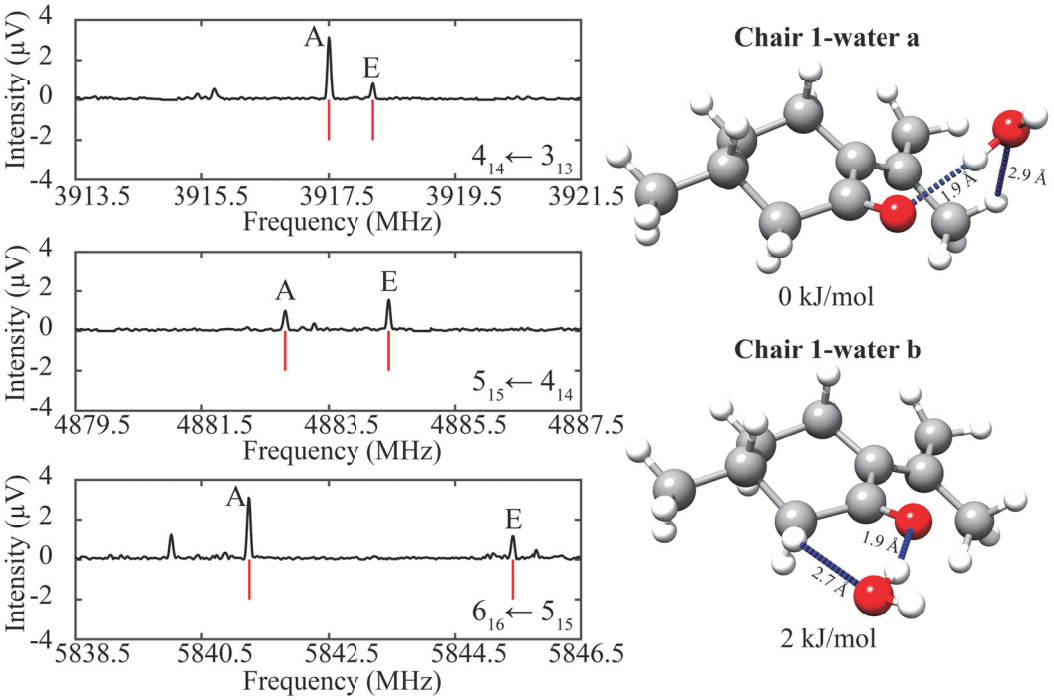

Figure 6.9: *Parts of the broadband rotational spectrum (2 million acquisitions and using neon as carrier gas) of pulegone with water. The three sections are zoom-ins of individual rotational transitions to illustrate the doublet structure due to internal dynamics. In all parts, the upper traces (black) are the experimentally obtained spectrum. The lower (red) traces are stick spectra (not taking into account specific intensity distributions) based on simulations using the fitted molecular constants for Chair 1-water a. The labelling of the rotational transitions follows the $J_{K_aK_c}$ scheme. On the right, two pulegone-water clusters calculated at the B3LYP-D3BJ/6-311++G(d,p) level of theory for the energetically lowest conformer of pulegone, Chair 1, are shown. The calculated hydrogen-bond distances are indicated.*

pulegone are also present in both clusters and stabilize further the cluster formation. These secondary interactions are different for Chair 1-water a and Chair 1-water b (Figure 6.9). In Chair 1-water a the oxygen of water is interacting with top 2 of Chair 1. In the case of Chair 1-water b the hydrogen of one of the cyclohexanone CH_2 groups is involved in the interaction instead.

One pulegone-water complex could be determined experimentally in the pulegone-water broadband spectrum. The obtained rotational parameters are given in Table 6.3. Direct comparison between the calculated and experimental parameters allows us to assign the experimentally observed species to the energetically most stable Chair 1–water a cluster. From Table 6.3, it can be seen that the rotational A and B constants calculated with the B3LYP-D3BJ/6-311++G(d,p) level of theory, match the experimental values better than M06-2X/6-311++G(d,p). The C constant calculated with the M06-2X/6-311++G(d,p) level of theory is, however, slightly closer to the experimental result, than the one from the B3LYP-D3BJ calculations. Other calculated parameters such as dipole moment components and centrifugal

distortion constants are similar for the two levels of theory.

Table 6.3: *Experimental and calculated molecular parameters for pulegone cluster with one water molecule (The experimental parameters of Chair 1-water a cluster were determined by fitting the internal rotation of methyl top 1 with XIAM). The observed rotational transitions are given using the following nomenclature: P branch $\triangle J = -1$, Q branch $\triangle J = 0$, R branch $\triangle J = +1$; a, b, and c correspond to the respective type of the rotational transitions.*

Parameter	Experimental	M06-2X*		B3LYP-D3BJ*	
		Chair 1-water a	Chair 1-water b	Chair 1-water a	Chair 1-water b
A | MHz	1289.8161 (16)	1356.52	966.72	1295.96	940.30
B | MHz	565.42463 (59)	568.05	674.96	566.34	677.32
C | MHz	467.25183 (44)	471.16	416.76	459.45	412.01
Δ_J | kHz	0.0501 (40)	0.05	0.08	0.05	0.40
Δ_{JK} | kHz	0.519 (23)	0.41	0.14	0.38	-0.77
Δ_K | kHz	-1.354 (89)	0.1	0.47	0.15	0.45
δ_J | kHz	0.0238 (27)	-0.01	0.02	-0.13	0.11
V_3 | kJ/mol	2.01013 (38)	1.93‡			
$\measuredangle\delta$ | rad	1.96917 (37)	1.89	-	-	-
$\measuredangle\varepsilon$ | rad	2.86344 (21)	2.48	-	-	-
D_{pi2J}** | MHz	-0.03842 (72)	-	-	-	-
D_{pi2K}** | MHz	0.280 (18)	-	-	-	-
μ_a | D	^aR	2.6	2.5	-2.6	2.9
μ_b | D	^bR, ^bQ	1.7	-2.6	1.8	-2.9
μ_b | D	^cR	0.3	-0.2	-0.5	-0.3
ΔE | kJ/mol		0	2.0	0	2.3
σ ◇ | kHz	9.83				
N †	84				

* 6-311++G(d,p)
** Empirical internal rotation (overall rotation distortion operator).
◇ RMS deviation of the fit.
† Number of fitted transitions.
‡ B3LYP/6-311G level of theory.

The energy difference between the two clusters is small, which means that in principle both of them can be observed experimentally. The fact that only Chair 1-water a was observed in the rotational spectrum may be due to a possible low interconversion barrier between the two clusters.

Since top 2 of pulegone is involved in the secondary interaction with water in the Chair 1-water a cluster, its internal rotation is hindered, while the internal rotation of top 1 remains feasible. The calculated (B3LYP/6-311G level of theory) V_3 barrier for top 1 is low enough (1.93 kJ/mol, see Table 6.3) to give rise to the splitting due to internal rotation. Because the internal dynamics from only one top is expected to be observed in the spectrum, the splitting should result in doublets (labelled as A and E states within the local mode picture) instead of multiplets. Indeed, several A and E internal rotation states (84 in total) could be fitted with

XIAM for the Chair 1-water a cluster (Table C.6). Some examples of the observed splitting pattern are given in Figure 6.9. The results for the internal rotation are given in Table 6.3. The experimentally determined V_3 barrier is 2.01013(38) kJ/mol, and thus de facto identical to the value for the Chair 1. This shows that top 1 indeed remains unaffacted by the addition of water, as was concluded from the calculated structure.

The SNR for the Chair 1–water a cluster was not sufficient (15:1) to observe any isotopically substituted species in natural abundance and to determine the exact structure of the cluster experimentally, so that we restrict this study to a structure identification via comparison with the calculated molecular parameters.

6.5 Summary

Two low-energy conformers of pulegone, including the lowest energy one, which was reported previously[5], were studied extensively with rotational spectroscopy. Both of them show splittings in the broadband spectrum due to the internal rotation of two inequivalent methyl tops attached to an sp^2-hybridized carbon atom. The structure of the lowest energy conformer, Chair 1, was determined experimentally, since the ^{13}C-monosubstituted isotopologues could be observed in natural abundance. The internal dynamics is feasible even when Chair 1 forms a stable cluster with one water molecule. However, in this case only one of the two methyl tops can rotate freely, while the other one is involved in the secondary interactions with the oxygen of water. The pulegone-water cluster reported here is of particular interest, since pulegone is largely water insoluble. Such a study helps to better understand the intermolecular interactions of a hydrophobic molecule with water. The cluster formation is stabilized here through dispersion interactions of the oxygen of water with the C-H groups of pulegone, and the strong hydrogen bond between the keto-group of pulegone and the oxygen of water. Additionally, an unambiguous differentiation of the enantiomers of the lowest energy conformer was carried out by applying the M3WM technique. This approach can be useful for future studies on pulegone in complex mixtures, such as essential oils, to gain insights into their enantiomeric composition. Overall, this study can be viewed as an example of a detailed analysis of a molecule with rich internal dynamics.

Bibliography

[1] K. H. Can Başer and G. Buchbauer, editors. *Handbook of ESSENTIAL OILS. Science,Technology and Applications.* CRC Press, 2010.

[2] W. Engel. In Vivo Studies on the Metabolism of the Monoterpene Pulegone in Humans Using the Metabolism of Ingestion-Correlated Amounts (MICA) Approach: Explanation for the Toxicity Differences between (S)-(–)- and (R)-(+)-Pulegone. *J. Agric. Food Chem.*, 51(22):6589–6597, 2003.

[3] W. P. Gordon, A. C. Huitric, C. L. Seth, R. H. McClanahan, and S. D. Nelson. The metabolism of the abortifacient terpene, (R)-(+)-pulegone, to a proximate toxin, menthofuran. *Drug Metab. Dispos.*, 15(5):589–594, 1987.

[4] C. Guo, R. D. Shah, R. K. Dukor, T. B. Freedman, X. Cao, and L. A. Nafie. Fourier transform vibrational circular dichroism from 800 to 10,000 cm^{-1}: Near-IR-VCD spectral standards for terpenes and related molecules. *Vib. Spectrosc.*, 42(2):254 – 272, 2006.

[5] J. R. Avilés-Moreno, E. U. Horno, F. P. Ureña, and J. J. López-González. IR–Raman–VCD study of R-(+)-Pulegone: Influence of the solvent. *Spectrochim. Acta Part A*, 79(4):767 – 776, 2011.

[6] E. Debie, P. Bultinck, W. Herrebout, and B. van der Veken. Solvent effects on IR and VCD spectra of natural products: an experimental and theoretical VCD study of pulegone. *Phys. Chem. Chem. Phys.*, 10:3498–3508, 2008.

[7] V. P. Nicu, E. Debie, W. Herrebout, B. Van der Veken, P. Bultinck, and E. J. Baerends. A VCD robust mode analysis of induced chirality: The case of pulegone in chloroform. *Chirality*, 21(1E):E287–E297, 2009.

[8] D. R. Farley and V. Howland. The natural variation of the pulegone content in various oils of peppermint. *J. Sci. Food Agr*, 31:1143–1151, 11 1980.

[9] C. Pérez, A. Krin, A. Steber, J. López, Z. Kisiel, and M. Schnell. Wetting Camphor: Multi-Isotopic Substitution Identifies the Complementary Roles of Hydrogen Bonding and Dispersive Forces. *J. Phys. Chem. Lett.*, 7:154–160, 12 2015.

[10] S. Blanco, P. Pinacho, and J. C. López. Hydrogen-Bond Cooperativity in Formamide2–Water: A Model for Water-Mediated Interactions. *Angew. Chem. Int. Ed.*, 55(32):9331–9335, 2016.

[11] G. G. Brown, B. C. Dian, K. O. Douglass, S. M. Geyer, S. T. Shipman, and B. H. Pate. A broadband Fourier transform microwave spectrometer based on chirped pulse excitation. *Rev. Sci. Instrum.*, 79(5):053103, 2008.

[12] D. Schmitz, V. A. Shubert, T. Betz, and M. Schnell. Multi-resonance effects within a single chirp in broadband rotational spectroscopy: The rapid adiabatic passage regime for benzonitrile. *J. Mol. Spectrosc.*, 280:77–84, 2012.

[13] D. Plusquellic. JB95. available at http://www.nist.gov/pml/electromagnetics/grp05/jb95.cfm.

[14] C. M. Western. PGOPHER: A program for simulating rotational, vibrational and electronic spectra. *J. Quant. Spectrosc. Ra.*, 186:221 – 242, 2017.

[15] H. M. Pickett. The Fitting and Prediction of Vibration-Rotation Spectra with Spin Interactions. *J. Mol. Spectrosc.*, 148:371–377, 1991.

[16] Z. Kisiel. Assignment and Analysis of Complex Rotational Spectra. In J. Demaison, K. Sarka, and E. A. Cohen, editors, *Spectroscopy from Space*, volume 20, pages 91–106. Springer, Dordrecht, 2001.

[17] J. Kraitchman. Determination of Molecular Structure from Microwave Spectroscopic Data. *Am. J. Phys.*, 21(1):17–24, 1953.

[18] Z. Kisiel. Least-squares mass-dependence molecular structures for selected weakly bound intermolecular clusters. *J. Mol. Spectrosc.*, 218(1):58 – 67, 2003.

[19] H. Hartwig and H. Dreizler. The Microwave Spectrum of trans-2,3-Dimethyloxirane in Torsional Excited States. *Z. Naturforsch.*, 51a:923–932, 1996.

[20] M. J. Frisch, G. W. Trucks, H. B. Schlegel, G. E. Scuseria, M. A. Robb, J. R. Cheeseman, G. Scalmani, V. Barone, B. Mennucci, G. A. Petersson, H. Nakatsuji, M. Caricato, X. Li, H. P. Hratchian, A. F. Izmaylov, J. Bloino, G. Zheng, J. L. Sonnenberg, M. Hada, M. Ehara, K. Toyota, R. Fukuda, J. Hasegawa, M. Ishida, T. Nakajima, Y. Honda, O. Kitao, H. Nakai, T. Vreven, J. A. Montgomery, J. E. Peralta, F. Ogliaro, M. Bearpark, J. J. Heyd, E. Brothers, K. N. Kudin, V. N. Staroverov, R. Kobayashi, J. Normand, K. Raghavachari, A. Rendell, J. C. Burant, S. S. Iyengar, J. Tomasi, M. Cossi, N. Rega, J. M. Millam, M. Klene, J. E. Knox, J. B. Cross, V. Bakken, C. Adamo, J. Jaramillo, R. Gomperts, R. E. Stratmann, O. Yazyev, A. J. Austin, R. Cammi, C. Pomelli, J. W. Ochterski, R. L. Martin, K. Morokuma, V. G. Zakrzewski, G. A. Voth, P. Salvador, J. J. Dannenberg, S. Dapprich, A. D. Daniels, O. Farkas, J. B. Foresman, J. V. Ortiz, J. Cioslowski, and D. J. Fox. Gaussian 09, 2009.

[21] D. Schmitz, V. A. Shubert, T. Betz, and M. Schnell. Exploring the conformational landscape of menthol, menthone, and isomenthone: a microwave study. *Front. Chem.*, 3(15):1–15, 2015.

[22] B. S. Ray. Über die Eigenwerte des asymmetrischen Kreisels. *Z. Phys.*, 78(1):74–91, Jan 1932.

[23] D. Schmitz, V. A. Shubert, B. M. Giuliano, and M. Schnell. The broadband microwave spectra of the

monoterpenoids thymol and carvacrol: Conformational landscape and internal dynamics. *J. Chem. Phys.*, 141(3):034304, 2014.

[24] C. Medcraft and M. Schnell. A Comparative Study of Two Bicyclic Ethers, Eucalyptol and 1,4-Cineole, by Broadband Rotational Spectroscopy. *Z. Phys. Chem.*, 230, 01 2015.

[25] J. M. Vacherand, B. P. V. Eijck, J. Burie, and J. Demaison. The rotational spectrum of acetone: Internal rotation and centrifugal distortion analysis. *J. Mol. Spectrosc.*, 118(2):355 – 362, 1986.

[26] H. Hartwig. XIAM Manual, 1996. available at http://www.ifpan.edu.pl/ kisiel/introt/xiam/xiam-v25.txt.

[27] M. O'Neil, editor. *The Merck Index - An Encyclopedia of Chemicals, Drugs, and Biologicals*. RSC Publishing, 2013.

[28] T.-W. Moon, J. W. Lee, K.-H. Jhee, K.-W. Khang, H.-S. Jeong, S.-A. Yang, and H.-J. Kim. Supramolecular Encapsulation of Pulegone from Oriental Herb, *Schizonepeta tenuifolia* Briquet by β and γ-Cyclodextrins. *Bull. Korean. Chem. Soc.*, 29(8):1579–1582, 2008.

7

Conformational analysis and internal dynamics of menthyl acetate

7.1 Introduction

The characterization of essential oil components with broadband rotational spectroscopy is one of the key points of this thesis. An overview of the rotational spectroscopy study on peppermint oil and thyme oil is given in Chapters 4 and 5. Chapter 6 is devoted to the analysis of one of the peppermint oil constituents, the monoterpene pulegone. In the present chapter the results of our study on the other component of peppermint oil, menthyl acetate, will be summarized.

Menthyl acetate is a chiral molecule with three stereogenic centers and thus eight stereoisomers. Its diastereomeric forms are: menthyl acetate, isomenthyl acetate, neomenthyl acetate, and neoisomenthyl acetate. Like other essential oil components, menthyl acetate has a wide application range. It is used in many consumer products such as toothpaste, tobacco, chewing gums etc.[1]. It is also interesting from a pharmaceutical point of view. For instance, it was reported to be one of the peppermint oil constituents which block the enzyme arylamine N-acetyltransferase (NAT)[2]. This enzyme is known to be involved in blood vessel formation and inflammation, two processes which accompany carcinogenesis.

No rotational spectroscopy study on menthyl acetate was reported so far. The aim of the present work was to analyze this biologically relevant molecule directly in peppermint oil. However, the observed rotational line intensity of this component was low (signal-to-noise ratio, SNR, 5:1) in the recorded peppermint oil broadband spectrum (Chapter 4). The reason might be a low relative amount of menthyl acetate in the used sample. According to the literature, the abundance of menthyl acetate in peppermint oil can range from 2.8 %[3] to

manuscript in preparation (experimental: 90%, data analysis: 60%)

15.6 %[4] depending on the origin of the peppermint plant and the method of the oil extraction. Since no characterization of menthyl acetate could be performed in the oil, a separate measurement on a pure sample was carried out instead.

In this study menthyl acetate was explored both experimentally and theoretically. The conformational landscape of menthyl acetate and its diastereomers was analyzed using computational approach. The obtained results aided the assignment of two menthyl acetate conformers in the broadband spectrum. Internal dynamics of the lowest energy conformer was studied, and the internal rotation barrier of one of its methyl tops (part of the acetate group) was determined experimentally. Additionally, chirality-sensitive microwave three-wave mixing (M3WM) experiments were performed. Theoretical background of this technique is explained in Chapter 2. Two M3WM cycles were determined for the lowest energy conformer of menthyl acetate. The results can be used for the upcoming chiral analysis of this component in peppermint oil.

7.2 Experimental techniques

Menthyl acetate ([5-methyl-2-propan-2-yl-cyclohexyl] acetate) was purchased from Sigma-Aldrich (97 % purity) and used without further purification. The sample is liquid at room temperature. In order to create sufficient vapor pressure, the sample was heated to 87 °C prior to being supersonically expanded into the vacuum chamber using neon (1 bar backing pressure) as a carrier gas.

The rotational broadband spectrum of menthyl acetate was measured on the chirped-pulse Fourier transform microwave (CP-FTMW) spectrometer COMPACT[5;6] in Hamburg in the frequency range from 2-8 GHz (2.3 million acquisitions). More details regrading the experimental set-up are given in Chapter 2. The assigned transitions were fitted to rotational Hamiltonian using the software PGOPHER[7], employing the I^r representation. Internal dynamics of the lowest energy conformer of menthyl acetate were analyzed with the program XIAM[8;9] to experimentally determine the internal rotation barrier of one of its methyl tops.

7.3 Quantum-chemical calculations

Several conformers of menthyl acetate and its diastereomers were expected to be observed in the spectrum due to the structural properties of this molecule. To aid the assignment of the spectrum, quantum-chemical calculations were performed. For this purpose, relaxed two-dimensional potential energy surface scans (2D-PES) using program Gaussian[10] were calculated at the B3LYP/6-31g level of theory (see Section 7.4.1 for more details). The lowest energy structures obtained from the PES were re-optimized in the second step on the B3LYP-D3BJ level of theory, including Grimme's empirical dispersion correction and the 6-311++g(d,p) basis set. Frequency calculations were carried out to ensure that the structures were indeed true minima of the PES and to obtain their zero-point corrected relative energies.

7.4 Results and Discussion

7.4.1 Conformational analysis

Menthyl acetate belongs to the group of molecules known as monoterpenes. It is the acetate ester of menthol and thus has the same cyclohexane core structure. The difference between these two molecules is an acetate group instead of a hydroxyl group attached to C1 (see Figure 7.1) of menthyl acetate.

Like menthol, menthyl acetate has three stereogenic centres. This gives rise to eight different stereoisomers, or four enantiomeric pairs. The resulting four diastereomers are menthyl acetate (m), isomenthyl acetate (iso), neomenthyl acetate (neo), and neoisomenthyl acetate (neoiso). They are depicted in Figure 7.1.

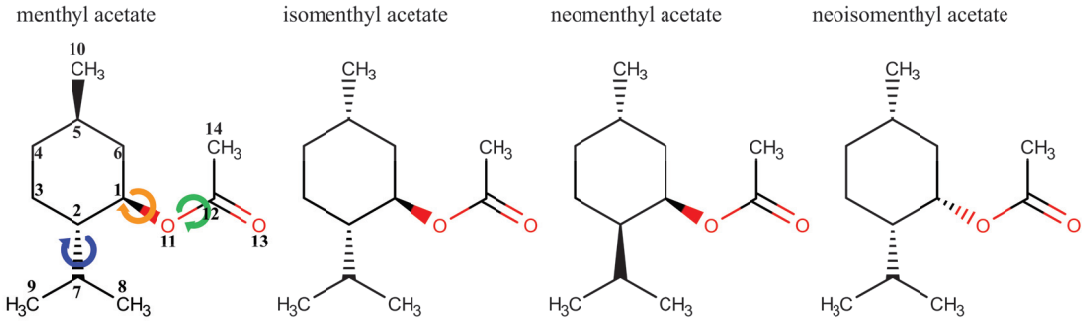

Figure 7.1: *Structures of the different stereoisomers of menthyl acetate: (–)-menthyl acetate, (–)-isomenthyl acetate, (–)-neomenthyl acetate,(–)-neoisomenthyl acetate. For each diastereomer, a two-dimensional potential energy surface (2D-PES) scan involving the dihedrals C9–C7–C2–C1 (rotation around C7–C2 bond, depicted as blue arrow) and C1–O11–C12–C14 (green arrow) was performed. An additional 2D-PES scan was done for the rotation around the dihedrals C9–C7–C2–C1 and C6–C1–O11–C12 (orange arrow).*

Because of the structural flexibility, each diastereomer can be present in different conformational forms. Since no information on the relative amount of menthyl acetate diastereomers in the purchased sample was provided by the supplier, an extensive conformational search was necessary to determine all possible lowest energy conformers of the respective diastereomers. Additionally, because cyclohexane is the core structure of this component, it can exhibit two chair conformations with the substituents being oriented axially or equatorially (see Figure 7.2). In the following, structures with the acetate group oriented axially with respect to the cyclohexane ring will be called "axial" (ax). Consequently, structures with the equatorially-oriented acetate group will be referred to as "equatorial" (eq).

In order to find the lowest energy conformers, relaxed PES scans as implemented in Gaussian were performed. As a first step, axial and equatorial conformers of each diastereomer were optimized at the B3LYP-D3BJ/6-311++g(d,p) level of theory. Next, a 2D-PES scan for each of the eight resulting structures was calculated (B3LYP/6-31g level of theory). During

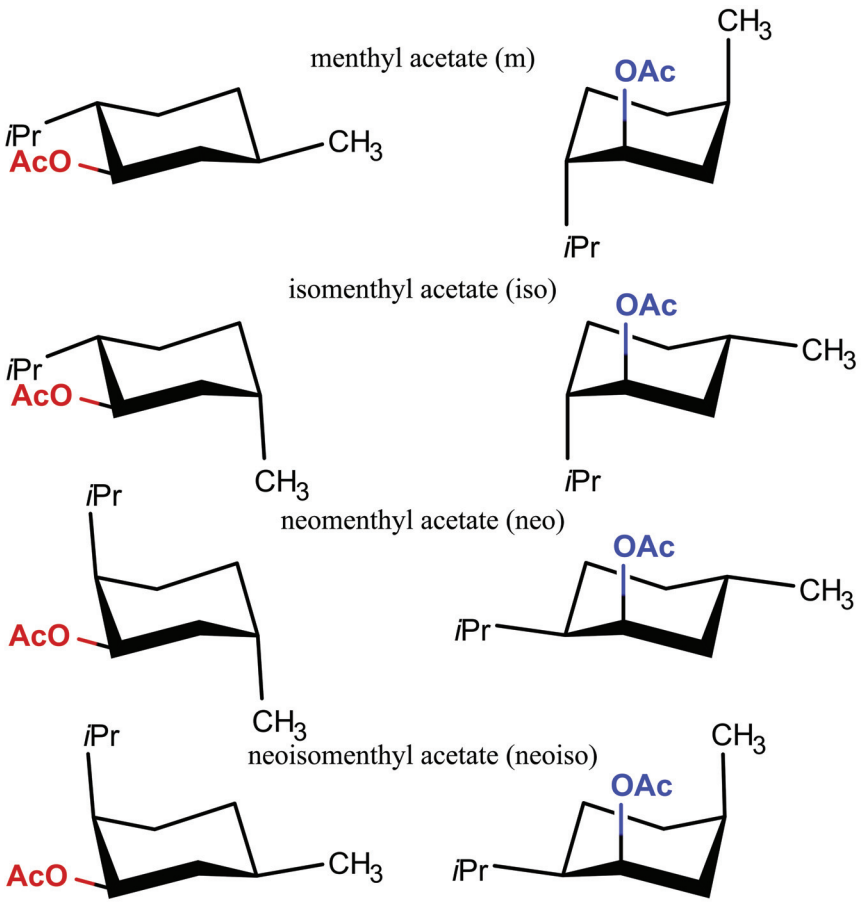

Figure 7.2: *Two chair conformations of menthyl acetate diastereomers: the substituents, methyl group, isopropyl group (iPr) and acetate group (OAc), are oriented either equatorially or axially. For a better visibility, the respective hydrogens are not shown here. In the following, labelling of the conformers as "axial" or "equatorial" will indicate the orientation of the acetate group (highlighted here in red and blue) with respect to the cyclohexane ring.*

the scans, the dihedrals of the isopropyl and the acetate groups were rotated in steps of 10 °. Since the acetate group has two rotatable dihedrals (see Figure 7.1), two separate scans involving the isopropyl group (C9–C7–C2–C1) and one of the acetate group dihedrals (either C1–O11–C12–C14 or C6–C1–O11–C12) were performed. Lowest energy structures resulting from the scans involving the rotation around the O11–C12 bond will be labelled with I. The results of the scans, where rotation around C1–O11 took place, are indicated as II. In total, four 2D-PES scans were performed for each of the menthyl acetate diastereomers. The procedure is schematically given in Figure 7.3. The obtained lowest energy structures were subsequently re-optimized at the B3LYP-D3BJ/6-311++g(d,p) level of theory. Overall, 51 different lowest energy conformers were determined for menthyl acetate and its diastereomers with the total zero-point corrected relative energy up to 50 kJ/mol. Here, only the results for the conformers with the relative energies up to 15 kJ/mol will be considered.

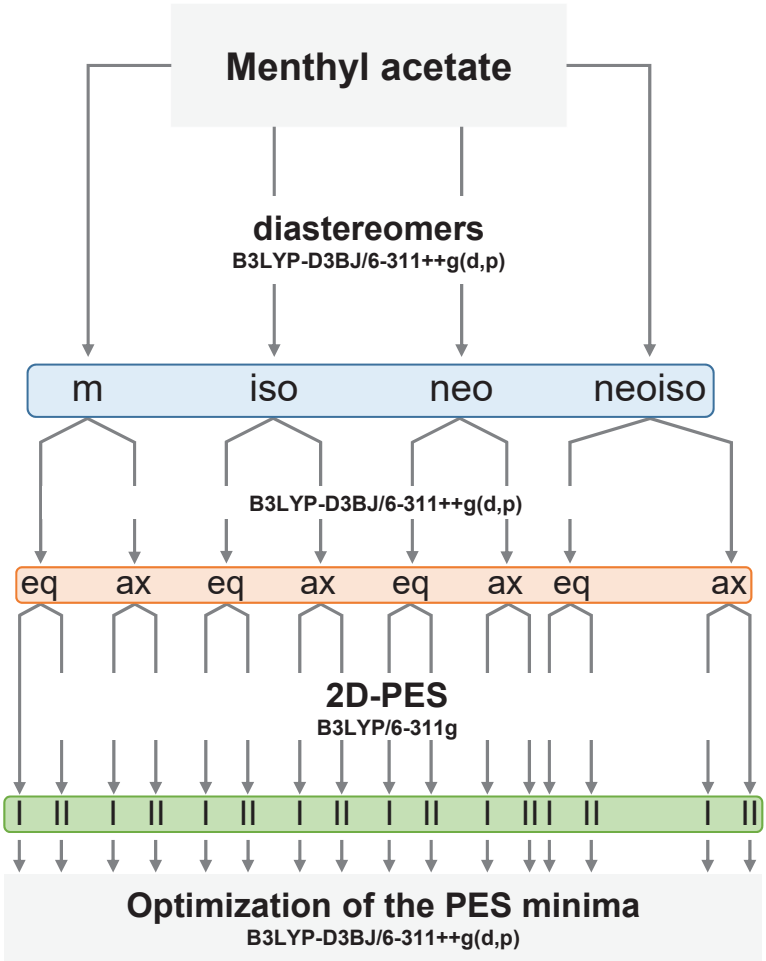

Figure 7.3: *A scheme of the applied procedure for determining the lowest energy conformers of menthyl acetate and its diastereomers. First, starting structures of menthyl acetate (m), isomenthyl acetate (iso), neomenthyl acetate (neo) and neoisomenthyl acetate (neoiso) were optimized at the B3LYP-D3BJ/6-311++g(d,p) level of theory. Next, two chair configurations with the acetate group being oriented equatorially (eq) or axially (ax) with respect to the cyclohexane ring were calculated using the same level of theory. A two-dimensional potential energy surface scan (2D-PES) was performed for each conformer as a function of the isopropyl and acetyl dihedral angles. Since the acetate group has two rotatable dihedral angles, two scans using either one dihedral (I: C1–O11–C12–C14) or the other one (II: C6–C1–O11–C12) were calculated per conformer. The minima of the PES were then optimized at the B3LYP-D3BJ/6-311++g(d,p) level of theory.*

The results are summarized in Table 7.1. The labelling of the conformers is as follows. The labels **m** (menthyl acetate), **iso** (isomenthyl acetate), **neo** (neomenthyl acetate) and **neoiso** (neoisomenthyl acetate) indicate which diastereomer the respective conformer belongs to. The conformer is designated as axial (**ax**) or equatorial (**eq**), regarding the orientation of the acetate group. Numbers **1,2,3** indicate the hierarchic order of the conformers belonging to the same diastereomer with respect to their zero-point corrected relative energy. Finally,

numbers **I** and **II** specify which of the dihedrals of the acetate group was changed during the scan.

Table 7.1: *Calculated (B3LYP-D3BJ/6-311++g(d,p)) lowest energy conformers of the diastereomers menthyl acetate (m), isomenthyl acetate (iso), neomenthyl acetate (neo) and neoisomenthyl acetate (neoiso) with a relative energy cut-off of 15 kJ/mol. The orientation of the acetate group, being either equatorial (eq) or axial (ax), is given. Numbers 1,2,3... indicate the hierarchy of the respective conformer among the other conformers of the same diastereomer regarding its zero-point corrected relative energy. Numbers I, II refer to the rotation around one of the dihedrals of the acetate group: I: C1–O11–C12–C14, II: C6–C1–O11–C12. Conformers are listed according to the total zero-point corrected relative energy. Only the magnitudes of the respective dipole moment components are provided.*

Conformer	A (MHz)	B (MHz)	C (MHz)	μ_a [a]	μ_b [a]	μ_c [a]	ΔE [b] (kJ/mol)
m_eq_1_II	698.03	565.19	356.65	0.67	0.96	1.63	0
neo_ax_1_I/II	674.58	617.22	382.69	0.4	1.36	1.65	1.1
m_eq_2_II	804.83	536.57	372.59	0.5	1.19	1.51	4.1
neo_ax_2_I/II	741.25	588.16	411.07	0.73	1.33	1.6	5.8
neo_ax_3_I/II	663.29	625.24	384.68	0.78	1.13	1.57	6.6
iso_eq_1_I	734.86	576.64	389.05	0.82	0.82	1.69	6.7
iso_ax_1_I	785.05	508.68	389.96	1.16	0.7	1.67	8.7
neoiso_ax_1_I/II	726.12	639.41	415.14	1.07	1.14	1.46	9.4
m_eq_3_I/II	744.38	571.45	383.86	0.13	0.49	1.62	10.5
iso_eq_2_I	816.81	563.73	405.69	0.6	1.19	1.56	10.8
m_eq_4_II	732.01	562.8	347.2	0.72	1.23	1.49	10.9
m_eq_5_II	703.37	566.85	347.68	0.51	1.07	1.47	11.4
neoiso_ax_2_I/II	705.49	680.41	451.41	0.84	1.43	1.4	14.2
neoiso_ax_3_I/II	760.56	603.53	422.66	1.21	0.85	1.41	14.5

[a] $D \approx 3.3356 * 10^{-30} C \cdot m$

[b] Zero-point corrected relative energy

The menthyl acetate conformer m_eq_1_II is the global minimum (Table 7.1). For some of the conformers, the same structures were obtained with the PES scans I and II, as it is e.g. the case for the predicted second lowest energy compound, neo_ax_1_I/II. This might be because the entire structure was re-optimized during each step of the relaxed scan, resulting in the same minimum structure in some particular cases (see Table 7.1). PES scans involving the structures listed in Table 7.1 are given in Figure 7.4. The respective optimized structures are presented in Figures 7.5 and D.2 - D.4.

In our previous broadband studies, conformers with relative energies up to 6 kJ/mol were observed experimentally[11], when neon was used as a carrier gas. Based on this result, m_eq_1_II, neo_ax_1_I/II, m_eq_2_II and neo_ax_2_I/II should be present in the broadband spectrum, due to their calculated relative energies (Table 7.1). It has to be pointed out that not only the relative energies, but also the interconversion barrier between the conformers is important in this context.

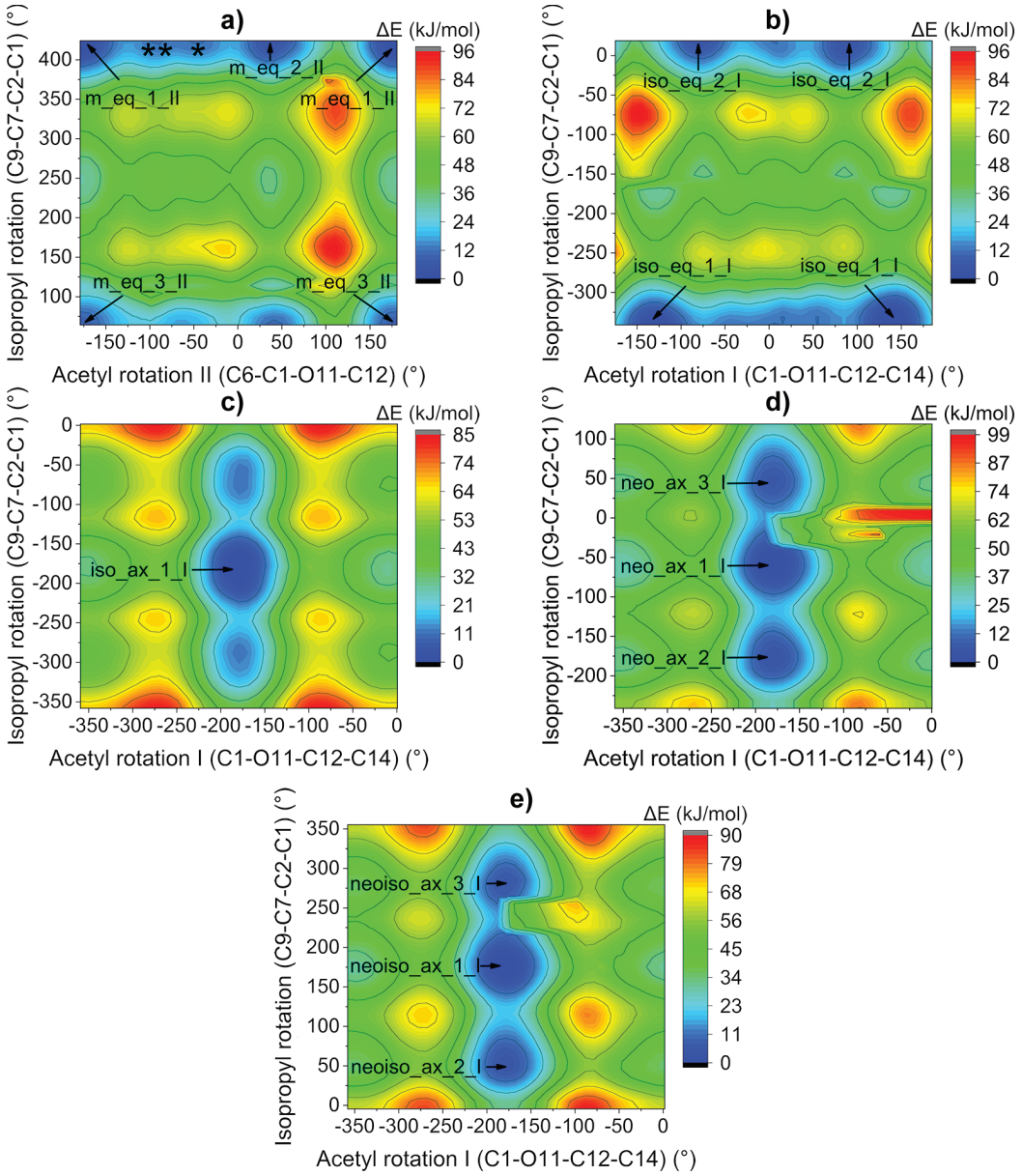

Figure 7.4: *Potential energy surface (PES) scan (B3LYP/6-31g level of theory) of a) menthyl acetate (asterisks ∗ and ∗∗ refer to the conformers m_eq_4_II and m_eq_5_II, respectively), b)-c) isomenthyl acetate, d) neomenthyl acetate and e) neoisomenthyl acetate as a function of the isopropyl and the acetyl dihedral angles (see Figure 7.2). Minima of the PES are labelled according to the nomenclature explained in the text. Here only minima with the zero-point corrected relative energy up to 15 kJ/mol, which are listed in Table 7.1, are given, while the others are not highlighted.*

Although the comformers m_eq_1_II and m_eq_2_II differ only in the orientation of the isopropyl group, their calculated (B3LYP-D3BJ/6-311++G(d,p) level of theory) interconversion barrier is around 30 kJ/mol (see Figure D.1), meaning that no relaxation of these two menthyl acetate conformers into each other is expected.

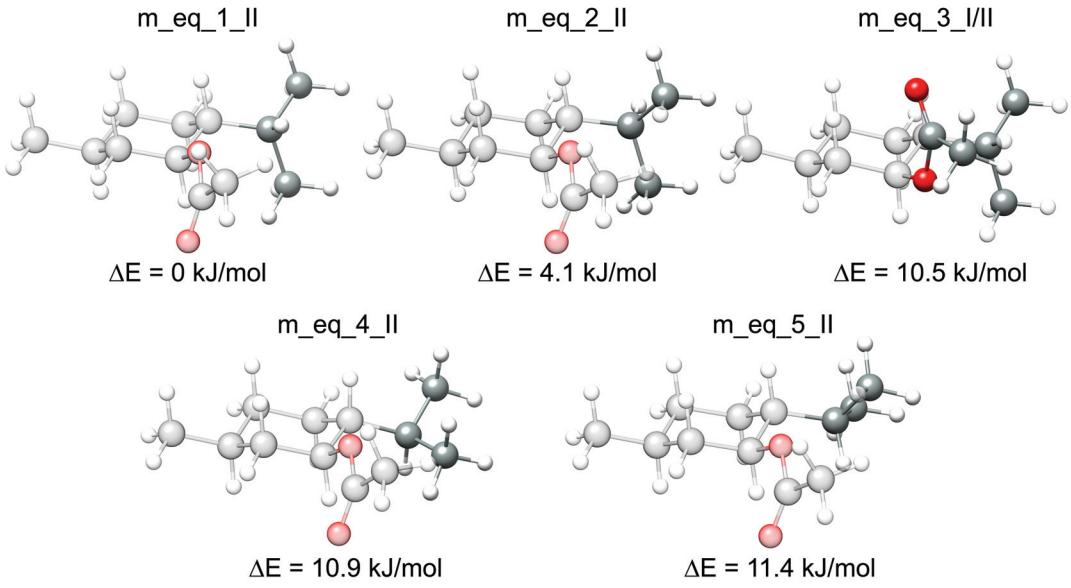

Figure 7.5: *Lowest energy conformers of menthyl acetate, as listed in Table 7.1. For better visibility, only the differences in the orientation of the respective substituents are highlighted, while the rest of the structures is kept transparent. Zero-point corrected relative energies are given.*

7.4.2 Broadband spectrum

A small section of the recorded menthyl acetate broadband spectrum is presented in Figure 7.6. According to the conformational analysis discussed in Section 7.4.1, the m_eq_1_II conformer is the global minimum. For this reason, it could be assumed that the most intense lines in the spectrum belong to this conformer. Guided by the computational results, 142 distinct rotational lines with an overall standard deviation of 7.46 kHz could be assigned to the conformer m_eq_1_II (Table D.1). The SNR of this component was around 200:1 for the strongest lines. A comparison between the calculated (B3LYP-D3BJ/6-311++g(d,p)) and the experimentally determined rotational parameters is given in Table 7.2. Additionally, the m_eq_1_II conformer was optimized using second-order Møller–Plesset perturbation theory (MP2) with the same basis set (see Table 7.2).

The calculated rotational constants A, B and C match the experimental ones well for both DFT (B3LYP-D3BJ/6-311++g(d,p)) and ab initio (MP2/6-311++g(d,p)) levels of theory (Table 7.2). All three calculated dipole moment components of m_eq_1_II are distinct from zero, meaning that a-, b- and c-type transitions should be observed experimentally, which is the case. The most intense transitions were c-type, which is in agreement with the calculations, since μ_c is predicted to be the strongest dipole moment component (see Table 7.2). There is no good agreement with the rotational parameters of the other conformers listed in Table 7.1, which corroborates the assumption that the observed species is m_eq_1_II.

Table 7.2: *Comparison between computationally determined rotational parameters of m_eq_1_II and m_eq_2_II and those obtained experimentally. The absolute values for the dipole moment components μ_a, μ_b and μ_c are given. Information about, whether the respective type of rotational transitions was observed (y) or not (n) is provided.*

	m_eq_1_II			**m_eq_2_II**		
Parameter	Experimental	B3LYP-D3BJ[a]	MP2[a]	Experimental	B3LYP-D3BJ[a]	MP2[a]
A | MHz	687.63760(38)	698.03	697.80	799.08195(49)	804.83	805.30
B | MHz	577.21406(15)	565.19	580.94	543.29356(15)	536.57	545.17
C | MHz	357.20359(12)	356.65	359.33	373.75452(13)	372.59	376.06
ΔJK | kHz	0.0705(80)			–		
ΔK | kHz	0.213(16)			0.203(17)		
μ_a | D[b]	*y*	0.67	0.36	*y*	0.50	0.36
μ_b | D	*y*	0.96	0.89	*y*	1.19	1.07
μ_c | D	*y*	1.63	1.48	*y*	1.51	1.31
ΔE | kJ/mol [c]		0	0		4.1	3.0
σ [d] | kHz	7.46			8.41		
N [e] | kHz	142			73		

[a] $6-311++G(d,p)$
[b] $D \approx 3.3356 * 10^{-30} C \cdot m$
[c] Zero-point corrected relative energy
[d] RMS deviation of the fit
[e] Number of fitted transitions

A characteristic pattern could be observed in the spectrum of m_eq_1_II for some of its transitions with J-values > 3. The pattern consists of four rotational lines. The two lines in the middle are a-type transitions. They are well separated (up to 5 MHz) and have very similar intensities. The other two lines, on the right and on the left side from the a-type transitions respectively, are of b-type. The b-type transitions, are about twice as strong as the a-type ones in the middle. An example of such a "baab" pattern is given in Figure 7.6. Using the experimentally obtained rotational parameters of m_eq_1_II, this lowest energy conformer of menthyl acetate could be subsequently assigned in the previously measured peppermint oil broadband spectrum (see Chapter 4).

Once the kinetically most stable conformer was identified, an extensive search for further low energy conformers (neo_ax_1_I/II, m_eq_2_II and neo_ax_2_I/II) was performed. The recorded spectrum is quite dense, which makes the assignment of the other possible conformers challenging. One of the approaches to aid the assignment was to identify similar patterns of four rotational lines as described above. This approach has proven to be beneficial, and 73 lines belonging to another component could be assigned in the spectrum (see Figure 7.6 and Table D.2). Additional spectral pattern ("bccb") was observed for this second component. Such pattern is presented in Figure 7.6.

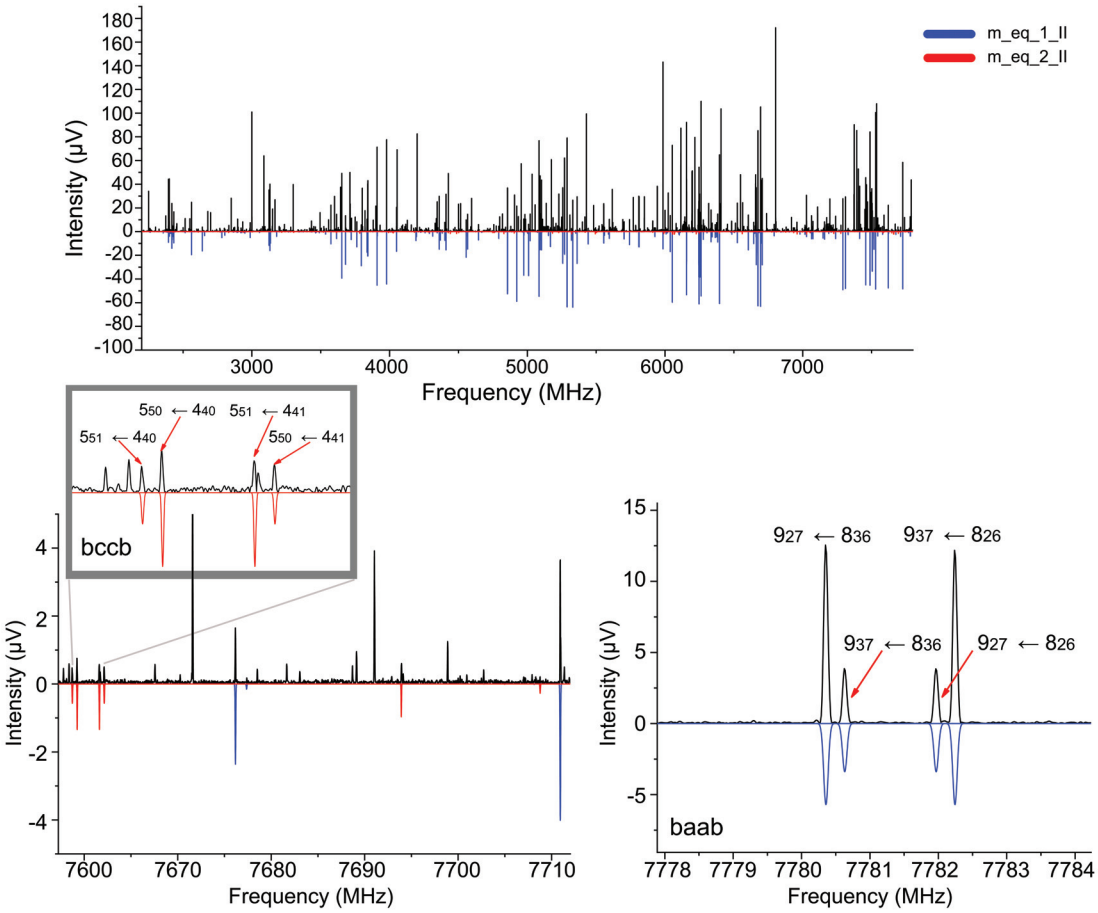

Figure 7.6: *The menthyl acetate broadband spectrum in the frequency range 2-8 GHz (2.3 million acquisitions, neon as a carrier gas). The upper (black) trace represents the experimental result, while the lower (red and blue) traces are the simulations based on the fitted parameters for m_eq_1_II and m_eq_2_II conformers of menthyl acetate. Note that m_eq_2_II is significantly weaker (SNR 5:1) in the present spectrum compared to m_eq_1_II (SNR 200:1). Examples for the experimentally observed patterns ("baab" and "bccb") are presented. The transitions are labelled according to the $J_{K_aK_c}$ nomenclature explained in Chapter 2.*

The experimental rotational parameters of the second identified component are summarized in Table 7.2. A comparison with the calculated rotational constants (B3LYP-D3BJ/6-311++g(d,p)) leads to an assumption that this species is the second lowest conformer of menthyl acetate, m_eq_2_II. The intensity of m_eq_2_II was lower (SNR 5:1) in the spectrum compared to m_eq_1_II. This result is expected, since the calculated energy difference between these conformers is about 4 kJ/mol (3 kJ/mol according to the MP2 calculations). The fact that both m_eq_1_II and m_eq_2_II were observed experimentally is consistent with the theoretical prediction (see Section 7.4.1). The observed SNR was not sufficient to experimentally determine the structures of m_eq_1_II and m_eq_2_II.

It is noticeable that neo_ax_1_I/II ($\Delta E = 1.1$ kJ/mol) could not be identified in the spectrum. This conformer belongs to the diastereomer neomenthyl acetate. Since the composition

of the present sample in terms of the different diastereomers is not known, it could be assumed that neomenthyl acetate is either not present, or its abundance is very low. This could also be the reason why the other neomenthyl acetate conformer, neo_ax_2_I/II, could not be assigned in the spectrum.

7.4.3 Internal rotation

Menthyl acetate has four methyl groups (Figure 7.1), which will be hereafter referred to as tops. The internal rotation of these methyl tops can result in observable splittings in the rotational spectrum. Because of the significantly higher intensity of m_eq_1_II in comparison to m_eq_2_II in the spectrum, only the internal dynamics of the m_eq_1_II conformer could be analyzed in detail.

Methyl top 1 includes C10 and is attached to an sp^3-hybridized carbon atom (Figure 7.1). In previous chapters, it was mentioned that the internal rotation barrier in such a case is expected to be too high to give rise to any observable fine structure. Indeed, the calculated (B3LYP/6-311g) internal rotation barrier of top 1 of m_eq_1_II is 12.5 kJ/mol.

Table 7.3: *Comparison of molecular parameters obtained with XIAM for the following components: n-butyl-, ethyl-, isoamyl-, and n-propyl-acetates, reported previously[12–15]. The experimentally determined V_3 barriers are highlighted.*

Parameters	*n*-Butyl acetate[13]	Ethyl acetate[12]	Isoamyl acetate[14]	*n*-Propyl acetate[15]
A | MHz	4894.9998(45)	8448.6787(97)	3279.9235(12)	5667.0873(20)
B | MHz	849.2464(11)	2094.03132(48)	711.5582(18)	1381.8194(92)
C | MHz	767.2614(11)	1733.52516(28)	689.7250(22)	1207.91173(70)
Δ_J | kHz	0.1251(13)	0.1727(16)	0.15753(67)	0.30668(61)
Δ_{JK} | kHz	-1.985(12)	1.376(12)	0.2849(42)	-1.1117(95)
Δ_K | kHz	21.63(94)	12.86(19)	3.986(21)	11.47(43)
V_3 | kJ/mol	**1.134323(96)**	**1.21548(28)**	**1.12393(16)**	**1.163985(67)**
$\measuredangle(i,a)$ | rad	60.4030(05)	43.0747(4)	60.2293(8)	52.8392(3)
$\measuredangle(i,b)$ | rad	30.4041(08)	46.9253(4)	30.7241(54)	37.7604(3)
$\measuredangle(i,c)$ | rad	83.6586(15)	[90.0000]	96.912(18)	84.2316(4)
D_{pi2J} [a] | kHz	80.38(21)	N/A[d]	61.55(16)	140.64(11)
D_{pi2-} [a] | kHz	42.410(86)	N/A[d]	32.68(47)	74.74(14)
σ [b] | kHz	12.7	2.9	17.0	4.7
N [c]	130	126	258	148

[a] empirical internal rotation (overall internal distortion operator)
[b] RMS deviation of the fit
[c] Number of fitted transitions
[d] Information not given in the respective reference

Methyl top 2, containing C14, is a part of an acetate group. Several studies reported before show that the V_3 internal rotation barrier of such a methyl top is commonly around 100 cm^{-1} or approximately 1 kJ/mol. Results of some previous internal rotation studies on acetates are summarized in Table 7.3. The calculated (B3LYP/6-311g) V_3 barrier for the methyl

top 2 of m_eq_1_II is about 0.9 kJ/mol, which is in agreement with the previous studies on similar molecular systems. Therefore, the internal rotation of top 2 should result in line splitting in our broadband spectrum.

Table 7.4: *Calculated and experimentally (XIAM) obtained parameters for the lowest energy conformer of menthyl acetate m_eq_1_II. The V_3 barrier due to the internal rotation of the methyl top 2 (including C14, see Figure 7.1) is highlighted.*

Parameters	Experimental	MP2[d]
A | MHz	687.09729(30)	697.80
B | MHz	577.21142(12)	580.94
C | MHz	357.148688(57)	359.33
Δ_{JK} | kHz	0.0695(31)	
Δ_K | kHz	0.2306(99)	
V_3 | kJ/mol	**1.1828960(70)**	**0.9**[e]
$\measuredangle(i,a)$ | rad	31.7065(11)	32.99
$\measuredangle(i,b)$ | rad	85.6334(85)	85.77
$\measuredangle(i,c)$ | rad	58.6661(25)	57.35
D_{pi2J} [a] | kHz	2.57(64)	
D_{pi2K} [a] | kHz	41.34(88)	
D_{pi2-} [a] | kHz	11.65(66)	
σ [b] | kHz	7.319	
N [c]	196	

[a] empirical internal rotation (overall internal distortion operator)
[b] RMS deviation of the fit
[c] Number of fitted transitions
[d] 6-311++g(d,p)
[e] Calculated at B3LYP/6-311g level of theory

The remaining two methyl tops, top 3 and 4 (containing C8 and C9 respectively), are parts of the isopropyl group. They are attached to the same sp^3-hybridized carbon atom C7 (Figure 7.1). Top 3 is located in the proximity of the acetate group. Due to the different chemical environments, the internal rotation barriers of the tops 3 and 4 are expected to be different. The computationally determined barriers of top 3 and of top 4 are, however, essentially the same, within the accuracy of calculation (11.6 kJ/mol vs. 12.0 kJ/mol, B3LYP/6-311G). This leads to the conclusion that the internal rotation of top 3 is not hindered by the intramolecular interaction with the oxygens of the acetate group (Figure 7.5). Because of the high calculated barriers, the internal rotation of tops 3 and 4 is not expected to give rise to any observable fine structure.

The splitting pattern represents doublets, as only top 2 is involved in the internal rotation. Based on the calculated frequencies obtained with the program XIAM, 196 rotational transitions belonging to A and E states could be assigned for m_eq_1_II (Table D.3). Small sections of the broadband spectrum presenting the results of the assignment for some transitions are given in Figure 7.7.

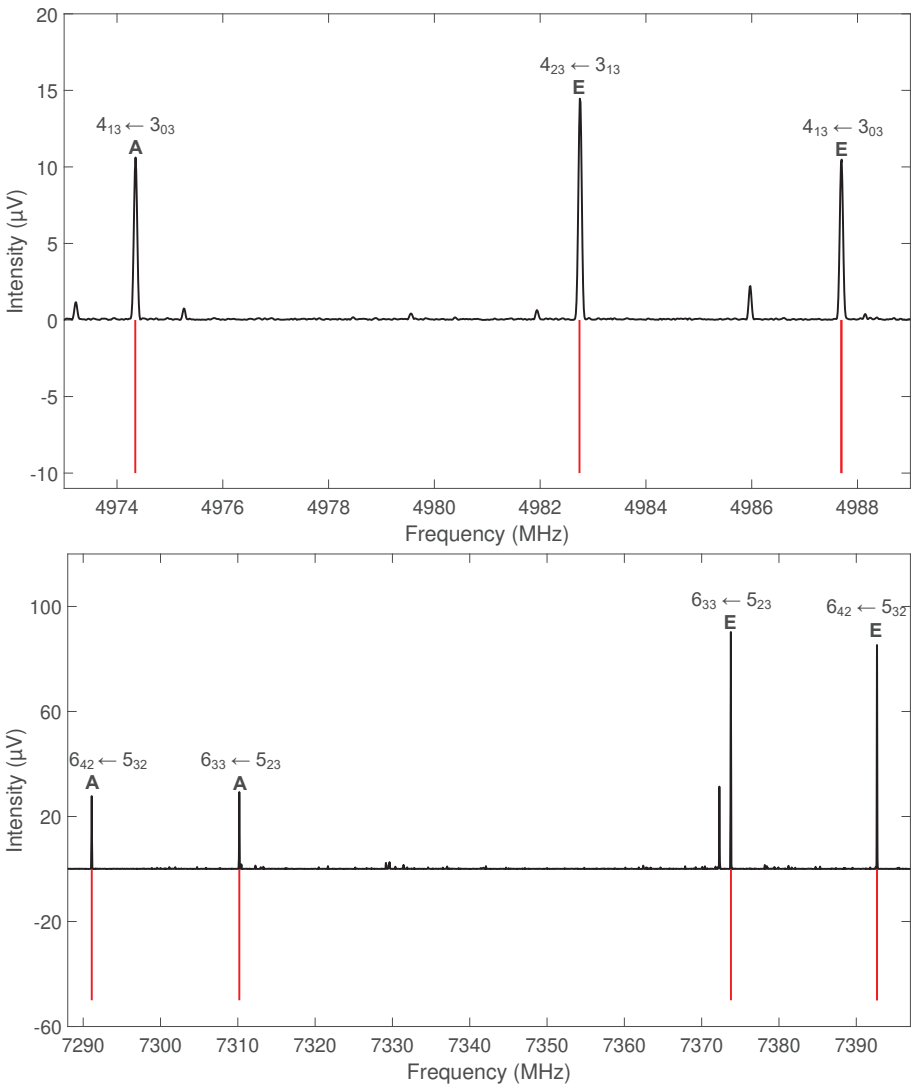

Figure 7.7: *Sections of the broadband rotational spectrum of menthyl acetate to illustrate the characteristic fine structure due to internal dynamics. In all parts, the upper traces (black) are the experimentally obtained spectra. The lower (red) traces are stick spectra (not taking into account specific intensity distributions) based on simulations using the fitted molecular constants for m_eq_1_II conformer of menthyl acetate and employing the program XIAM.*

The experimentally determined value for the V_3 barrier of top 2 is 1.1828960(70) kJ/mol. The calculated barrier hight of 0.9 kJ/mol is thus close to the experimental result. All parameters including experimentally determined angles between the internal rotation axis and the principal axes a, b and c, are given in Table 7.4. The calculated (MP2/6-311++g(d,p)) angles match the experimental ones well. This fact further corroborates the assignment of the strongest component in the spectrum to the calculated global minimum m_eq_1_II.

An overall comparison between the values for the internal rotation barrier of m_eq_1_II and of other acetates shows that they are indeed similar, around 1 kJ/mol (highlighted in

Tables 7.3 and 7.4), in spite of different chemical structures. This leads to a conclusion that the rest of the molecular structure does not have a significant impact on the acetyl methyl top rotation barrier as stated by Nguyen et. al in Ref. 16.

7.4.4 Microwave three-wave mixing

Since menthyl acetate belongs to the main constituents of peppermint oil, it is of interest to perform a M3WM experiment on it directly in the oil to further benchmark the technique. The M3WM could be successfully applied to menthone and isomenthone (see Chapter 4), the other components of peppermint oil. Including menthyl acetate in this analysis would allow us to have a more comprehensive chiral study of this essential oil.

As a first step, suitable M3WM cycles for menthyl acetate have to be identified. Because m_eq_1_II is the lowest energy conformer of menthyl acetate, which was also assigned in the peppermint oil broadband spectrum, M3WM cycles involving its strongest rotational transitions observed in the spectrum had to be determined. The strongest dipole moment component of m_eq_1_II is μ_c (see Table 7.2). For this reason, it is of advantage to choose a c-type transition for "listen". Two possible M3WM cycles could be determined for menthyl acetate based on this criterion. They are depicted in Figure 7.8. Here, the cycles consist of high energy transitions with K_a values greater than 1. It is noticeable that in both cycles the same transition ($|3_{30}\rangle \leftarrow |3_{31}\rangle$ at 72.64 MHz) was used as a "twist".

In order to determine the optimal pulse duration for the excitation, nutation curves for "drive" and "twist" pulses have to be recorded. During this procedure, the intensity of the respective rotational transition is monitored as a function of the excitation pulse duration. However, since the frequency of the twist pulse in this case was below the operation range of our horn antennas (2-18 GHz), the intensity of the transition, resonant with the twist pulse could not be monitored directly. Instead, the intensity of the "listen" transition (M3WM signal) was recorded as a function of the twist pulse duration (0-800 ns).

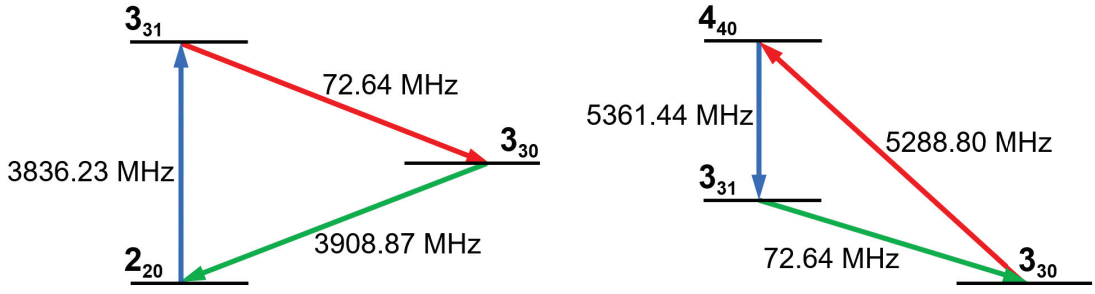

Figure 7.8: *Two M3WM cycles determined for the lowest energy conformer of menthyl acetate, m_eq_1_II with "drive" (blue), "twist" (red), and "listen" (green) transitions .*

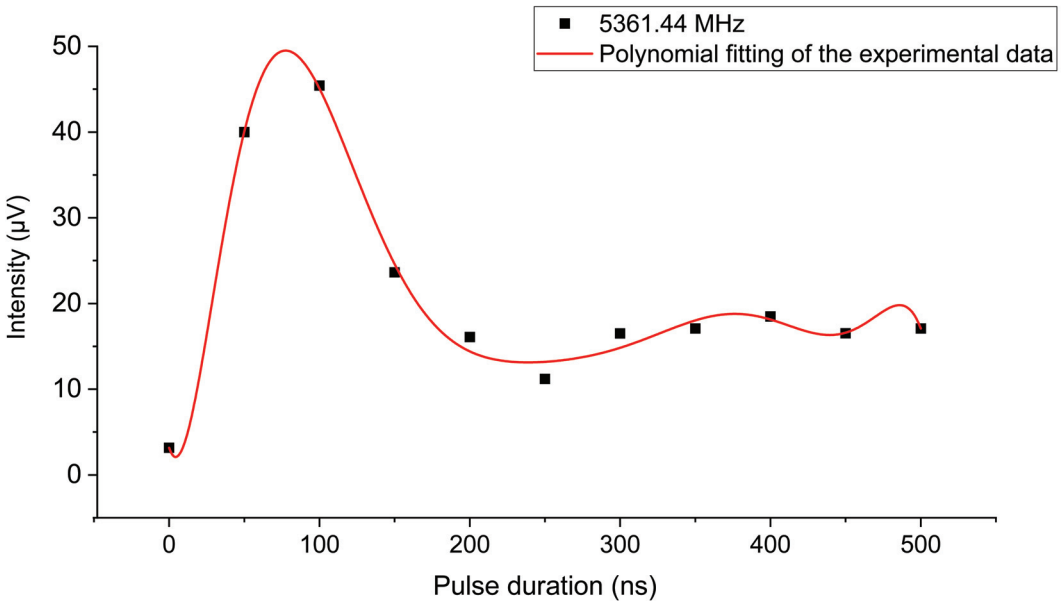

Figure 7.9: *Nutation curve for the drive pulse ($|3_{31}\rangle \leftarrow |4_{40}\rangle$ b-type transition at 5361.44 MHz) of menthyl acetate conformer, m_eq_1_II. The pulse duration was determined by direct excitation. The plot was generated in increments of 50 ns.*

A commercially available sample of menthyl acetate used previously for the broadband measurement was also utilized in the M3WM experiment. The optimal drive pulse duration for cycle 1 was determined to be 50 ns. This pulse is resonant with the $|3_{31}\rangle \leftarrow |2_{20}\rangle$ transition of m_eq_1_II at 3836.23 MHz. For cycle 2, the optimal drive pulse duration ($|3_{31}\rangle \leftarrow |4_{40}\rangle$ transition at 5361.44 MHz) was 100 ns (see Figure 7.9).

The M3WM experiment on m_eq_1_II was successful, as evident from Figure 7.10. An insignificantly higher intensity of the "listen" signal was observed with a twist pulse durations of 500 ns and 750 ns for the cycles 1 and 2 respectively, compared to the results by using other pulse durations. The low SNR (2.7:1) of the recorded signal is due to the fact that only 5.000 acquisitions were averaged here for the final result. In order to improve the SNR, the number of the recorded acquisitions should be increased.

After these preparatory experiments, the next step is the M3WM measurement in peppermint oil. However, since the intensity of menthyl acetate was insufficient in the recorded broadband spectrum, no M3WM on menthyl acetate could be performed in the oil. To rectify this, a peppermint oil sample containing a higher concentration of menthyl acetate would need to be required. Nevertheless, the obtained M3WM cycles can be tabulated and applied in future experiments.

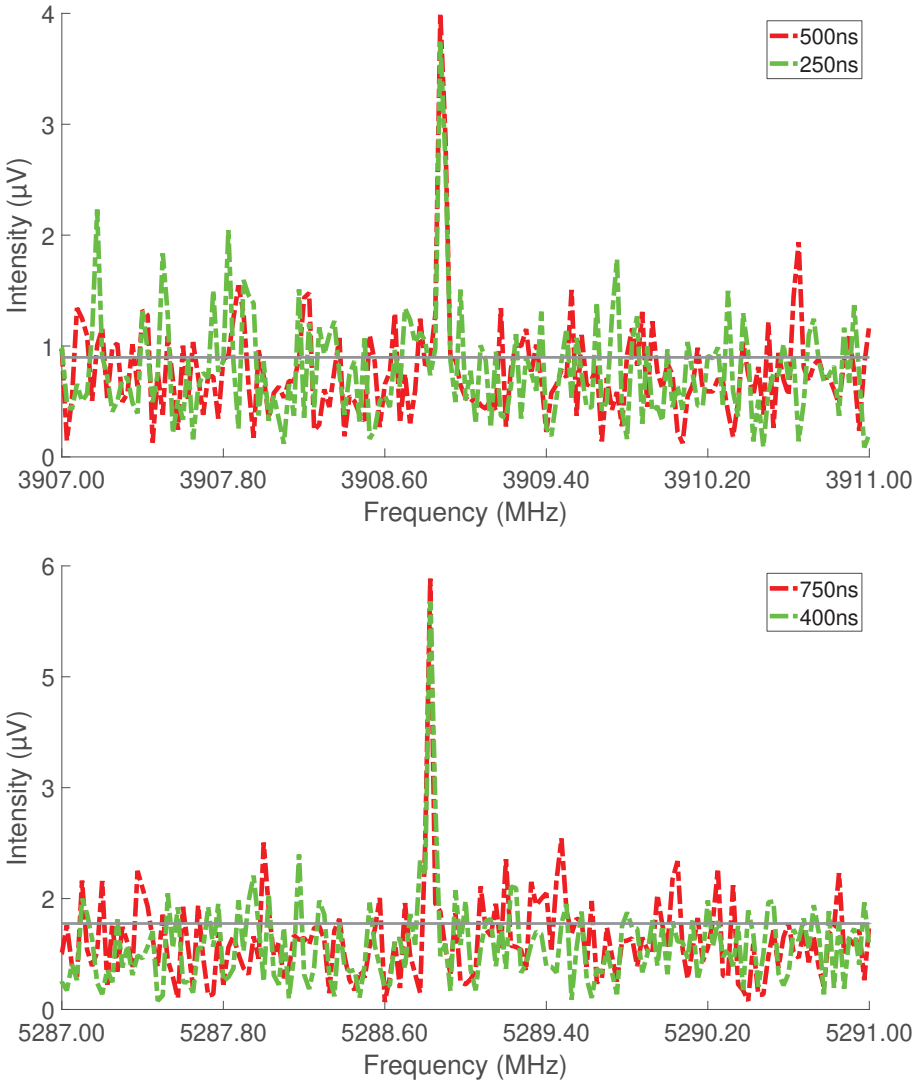

Figure 7.10: *M3WM results for the m_eq_1_II conformer of menthyl acetate. M3WM signals for the "listen" transitions* $|2_{20}\rangle \leftarrow |3_{30}\rangle$ *at 3908.87 MHz, (drive pulse duration=50 ns) and* $|4_{40}\rangle \leftarrow |3_{30}\rangle$ *at 5288.80 MHz (drive pulse duration=100 ns) are plotted. A comparison of the results for different twist pulse duration (500 ns vs. 250 ns, for obtaining a signal at 3908.87 MHz, and 750 ns vs. 400 ns for the signal at 5288.80 MHz) is presented. In all measurements, 5.000 acquisitions were coadded. The horizontal gray lines in the upper and the lower plots present the noise levels (upper quartile). Note that the noise levels of the respective data sets in the top and in the bottom figure panels are nearly identical and therefore indistinguishable here.*

7.5 Summary

In this study, menthyl acetate was analyzed in detail, theoretically and experimentally. PES scans performed in the scope of this work revealed as expected a rich conformational land-

scape of menthyl acetate diastereomers. Several stable conformers could be identified using a computational approach. Two of the lowest energy conformers of menthyl acetate were subsequently assigned in the broadband rotational spectrum. The other calculated lowest energy conformers with the zero-point corrected relative energy cut-off of 6 kJ/mol, belonging to the diastereomer neomenthyl acetate, were not identified. This fact leads to an assumption that this diastereomer, if present, has a very low abundance in the utilized sample.

The lowest energy conformer, m_eq_1_II, shows internal dynamics due to the internal rotation of its acetyl methyl top, which results in observable splittings (doublets) in the spectrum. Using the XIAM program, the experimental V_3 barrier could be determined accurately. The obtained value for the V_3 barrier of menthyl acetate is 1.1828960(70) kJ/mol. This result is very close to the previously reported internal rotation barriers of different acetates (about 1 kJ/mol). It points to the conclusion that the internal rotation barrier of the acetyl methyl group is unaffected by the rest of the structure, as was reported in Ref. 16.

Finally, two M3WM cycles were identified for m_eq_1_II. This conformer was also assigned in the recorded peppermint oil spectrum, which would allow us to perform a M3WM experiment directly in the oil. Since the intensity of menthyl acetate was low in the measured oil spectrum, a sample with a higher concentration of menthly acetate should be used in the future experiments. This is possible because of the fact that the relative ratio of menthyl acetate in the peppermint oil can be up to 16 %[4].

Bibliography

[1] G. Zhu, Z. Xiao, R. Zhou, G. Zhu, and Y. Niu. Kinetics and release characteristics of menthyl acetate from its β-cyclodextrin inclusion complex by thermogravimetric analysis. *J. Incl. Phenom. Macrocycl. Chem.*, 84(3):219–224, 2016.

[2] H. Rasouli and H. Adibi. Peppermint and Its Functionality: A Review. *Arch. Clin. Microbiol.*, 8(4):1–16, 2017.

[3] R. J. Clark and R. C. Menary. Environmental Effects on Peppermint (Mentha piperita L.). I. Effect of Daylength, Photon Flux Density, Night Temperature and Day Temperature on the Yield and Composition of Peppermint Oil. *Functional Plant Biol.*, 7(6):685–692, 1980.

[4] R. J. Clark and R. C. Menary. Variations in composition of peppermint oil in relation to production areas. *Econ. Bot.*, 35(1):59–69, 1981.

[5] G. G. Brown, B. C. Dian, K. O. Douglass, S. M. Geyer, S. T. Shipman, and B. H. Pate. A broadband Fourier transform microwave spectrometer based on chirped pulse excitation. *Rev. Sci. Instrum.*, 79(5):053103, 2008.

[6] D. Schmitz, V. A. Shubert, T. Betz, and M. Schnell. Multi-resonance effects within a single chirp in broadband rotational spectroscopy: The rapid adiabatic passage regime for benzonitrile. *J. Mol. Spectrosc.*, 280:77–84, 2012.

[7] C. M. Western. PGOPHER: A program for simulating rotational, vibrational and electronic spectra. *J. Quant. Spectrosc. Ra.*, 186:221 – 242, 2017.

[8] H. Hartwig and H. Dreizler. The Microwave Spectrum of trans-2,3-Dimethyloxirane in Torsional Excited States. *Z. Naturforsch.*, 51a:923–932, 1996.

[9] H. Hartwig. XIAM Manual, 1996. available at http://www.ifpan.edu.pl/ kisiel/introt/xiam/xiam-v25.txt.

[10] M. J. Frisch, G. W. Trucks, H. B. Schlegel, G. E. Scuseria, M. A. Robb, J. R. Cheeseman, G. Scalmani, V. Barone, B. Mennucci, G. A. Petersson, H. Nakatsuji, M. Caricato, X. Li, H. P. Hratchian, A. F. Iz-

maylov, J. Bloino, G. Zheng, J. L. Sonnenberg, M. Hada, M. Ehara, K. Toyota, R. Fukuda, J. Hasegawa, M. Ishida, T. Nakajima, Y. Honda, O. Kitao, H. Nakai, T. Vreven, J. A. Montgomery, J. E. Peralta, F. Ogliaro, M. Bearpark, J. J. Heyd, E. Brothers, K. N. Kudin, V. N. Staroverov, R. Kobayashi, J. Normand, K. Raghavachari, A. Rendell, J. C. Burant, S. S. Iyengar, J. Tomasi, M. Cossi, N. Rega, J. M. Millam, M. Klene, J. E. Knox, J. B. Cross, V. Bakken, C. Adamo, J. Jaramillo, R. Gomperts, R. E. Stratmann, O. Yazyev, A. J. Austin, R. Cammi, C. Pomelli, J. W. Ochterski, R. L. Martin, K. Morokuma, V. G. Zakrzewski, G. A. Voth, P. Salvador, J. J. Dannenberg, S. Dapprich, A. D. Daniels, O. Farkas, J. B. Foresman, J. V. Ortiz, J. Cioslowski, and D. J. Fox. Gaussian 09, 2009.

[11] S. R. Domingos, C. Pérez, C. Medcraft, P. Pinacho, and M. Schnell. Flexibility unleashed in acyclic monoterpenes: conformational space of citronellal revealed by broadband rotational spectroscopy. *Phys. Chem. Chem. Phys.*, 18:16682–16689, 2016.

[12] D. Jelisavac, D. C. Gómez, H. V. L. Nguyen, L. W. Sutikdja, W. Stahl, and I. Kleiner. The microwave spectrum of the trans conformer of ethyl acetate. *J. Mol. Spectrosc.*, 257(2):111 – 115, 2009.

[13] T. Attig, L. W. Sutikdja, R. Kannengießer, I. Kleiner, and W. Stahl. The microwave spectrum of n-butyl acetate. *J. Mol. Spectrosc.*, 284-285:8 – 15, 2013.

[14] L. W. Sutikdja, D. Jelisavac, W. Stahl, and I. Kleiner. Structural studies on banana oil, isoamyl acetate, by means of microwave spectroscopy and quantum chemical calculations. *Mol. Phys.*, 110(23):2883–2893, 2012.

[15] L. W. Sutikdja, W. Stahl, V. Sironneau, H. V. L. Nguyen, and I. Kleiner. Structure and internal dynamics of n-propyl acetate studied by microwave spectroscopy and quantum chemistry. *Chem. Phys. Lett.*, 663:145 – 149, 2016.

[16] H. V. L. Nguyen, A. Jabri, V. Van, and W. Stahl. Methyl Internal Rotation in the Microwave Spectrum of Vinyl Acetate. *J. Phys. Chem. A*, 118(51):12130–12136, 2014.

Part II

Advanced applications of M3WM

8

Coherent enantiomer - selective population enrichment using tailored microwave fields

8.1 Introduction

It was already emphasized that chirality is an important and intriguing phenomenon in nature. Numerous analytical tools for the characterization of chiral molecules were developed over the years. A short overview over some of these methods is given in Chapter 1.

In spite of the variety of these techniques, which can be used for addressing different analytical questions, some challenges still remain. One of them is enantioseparation in a mixture, containing several chiral species. This process is of interest in the context of academic research, and is of utmost significance in pharmacy, medicine, food industry, and other fields of application. For instance, strict regulations came into force with respect to the approval of new chiral drugs. Many of the top-selling drugs are single enantiomers, and the number of such products available on the market grows constantly worldwide[1].

So far, the methods of choice for enantiomeric separation are mainly capillary electrophoresis[2] and chiral chromatography[3]. In case of the chromatography, separation can be achieved chemically, by the interaction of the enantiomers with a so-called chiral selector. The selector can either be a part of a chiral stationary phase, or act as a mobile phase. However, the choice of a suitable chiral selector for a particular enantiomeric pair can be challenging and time-consuming, since it is often based on a trial-and-error approach[1]. One of the limitations is the lack of reliable chiral recognition models for the systems of interest, which would allow an accurate prediction of the separability and the magnitude of enantioselectivity[1]. Moreover, the selectors should meet further requirements such as robustness, thermal stability and

This chapter is based on the following publication:

C. Pérez, A. L. Steber, S. R. Domingos, A. Krin, D. Schmitz, M. Schnell, *Angew. Chem. Int. Ed.* **2017**, *56*, 12512. (experimental: 40%, data analysis: 40%; writing up: 20%)

chemical inertness. Their synthesis is therefore often a laborious multi-step procedure, which is another time-consuming factor. Furthermore, the chemistry-based separation techniques such as chiral chromatography are not suitable for rapidly racemizing compounds, since the timing required for the separation procedure is here longer than seconds[4].

Recently, enantioseparation and enrichment by purely optical methods[5;6] were reported. It was shown theoretically that enantiomers present in a racemic mixture can be selectively manipulated to populate different quantum states by a cyclic population transfer (CPT)[6;7]. This coherent process of enantioseparation in a three-level system is based on the sign difference between the various electric-dipole matrix elements of the enantiomers[8]. The principle behind this study was applied in the buffer gas cell experiment[4] using 1,2-propanediol, where the population transfer occurred between three electric dipole-allowed rotational transitions, connected over three mutually orthogonal microwave fields. The approach can be viewed as a modification of the microwave three-wave mixing (M3WM), exploiting the features of traditional rotational spectroscopy such as mixture compatibility, high resolution and sensitivity. The M3WM was already introduced in previous chapters. Theoretical background required for understanding the principles behind this technique is provided in Chapter 2.

The methodology of the study presented in this chapter is based on the one described in Ref. 4. By applying sequences of resonant microwave pulses in a phase- and polarization-controlled manner, the enantiomers can be transferred to a rotational level of choice (see Chapter 2). By working under the supersonic conditions of a molecular beam, an enhancement of one order of magnitude for the enantiomeric enrichment could be achieved in comparison to the result of the previous experiment[4]. Two chiral species, menthone and carvone, were chosen as molecular systems. These molecules have been successfully used in M3WM experiments before, in order to demonstrate the possibility of the enantiomeric differentiation[9;10] (see also Chapter 4). A controlled manipulation of enantiomers using tailored microwave fields renders the approach discussed here a new powerful tool for a broad range of analytical and spectroscopic applications.

8.2 Instrumental set-up

The experiment was performed on the chirped-pulse Fourier transform microwave (CP-FTMW) spectrometer COMPACT[11;12]. Menthone ((–)-menthone, 90% purity; (+)-menthone, 98%; mixture of isomers, 97%) and carvone ((–)-carvone, 98% purity; (+)-carvone, 96%) were purchased from Sigma Aldrich and used without further purification. In order to bring samples into the gas phase, the same conditions for menthone (112 °C, 3 bar backing pressure with neon as a carrier gas) and carvone (80 °C, 2 bar backing pressure with neon as a carrier gas) as used in previous studies[13;14] were applied.

The set-up corresponds in general to the one used in M3WM experiments (Chapter 3) with some modifications. To achieve population transfer, a third excitation pulse (transfer pulse) was applied in addition to drive and twist (see Chapter 2 for more details).

The transfer pulse was amplified with an amplifier working in 2-8 GHz range. For the twist pulse amplification an RF-amplifier (30-2300 MHz operation range) was used. Since this amplifier was not equipped with an internal switch, an external switch for the noise reduction was necessary. The drive and the transfer pulses were broadcast from the same channel of the arbitrary wave form generator (AWG). For that reason, an additional switch was introduced into the set-up for transmitting these two pulses in a controlled manner. A more detailed scheme of the set-up is presented in Figure 8.1.

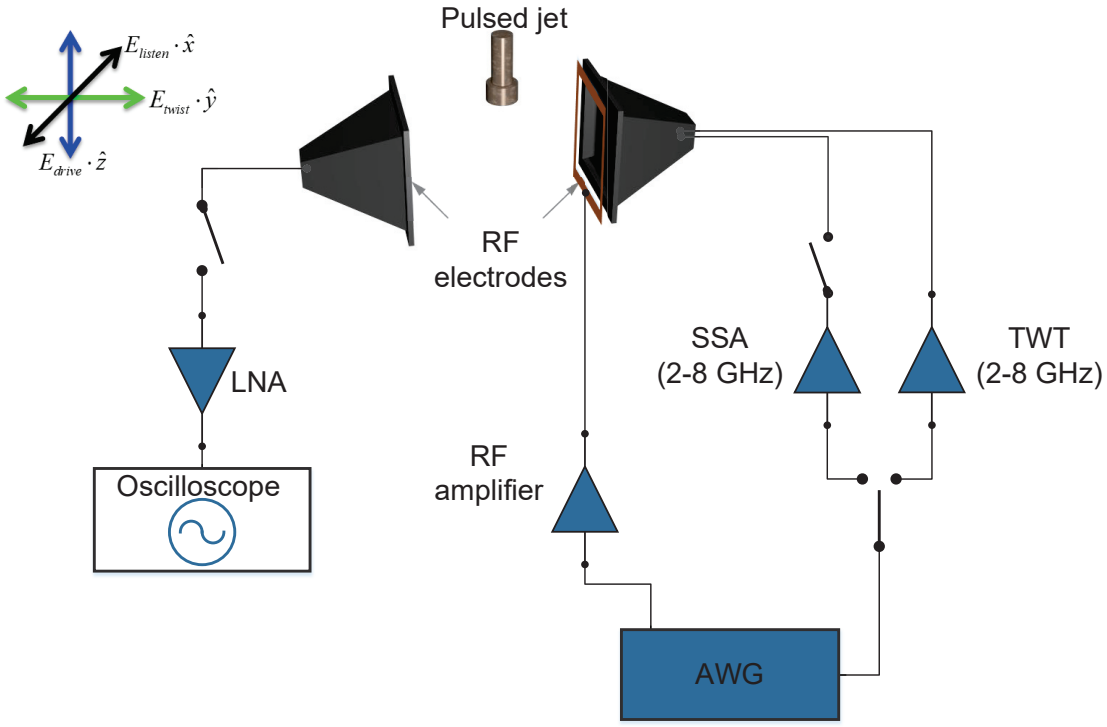

Figure 8.1: *Schematic representation of the experimental set-up. All excitation pulses were generated with the same arbitrary wave form generator (AWG). Drive pulse (in z direction) was enhanced with a travelling wave tube (TWT) amplifier, twist (in y direction) with an RF amplifier, transfer pulse (in x direction) with a solid state amplifier (SSA). Since the SSA was not equipped with an internal switch, an external switch was used for noise reduction. An additional switch was required, because drive and transfer pulses were broadcast from the same channel of AWG. The molecular signal was amplified with a low-noise amplifier (LNA) and recorded with an oscilloscope.*

8.3 Experimental details

It was explained in Chapter 2 that the M3WM experiment comprises of a two-photon process. Adding a transfer pulse, which excites a single rotational transition, induces a one-photon process. The constructive or destructive interference between these two processes can be used for an accurate determination of the enantiomeric excess (*ee*) in a sample. This is demonstrated here on the example of menthone A (Section 8.4.1). Once one- and two-photon processes are applied simultaneously, a state-specific population enrichment is achieved. This approach is explained in Section 8.4.2 by using carvone (EQ2) as the molecular system. Before presenting the experimental results, some details on the applied excitation pulse schemes will be given.

8.3.1 Energy level scheme of menthone

The previously reported[9] M3WM cycle for the conformer A of menthone was used in this experiment (Figure 8.2 a)). The optimal pulse duration of the excitation pulses was determined by measuring the nutation curves at the frequencies of the three transitions, depicted in Figure 8.2. The obtained results are summarized in Figure 8.3. The pulse duration of the drive pulse at 4036.98 MHz ($|2_{11}\rangle \leftarrow |1_{01}\rangle$) was determined to be 120 ns.

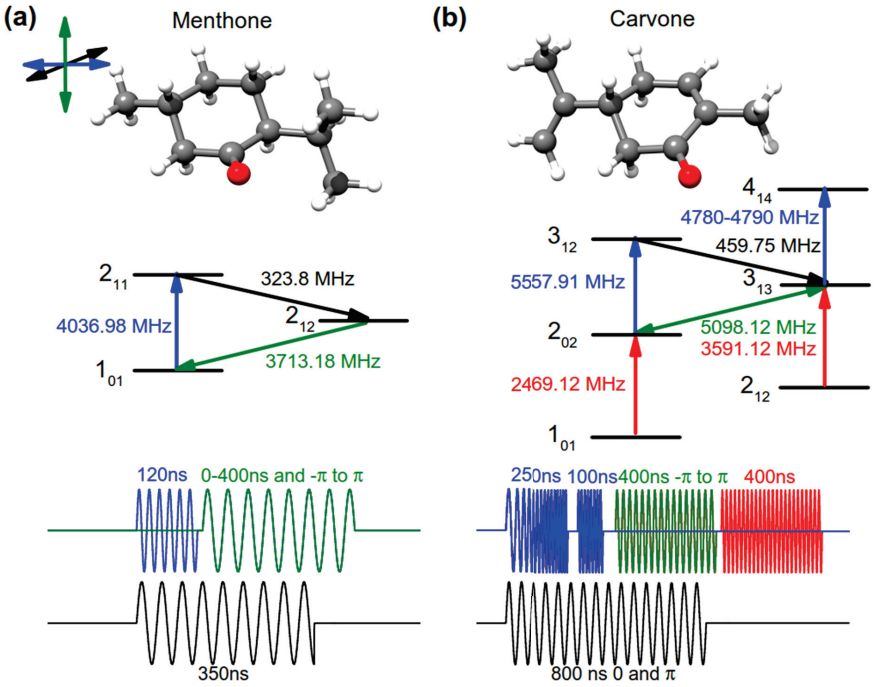

Figure 8.2: *Energy scheme of a) menthone (conformer A) and b) carvone (EQ 2) used in the experiment. The orientation of the applied polarized microwave fields is depicted in the top-left. The determined optimal pulse durations are shown in the bottom panels.*

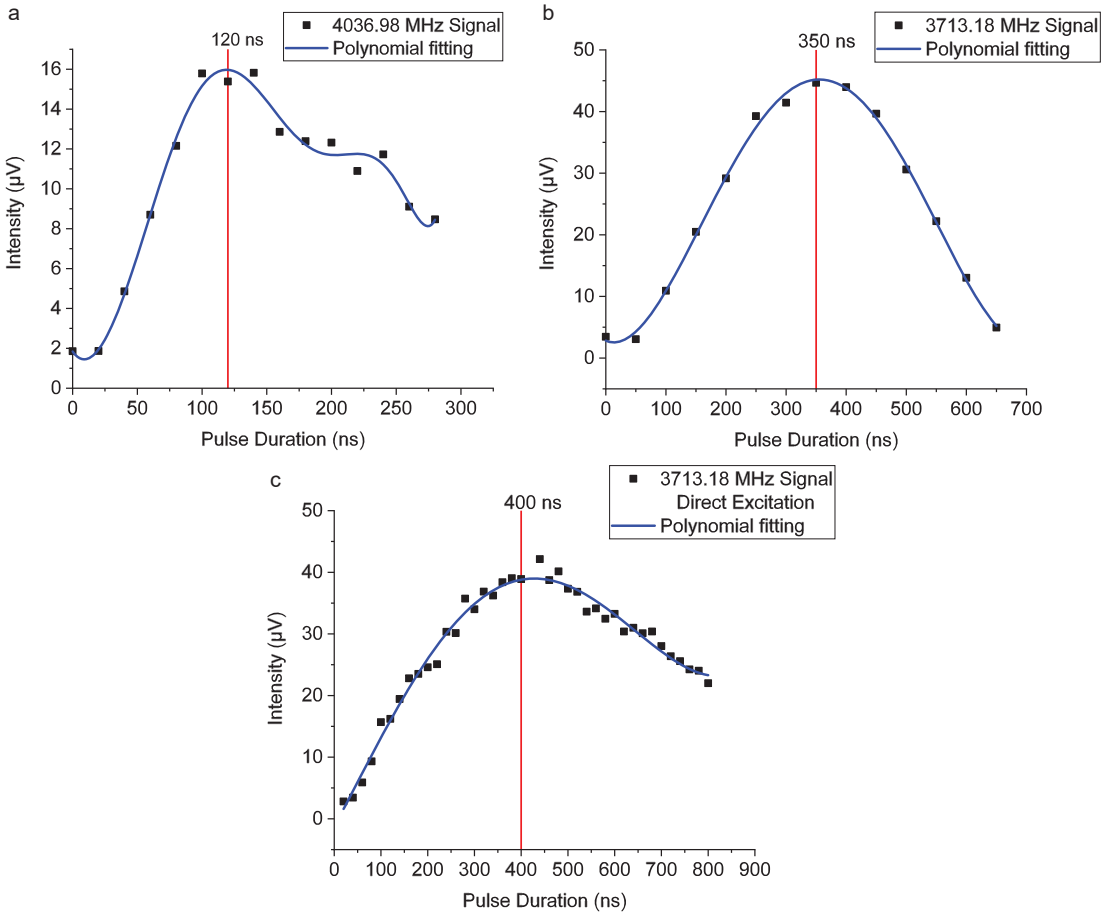

Figure 8.3: *a) Nutation curves for the MW drive pulse ($|2_{11}\rangle \leftarrow |1_{01}\rangle$ c-type transition at 4036.98 MHz) of menthone (conformer A). Optimal coherence is created under the $\pi/2$ pulse condition, which corresponds to about 120 ns. b) Optimization for the RF twist pulse ($|2_{12}\rangle \leftarrow |2_{11}\rangle$ a-type transition at 323.8 MHz) of menthone (conformer A), which is recorded indirectly by monitoring the intensity of the chiral signal at 3713.18 MHz. Optimal signal is obtained under the π pulse condition, which corresponds to about 350 ns. c) Determination of the optimal pulse duration for the transfer pulse of menthone (conformer A) with direct excitation. The maximal intensity for this $|1_{01}\rangle \leftarrow |2_{12}\rangle$ b-type transition at 3713.18 MHz is achieved when the pulse duration of the respective single excitation pulse is around 400 ns.*

Note that the intensity of the twist pulse could not be directly measured with our set-up, since the frequency of the respective rotational transition is below the operation mode of the microwave horn antennas (2-18 GHz). Instead, the intensity of the listen transition ($|1_{01}\rangle \leftarrow |2_{12}\rangle$) was recorded by varying the twist pulse duration. Maximum signal was achieved by applying a twist pulse of 350 ns. The optimal pulse duration for the single frequency excitation of the $|1_{01}\rangle \leftarrow |2_{12}\rangle$ transition at 3713.18 MHz (one-photon process) was 400 ns (Figure 8.3). For the subsequent *ee* determination, both pulse duration (from 0 to 400 ns) and phase (from $-\pi$ to π) of the transfer pulse were monitored.

8.3.2 Energy level scheme of carvone

A similar procedure was applied to the EQ2 conformer of carvone, analyzed before[10]. The scheme of the respective energy levels is presented in Figure 8.2. The nutation curves for drive ($|3_{12}\rangle \leftarrow |2_{02}\rangle$ at 5557.91 MHz) and twist ($|3_{13}\rangle \leftarrow |3_{12}\rangle$ at 459.75 MHz) pulses are given in Figure 8.4. Since here again the frequency of the twist pulse is out of the frequency range of our microwave horn antennas, the pulse duration was determined indirectly in a double-resonance approach by monitoring the intensity of the transition at 5098.12 MHz, which corresponds to the "listen". The determined optimum pulse durations were around 100 ns and 800 ns for the drive and the twist pulse respectively.

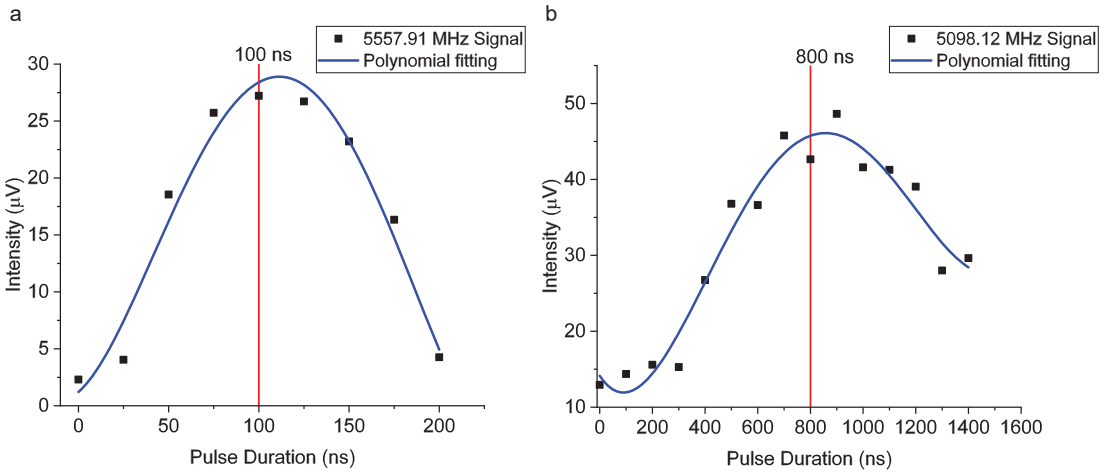

Figure 8.4: *a) Nutation curve for the MW drive pulse ($|3_{12}\rangle \leftarrow |2_{02}\rangle$ c-type transition at 5557.91 MHz) of carvone (conformer EQ 2). Optimal coherence is created under the $\pi/2$ pulse condition, which corresponds to about 100 ns. b) Optimization for the RF twist pulse ($|3_{13}\rangle \leftarrow |3_{12}\rangle$ a-type transition at 459.75 MHz) of carvone, which is indirectly recorded by monitoring the intensity of the chiral signal at 5098.12 MHz. Maximal signal is observed for π pulse condition, which is about 800 ns.*

In order to detect the population enrichment, two pulses, sharing energy levels with the transfer pulse ($|2_{02}\rangle \leftarrow |3_{13}\rangle$ at 5098.12 MHz) were applied. The pulses are $|2_{02}\rangle \leftarrow |1_{01}\rangle$ at 2469.12 MHz and $|3_{13}\rangle \leftarrow |2_{12}\rangle$ at 3591.12 MHz (see Figure 8.2). While their polarization direction and phases are not important for the experiment, modulation in their intensity with the phase scanning of the transfer pulse gives quantitative information about the successful population transfer. As in case of menthone, both pulse duration (0-400 ns) and phase (from $-\pi$ to π) were scanned for the transfer pulse.

The initial population distribution of the rotational states cooled into during the supersonic expansion[15] is crucial to achieve significant enantiomeric enrichment. Even under the low temperature conditions there will be a net population in the rotational states chosen to probe the enantiomeric enrichment, here states $|2_{02}\rangle$ and $|3_{13}\rangle$. To maximize the population difference, a strong chirped pulse, spanning 10 MHz (4780–4790 MHz) around $|4_{14}\rangle \leftarrow |3_{13}\rangle$ in a rapid adiabatic passage (RAP) regime was used. The RAP pulse can result in population

inversion[15]. This short pulse (250 ns) allowed to transfer the initial population of the $|3_{13}\rangle$ state to higher, less populated rotational states and to create better starting conditions. For this reason, it was applied before the experimental pulse sequence for the single frequency excitations (see Figure 8.2).

8.4 Results

8.4.1 Interference between one- and two-photon processes

Measurements with nearly enantiopure menthone and a commercially available mixture of isomers (non-racemic[9]), containing menthone and isomenthone, were performed. Changes in the amplitude of the $|1_{01}\rangle \leftarrow |2_{12}\rangle$ transition due to the stepwise variation of the phase and the duration of the transfer pulse (see Section 8.3.1) are depicted in Figure 8.5. All signals were normalized with respect to the standard M3WM experiment, when the transfer pulse was not applied. The results show a significant phase dependence of the observed signal upon changes in the phase of the transfer pulse. Maxima (red) and minima (blue) of the measured signal amplitude can be interpreted as the consequence of constructive and destructive interference between one- and two-photon processes. The enantiomers show as expected an opposite behavior with respect to the signal variation (Figure 8.5, a) and b)). For (–)-menthone, an almost complete destructive interference (signal modulation of around 80% compared to the basic M3WM signal level) is observed, when the phase of the transfer pulse is shifted by $\pi/2$ radians with respect to the other two excitation pulses. For the (+)-menthone, such observation occurs with the phase shift of $-\pi/2$ radians, while a $\pi/2$ shift results in constructive interference.

By comparing the results for the enantiopure menthone and the mixture of isomers, the *ee* of the mixture can be obtained. This requires determination of the transfer pulse duration, at which the maximal destructive interference for both the enantiopure sample and the mixture of isomers is evident (see Chapter 2). This information can be extracted directly from Figure 8.5. It is noticeable that the signal amplitude variation observed in the mixture (by scanning the phase of the transfer pulse from $-\pi$ to π radians) is the same as in (–)-menthone. This observation leads to the conclusion that (–)-menthone should be in excess in the mixture. In case of (–)-menthone, maximal destructive interference and thus minimal signal is observed, when the transfer pulse duration is roughly 150 ns. For the mixture, minimal signal is obtained with a transfer pulse of 125 ns. This shift to lower values points to the lower *ee* in the mixture as expected. The relative ratio of the transfer pulse durations mentioned above is therefore 125:150. Once this result is normalized with respect to the enantiopure (–)-menthone (set as unity), its relative abundance in mixture can be estimated. In this case, it is roughly 0.83:1 or 83%. In the previous experiment reported in Ref. 9 the *ee* value of the mixture utilized here was determined to be 62.5% ± 24.2% with (–)-menthone being the most abundant enantiomer in the mixture. Within the experimental uncertainty, this value is in consistency

with our result. Higher accuracy in the *ee* determination can be achieved by e.g. scanning the respective transfer pulse duration in smaller increments.

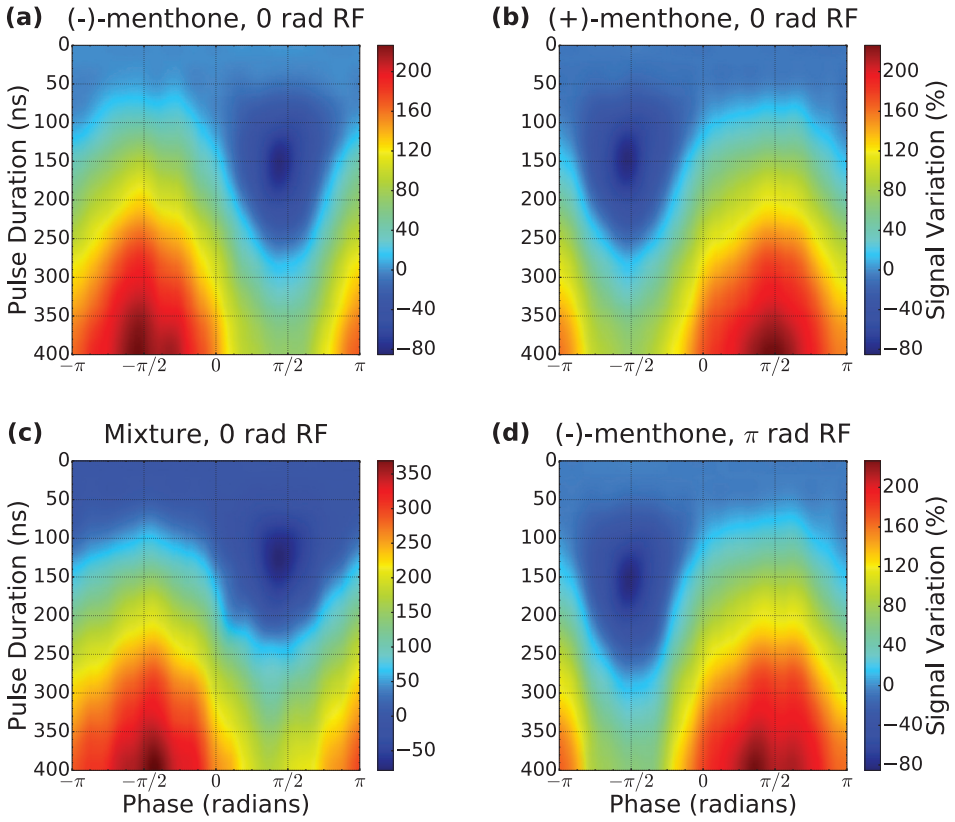

Figure 8.5: *The variation of the signal amplitude of the $|1_{01}\rangle \leftarrow |2_{12}\rangle$ transition for menthone A was monitored as a function of the phase and pulse duration of the transfer pulse at 3713.18 MHz. The signal was normalized with respect to the basic M3WM signal, when the transfer pulse was off. The results of destructive interference between $|1_{01}\rangle \leftarrow |2_{12}\rangle$ and $|2_{12}\rangle \leftarrow |2_{11}\rangle \leftarrow |1_{01}\rangle$ pathways is shown for a) (–)-menthone, b) (+)-menthone, and c) mixture of isomers. In d) the phase of the RF twist pulse was shifted by π for (–)-menthone, resulting in the signal behavior similar to (+)-menthone.*

To further investigate the degree of achievable control and robustness of our experimental approach, we shifted the phase of the other excitation pulse, the RF twist pulse at 323.8 MHz, by π radians for (–)-menthone (Figures 8.5 a) and d)). Under these experimental conditions, we were able to reverse the observed signal variation and to obtain a similar behavior to that of (+)-menthone. This fact, therefore, confirms the validity of our experimental method and proves experimentally that the interference processes presented here can be used to selectively discriminate between left- and right-handed chiral systems.

8.4.2 State-specific population transfer

Once the molecular interferomic effects could be analyzed, the approach was extended for selectively transferring enantiomers to the rotational levels of choice, which corresponds to a separation in energy. This procedure can be regarded as a first step towards the actual enantioseparation in space, which can be achieved in future experiments.

The monoterpenoid carvone was chosen as the molecular system to demonstrate the approach discussed here. Two pulses at 2469.12 MHz and 3591.12 MHz, sharing energy levels with the $|2_{02}\rangle \leftarrow |3_{13}\rangle$ transfer pulse (Section 8.3.2) were used to probe the state-specific enrichment of carvone. The changes in their amplitude with the phase of the transfer pulse (from $-\pi$ to π) allow the determination of the enantiomer-selective enrichment in states $|2_{02}\rangle$ (by using the $|2_{02}\rangle \leftarrow |1_{01}\rangle$ transition at 2469.12 MHz as a probe) or $|3_{13}\rangle$ (by using the $|3_{13}\rangle \leftarrow |2_{12}\rangle$ transition at 3591.12 MHz as a probe). The duration of the transfer pulse was 400 ns. The obtained results are shown in Figure 8.6.

The first set of experiments was performed with (–)-carvone using the $|3_{13}\rangle \leftarrow |2_{12}\rangle$ transition at 3591.12 MHz as a probe. A sinusoidal behavior of the amplitude of this "probing" transition with the phase of the transfer pulse is observed (Figure 8.6 a)). The opposite signal behavior of the other enantiomer can be achieved by introducing a π phase shift to one of the excitation pulses (see Section 8.4.1). Here, the phase of the twist pulse at 459.75 MHz was shifted by π radians. As expected, the resulting sinusoidal behavior is opposite to the one observed previously and represents the response of the other enantiomer, (+)-carvone.

In the next set of experiments, another pulse at 2469.12 MHz sharing the $|2_{02}\rangle$ level with the transfer pulse was applied (see Figure 8.2). A comparison of the results for (–)-carvone (Figure 8.6 a) and b)) shows a clear π shift with respect to the sinusoidal signal behavior. This means that the population or depopulation of the enantiomer either in $|3_{13}\rangle$ or in $|2_{02}\rangle$ level occurs. Afterwards, the phase of the twist pulse was shifted by π radians , as previously. This again resulted in reversion of the sinusoidal behavior, as would be the case, once (+)-carvone is used as the molecular sample. This demonstrates a successful population enrichment of the enantiomers of carvone in the rotational states of choice. While one of the enantiomers is transferred to the upper state $|3_{12}\rangle$, the other can be observed in the lower $|2_{02}\rangle$ state and vice versa.

The achieved enantiomer-selective enrichment was quantified. The signal was normalized with respect to the intensity of the "probing" transition without the transfer pulse. The results are depicted in Figure 8.6 c) and d) showing the enrichment in the states $|3_{13}\rangle$ and $|2_{02}\rangle$ of about 6%. Previously reported state-specific enatiomeric enrichment with 1,2-propanediol prepared in buffer gas cell was 0.6%[4], which is one order of magnitude lower than the result presented here. This is due to several reasons. Lower rotational temperatures (around 1-2 K attributable to the conditions of a supersonic jet) are achieved in our instrument compared to the buffer gas experiment (7-10 K). This ensures larger initial population difference between the rotational transitions involved, which increases the contrast. In addition, a strong RAP pulse, preceding the experiment, enhances the contrast in the achieved population transfer

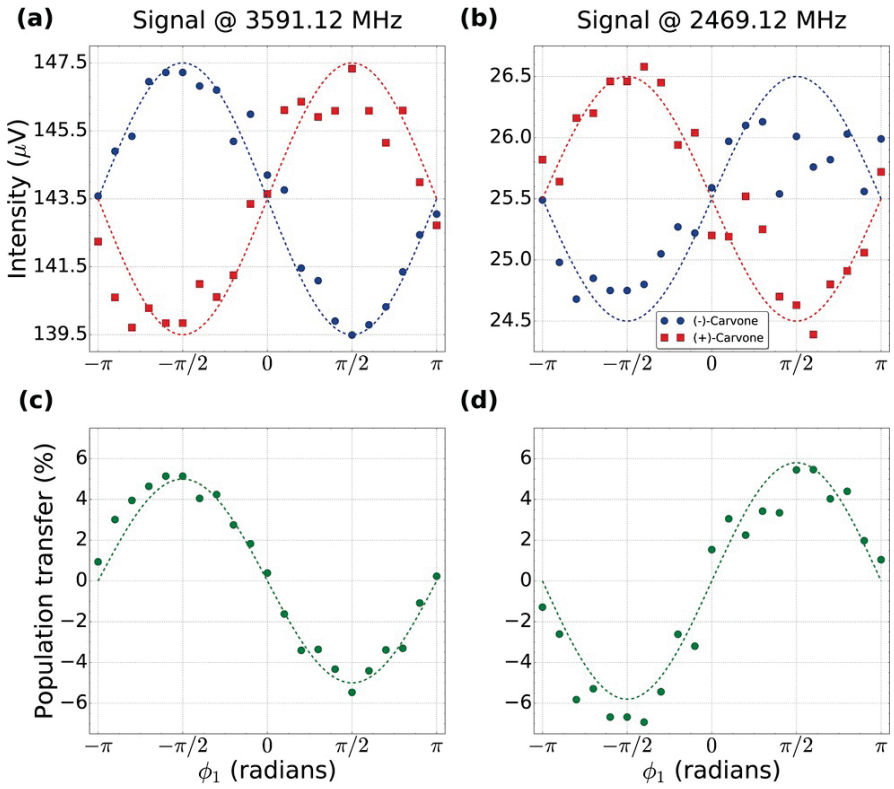

Figure 8.6: *(a) Enantiomer-selective enrichment of carvone in the $|3_{13}\rangle$ rotational level by monitoring the phase-dependent amplitude of the $|3_{13}\rangle \leftarrow |2_{12}\rangle$ transition at 3591.12 MHz. The blue trace shows the signal of (−)-carvone (25000 averages). The red trace represents the signal of (+)-carvone (25000 averages), once the phase of the RF pulse at 459.75 MHz was shifted by π radians. The phase of the transfer pulse, ϕ_1, was changed in 18 degrees step. (b) Enantiomeric enrichment in the $|2_{02}\rangle$ rotational state, probed by monitoring the amplitude of the $|2_{02}\rangle \leftarrow |1_{01}\rangle$ transition at 2469.12 MHz. Panels (c) and (d) show the achieved enrichment in $|3_{13}\rangle$ and $|2_{02}\rangle$ states, which is about 6%. The signal was normalized with respect to the intensity of the monitored transitions $|3_{13}\rangle \leftarrow |2_{12}\rangle$ and $|2_{02}\rangle \leftarrow |1_{01}\rangle$ without the transfer pulse.*

even further. The results reported here can still be improved by increasing the power of the applied electric fields and using more advanced RAP pulse schemes to also account for the different M states involved (see Chapter 2).

8.5 Summary and Outlook

In summary, a new method for manipulating chiral samples based on the M3WM is presented. It can be used for an *ee* determination and for a state selective population enrichment. The achieved population transfer of 6%, shown on the example of carvone, is an order of magnitude higher than reported before[4].

The approach demonstrated here provides chemists potentially with an additional analytical tool with a wide range of applications. Once the enantiomers are selectively transferred to

the rotational levels of choice, they can be spatially separated by e.g. using electrostatic deflectors. The great advantage of our method is that it can be applied in cases, which are still challenging for the analysis with any conventional methods. For instance, it can be used for studying isotopic molecular chirality[16]. Moreover, the approach is particularly useful for enantiomeric pairs, which undergo rapid racemization and cannot be separated with e.g. chromatography. Finally, the method discussed here could once serve as a basis for investigating the energy difference between enantiomers resulting from parity violation, as described by Eibenberger et.al.[4].

Bibliography

[1] N. M. Maier, P. Franco, and W. Lindner. Separation of enantiomers: needs, challenges, perspectives. *J. Chromatogr. A*, 906(1):3 – 33, 2001.

[2] G. Gübitz and M. G. Schmid. Recent advances in chiral separation principles in capillary electrophoresis and capillary electrochromatography. *Electrophoresis*, 25(23-24):3981–3996, 2004.

[3] T. E. Beesley and R. P. W. Scott. In R. P. W. Scott, C. F. Simpson, and E. D. Katz, editors, *Chiral Chromatography*. John Wiley & Sons, 1999.

[4] S. Eibenberger, J. Doyle, and D. Patterson. Enantiomer-Specific State Transfer of Chiral Molecules. *Phys. Rev. Lett.*, 118:123002, 2017.

[5] M. Shapiro, E. Frishman, and P. Brumer. Coherently Controlled Asymmetric Synthesis with Achiral Light. *Phys. Rev. Lett.*, 84:1669–1672, 2000.

[6] P. Král and M. Shapiro. Cyclic Population Transfer in Quantum Systems with Broken Symmetry. *Phys. Rev. Lett.*, 87:183002, 2001.

[7] A. Jacob and K. Hornberger. Effect of molecular rotation on enantioseparation. *J. Chem. Phys.*, 137(4):044313, 2012.

[8] X. Li and M. Shapiro. Theory of the optical spatial separation of racemic mixtures of chiral molecules. *J. Chem. Phys.*, 132(19):194315, 2010.

[9] V. A. Shubert, D. Schmitz, and M. Schnell. Enantiomer-sensitive spectroscopy and mixture analysis of chiral molecules containing two stereogenic centers – Microwave three-wave mixing of menthone. *J. Mol. Spectrosc.*, 300:31 – 36, 2014.

[10] V. A. Shubert, D. Schmitz, D. Patterson, J. M. Doyle, and S. Melanie. Identifying Enantiomers in Mixtures of Chiral Molecules with Broadband Microwave Spectroscopy. *Angew. Chem. Int. Ed.*, 53(4):1152–1155, 2014.

[11] D. Schmitz, V. A. Shubert, T. Betz, and M. Schnell. Multi-resonance effects within a single chirp in broadband rotational spectroscopy: The rapid adiabatic passage regime for benzonitrile. *J. Mol. Spectrosc.*, 280:77–84, 2012.

[12] G. G. Brown, B. C. Dian, K. O. Douglass, S. M. Geyer, S. T. Shipman, and B. H. Pate. A broadband Fourier transform microwave spectrometer based on chirped pulse excitation. *Rev. Sci. Instrum.*, 79(5):053103, 2008.

[13] D. Schmitz, V. A. Shubert, T. Betz, and M. Schnell. Exploring the conformational landscape of menthol, menthone, and isomenthone: a microwave study. *Front. Chem.*, 3:15, 2015.

[14] J. R. A. Moreno, T. R. Huet, and J. J. L. González. Conformational relaxation of S-(+)-carvone and R-(+)-limonene studied by microwave Fourier transform spectroscopy and quantum chemical calculations. *Struct. Chem.*, 24(4):1163–1170, 2013.

[15] V. Malinovsky and J. Krause. General theory of population transfer by adiabatic rapid passage with intense, chirped laser pulses. *Eur. Phys. J.*, 14(2):147–155, 2001.

[16] D. W. Pratt and B. H. Pate. Chiral Imprinting in the Gas Phase. *Angew. Chem. Int. Ed.*, 56(51):16122–16124, 2017.

9

State-Specific Enrichment of Chiral Conformers with Microwave Spectroscopy

9.1 Introduction

In the previous chapters several examples of an unambiguous differentiation between the enantiomers of chiral molecules using microwave three-wave mixing (M3WM) were given. One interesting modification of this technique, coherent population transfer (CPT), was presented in Chapter 8. It was shown that by simultaneously exciting all three kinds of electric dipole-allowed rotational transitions in a phase- and polarization-controlled manner, state-specific enantiomeric enrichment can be achieved[1]. Here we combine CPT and M3WM to manipulate chiral conformers of a molecule without stereogenic center and to transfer them to the rotational levels of choice.

In principle, a non-chiral molecule can become chiral due to some spatial arrangements of its conformers. Two mirror images of the respective molecule can be obtained in the simplest way by rotation about single bonds of one of the conformers. If the barrier for such rotation is low, the two conformers will continuously undergo interconversion into one another via tunnelling motions through the barrier. This internal dynamics can be observed in rotational spectroscopy, since it results in splittings of the rotational transitions in the spectrum. However, if the barrier is high enough, the two conformers will be "trapped" in their respective potential energy wells under the cold conditions of the supersonic jet. Since they represent an enantiomeric pair, no differentiation between them is possible using rotational broadband

This chapter is based on the following publication:

C. Pérez, A. L. Steber, A. Krin, and M. Schnell *J. Phys. Chem. Lett.* **2018** *9* (16), 4539-4543. (experimental: 40%, data analysis: 40%; writing up: 20%)

spectroscopy, because the rotational constants of the two enantiomers are identical (see Chapter 1). M3WM is also not applicable in this case, because the two enantiomers are present as a racemic mixture, as long as there is no chiral environment influence[2].

Our approach for the differentiation between such chiral conformers in the gas phase is a two-step procedure. The first step in this case involves the preparation of the enantiomeric pair in two different rotational states of choice, using the CPT method. The achieved enantiomeric enrichment is probed with subsequent M3WM cycle. A racemic mixture yields zero signal in M3WM (Chapter 2). For this reason, such an approach results in a measurable molecular signal only if one of the enantiomers is in excess in a particular rotational level, which renders it very sensitive to an enantiomeric excess (*ee*).

The experiment described here was performed with cyclohexylmethanol (CHM). This molecule was studied previously by jet-FTIR spectroscopy, complemented by Raman spectroscopy and quantum chemical calculations, which also included a detailed conformational analysis of CHM[3].

9.2 Experimental and computational analysis of CHM

In order to determine the set of rotational transitions with high intensity, which could be used in the subsequent population transfer experiment, a broadband spectrum of CHM was measured. The spectrum was recorded in the 2-8 GHz frequency range (2 million acquisitions) on the chirped-pulse Fourier transform microwave (CP-FTMW) spectrometer COMPACT[4;5]. CHM is liquid at room temperature. The sample was heated (70° C) prior to being supersonically expanded into the vacuum chamber using neon (3 bar backing pressure) as a carrier gas. The broadband spectrum of CHM is presented in Figure 9.2. The measured rotational transitions were fitted to an asymmetric rigid rotor Hamiltonian, using JB95 program[6]. All the strongest lines in the spectrum were assigned to one species (blue in Figure 9.2) with a signal to noise ratio (SNR) of about 3000:1. The obtained fit was subsequently refined with the SPFIT program[7] (see Table E.1).

The conformational study on CHM reported in Ref. 3 revealed five equatorial conformers of this molecule, three *gauche* and two *trans* forms. The conformers with an axially orientated hydroxymethyl group are predicted to be at least 4 kJ/mol higher in energy than the ones, where the hydroxymethyl group is orientated equatorially, and were therefore neglected[3]. The *trans*-conformers were found to be consistently less favorable than *gauche* due to the stereochemical effects[3]. They were not observed experimentally in the respective FTIR and Raman jet spectra[3]. The *trans*-conformers will also not be treated in the present study.

The calculated zero-point corrected relative energies of the *gauche* structures Gt, Gg and Gg', lie within less than 1 kJ/mol. Since no rotational parameters are reported in Ref. 3, the conformers Gt, Gg and Gg' were optimized in the scope of our study at the B3LYP-D3/6-311++G(d,p) level of theory. A comparison between computationally predicted and

experimentally determined rotational parameters is provided in Table 9.1. Calculated rotational constants of Gt show the smallest difference to the experimentally determined ones. For this reason, the component observed in our broadband spectrum was assigned to Gt. Another aspect, which further corroborates this assumption, are the dipole moment components. The most intense lines in the spectrum are of b-type, while the weakest ones belong to a-type. This is in accordance with the fact that the calculated μ_b is the strongest dipole moment component of Gt, while μ_a is the weakest one (see Table 9.1). Gt conformer was also found to be the most stable conformer in the previous FTIR/Raman experiment[3].

No further conformers were observed in our spectrum. Since Gt, Gg and Gg' differ only in the orientation of the hydroxyl group (Figure 9.3), the internal rotation of the OH group was further investigated. The calculated (B3LYP-D3/6-311++G(d,p) level of theory) potential energy barrier is depicted in Figure 9.1. It is evident that the barrier hindering the internal rotation of the hydroxyl group is relatively low (around 600 cm^{-1}). In the previous Raman jet study on CHM, all three conformers were observed experimentally[3]. It should be pointed out that the experiment reported in Ref. 3 was conducted using helium as a carrier gas. The usage of neon instead of helium in our case enables better cooling of the internal motions. This explains the fact that only one CHM conformer could be identified in our rotational broadband spectrum.

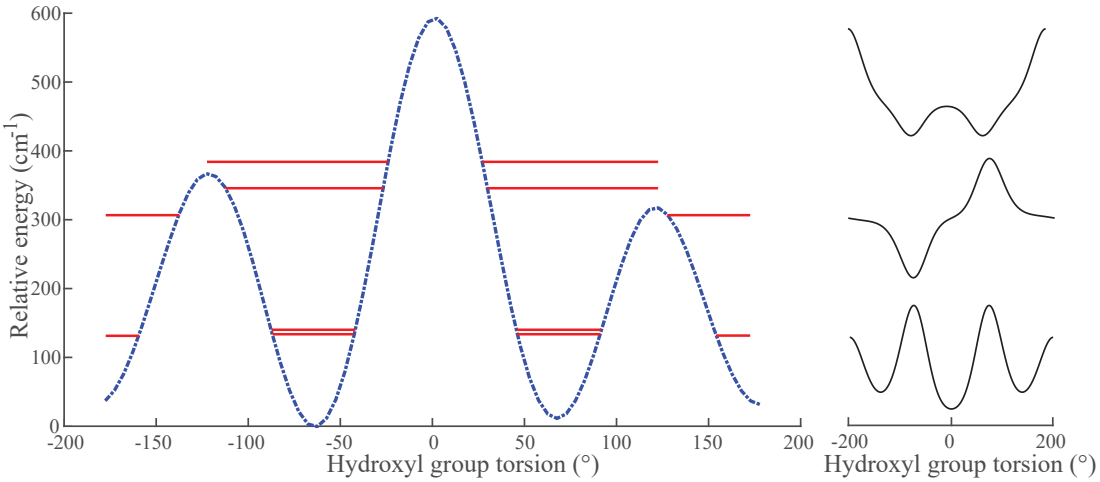

Figure 9.1: *Calculated potential energy barrier for the internal rotation of the OH group of CHM (B3LYP-D3/6-311++G(d,p)). The tunnelling splittings were determined computationally using the program package LAMPA-IntRoVer[8]. The respective wave functions of the three lowest states are presented.*

Tunnelling splittings due to the internal rotation of the hydroxyl group are expected in the spectrum. The calculated (by using the program package LAMPA-IntRoVer[8]) splitting in the vibrational ground state is of the order of 2 cm^{-1} or 60 GHz (see Figure 9.1), and therefore not observable in our spectral range. This result is in agreement with the published experimental data on a related molecule, cyclohexanol. There the tunnelling splittings were determined to be 52(2) GHz[9] and thus close to our estimated value.

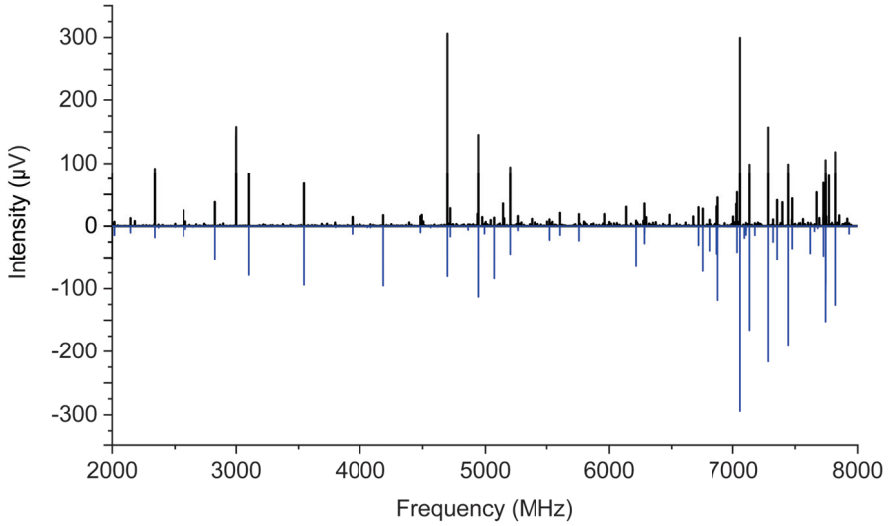

Figure 9.2: *The 2-8 GHz spectrum (2 million acquisitions, neon as a career gas) of cyclohexylmethanol (CHM). The black trace shows the experimental spectrum, while the lower trace (blue) represents simulations based on the calculated rotational parameters for the CHM conformer Gt.*

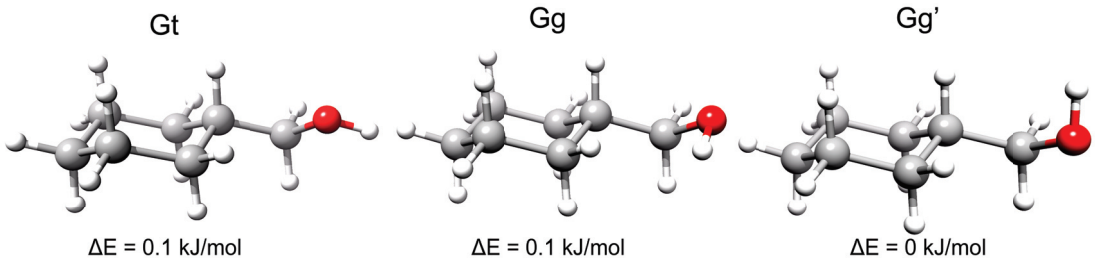

Figure 9.3: *Three lowest energy conformers of CHM[3], optimized at the B3LYP-D3/6-311++G(d,p) level of theory. The three conformers differ in the orientation of the OH group.*

In following, we will focus on the experimentally assigned conformer Gt. The calculated structure of this conformer is depicted in Figure 9.3. By rotation around the dihedral angle C1–C2–C3–O (see Figure 9.4 for labelling) an enatiomeric pair can be created, where the dipole moment component along the b-axis has an opposite direction and thus an opposite sign (yellow in Figure 9.4), while the two other dipole moment components, along the a- and c-axis respectively, remain orientated in the same way. In order to determine the barrier height for the interconversion of these two enantiomers into each other, a potential energy scan (PES) using Gaussian software[10] was performed at the MP2/6-311++G(d,p) level of theory. According to the result from the PES, the racemization barrier is around 15 kJ/mol (see Figure 9.4). The interconversion occurs through a C_s symmetric transition state structure. Due to the calculated barrier height, it is expected that under supersonic expansion conditions the two enantiomers are present as a racemic mixture in the molecular jet.

Table 9.1: *Comparison between experimental and calculated molecular parameters of the lowest energy conformers of cyclohexylmethanol (CHM). The labelling of the CHM conformers corresponds to Ref. 3.*

	Experimental	B3LYP-D3/6-311++g(d,p)					
		Gt		**Gg**		**Gg'**	
			Δ^a		Δ		Δ
A | MHz	3886.81327(49)	3874.69	+12	3875.68	+11	3865.87	+21
B | MHz	1311.67154(26)	1306.47	+5	1291.46	+20	1293.89	+18
C | MHz	1057.33702(19)	1052.36	+5	1041.24	+16	1045.78	+12
Δ_J | kHz	0.0889(43)						
Δ_{JK} | kHz	−0.0570(40)						
ΔE [b] | kJ/mol		0.1		0.1		0	
N[c]	53						
σ | kHz	4.18						
μ_a | D		−0.3		−1.7		−1.2	
μ_b | D		1.1		0.4		−0.9	
μ_c | D		0.9		0.9		−1.0	

[a] Deviation from the experimentally determined values.

[b] Zero-point corrected relative energy.

[c] Number of assigned lines.

9.3 Preparative steps for the chiral-sensitive experiment with CHM

9.3.1 Selected rotational energy level cycles

The experiment consists of two parts. In the first part, the enantiomers of CHM are selectively transferred to two rotational levels of choice. Due to this population transfer procedure, an enatiomeric excess (*ee*) in both rotational levels is created. The experiment requires three excitation pulses (drive, twist, and transfer pulse), as described in more detail in Ref. 1 and in Chapter 8.

In the second part, the achieved *ee* is probed by the subsequent M3WM experiment. Here a sequence of only two excitation pulses, drive and twist, is necessary. Overall, two cycles of dipole-allowed rotational transitions, which share a rotational energy level, have to be selected to perform a chiral-sensitive measurement on the molecule of choice.

A set of rotational transitions was determined for the population transfer and the M3WM cycles of Gt. As depicted in Figure 9.5 (by using the same colors for the respective transitions), the excitation pulses in both cycles need to have a specific polarization. Drive pulses (in blue) for both the state-specific enantiomeric enrichment and M3WM have to be applied in the same polarization direction. The same is true for the two twist pulses (in red). Drive and

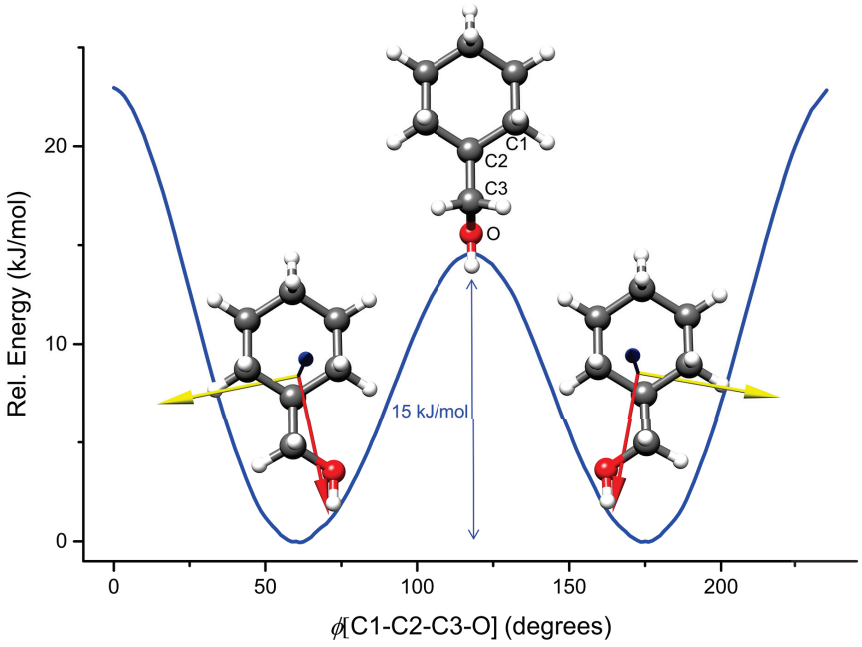

Figure 9.4: *Potential energy scan for the interconversion between the two enantiomers of the cyclohexylmethanol (CHM) conformer Gt calculated at the MP2/6-311++g(d,p) level of theory. The interconversion occurs through a transition state structure with C_s symmetry by rotation of the dihedral angle C1–C2–C3–O. The dipole moment components in the principal axis system for the two enantiomers are represented by the coloured arrows (a-red, b-yellow, and c-blue, respectively).*

twist excitation pulses are orthogonal to each other (Chapter 2). The obtained molecular signal (listen, depicted in green) in M3WM will be recorded as a free induction decay (FID) in the third mutually orthogonal direction.

The b-type transitions of Gt show the highest intensity in the spectrum (see Section 9.2). For this reason, the chosen listen transition was of b-type ($|2_{02}\rangle \leftarrow |3_{13}\rangle$, see Figure 9.5). The dipole moment component μ_c is the second strongest of CHM. Due to the power limitation of the amplifier used for the twist pulses, transitions of c-type were selected as a twist ($|2_{02}\rangle \leftarrow |2_{12}\rangle$ and $|3_{13}\rangle \leftarrow |3_{03}\rangle$, see Figure 9.5). A high-power amplifier was used for the drive pulses, meaning that transitions for drive could be of a-type, since μ_a is the weakest dipole moment components of Gt. More details on the experimental set-up are provided in the next section. General description of the instrumentation is given in Chapter 3. Note that since it was challenging to find two connected cycles of six rotational transitions, which would fulfil all the criteria listed above and show measurable intensity in our frequency range, one of the chosen "drive" transitions was of b- ($|2_{12}\rangle \leftarrow |1_{01}\rangle$ transition at 7058.82 MHz), while the other one ($|3_{03}\rangle \leftarrow |2_{02}\rangle$ transition at 7035.92 MHz) was of a-type (see Figure 9.5).

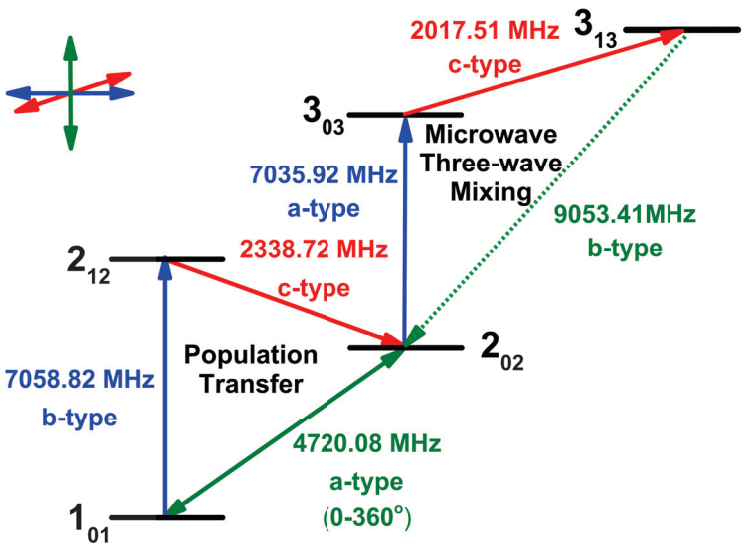

Figure 9.5: *Energy level scheme of cyclohexylmethanol applied for the coherent population transfer and the subsequent microwave three-wave mixing experiments (M3WM) for detection. The rotational levels are denoted using the $J_{K_aK_c}$ notation for an asymmetric top. The color code indicates the orientation of the applied electric fields. The first loop of transitions on the left ("population transfer") creates an enantiomer-dependent population difference between the $|2_{02}\rangle$ and $|1_{01}\rangle$ rotational levels by varying the relative phase of the transfer pulse at 4720.08 MHz. This results in an opposite enantiomeric excess in both levels. The achieved enantiomeric excess is then probed by the second cycle (M3WM) shown on the right. The pulses at 7035.92 MHz (drive) and 2017.51 MHz (twist) create a measurable coherence between the states $|3_{13}\rangle$ and $|2_{02}\rangle$ that is chirality selective and is recorded as a free induction decay (FID).*

9.3.2 Experimental set-up

The set-up for the experiment resembles the one for M3WM (see Chapter 3), with some modifications. The scheme of the set-up is given in Figure 9.6. All pulses were generated using the same source (a two-channel arbitrary waveform generator, AWG) to ensure the pulse phase stability and reproducibility of the experiment. Several amplification pathways were required.

The two drive pulses were amplified using a solid-state amplifier, which operates in the 6-18 GHz frequency range. The pulses were subsequently broadcast across the vacuum chamber via a dual polarization Q-Par horn antenna (2-18 GHz frequency range). This antenna was also used to broadcast the transfer pulse for CPT in the orthogonal direction, after it was amplified with the travelling-wave tube amplifier (TWT). The twist pulses for the population transfer and for the M3WM were transmitted from the second channel of the AWG, amplified via a 30-2300 MHz amplifier, and broadcast using a microwave horn antenna operating in the 1-10 GHz frequency range. This horn antenna was incorporated into the set-up instead of

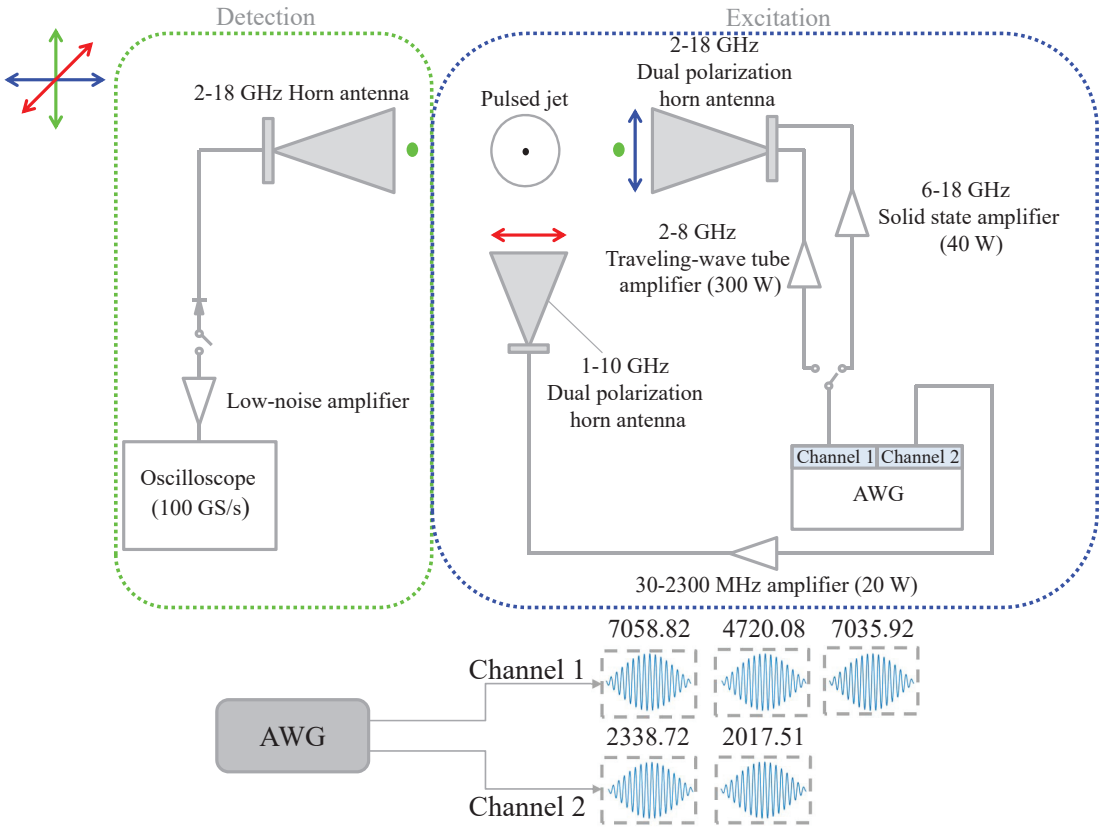

Figure 9.6: *The experimental set-up consists of a modified chirped-pulse Fourier transform microwave (CP-FTMW) spectrometer. The main difference with respect to previous designs is the inclusion of an additional horn antenna operating from 1 to 10 GHz instead of radio frequency plates for the twist pulse. All the microwave pulses were generated from the same source (AWG), to ensure phase stability and reproducibility. Since two amplification pathways were implemented for the excitation pulses coming from channel 1 of the AWG, a switch was used in order to ensure the correct pulse sequence was produced. The applied pulse sequence is depicted in the bottom image inset.*

the previously used radio frequency (RF) electrodes. The main purpose of it is to widen the applicability range of the spectrometer to the different target molecules. The drive and the transfer pulses were transmitted from the same channel of the AWG (see Figure 9.6). However, a time delay was necessary to ensure the correct pulse sequence, where first population transfer and then M3WM takes place. For this reason, a switch was used, as it is shown in Figure 9.6. The applied pulse sequence is summarized in the lower inset of the Figure 9.6.

9.3.3 Optimization of the pulse durations

The drive pulse, which is resonant with the $|2_{12}\rangle \leftarrow |1_{01}\rangle$ transition at 7058.82 MHz in the population transfer cycle (see Figure 9.5), creates a coherence between the two rotational

states $|1_{01}\rangle$ and $|2_{12}\rangle$. As explained in Chapter 2, to achieve the maximal coherence, the pulse has to fulfil a $\pi/2$ condition. Next, the twist pulse for the $|2_{02}\rangle \leftarrow |2_{12}\rangle$ transition at 2338.72 MHz transfers this coherence into a double coherence between the $|1_{01}\rangle$ and $|2_{02}\rangle$ states. This pulse should obey the π condition. The following transfer pulse at 4720.08 MHz converts this double coherence back into the population difference between the rotational states $|1_{01}\rangle$ and $|2_{02}\rangle$. Like the drive pulse, the transfer pulse has to meet the $\pi/2$ condition. The achieved population difference is opposite for both enantiomers. While one of them is promoted to the upper level, the second one is transferred to the lower one. The situation can be reversed by varying the phase of one of the excitation pulses. Here the phase of the transfer pulse was changed from 0 ° to 360 ° in steps of 18 °.

Table 9.2: *Optimized pulse duration for the single-frequency excitation pulses applied for the cyclic population transfer (CPT) and the subsequent microwave three-wave mixing experiment (M3WM) with CHM.*

Pulse	**Transition quantum numbers**	**Frequency (MHz)**	**Pulse duration (ns)**	**Pulse condition**	μ_i^2 [a] (D^2)
drive/CPT	$2_{12} \leftarrow 1_{01}$	7058.82	75	$\pi/2$	1.21
twist/CPT	$2_{02} \leftarrow 2_{12}$	2338.72	2000	π	0.81
transfer pulse/CPT	$1_{01} \leftarrow 2_{02}$	4720.08	175	$\pi/2$	0.09
drive/M3WM cycle	$3_{03} \leftarrow 2_{02}$	7035.92	350	$\pi/2$	0.09
twist/M3WM cycle	$3_{13} \leftarrow 3_{03}$	2017.51	2000	π	0.81

[a] B3LYP-D3/6-311++g(d,p)

Since the molecular ensemble is not racemic any more, a subsequent M3WM experiment can be performed to differentiate between the enantiomers and to probe the obtained *ee*. The differentiation is possible due to the expected characteristic π shift of the FIDs in the time domain at the "listen" frequency (here 9053.41 MHz). M3WM can be applied to probe either the $|1_{01}\rangle$ or the $|2_{02}\rangle$ states, in which the population difference was created. Here the $|2_{02}\rangle$ state was chosen. An experiment involving the $|1_{01}\rangle$ rotational state would be analogous.

For the efficiency of the procedure, the optimization of the excitation pulse duration should take place prior to the actual chiral-sensitive experiment. For this purpose, so-called nutation curves are measured. In this case, the magnitude of the molecular response is monitored as a function of the pulse duration. The results for all five excitation pulses applied for CHM are summarized in Table 9.2. The optimal pulse duration depends on the excitation field strength, the power of the amplifier, and the μ_i^2 values with μ_i being the respective dipole moment components.

9.4 Results

Once the duration of the respective excitation pulses was optimized, the five-pulse sequence scheme given in Figure 9.5 was applied to CHM. The amplitude of the "listen" transition at 9053.41 MHz was recorded as a function of the transfer pulse phase. The results are depicted in Figure 9.7. The maximal response was observed when the phases of the transfer pulse were either 126 ° or 306 °, meaning that the two maxima are separated by 180 ° (see Figure 9.7).

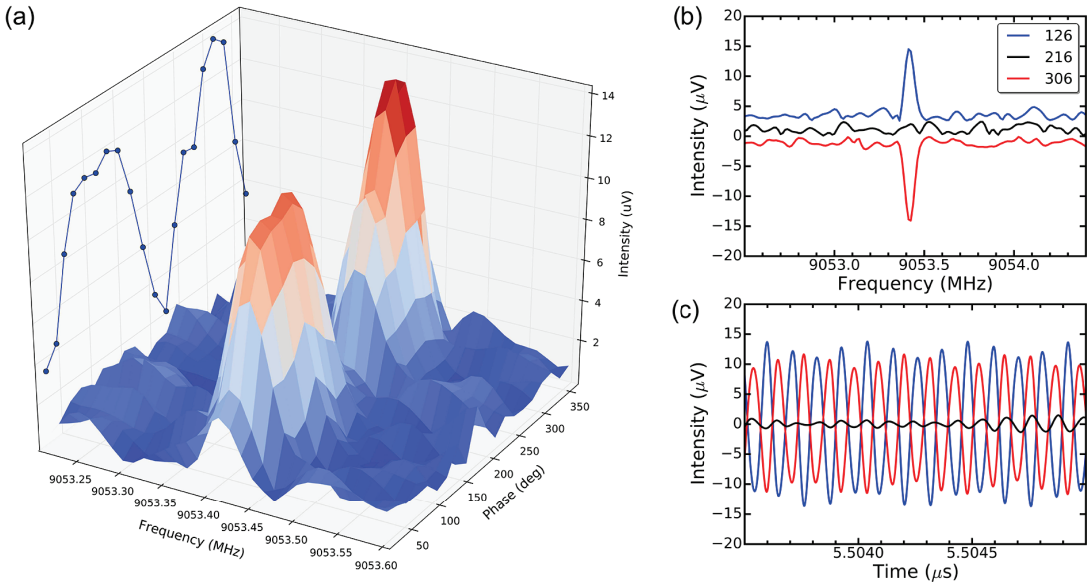

Figure 9.7: *Experimental demonstration of the state-specific population enrichment of CHM. a) The amplitude of the molecular signal at 9053.41 MHz was monitored as a function of the transfer pulse phase (0 °-360 ° in 18 ° steps, 100.000 averages) Maximum signal was observed when the transfer pulse phases were 126 °, and 306 ° respectively. This corresponds to the two enantiomers selectively populating or depopulating the $|2_{02}\rangle$ rotational level, creating an enantiomeric excess (ee). (b) The results in the frequency domain for the recorded M3WM signal at the relevant relative phases (red=306 ° and blue=126 °) are given. The intermediate point at 216,° (black trace) exhibits no signal, as no population enrichment takes place for that particular phase. For the sake of clarity, the red trace is shown in the negative scale and a small offset in the vertical direction was added. (c) A portion of the corresponding FIDs in the time domain is given. The phases of the obtained M3WM signal at the two maxima (126 ° and 306 °) show a π shift, as expected for the two enantiomers, which are no longer present as a racemic mixture.*

The transfer pulse phases of 126 ° or 306 ° yield the optimal enantiomer-specific enrichment in the $|2_{02}\rangle$ rotational state, which could be successfully probed in the M3WM procedure. When population transfer does not take place, no M3WM signal is observed, as it is the case when the transfer pulse phase was 216 ° (see Figure 9.7).

To further validate the observation that both enantiomers can be selectively manipulated, the results in the time domain for the recorded "listen" signal (Figure 9.7 c) were analyzed.

The phases of the M3WM signal at 9053.41 MHz show a clear π shift for a transfer pulse phase of either 126 ° or 306 °, which proves that both enantiomers were selectively transferred to the target $|2_{02}\rangle$ rotational level.

9.5 Summary and Outlook

This study is a unique example for coherent control and manipulation of the two conformers of a non-chiral molecule in a chirality-sensitive manner. The two conformers are mirror images of each other, resulting in an enatiomeric pair, which is present under the cold conditions of a supersonic expansion. They initially form a racemic mixture. By selectively transferring these enantiomers to the rotational state of choice, an *ee* is created, which is probed with a M3WM experiment. The population or depopulation of the respective enantiomer occurs via the variation of the phase of one of the pulses. The magnitude of the obtained signal depends on the initial thermal population between the rotational states. The enhancement can be achieved in future experiments by e.g. using more sophisticated pulse sequences. For instance, the initial population in the rotational levels of choice can be transferred to higher rotational states with a short pulse in a rapid adiabatic regime (RAP) . This would allow to have better starting experimental conditions as demonstrated in Chapter 8. Alternatively, by applying laser pulses the enantiomers can be promoted to higher, less populated vibrational or electronic levels.

This technique extends the possibilities of the M3WM approach. One of the interesting cases for an analysis can be a system where the two conformers become pseudo chiral due to some stabilizing intra-molecular hydrogen bonds. Such pharmaceutically relevant component, the derivative of *N*-benzylamide, was presented recently[11]. The most intriguing aspect is that the two its pseudo-enantiomeric conformers reported in the Ref. 11 have different analgesic activity, making a reliable discrimination between them in a mixture of other possible components even more important. This is only one of the few examples, which shows a significance of the approach presented here.

Bibliography

[1] C. Pérez, A. L. Steber, S. R. Domingos, A. Krin, D. Schmitz, and M. Schnell. Coherent Enantiomer-Selective Population Enrichment Using Tailored Microwave Fields. *Angew. Chem. Int. Ed.*, 56(41):12512–12517, 2017.

[2] N. Borho and Y. Xu. Lock-and-Key Principle on a Microscopic Scale: The Case of the Propylene Oxide Ethanol Complex. *Angew. Chem. Int. Ed.*, 46(13):2276–2279, March 2007.

[3] J. Altnöder, S. Oswald, and M. A. Suhm. Phenyl- vs Cyclohexyl-Substitution in Methanol: Implications for the OH Conformation and for Dispersion-Affected Aggregation from Vibrational Spectra in Supersonic Jets. *J. Phys. Chem. A*, 118(18):3266–3279, 2014.

[4] G. G. Brown, B. C. Dian, K. O. Douglass, S. M. Geyer, S. T. Shipman, and B. H. Pate. A broadband Fourier transform microwave spectrometer based on chirped pulse excitation. *Rev. Sci. Instrum.*, 79(5):053103, 2008.

[5] D. Schmitz, V. A. Shubert, T. Betz, and M. Schnell. Multi-resonance effects within a single chirp in broadband rotational spectroscopy:The rapid adiabatic passage regime for benzonitrile. *J. Mol. Spectrosc.*, 280:77–84, 2012.

[6] D. Plusquellic. JB95. available at http://www.nist.gov/pml/electromagnetics/grp05/jb95.cfm.

[7] H. M. Pickett. The Fitting and Prediction of Vibration-Rotation Spectra with Spin Interactions. *J. Mol. Spectrosc.*, 148:371–377, 1991.

[8] Large Amplitude Motion Potential surface Analyzer, LAMPA v0.1i. https://sourceforge.net/projects/edsoftware/files/LAMPA/LAMPA-IntRoVer.ta/.

[9] M. Juanes, W. Li, L. Spada, L. Evangelisti, A. Lesarri, and W. Caminati. Internal dynamics of cyclohexanol and the cyclohexanol–water adduct. *Phys. Chem. Chem. Phys.*, 21:3676–3682, 2019.

[10] M. J. Frisch, G. W. Trucks, H. B. Schlegel, G. E. Scuseria, M. A. Robb, J. R. Cheeseman, G. Scalmani, V. Barone, B. Mennucci, G. A. Petersson, H. Nakatsuji, M. Caricato, X. Li, H. P. Hratchian, A. F. Izmaylov, J. Bloino, G. Zheng, J. L. Sonnenberg, M. Hada, M. Ehara, K. Toyota, R. Fukuda, J. Hasegawa, M. Ishida, T. Nakajima, Y. Honda, O. Kitao, H. Nakai, T. Vreven, J. A. Montgomery, J. E. Peralta, F. Ogliaro, M. Bearpark, J. J. Heyd, E. Brothers, K. N. Kudin, V. N. Staroverov, R. Kobayashi, J. Normand, K. Raghavachari, A. Rendell, J. C. Burant, S. S. Iyengar, J. Tomasi, M. Cossi, N. Rega, J. M. Millam, M. Klene, J. E. Knox, J. B. Cross, V. Bakken, C. Adamo, J. Jaramillo, R. Gomperts, R. E. Stratmann, O. Yazyev, A. J. Austin, R. Cammi, C. Pomelli, J. W. Ochterski, R. L. Martin, K. Morokuma, V. G. Zakrzewski, G. A. Voth, P. Salvador, J. J. Dannenberg, S. Dapprich, A. D. Daniels, O. Farkas, J. B. Foresman, J. V. Ortiz, J. Cioslowski, and D. J. Fox. Gaussian 09, 2009.

[11] I. V. Ukrainets, L. A. Petrushova, S. Shishkina, L. A. Grinevich, and G. Sim. Synthesis, Spatial Structure and Analgesic Activity of Sodium 3-Benzylaminocarbonyl-1-methyl-2,2-dioxo-1H-2λ,1-benzothiazin-4-olate Solvates. *Sci. Pharm.*, 84:704–715, 12 2016.

10

Summary

Essential oils are mixtures of volatile components, which possess various biological properties. They represent the subject of ongoing research. The crucial points in a detailed characterization of their constituents are structure determination, analysis of their inter- and intramolecular interactions, conformational flexibility, and an unambiguous differentiation between the enantiomers. The last aspect is of importance, since the enantiomers can differ in their biological effects. All these questions can be addressed with broadband rotational spectroscopy. It is a powerful tool for a detailed analysis of the volatile oil components due to its conformer selectivity and mixture compatibility. This was illustrated in the scope of this thesis on the examples of some constituents of peppermint oil and thyme oil. The obtained information complements the one gained with other methods for an analytical study of essential oils, such as gas chromatography (GC).

In the following, results of the structural, dynamical, and chiral analysis for some of the oil constituents presented in this work will be summarized. Additionally to such qualitative analysis, a semi-quantitative study of two chemotypes of thyme essential oil was performed and compared to the GC data. The results are given in Chapter 5. The relative ratios of the main oil constituents determined with rotational spectroscopy show a good agreement with GC. However, for a more accurate characterization, the experiment needs to be conducted 1) using a broad temperature range to test the influence of the experimental conditions on the estimated relative ratios, 2) including experimentally determined dipole moments (if available) into the analysis, 3) accounting for the instrumental effects of several set-up components such as horn antennas, amplifiers.

A detailed structural analysis can help to understand the functionality of the component of interest and to decipher some major aspects in its way of interaction with other molecules. Thus, an accurate structure determination of compounds prevailing in essential oils is of great benefit and importance. For instance, menthol, the main component of peppermint oil, is known to inhibit our nicotinic acetylcholine receptors. Structural and conformational analysis of this molecule may provide new insights in this biochemical process. The structure of the lowest energy conformer of menthol was determined in this work. The signal-to-noise ratio (SNR) was sufficient to obtain such information directly from the recorded oil broadband

spectrum. The results are summarized in Chapter 4. Additionally, another menthol conformer was identified in the spectrum. Its assignment was guided by a separate measurement on a pure menthol sample.

Structures of some other oil constituents were determined experimentally and reported in this thesis. These were the lowest energy conformers of thymol, linalool (see Chapter 5), and pulegone (Chapter 6). In case of linalool and pulegone, the SNR was not sufficient for their structure determination directly from the oil spectrum. To aid the analysis, separate broadband measurements on the pure samples of the respective components were performed instead.

The components analyzed in this thesis are structurally flexible and can possess different conformational and isomeric forms. Menthyl acetate, a monoterpene present in peppermint oil, is one example for this conformational complexity. It is a chiral molecule, and has three stereogenic centers and thus four diastereomers: menthyl acetate, isomenthyl acetate, neomenthyl acetate, and neoisomenthyl acetate. An extensive computational analysis was performed with the aim to determine all possible lowest energy conformers and to assign them in the broadband spectrum. Two lowest energy conformers of menthyl acetate were identified in the spectrum. Other diastereomers were not observed, which indicates their low concentration in the used sample. Since menthyl acetate is of pharmaceutical interest as e.g. a potential blocker of the enzyme arylamine N-acetyltransferase (NAT), the conformational analysis presented here can be useful in the context of its further characterization.

Another conformational study conducted in this work is focused on one of the menthol diastereomers, neomenthol (Chapter 4). Like menthol, it has a wide range of applications in pharmacology and medicine. Neomenthol could not be observed experimentally in the peppermint oil broadband spectrum discussed here, possibly due to its low abundance in the analyzed sample. Nevertheless, its theoretical conformational analysis can still be of interest for the future exploration of this compound.

Some components discussed here show internal dynamics, resulting from the internal rotation of their methyl tops. In the present work the internal rotation barriers were determined for linalool (Chapter 5), *trans*-thymol-B (Chapter 5), pulegone (Chapter 6), and menthyl acetate (Chapter 7). Linalool and pulegone show some similarities with respect to their observed internal rotation. Two inequivalent methyl tops attached to an sp^2-hybridized C-atom are involved in the internal rotation for both of these molecules. This gives rise to a characteristic fine structure in the broadband spectra with AA, AE, EA, EE and EE* states. However, the AE states could not be resolved for pulegone and in most cases for linalool. The determined rotation barriers were higher for the two tops of linalool (4.7707(95) kJ/mol and 9.2581(74) kJ/mol) in comparison to pulegone (1.961911(46) kJ/mol and 6.3617(12) kJ/mol). The internal rotation of one of the linalool methyl tops was analyzed previously by Nguyen et al. Our experimentally determined internal rotation barrier (4.7707(95) kJ/mol or 398.81(80) cm^{-1}) shows a good agreement with the previously reported result (400.20(64) cm^{-1}).

In case of *trans*-thymol-B and menthyl acetate, the internal rotation barrier of only one methyl top is low enough to result in observable splittings in the spectrum. Therefore, the splitting pattern represents doublets. The experimentally determined V_3 barrier of *trans*-thymol-B is 0.300330(17) kJ/mol, and is consistent with the theoretically predicted value obtained in the previous study on thymol (0.261 kJ/mol, B3LYP/6-311++G(d,p)).

For menthly acetate, the methyl top involved in the internal rotation is part of the acetate group. Due to the observed SNR, the internal dynamics of only the lowest energy conformer of menthyl acetate was characterized here. The determined internal rotation barrier of 1.1828960(70) kJ/mol agrees well with the barriers of other acetates such as *n*-butyl acetate (1.134323(96) kJ/mol), ethyl acetate (1.21548(28) kJ/mol), isoamyl acetate (1.12393(16) kJ/mol) published in literature. This shows that the core structure of the molecule has low influence on the acetyl methyl top internal rotation.

Several oil compounds analyzed in this work are chiral. The differentiation between their enantiomers is possible with the recently developed microwave three-wave mixing (M3WM) technique, which is based on broadband rotational spectroscopy. The excitation of the sample is performed with two orthogonally polarized pulses drive and twist, while the molecular signal is recorded as a free induction decay in the third mutually orthogonal direction ("listen", see Chapter 2 for more details). The M3WM experiments were conducted on some of the peppermint oil constituents such as menthone and isomenthone (Chapter 5) directly in the oil. In particular, (–)-menthone was determined to be the excess enantiomer in peppermint oil. This is in accordance with the results from previous chiral GC-MS studies, and shows the capability of our technique. For isomenthone, no such comparison could be done due to the lack of an enantiopure isomenthone sample as a reference for our M3WM experiment. The M3WM experiments on other peppermint oil components such as pulegone or menthyl acetate could not be performed directly in the oil because of their low abundance in the utilized oil sample. For this reason, a separate experiment was carried out on the enantio-enriched samples of these molecules to determine possible M3WM cycles (Chapters 6 and 7). Since natural essential oils differ in their chemical composition, the idea would be to repeat the M3WM experiment with oil samples containing higher amount on pulegone and menthyl acetate. This would allow to benchmark our technique as a tool for a comprehensive chiral analysis of complex mixtures.

Another important analytical question is the quantification of the enantiomeric excess (*ee*), the ratio of the enantiomers to each other. In Chapter 8 it was demonstrated on the example of menthone that the *ee* can be determined by monitoring the constructive or destructive interference between the applied M3WM pulse sequence ("two-photon process"), and the direct excitation of the listen transition ("one-photon process"). The experiment was not performed on essential oils, but a commercially available menthone sample (mixture of isomers) was used instead. According to our results, (–)-menthone is with 83% in excess in the used sample. In the previous experiment reported by Schmitz et al. the *ee* value of (–)-menthone in the mixture used here was determined to be 62.5% ± 24.2%. Within the experimental uncertainty, this is in agreement with the results discussed in Chapter 8.

Recently, M3WM was extended to allow state-specific enantiomeric enrichment. In contrast to M3WM, a sequence of three instead of two orthogonally polarized excitation pulses is required for this purpose. The approach was introduced in Chapter 8. It was shown that by the simultaneous excitation of all three kinds of electric dipole-allowed rotational transitions the enantiomers can be separated in two rotational levels of choice. The obtained enantiomeric enrichment can than be probed by an additional fourth pulse, which shares the energy level with one of the chosen rotational states. In the present study a 6% enantiomeric enrichment was achieved, which is one order of magnitude larger than the result reported in a buffer-gas cell experiment. The coherent population transfer (CPT) approach establishes a novel method for controlled manipulation of enantiomers using tailored microwave fields. It can be viewed as a step towards robust and accessible methods for the enantiomeric separation. In fact, such separation can be realized in the future by using inhomogeneous Stark effect.

Once the CPT was combined with the M3WM experiment, conformers of a molecule without stereogenic center could be manipulated in a chirality-sensitive manner. In this case cyclohexylmethanol was used as a test molecule for the proof of principle (Chapter 9). The two chiral conformers of cyclohexylmethanol with a high interconversion barrier are present as a racemic mixture in the molecular beam. After the CPT the two conformers populate two different rotational states, creating an *ee*. The achieved *ee* was successfully probed with the subsequent M3WM experiment. This is the first demonstration of the enantiomer-specific population enrichment in a pair of chiral conformers. Such an approach opens doors to the experiments on a variety of molecular classes including those with low racemization barriers.

Overall, this thesis not only demonstrates the power of rotational spectroscopy as a technique for a detailed analysis of complex mixtures, a fact known from numerous other studies. The examples discussed here also show the applicability of rotational spectroscopy as a potential tool for chiral analysis, which allows an unambiguous enantiomeric differentiation, *ee* determination, and enantiomeric enrichment in the rotational levels of choice.

Acknowledgments

Scientific research is unthinkable without teamwork. I had a great pleasure to work in the international and friendly team in the group of Prof. Dr. Melanie Schnell in Hamburg. I would like to thank each and every member (current and former) for their help and support during my internship and PhD there. Particularly, I would like to thank the group leader, Prof. Dr. Melanie Schnell, for giving me the chance, to do my first step in scientific carrier, to broaden my horizon, and to enjoy science beyond the walls of a lecture hall.

I am very thankful to Dr. V. Alvin Shubert and Dr. Cristóbal Pérez for introducing me to the intriguing filed of rotational spectroscopy. Several experiments presented in this thesis and beyond were carried out in a collaborative effort with my colleagues. I would like to thank Dr. V. Alvin Shubert, Dr. Pablo Pinacho, Dr. María Quesada-Moreno, and Dr. Sérgio R. Domingos for this fruitful collaboration, and for their patience, while working with me on the experiments. Especially, I would like to thank Dr. Cristóbal Pérez for the opportunity to work with him on the novel experimental approaches in chiral analysis, and to learn from him "to think outside the box".

I greatly appreciate the hospitality and support by Prof. Dr. Yunjie Xu and Prof. Dr. Wolfgang Jäger during my research stay at the University of Alberta in Edmonton, Canada. I would also like to thank M.Sc. Amin Moazeni for helping me with my very first VCD experiments (not discussed in this thesis).

I am also very thankful to M.Sc. Benjamin E. Arenas, M.Sc. Mariyam Fatima, and Dr. Denis Tikhonov for proofreading this manuscript and for their helpful comments and suggestions.

I acknowledge the funding by the International Max Planck Research School, IMPRS (a three-year scholarship) and the German Academic Exchange Service, DAAD (short-term grant for doctoral students).

Finally, I would like to thank my family, especially my Dad, my husband Dimitri Krush, and my daughter Alexandra for giving me the strength to finish this work.

Eidesstattliche Versicherung

Hiermit erkläre ich an Eides statt, dass ich die vorliegende Dissertationsschrift selbst verfasst und keine anderen als die angegebenen Quellen und Hilfsmittel benutzt habe.

Hamburg, 29.11.2019

Unterschrift

List of chemical compounds used in the thesis

Table 1: *Hazard and precautionary statements for chemical compounds listed in the thesis.*

Compound	IUPAC	Hazard statement(s)[1]	Precautionary statement(s)[1]
Carvone	2-methyl-5-prop-1-en-2-ylcyclohex-2-en-1-one	H302, H317	P261, P264, P270, P272, P280, P301+P312, P302+P352, P321, P330, P333+P313, P363, P501
Cyclohexylmethanol	cyclohexylmethanol	H227, H315, H319, H335	P210, P261, P264, P271, P280, P302+P352, P304+P340, P305+P351+P338, P312, P321, P332+P313, P337+P313, P362, P370+P378, P403+P233, P403+P235, P405, P501
Ethanol	ethanol	H225	P210, P233, P240, P241, P242, P243, P280, P303+P361+P353, P370+P378, P403+P235, P501
Isomenthone	5-methyl-2-propan-2-ylcyclohexan-1-one	H315, H317,412	P261, P264, P272, P273, P280, P302+P352, P321, P332+P313, P333+P313, P362, P363, P501
Linalool	3,7-dimethylocta-1,6-dien-3-ol	H315, H317, H319	P261, P264, P272, P280, P302+P352, P305+P351+P338, P321, P332+P313, P333+P313, P337+P313, P362, P363, P501
Menthone	5-methyl-2-propan-2-ylcyclohexan-1-one	H315, H317, H319	P261, P264, P272, P280, P302+P352, P305+P351+P338, P321, P332+P313, P333+P313, P337+P313, P362, P363, P501
Menthyl acetate	(5-methyl-2-propan-2-ylcyclohexyl) acetate	H410	P273, P391, P501
Peppermint oil	_____	H227, H315, H317	P264, P270, P280, P301+P312, P302+P352, P305+P351+P338, P321, P330, P332+P313, P337+P313, P362, P501
Pulegone	5-methyl-2-propan-2-ylidenecyclohexan-1-one	H302	P264, P270, P301+P312, P330, P501
Thyme oil	_____	H226, H302, H304, H314, H317, H361, H411	P210, P273, P280, P301+P310, P301+P330+P331, P303+P361+P353, P304+P340+P310

[1]according to the Global Harmonized System (GHS) within the EU

Appendix

A

Structural and chiral analysis of the components in peppermint oil

Table A.1: *Rotational parameters for ^{13}C single isotopically substituted species of EQ1ext. For atom labelling see Figure 4.3.*

	C1	C2	C3	C4	C5
A | (MHz)	1778.4889(16)	1765.9039(13)	1767.53200(84)	1778.9892(16)	1772.1706(16)
B | (MHz)	687.83821(41)	690.61883(44)	692.60128(27)	692.09669(37)	692.60342(53)
C | (MHz)	570.10432(50)	570.57394(42)	572.10285(18)	573.07249(28)	572.57348(44
Δ_J | (kHz)	*a*	*a*	*a*	*a*	*a*
N_{lines}[b]	12	21	17	17	16
σ | (kHz)	8.04	8.06	5.14	5.23	5.79

	C6	C7	C8	C9	C10
A | (MHz)	1773.3409(27)	1779.05350(89)	1779.7508(11)	1768.6344(86)	1767.942(43)
B | (MHz)	690.23956(16)	679.85227(17)	688.10184(38)	684.62473(43)	683.66514(60)
C | (MHz)	571.08024(16)	564.49396(19)	570.2554(42)	569.01546(38)	566.99040(56)
Δ_J | (kHz)	*a*	*a*	*a*	*a*	*a*
N_{lines}[b]	17	22	18	14	11
σ | (kHz)	4.80	6.31	6.54	4.96	4.30

[a] Kept fixed at the value for the normal species $\Delta_J = 0.0168(45)$.

[b] The number of fitted lines.

Table A.2: *Experimentally (r_0, r_s) and computationally (r_e, MP2/6-311++G(d,p)) determined structural parameters for the EQ1ext conformer of menthol.*

	r_0	r_s	Ab initio r_e
r(C1-C2) | Å	1.549(16)	1.5514 (56)	1.53
r(C2-C3) | Å	1.532(22)	*1.4951(30)*[a]	1.53
r(C3-C4) | Å	1.540(15)	*1.6355(33)*	1.54
r(C4-C5) | Å	1.533(16)	*1.3781(42)*	1.53
r(C5-C6) | Å	1.5303(93)	*1.6154(28)*	1.53
r(C1-C6) | Å	[1.53][b]	1.5306(60)	1.53
r(C1-C7) | Å	1.5329(49)	1.522(11)	1.54
r(C4-C8) | Å	1.5493(58)	*1.5598(34)*	1.53
r(C8-C9) | Å	1.5469(92)	*1.516(13)*	1.53
r(C8-C10) | Å	1.5379(65)	*1.5333(75)*	1.53
∡(C1-C2-C3) | °	111.32(43)	*110.10(33)*	111.82
∡(C2-C3-C4) | °	111.52(52)	*110.52(30)*	111.46
∡(C3-C4-C5) | °	[108.84]	*110.93(32)*	108.84
∡(C4-C5-C6) | °	110.21(57)	*109.89(36)*	111.13
∡(C5-C6-C1) | °	[111.96]	*112.72(34)*	111.96
∡(C6-C1-C2) | °	[109.33]	108.40(28)	109.33
∡(C7-C1-C2) | °	110 (1)	111.83(94)	111.67
∡(C7-C1-C6) | °	[111.28]	112.02(93)	111.28
∡(C5-C4-C8) | °	[112.49]	*113.82(32)*	112.49
∡(C3-C4-C8) | °	[114.42]	*109.69(26)*	114.42
∡(C4-C8-C10) | °	[111.37]	*114.31(55)*	111.37
∡(C4-C8-C9) | °	113.16(41)	*114.74(66)*	113.50
∡(C9-C8-C10) | °	[110.32]	*111.37(35)*	110.32
∡(C7-C1-C2-C3) | °	[-178.37]	*178(1)*	-178.37
∡(C7-C1-C6-C5) | °	[179.38]	*179(1)*	179.38
∡(C1-C2-C3-C4) | °	[56.99]	*58.17(67)*	56.99
∡(C1-C6-C5-C4) | °	[-58.32]	*-57.87(82)*	-58.32
∡(C2-C3-C4-C8) | °	[176.18]	*172.91(64)*	176.18
∡(C3-C4-C8-C9) | °	58.17(91)	*64.66(35)*	65.34
∡(C3-C4-C8-C10) | °	-64.72(88)	*-65.77(84)*	-59.88
∡(C5-C4-C3-C2) | °	[-57.03]	*-60.49(65)*	-57.03
∡(C6-C5-C4-C3) | °	59(1)	*56.37(69)*	57.53
∡(C5-C4-C8-C9) | °	[-59.54]	*-60.29(47)*	-59.54
∡(C5-C4-C8-C10) | °	[175.24]	*169.29(58)*	175.24

[a] The distances and angles which involve C3, C4, C5, C8, and C9 atoms (in italics) have been calculated by setting the imaginary r_s coordinates to zero.

[b] Values kept fixed to ab initio predicted structure.

Table A.3: *Measured rotational transitions ($\nu_{\rm obs}$) for EQ3ext, and the residuals ($\nu_{\rm obs} - \nu_{\rm calc}$) for the fit reported in Table 4.2.*

J'	K'_a	K'_c	$\leftarrow$	J''	K''_a	K''_c	$\nu_{\rm obs}$(GHz)	$\nu_{\rm obs} - \nu_{\rm calc}$ (MHz)
3	1	3	$\leftarrow$	2	1	2	3.6139419	-0.0008
3	0	3	$\leftarrow$	2	0	2	3.7366561	0.0038
3	1	2	$\leftarrow$	2	1	1	3.8916596	0.0082
4	1	4	$\leftarrow$	3	1	3	4.8133261	-0.0036
4	0	4	$\leftarrow$	3	0	3	4.9604042	0.0020
4	1	3	$\leftarrow$	3	1	2	5.1828892	0.0094
5	1	5	$\leftarrow$	4	1	4	6.0086546	0.0008
8	3	6	$\leftarrow$	8	2	6	6.0538828	0.0231
5	0	5	$\leftarrow$	4	0	4	6.1671658	0.0059
5	2	4	$\leftarrow$	4	2	3	6.2489780	-0.0089
5	3	2	$\leftarrow$	4	3	1	6.2778895	-0.0016
5	2	3	$\leftarrow$	4	2	2	6.3414643	-0.0029
5	1	4	$\leftarrow$	4	1	3	6.4685047	0.0090
6	1	6	$\leftarrow$	5	1	5	7.1994202	-0.0006
11	2	10	$\leftarrow$	11	0	11	7.3149652	0.0077
6	0	6	$\leftarrow$	5	0	5	7.3559241	0.0168
6	2	5	$\leftarrow$	5	2	4	7.4900059	0.0064
6	3	4	$\leftarrow$	5	3	3	7.5338714	-0.0112
6	3	3	$\leftarrow$	5	3	2	7.5425271	-0.0070
6	1	5	$\leftarrow$	5	1	4	7.7465097	0.0112
6	4	3	$\leftarrow$	5	4	2	7.5279076	-0.0041
6	4	2	$\leftarrow$	5	4	1	7.5280561	-0.0069
2	2	1	$\leftarrow$	1	1	0	6.4666944	-0.0097
5	3	3	$\leftarrow$	4	3	2	6.2746205	-0.0043
7	1	6	$\leftarrow$	6	2	4	5.6157278	0.0079
4	2	2	$\leftarrow$	3	2	1	5.0513318	-0.0007
4	2	3	$\leftarrow$	3	2	2	5.0040043	0.0067
5	2	4	$\leftarrow$	5	1	5	4.7209467	0.0057
2	1	1	$\leftarrow$	1	0	1	3.9791837	-0.0019
2	1	2	$\leftarrow$	1	1	1	2.4112516	0.0010
6	2	4	$\leftarrow$	5	2	3	7.6455317	-0.0136
6	3	3	$\leftarrow$	5	3	2	7.5425270	-0.0071
4	3	1	$\leftarrow$	4	2	3	6.6988239	-0.0179
2	2	1	$\leftarrow$	1	1	0	6.4666944	-0.0097
2	0	2	$\leftarrow$	1	0	1	2.4990642	0.0022
							RMS	8.638 kHz

B

Rotational spectroscopy study of two chemotypes of thyme oil

Table B.1: *Rotational parameters for* ^{13}C *single isotopically substituted species of trans-thymol-A. For atom labelling see Figure 5.4.*

	C1	C2	C3	C4	C5
A | MHz	2047.4951(82)	2048.256(65)	2055.449(41)	2039.283(32)	2040.516(88)
B | MHz	739.13783(78)	736.5987(13)	733.88943(84)	736.85042(60)	739.1859(26)
C | MHz	590.83356(50)	589.2441(10)	588.09237(70)	588.65962(62)	590.2372(17)
N_{lines}[a]	16	10	13	12	7
σ(kHz)	7.22	8.63	5.85	4.58	7.89

	C6	C7	C8	C9	C10
A | MHz	2055.658(41)	2055.692(46)	2042.70280(85)	2037.441(41)	2055.130(34)
B | MHz	738.78814(60)	734.3329(11)	730.14210(38)	730.37175(78)	724.46602(56)
C | MHz	591.27520(57)	588.44167(79)	586.63359(25)	584.90937(73)	582.02802(60)
N_{lines}[a]	10	10	5	12	11
σ(kHz)	4.43	5.45	1.10	5.40	4.35

[a]Number of fitted lines.

Table B.2: *Experimentally (r_0, r_s) and computationally (r_e, MP2/6-311++G(d,p)) determined structural parameters of trans-thymol-A conformer of thymol.*

	r_0	r_s	Ab initio r_e
r(C1-C2) | Å	1.419(35)	1.446(15)	1.40
r(C2-C3) | Å	1.384(23)	1.3968(87)	1.40
r(C3-C4) | Å	1.389 (17)	1.3968(69)	1.40
r(C4-C5) | Å	1.391(30)	*1.4711(18)*[a]	1.40
r(C5-C6) | Å	1.437(32)	*1.374(13)*	1.40
r(C3-C10) | Å	1.5085(74)	1.5093(22)	1.51
r(C6-C7) | Å	1.518(26)	*1.5395(37)*	1.51
r(C7-C8) | Å	1.533(25)	*1.5530(99)*	1.54
r(C7-C9) | Å	1.544(19)	*1.5901(35)*	1.53
∠(C1-C2-C3) | °	121(1)	*120.67(27)*	121.0
∠(C2-C3-C4) | °	118.22(67)	117.94(25)	118.1
∠(C2-C3-C10) | °	[120.5][b]	120.77(54)	120.5
∠(C3-C4-C5) | °	120.55(76)	*120.52(27)*	118.1
∠(C4-C3-C10) | °	[121.5]	121.25(57)	121.5
∠(C4-C5-C6) | °	[121.9]	*117.75(33)*	121.9
∠(C5-C6-C7) | °	[123.4]	*120.46(81)*	123.4
∠(C5-C6-C1) | °	[117.0]	*123.11(62)*	117.0
∠(C6-C1-C2) | °	[121.4]	119.92(66)	121.4
∠(C6-C7-C8) | °	109.24(75)	*109.32(73)*	109.3
∠(C6-C7-C9) | °	113.41(83)	*110.96(56)*	113.3
∠(C8-C7-C9) | °	[110.7]	*108.45(37)*	110.7
∠(C1-C2-C3-C10) | °	[-178.1]	-179(2)	-178.1
∠(C10-C3-C4-C5) | °	[178.4]	*-180(2)*	178.4
∠(C4-C5-C6-C7) | °	[-178.0]	*-177(1)*	-178.0
∠(C5-C6-C7-C8) | °	[96.2]	*96.14(95)*	96.2
∠(C5-C6-C7-C9) | °	-21(2)	-23(1)	-28.0
∠(C1-C6-C7-C8) | °	[-80.5]	*-80(1)*	-80.5
∠(C1-C6-C7-C9) | °	[155.3]	*160.62(90)*	155.3
∠(C6-C7-C8-C9) | °	[-125.7]	*-121.10(67)*	-125.7

[a] The distances and angles which involve C5 and C7 atoms (in italics) have been calculated by setting the imaginary r_s coordinates to zero.

[b] Values kept fixed to ab initio predicted structure.

Table B.3: *Measured rotational transitions (ν_{obs}) and the residuals ($\nu_{\mathrm{obs}} - \nu_{\mathrm{calc}}$) of trans-thymol-B as obtained after the fit with the programm XIAM.*

J'	K'_a	K'_c	$\leftarrow$	J''	K''_a	K''_c		$\nu_{\mathrm{obs}} - \nu_{\mathrm{calc}}$ (MHz)	ν_{obs}(GHz)
2	0	2	$\leftarrow$	1	0	1	A	.0084	2.6371620
1	1	1	$\leftarrow$	0	0	0	A	.0047	2.8729302
3	1	3	$\leftarrow$	2	1	2	A	-.0005	3.8140600
							E	.0052	3.8077337
4	0	4	$\leftarrow$	3	1	3	A	.0056	3.9107720
3	0	3	$\leftarrow$	2	0	2	A	.0088	3.9447720
							E	.0026	3.9205170
2	1	2	$\leftarrow$	1	0	1	A	.0029	4.0966511
3	1	2	$\leftarrow$	2	1	1	A	-.0039	4.1051100
6	2	4	$\leftarrow$	6	1	5	A	-.0059	4.1176592
4	2	2	$\leftarrow$	4	1	3	A	-.0044	4.3908747
4	1	4	$\leftarrow$	3	1	3	A	.0026	5.0805550
							E	.0034	5.0739328
4	0	4	$\leftarrow$	3	0	3	A	.0017	5.2395600
							E	-.0012	5.2179010
4	2	3	$\leftarrow$	3	2	2	A	.0084	5.2797050
4	2	2	$\leftarrow$	3	2	1	A	.0007	5.3232651
5	0	5	$\leftarrow$	4	1	4	A	.0030	5.3485381
4	1	3	$\leftarrow$	3	1	2	A	-.0022	5.4680370
							E	.0115	5.4797150
4	1	4	$\leftarrow$	3	0	3	A	.0077	6.4093520
5	0	5	$\leftarrow$	4	0	4	A	.0060	6.5183270
							E	-.0002	6.5030840
5	2	4	$\leftarrow$	4	2	3	A	.0031	6.5941140
5	3	3	$\leftarrow$	4	3	2	A	-.0069	6.6177900
5	3	2	$\leftarrow$	4	3	1	A	-.0066	6.6204138
5	2	3	$\leftarrow$	4	2	2	A	-.0007	6.6796770
6	0	6	$\leftarrow$	5	1	5	A	-.0072	6.7847420
5	1	4	$\leftarrow$	4	1	3	A	-.0042	6.8259080
							E	.0132	6.8246813
5	1	5	$\leftarrow$	4	1	4	A	.0060	6.3432436
							E	.0019	6.3363895
2	2	0	$\leftarrow$	1	1	1	A	.0038	7.4965250
5	1	5	$\leftarrow$	4	0	4	A	.0075	7.5130310
							E	-.0031	7.5669720
6	1	6	$\leftarrow$	5	1	5	A	-.0068	7.6015842
							E	-.0097	7.5948725
6	0	6	$\leftarrow$	5	0	5	A	.0029	7.7794546
							E	-.0134	7.7720585
6	3	4	$\leftarrow$	5	3	3	A	-.0065	7.9455730
6	3	3	$\leftarrow$	5	3	2	A	-.0130	7.9525263
								RMS	6.950 kHz

Table B.4: *Rotational parameters for ^{13}C single isotopically substituted species of energetically lowest conformer of linalool, which was analyzed previously with rotational spectroscopy (Nguyen, et. al, Phys. Chem. Chem Phys, 15:10012-10018, 2013). For atom labelling see Figure 5.5*

	C1	C2	C3	C4	C5
A | MHz	1646.4221(21)	1634.7710(14)	1632.25(18)	1642.9206(36)	1638.6873(35)
B | MHz	679.64186(50)	680.57096(66)	680.5122(14)	673.28321(70)	679.27907(61)
C | MHz	616.62645(61)	616.60856(62)	617.9447(11)	611.36498(96)	615.6117(10)
N_{lines}[a]	18	17	14	11	15
σ(kHz)	9.2	7.9	8.5	9.6	8.3

	C6	C7	C8	C9	C10
A | MHz	1640.4013(31)	1646.8114(48)	1639.9475(21)	1636.0335(29)	1620.0631(35)
B | MHz	680.3364(11)	677.40273(95)	671.10972(70))	676.77637(93))	680.88714(72)
C | MHz	616.49375(83)	614.80495(80)	610.41089(71)	613.33782(56)	613.86295(74)
N_{lines}[a]	13	11	17	17	12
σ(kHz)	7.8	7.0	9.1	8.0	7.1

[a]Number of fitted lines.

Table B.5: *Experimentally (r_0, r_s) and computationally (r_e, MP2/6-311++G(d,p)) determined structural parameters of the lowest energy conformer of linalool.*

	r_0	r_s	Ab initio r_e
r(C1-O1) | Å	1.440(32)	-	1.43
r(C1-C2) | Å	1.550(21)	1.5205(92)	1.54
r(C1-C5) | Å	1.505(16)	1.4758(88)	1.51
r(C1-C4)| Å	1.5227(98)	1.5438(44)	1.53
r(C5-C10)| Å	1.332(16)	*1.3531(19)*[a]	1.34
r(C2-C3)| Å	1.551(29)	1.524(26)	1.54
r(C3-C6)| Å	1.464(35)	1.475(22)	1.50
r(C6-C7)| Å	1.374(20)	*1.4220(18)*	1.35
r(C7-C8)| Å	1.515(11)	*1.5388(15)*	1.51
r(C7-C9)| Å	1.475(16)	*1.4293(15)*	1.51
∡(C2-C1-O1)| °	107.57(99)	-	110.9
∡(C4-C1-O1)| °	[105.1][b]	-	105.1
∡(C5-C1-O1)| °	117(1)	-	111.9
∡(C1-C5-C10)| °	[124.9]	*125.40(44)*	124.9
∡(C4-C1-C5)| °	[109.3]	110.29(29)	109.3
∡(C4-C1-C2)| °	[109.7]	109.45(44)	109.7
∡(C1-C2-C3)| °	115.56(73)	114.87(36)	115.2
∡(C2-C3-C6)| °	115.39(61)	114.57(55)	113.0
∡(C3-C6-C7)| °	130(1)	*126.93(46)*	128.2
∡(C6-C7-C8)| °	[120.5]	*116.80(22)*	120.5
∡(C6-C7-C9)| °	124.33(80)	*125.80(16)*	124.9
∡(C5-C1-C2)| °	[109.8]	112.92(75)	109.8
∡(C8-C7-C9)| °	[114.6]	*117.38(18)*	114.6
∡(C3-C2-C1-O1)| °	[-69.0]	-	-69.0
∡(C4-C1-O1-C2)| °	117.48(83)	-	118.5
∡(C5-C1-O1-C4)| °	[118.5]	-	118.5
∡(C10-C5-C1-C4)| °	[110.0]	*110.07(49)*	110.0
∡(C10-C5-C1-C2)| °	[-129.6]	*-127.12(45)*	-129.6
∡(C1-C2-C3-C6)| °	[65.6]	71.25(84)	65.6
∡(C4-C1-C2-C3)| °	[175.3]	178.40(68)	175.3
∡(C2-C3-C6-C7)| °	-121.85(86)	*-122.77(57)*	-122.9
∡(C3-C6-C7-C9)| °	[-0.7]	*-2.92(99)*	-0.7
∡(C3-C6-C7-C8)| °	[-179.6]	*178.95(94)*	-179.6
∡(C6-C7-C8-C9)| °	[179.0]	*178.29(20)*	179.0

[a] The distances and angles which involve C7 and C10 atoms (in italics) have been calculated by setting the imaginary r_s coordinates to zero.

[b] Values kept fixed to ab initio predicted structure.

Table B.6: *Measured rotational transitions (ν_{obs}) and the residuals ($\nu_{\mathrm{obs}} - \nu_{\mathrm{calc}}$) for linalool, determined with XIAM.*

J'	K'_a	K'_c	$\leftarrow$	J''	K''_a	K''_c		$\nu_{\mathrm{obs}} - \nu_{\mathrm{calc}}$ (MHz)	ν_{obs} (GHz)
7	2	6	$\leftarrow$	7	1	6	AA	-.0186	2.1491649
							EA	-.0113	2.1492959
1	1	0	$\leftarrow$	0	0	0	AA	-.0187	2.3289212
6	2	5	$\leftarrow$	6	1	5	AA	-.0062	2.3491437
							EA	-.0050	2.3492381
4	1	3	$\leftarrow$	3	2	1	AA	-.0048	2.5089019
							EA	.0060	2.5087906
5	2	4	$\leftarrow$	5	1	4	AA	-.0032	2.5262840
							EA	.0035	2.5263563
2	1	2	$\leftarrow$	1	1	1	AA	-.0094	2.5384458
2	0	2	$\leftarrow$	1	0	1	AA	-.0068	2.5988730
2	1	1	$\leftarrow$	1	1	0	AA	-.0076	2.6653508
4	2	3	$\leftarrow$	4	1	3	AA	.0312	2.6774551
6	2	5	$\leftarrow$	5	3	3	AA	-.0001	2.7845499
							EA	.0069	2.7848117
							EE	.0091	2.7849103
							EE*	.0108	2.7847315
3	0	3	$\leftarrow$	2	1	1	AA	-.0224	2.7963023
3	2	2	$\leftarrow$	3	1	2	AA	.0068	2.8003598
2	2	1	$\leftarrow$	2	1	1	AA	-.0028	2.8935934
							EA	-.0061	2.8934752
6	2	4	$\leftarrow$	5	3	2	AA	-.0041	2.9846165
							EA	.0127	2.9841564
							EE	-.0016	2.9840505
							EE*	.0002	2.9842328
5	1	5	$\leftarrow$	4	2	3	AA	.0201	3.0224945
2	2	0	$\leftarrow$	2	1	2	AA	.0045	3.0869848
							EA	-.0027	3.0871211
3	2	1	$\leftarrow$	3	1	3	AA	.0072	3.1960748
4	2	2	$\leftarrow$	4	1	4	AA	-.0147	3.3562557
8	3	5	$\leftarrow$	7	4	3	AA	-.0131	3.5166831
							AE	-.0142	3.5166012
5	2	3	$\leftarrow$	5	1	5	AA	.0091	3.5790609
							EA	-.0036	3.5789745
2	1	1	$\leftarrow$	1	0	1	AA	.0195	3.6933625
							EA	-.0071	3.6933126
3	1	3	$\leftarrow$	2	1	2	AA	.0092	3.8058375
							EA	-.0061	3.8058000
6	2	4	$\leftarrow$	6	1	6	AA	.0198	3.8766493
							EA	.0008	3.8764971
11	3	9	$\leftarrow$	11	2	9	AA	.0951	3.8875012
3	0	3	$\leftarrow$	2	0	2	AA	-.0186	3.8907693
3	2	2	$\leftarrow$	2	2	1	AA	.0081	3.9028551
							EE	-.0143	3.9029396
3	2	1	$\leftarrow$	2	2	0	AA	-.0005	3.9149152
							EA	-.0058	3.9147610
5	1	4	$\leftarrow$	4	2	2	AA	-.0001	3.9267244
							EA	.0084	3.9266060
4	0	4	$\leftarrow$	3	1	2	AA	-.0342	3.9741203
3	1	2	$\leftarrow$	2	1	1	AA	-.0227	3.9960675
7	2	6	$\leftarrow$	6	3	4	AA	-.0122	4.0477758
							EA	.0001	4.0478250
6	1	6	$\leftarrow$	5	2	4	AA	.0001	4.1179884
10	3	8	$\leftarrow$	10	2	8	AA	.0929	4.1556482
7	2	5	$\leftarrow$	7	1	7	AA	.0494	4.2601906
9	3	7	$\leftarrow$	9	2	7	AA	.0788	4.3868742
7	2	5	$\leftarrow$	6	3	3	AA	-.0051	4.3933869
							EA	.0107	4.3931080
8	3	6	$\leftarrow$	8	2	6	AA	.0349	4.5772823
							EA	.0115	4.5773451
7	3	5	$\leftarrow$	7	2	5	AA	.0405	4.7254123
							EA	-.0463	4.7253537

9	3	7	←	8	4	5	AA	-.0074	4.7880420
							EA	.0096	4.7887760
							EE*	.0074	4.7886016
6	3	4	←	6	2	4	AA	-.0036	4.8326854
							EA	-.0167	4.8326010
5	3	3	←	5	2	3	AA	-.0032	4.9039287
							EA	-.0027	4.9036240
							EE	.0007	4.9035280
							EE*	-.0045	4.9037070
5	3	2	←	5	2	3	EA	-.0067	4.9068330
							EE	-.0053	4.9069250
							EE*	-.0021	4.9067490
4	3	2	←	4	2	2	AA	-.0074	4.9462942
							EA	.0062	4.9456040
							EE	.0114	4.9454620
							EE*	.0033	4.9457400
3	3	1	←	3	2	1	AA	.0049	4.9680465
							EA	.0047	4.9670947
							AE	.0126	4.9679419
							EE	.0028	4.9669336
							EE*	-.0024	4.9672398
3	3	1	←	3	2	2	AA	-.0989	4.9830400
							EA	.0061	4.9822480
							EE	.0058	4.9821070
							EE*	.0057	4.9823840
3	3	0	←	3	2	2	AA	.0054	4.9832348
							EA	-.0045	4.9842331
							AE	.0016	4.9833377
							EE	-.0011	4.9843901
							EE*	-.0035	4.9840763
4	3	1	←	4	2	3	AA	.0056	4.9919125
							EA	-.0020	4.9926676
							AE	.0149	4.9919518
							EE	-.0032	4.9928079
							EE*	.0010	4.9925260
5	3	3	←	5	2	4	EA	.0003	5.0071530
							EE	.0007	5.0070570
							EE*	-.0006	5.0072350
5	3	2	←	5	2	4	AA	.0148	5.0100120
							EA	.0020	5.0103677
							EE	.0003	5.0104596
							EE*	.0045	5.0102797
6	3	3	←	6	2	5	AA	.0060	5.0428268
							EA	-.0085	5.0429533
4	1	4	←	3	1	3	AA	.0188	5.0711194
							EA	-.0102	5.0710624
3	1	2	←	2	0	2	AA	-.0223	5.0905311
5	0	5	←	4	1	3	AA	-.0259	5.0959138
7	3	4	←	7	2	6	AA	.0134	5.0972387
4	0	4	←	3	0	3	AA	-.0305	5.1738894
7	1	7	←	6	2	5	AA	.0393	5.1761109
8	3	5	←	8	2	7	AA	.0034	5.1817688
4	2	3	←	3	2	2	AA	.0174	5.2014453
							EA	-.0153	5.2013849
4	3	2	←	3	3	1	AA	-.0026	5.2095608
							EA	.0036	5.2097413
							AE	-.0017	5.2096375
4	3	1	←	3	3	0	AA	.0012	5.2101066
							EA	.0030	5.2098352
							AE	-.0072	5.2100215
4	2	2	←	3	2	1	AA	.0026	5.2313060
							EA	.0021	5.2312320
9	3	6	←	9	2	8	AA	-.0052	5.3067836
							EA	-.0130	5.3067248
4	1	3	←	3	1	2	AA	.0033	5.3243603
							EA	.0070	5.3243020
6	1	5	←	5	2	3	AA	.0050	5.3393371
							EA	.0096	5.3391980
10	3	7	←	10	2	9	AA	-.0756	5.4842286
2	2	0	←	1	1	0	AA	.0046	5.5619879

							EA	.0015	5.5621170
2	2	1	←	1	1	1	AA	.0002	5.6224070
							EA	-.0078	5.6222500
8	2	6	←	7	3	4	AA	.0089	5.8372574
							EA	.0140	5.8370058
6	0	6	←	5	1	4	AA	.0071	6.1533411
							EA	-.0431	6.1532755
10	3	7	←	9	4	5	AA	-.0256	6.2404487
							EE*	-.0136	6.2398610
5	1	5	←	4	1	4	AA	.0088	6.3337809
							EA	-.0157	6.3337244
5	0	5	←	4	0	4	AA	-.0315	6.4461107
5	2	4	←	4	2	3	AA	-.0266	6.4979579
5	3	3	←	4	3	2	AA	-.0147	6.5141690
							EA	.0087	6.5145140
							AE	.0237	6.5142310
5	3	2	←	4	3	1	AA	.0114	6.5160862
							EA	-.0021	6.5156260
							AE	.0359	6.5160862
4	1	3	←	3	0	3	AA	-.0252	6.5240973
5	2	3	←	4	2	2	AA	-.0110	6.5565424
							EA	-.0014	6.5564750
5	1	4	←	4	1	3	AA	.0045	6.6491257
							EA	.0038	6.6490467
7	1	6	←	6	2	4	AA	.0041	6.7312976
							EA	.0059	6.7311413
10	4	7	←	10	3	7	AA	-.0369	6.8028038
							EA	.0104	6.8026794
							EE	.0400	6.8026254
3	2	1	←	2	1	1	AA	.0132	6.8115537
9	4	6	←	9	3	6	AA	-.0104	6.8682840
							EA	.0115	6.8678436
							EE	.0204	6.8677064
							EE*	.0220	6.8679803
8	4	5	←	8	3	5	AA	-.0246	6.9112187
7	4	4	←	7	3	4	AA	.0106	6.9381709
							EA	-.0045	6.9369965
							AE	.0026	6.9380728
							EE	-.0029	6.9367831
							EE*	-.0127	6.9371923
7	4	3	←	7	3	4	EA	-.0067	6.9396720
							EE	-.0024	6.9398500
							EE*	-.0030	6.9394920
9	4	5	←	9	3	7	AA	.0070	6.9513480
							EA	-.0153	6.9518950
							EE	-.0210	6.9520270
							EE*	-.0118	6.9517640
8	4	5	←	8	3	6	EA	-.0058	6.9511470
							EE	-.0108	6.9509630
6	4	3	←	6	3	3	EA	.0024	6.9528390
							AE	.0084	6.9540495
							EE	.0074	6.9526040
							EE*	.0046	6.9530680
6	4	2	←	6	3	3	EA	-.0146	6.9554790
							AE	.0088	6.9544550
							EE	-.0017	6.9556440
							EE*	-.0104	6.9553180
10	4	6	←	10	3	8	AA	.0112	6.9551669
7	4	3	←	7	3	5	AA	.0133	6.9572535
							EA	.0046	6.9584927
							AE	.0147	6.9573369
							EE	.0075	6.9587026
							EE*	.0175	6.9582936
6	4	2	←	6	3	4	AA	.0024	6.9618409
							AE	.0024	6.9619920
5	4	2	←	5	3	2	AA	.0030	6.9632080
							EA	.0136	6.9615958
							AE	.0006	6.9630066
5	4	1	←	5	3	2	EA	-.0025	6.9642368
							EE	-.0046	6.9643320

							EE*	-.0018	6.9641239
5	4	2	←	5	3	3	EA	-.0022	6.9647930
							EE	-.0009	6.9646890
							EE*	-.0068	6.9648940
5	4	1	←	5	3	3	AA	.0142	6.9657629
							AE	-.0003	6.9659395
4	4	1	←	4	3	1	AA	.0490	6.9679354
							AE	.0233	6.9676779
							EE	.0249	6.9655525
4	4	0	←	4	3	2	AA	-.0006	6.9685205
3	2	2	←	2	1	2	AA	-.0178	6.9867808
							EA	-.0137	6.9867250
7	0	7	←	6	1	5	AA	-.0474	7.1398643
6	1	6	←	5	1	5	AA	-.0260	7.5934724
6	0	6	←	5	0	5	AA	.0096	7.7065252
							EA	.0110	7.7064684
6	2	5	←	5	2	4	AA	-.0102	7.7920134
							EA	.0075	7.7919650
6	3	4	←	5	3	3	AA	-.0162	7.8198170
							EA	-.0135	7.8199610
6	3	3	←	5	3	2	AA	-.0108	7.8248364
							EA	-.0016	7.8245520
6	2	4	←	5	2	3	AA	-.0123	7.8910638
							EA	-.0055	7.8909780
6	1	5	←	5	1	4	AA	-.0010	7.9691600
							EA	.0003	7.9690675
5	1	4	←	4	0	4	AA	-.0091	7.9993146
							EA	.0108	7.9992387
8	1	7	←	7	2	5	AA	.0126	8.0867860
							EA	.0039	8.0866130
4	2	3	←	3	1	3	AA	-.0393	8.3823590
7	1	7	←	6	1	6	AA	-.0329	8.8500740
3	3	0	←	2	2	0	AA	.0052	8.8830530
							EA	.0095	8.8838620
							AE	.0387	8.8831890
							EE	.0323	8.8839870
							EE*	.0018	8.8837410
3	3	1	←	2	2	1	AA	.0271	8.8860130
							EA	.0115	8.8851750
							AE	.0059	8.8858830
							EE	-.0021	8.8850530
							EE*	.0405	8.8853110
10	5	6	←	10	4	6	AA	-.0125	8.9206410
							AE	-.0044	8.9204570
10	5	5	←	10	4	7	AA	-.0112	8.9273870
							AE	-.0068	8.9275730
9	5	5	←	9	4	5	AA	.0057	8.9355160
							AE	.0014	8.9352720
9	5	4	←	9	4	6	AA	.0003	8.9384070
							AE	-.0110	8.9386250
8	5	4	←	8	4	4	AA	.0048	8.9457820
							AE	.0067	8.9455070
8	5	3	←	8	4	5	AA	.0051	8.9468970
							AE	-.0065	8.9471520
7	5	3	←	7	4	3	AA	-.0002	8.9527150
7	5	2	←	7	4	4	AA	-.0146	8.9530720
7	0	7	←	6	0	6	AA	-.0626	8.9556760
7	3	4	←	6	3	3	AA	-.0113	9.1374644
7	2	5	←	6	2	4	AA	.0271	9.2336457
							EA	.0122	9.2335194
7	1	6	←	6	1	5	AA	.0144	9.2830520
							EA	-.0064	9.2829240
9	1	8	←	8	2	6	AA	.0072	9.3910000
							EA	.0007	9.3908360
6	1	5	←	5	0	5	AA	.0075	9.5223500
							EA	.0189	9.5222250
4	3	1	←	3	2	1	AA	.0155	10.178253
							EA	-.0089	10.178909
							EE	-.0086	10.179038
							EE*	-.0214	10.178762

4	3	2	←	3	2	2	EA	-.0006	10.191979
							EE	-.0135	10.191831
							EE*	.0133	10.192121
8	4	5	7	4	4		EA	-.0022	10.428475
							AE	-.0069	10.428351
8	4	4	←	7	4	3	AA	.0131	10.429053
							EA	-.0062	10.428661
							AE	-.0381	10.428950
8	3	5	←	7	3	4	AA	.0034	10.455228
							EA	-.0019	10.455085
6	2	4	←	5	1	4	EA	-.0043	10.520858
8	2	6	←	7	2	5	AA	-.0082	10.581324
							EA	.0307	10.581232
8	1	7	←	7	1	6	AA	-.0085	10.589090
							EA	-.0060	10.588975
9	6	3	←	9	5	5	AA	-.0147	10.941064
6	2	5	←	5	1	5	AA	-.0008	11.267533
							EA	-.0316	11.267378
5	3	2	←	4	2	2	AA	.0001	11.463009
							EA	-.0041	11.463312
5	3	3	←	4	2	3	AA	-.0011	11.505457
							EA	.0293	11.505114
9	6	3	←	8	6	2	AA	-.0013	11.723122
							EA	-.0097	11.723000
9	6	4	←	8	6	3	AA	-.0009	11.723122
							EA	-.0123	11.723000
9	5	4	←	8	5	3	AA	-.0087	11.728050
							EA	-.0011	11.727925
9	4	6	←	8	4	5	AA	.0141	11.736558
							EA	-.0105	11.736783
9	4	5	←	8	4	4	AA	.0090	11.738299
							EA	.0209	11.737830
9	3	7	←	8	3	6	AA	.0227	11.740044
							EA	.0318	11.739951
9	3	6	←	8	3	5	AA	.0072	11.779500
							EA	.0012	11.779354
9	1	8	←	8	1	7	AA	.0104	11.885562
							EA	-.0126	11.885415
4	4	1	←	3	3	1	AA	-.0263	12.178056
							EA	-.0220	12.177675
7	2	6	←	6	1	6	AA	.0175	12.757124
							EA	.0071	12.756946
10	7	3	←	10	6	5	AA	.0098	12.934355
							EA	.0140	12.938745
							EE*	-.0039	12.938083
9	7	2	←	9	6	4	AA	-.0024	12.938363
							EE	.0163	12.943400
9	7	3	←	9	6	3	AA	-.0019	12.938363
							EE*	-.0152	12.934740
10	7	3	←	9	7	2	AA	.0034	13.024346
							EA	-.0029	13.024214
10	7	4	←	9	7	3	AA	.0034	13.024346
							EA	-.0057	13.024214
10	6	4	←	9	6	3	AA	.0048	13.028369
							EA	.0084	13.028245
10	6	5	←	9	6	4	AA	.0062	13.028369
							EA	.0052	13.028245
10	3	8	←	9	3	7	AA	.0204	13.046116
							EA	-.0309	13.045944
10	4	6	←	9	4	5	AA	-.0223	13.049888
							EA	-.0028	13.049511
10	1	9	←	9	1	8	AA	.0135	13.170673
							EA	.0171	13.170550
5	4	2	←	4	3	2	AA	-.0173	13.479895
							EA	-.0035	13.479297
							AE	-.0129	13.479741
7	3	5	←	6	2	5	AA	.0094	14.161594
							EA	-.0082	14.161451
8	2	7	←	7	1	7	AA	.0349	14.277719
							EA	.0093	14.277471

9	2	7	←	8	1	7	AA	.0269	14.425059
							EA	.0343	14.424950
11	1	10	←	10	1	9	AA	-.0221	14.443063
							EA	-.0473	14.442912
6	4	2	←	5	3	2	AA	.0049	14.779153
							EA	.0268	14.780074
							AE	.0118	14.779299
							EE*	.0017	14.779935
6	4	3	←	5	3	3	AA	.0050	14.781576
							EA	-.0013	14.780602
							AE	.0022	14.781425
12	1	12	←	11	1	11	EA	-.0110	15.091044
5	5	0	←	4	4	0	EA	.0033	15.471801
							AE	-.0198	15.471500
5	5	1	←	4	4	1	EA	.0169	15.471150
12	4	9	←	11	4	8	AA	.0114	15.669152
							EA	-.0122	15.669031
12	4	8	←	11	4	7	AA	.0001	15.682796
							EA	.0032	15.682574
12	3	9	←	11	3	8	AA	-.0634	15.802150
							EA	-.0526	15.801963
10	2	8	←	9	1	8	EA	-.0044	15.816652
7	4	3	←	6	3	3	AA	.0080	16.076012
							EA	-.0145	16.076971
							EE*	-.0218	16.076800
10	1	9	←	9	0	9	AA	-.1012	16.161712
6	5	2	←	5	4	2	AA	-.0028	16.773188
							EA	-.0027	16.772823
							AE	-.0226	16.773104
6	5	1	←	5	4	1	EA	-.0010	16.773489
9	3	7	←	8	2	7	AA	.0030	16.881061
							EA	-.0336	16.880886
13	3	11	←	12	3	10	AA	.0048	16.952660
							EA	.0479	16.952547
13	4	10	←	12	4	9	AA	-.0119	16.982005
							EA	.0043	16.981878
11	2	9	←	10	1	9	AA	.0059	17.265026
13	2	11	←	12	2	10	AA	-.1188	17.277099
							EA	-.0453	17.276966
10	2	9	←	9	1	9	AA	.0291	17.408575
							EA	-.0330	17.408125
11	1	10	←	10	0	10	AA	.0009	17.942727
								RMS	10.772 kHz

C

Structure determination, internal dynamics, and chiral analysis of pulegone and its complex with water

Table C.1: *Experimentally determined rotational and quartic centrifugal distortion constants for the normal and the ^{13}C substituted species of pulegone, Chair 1.*

	normal species	^{13}C1	^{13}C2	^{13}C3
A | MHz	1909.05435(71)	1908.82932(75)	1894.60622(64)	1891.8428(10)
B | MHz	739.06297(21)	733.63115(48)	736.70257(32)	738.63051(34)
C | MHz	578.14181(21)	574.81129(34)	575.35935(30)	576.85245(33)
Δ_J | kHz	0.0302(24)	[0.0302][a]	[0.0302]	[0.0302]
Δ_{JK} | kHz	−0.273(10)	[−0.273]	[−0.273]	[−0.273]
Δ_K | kHz	1.079(48)	[1.079]	[1.079]	[1.079]
N_{lines}	97	32	29	24
σ | kHz	7.5	10.3	8.4	10.1

	^{13}C4	^{13}C5	^{13}C6	^{13}C7
A | MHz	1908.22352(64)	1900.38586(46)	1900.44453(54)	1907.22272(57)
B | MHz	738.48520(23)	739.04968(25)	736.77871(29)	724.92918(31)
C | MHz	577.81614(22)	577.41426(19)	576.09403(29)	569.59083(27)
Δ_J | kHz	[0.0302]	[0.0302]	[0.0302]	[0.0302]
Δ_{JK} | kHz	[−0.273]	[−0.273]	[−0.273]	[−0.273]
Δ_K | kHz	[1.079]	[1.079]	[1.079]	[1.079]
N_{lines}	30	27	25	26
σ | kHz	8.1	5.8	7.1	7.5

	^{13}C8	^{13}C9	^{13}C10	^{18}O1
A | MHz	1908.35143(60)	1900.95685(57)	1891.52188(76)	1842.0286(32)
B | MHz	734.62714(32)	730.04926(30)	730.47932(41)	737.5350(22)
C | MHz	575.38085(27)	572.35728(22)	571.30610(32)	571.93637(74)
Δ_J | kHz	[0.0302]	[0.0302]	[0.0302]	[0.0302]
Δ_{JK} | kHz	[−0.273]	[−0.273]	[−0.273]	[−0.273]
Δ_K | kHz	[1.079]	[1.079]	[1.079]	[1.079]
N_{lines}	29	26	21	5
σ | kHz	7.8	7.2	8.2	8.3

[a] fixed to the value determined for the normal species

Table C.2: *Comparison between the results for the r_s, r_0, and r_e (MP2/6-311++G(d,p)) structures. All coordinates are in Å.*

	atom	a	b	c
r_s		2.25040(67)	−0.129(12)	0.122(12)
r_0	C1	2.2484(27)	−0.1132(52)	0.1732(39)
r_e		2.239	−0.125	0.157
r_s		1.4820(10)	−1.4300(10)	$-0.0948i$
r_0	C2	1.4769(69)	−1.4300(52)	−0.057(10)
r_e		1.467	−1.429	−0.035
r_s		$0.1644i$	−1.4081(11)	0.6582(23)
r_0	C3	0.142(11)	−1.4152(59)	0.640(11)
r_e		0.121	−1.398	0.701
r_s		−0.6764(22)	0.1914(79)	0.2813(54)
r_0	C4	−0.6976(66)	−0.243(10)	0.1923(94)
r_e		−0.725	−0.227	0.250
r_s		$0.2166i$	1.0731(14)	0.2444(62)
r_0	C5	0.024(11)	1.0692(90)	0.203(14)
r_e		0.000	1.083	0.226
r_s		1.4195(11)	1.0495(14)	−0.3277(46)
r_0	C6	1.4199(70)	1.0585(92)	−0.342(11)
r_e		1.400	1.048	−0.362
r_s		3.62451(42)	−0.1528(99)	−0.4872(31)
r_0	C7	3.6260(26)	−0.1286(85)	−0.4733(68)
r_e		3.604	−0.164	−0.528
r_s		−2.03111(74)	−0.2874(52)	−0.127(12)
r_0	C8	−2.0240(51)	−0.320(14)	−0.248(15)
r_e		−2.021	−0.304	−0.151
r_s		−2.84277(53)	0.8805(17)	−0.6128(25)
r_0	C9	−2.8433(38)	0.887(11)	−0.603(15)
r_e		−2.808	0.877	−0.662

r_s		−2.82829(53)	−1.57903(96)	−0.124(12)
r_0	C10	−2.8276(39)	−1.5875(70)	−0.071(21)
r_e		−2.825	−1.580	−0.139

r_s		−0.5598(27)	2.11240(72)	0.6437(24)
r_0	O1	−0.563(10)	2.1152(29)	0.6313(92)
r_e		−0.492	2.124	0.645

Table C.3: *Structural parameters obtained from r_0 and r_s fits in comparison to the computationally determined values (r_e structure, MP2/6-311++G(d,p)) for Chair 1.*

	r_0	r_s	Ab initio r_e
r(C1-C2) | Å	1.5434(81)	*1.515(10)*[a]	1.53
r(C2-C3) | Å	1.505(12)	*1.6217(13)*	1.53
r(C3-C4) | Å	1.511(16)	*1.4423(70)*	1.51
r(C4-C5) | Å	1.497(15)	*1.4345(71)*	1.49
r(C5-C6) | Å	[1.52][b]	*1.5306(30)*	1.52
r(C6-C1) | Å	1.524(13)	1.511(10)	1.53
r(C7-C1) | Å	1.5219(55)	1.5031(52)	1.52
r(C4-C8) | Å	1.3999(91)	1.4181(44)	1.36
r(C8-C9) | Å	1.501(17)	1.5029(58)	1.51
r(C8-C10) | Å	1.511(16)	1.5178(46)	1.51
r(C5-O1) | Å	1.2736(97)	*1.2462(28)*	1.23
∡(C1-C2-C3) | °	[111.4]	*114.78(30)*	111.4
∡(C2-C3-C4) | °	[111.3]	*109.50(18)*	111.3
∡(C3-C4-C5) | °	[114.2]	*121.95(19)*	114.2
∡(C4-C5-C6) | °	[115.7]	*115.67(24)*	115.7
∡(C5-C6-C1) | °	[113.0]	*114.26(37)*	113.0
∡(C6-C1-C2) | °	[109.5]	*111.53(28)*	109.5
∡(C7-C1-C2) | °	[111.9]	*114.70(79)*	111.9
∡(C7-C1-C6) | °	[110.9]	113.22(80)	110.9
∡(C6-C5-O1) | °	123(1)	*123.32(15)*	121.5
∡(O1-C5-C4) | °	[122.8]	*121.00(26)*	122.8
∡(C5-C4-C8) | °	[120.5]	*120.18(53)*	120.5
∡(C3-C4-C8) | °	[125.3]	*117.78(53)*	125.3
∡(C4-C8-C9) | °	123.14(79)	123.80(45)	123.6
∡(C4-C8-C10) | °	120.89(91)	123.97(53)	123.7
∡(C9-C8-C10) | °	[112.8]	112.23(28)	112.8
∡(C3-C4-C8-C9) | °	-183(1)	*-176.81(63)*	-176.7
∡(C5-C4-C8-C10) | °	[180.8]	*179.95(83)*	180.8
∡(C1-C6-C5-O1) | °	136(2)	*139.23(63)*	134.5

[a] The distances and angles which involve C2, C3 and C5 atoms (in italics) have been calculated by setting the imaginary r_s coordinates to zero.

[b] Values kept fixed to ab initio predicted structure.

Table C.4: *Measured rotational transitions (ν_{obs}) and the residuals ($\nu_{\mathrm{obs}} - \nu_{\mathrm{calc}}$) for the pulegone conformer Chair 1, as obtained after the fit with the programm XIAM.*

J'	K'_a	K'_c	$\leftarrow$	J''	K''_a	K''_c		$\nu_{\mathrm{obs}} - \nu_{\mathrm{calc}}$ (MHz)	ν_{obs}(GHz)
6	0	6	$\leftarrow$	5	1	4	AA	-.0106	4.6380420
7	0	7	$\leftarrow$	6	1	5	AA	-.0134	5.0167800
							EA	.0092	5.0196240
							EE	.0039	5.0196240
							EE*	-.0158	5.0196240
6	1	5	$\leftarrow$	5	2	3	AA	.0001	5.1182580
6	1	5	$\leftarrow$	5	2	4	AA	-.0003	5.6153480
							EA	.0033	5.6454730
							EE	.0031	5.6460130
							EE*	.0021	5.6449130
8	2	6	$\leftarrow$	7	3	5	AA	.0037	5.9438960
							EA	.0008	6.0909040
							EE	-.0023	6.0922710
							EE*	.0040	6.0895150
7	1	6	$\leftarrow$	6	2	4	AA	.0036	6.3764780
5	3	3	$\leftarrow$	4	3	2	AA	.0053	6.6301280
7	1	6	$\leftarrow$	6	2	5	AA	-.0016	7.3042490
							EA	.0012	7.3130830
							EE	-.0009	7.3134370
							EE*	-.0028	7.3126950
6	4	3	$\leftarrow$	5	4	2	AA	.0014	7.9553790
6	4	2	$\leftarrow$	5	4	1	AA	.0044	7.9570530
3	1	3	$\leftarrow$	2	0	2	AA	-.0003	4.7255370
							EA	-.0002	4.7220130
							EE	.0003	4.7219020
							EE*	-.0008	4.7221120
5	2	4	$\leftarrow$	4	2	3	AA	-.0018	6.5516370
							EA	-.0063	6.5830080
							EE	-.0057	6.5833050
							EE*	-.0072	6.5826920
5	2	3	$\leftarrow$	4	2	2	AA	-.0046	6.8253750
							EA	-.0033	6.7919530
							EE	-.0048	6.7916150
							EE*	-.0045	6.7922630
4	2	2	$\leftarrow$	3	2	1	AA	.0007	5.4036120
							EA	.0008	5.3613070
							EE	-.0008	5.3610950
							EE*	-.0005	5.3614990
4	2	3	$\leftarrow$	3	2	2	AA	-.0001	5.2567500
							EA	.0013	5.2974950
							EE	.0008	5.2976730
							EE*	-.0019	5.2972960
4	1	4	$\leftarrow$	3	0	3	AA	-.0108	5.7535400
							EA	-.0044	5.7536120
							EE	.0207	5.7535400
							EE*	-.0159	5.7536870
5	0	5	$\leftarrow$	4	1	4	AA	-.0080	5.6802390
							EA	-.0062	5.6776120
							EE	-.0114	5.6777000
							EE*	.0023	5.6775120
5	1	5	$\leftarrow$	4	0	4	AA	-.0137	6.7566780
							EA	-.0040	6.7583870
							EE	-.0035	6.7583000
							EE*	.0054	6.7584750
6	1	6	$\leftarrow$	5	0	5	AA	.0333	7.7649750
							EA	.0022	7.7669500
							EE	-.0002	7.7668700
							EE*	-.0066	7.7670120
6	0	6	$\leftarrow$	5	1	5	AA	-.0111	7.0260360
							EA	.0027	7.0232870
							EE	-.0025	7.0233500
							EE*	.0035	7.0232000

4	1	3	←	3	1	2	AA	-.0468	5.5566720
							EA	.0073	5.5514820
							EE	.0312	5.5514820
							EE*	.0040	5.5514820
3	2	2	←	2	1	1	AA	.0278	7.4616120
							EA	.0068	7.3347880
							EE	-.0025	7.3336910
							EE*	-.0060	7.3358290
2	1	2	←	1	0	1	AA	-.0073	3.6434750
							EA	.0094	3.6330070
							EE	.0076	3.6328430
							EE*	.0038	3.6331510
5	1	4	←	4	1	3	AA	-.0047	6.9103500
6	0	6	←	5	0	5	AA	-.0077	7.4708370
6	1	6	←	5	1	5	AA	.0059	7.3201500
4	0	4	←	3	1	3	AA	.0005	4.2869740
							EA	-.0094	4.2861130
							EE	-.0068	4.2862470
							EE*	-.0070	4.2859730
3	0	3	←	2	1	2	AA	.0138	2.8660640
							EA	.0070	2.8711580
							EE	-.0094	2.8713420
							EE*	-.0021	2.8709430
4	1	4	←	3	1	3	AA	.0045	4.9186250
5	1	5	←	4	1	4	AA	.0324	6.1250770
4	1	3	←	4	0	4	AA	.0016	2.2343330
4	1	3	←	3	2	2	AA	.0080	2.2779480
							EA	-.0163	2.3933450
							EE	-.0025	2.3943390
							EE*	-.0096	2.3923690
1	1	1	←	0	0	0	AA	-.0135	2.4871840
							EA	.0285	2.4584290
							EE	-.0178	2.4580420
							EE*	-.0181	2.4587110
7	2	6	←	6	3	4	AA	.0067	2.5908220
							EA	-.0029	2.7609020
							EE	-.0022	2.7622370
							EE*	-.0027	2.7595900
2	0	2	←	1	0	1	AA	-.0025	2.6189230
1	1	0	←	0	0	0	AA	-.0048	2.6481130
							EA	.0139	2.6766110
							EE	-.0016	2.6769070
							EE*	.0075	2.6762820 .
2	1	1	←	1	1	0	AA	.0014	2.7953320
5	1	4	←	5	0	5	AA	-.0091	2.8327830
4	2	3	←	4	1	3	AA	-.0111	2.9787990
							EA	-.0014	2.9041310
							EE	-.0118	2.9033190
							EE*	.0017	2.9049210
5	2	3	←	5	1	4	AA	-.0045	3.1171800
							EA	-.0061	3.1559720
							EE	.0008	3.1563430
							EE*	-.0025	3.1555970
6	2	4	←	6	1	5	AA	-.0039	3.1464120
							EA	.0040	3.1739020
							EE	.0050	3.1739970
							EE*	-.0013	3.1737830
4	2	2	←	4	1	3	AA	.0034	3.2021630
							EA	-.0099	3.2680790
							EE	.0014	3.2688010
							EE*	-.0035	3.2673610
4	0	4	←	3	1	2	AA	-.0063	3.3223810
7	2	5	←	7	1	6	AA	-.0144	3.3260740
							EA	.0046	3.3487230
							EE	-.0081	3.3486500 .
3	2	1	←	3	1	2	AA	.0049	3.3552720
							EA	-.0133	3.4582440
							EE	-.0076	3.4591470
							EE*	-.0080	3.4573350
3	1	3	←	2	1	2	AA	.0016	3.7009820

5	1	4	←	4	2	2	AA	.0009	3.7081960
							EA	.0098	3.6359880
							EE	-.0026	3.6352750
							EE*	-.0020	3.6366660
3	0	3	←	2	0	2	AA	.0050	3.8906120
5	1	4	←	4	2	3	AA	.0053	3.9315500
							EA	.0084	3.9999430
							EE	.0016	4.0007480
							EE*	.0008	3.9991140
5	0	5	←	4	1	3	AA	-.0086	4.0775540
9	2	7	←	9	1	8	AA	-.0151	4.2353300
7	1	6	←	7	0	7	AA	.0021	4.5060990
4	0	4	←	3	0	3	AA	.0003	5.1219040
6	2	5	←	6	1	6	AA	-.0116	5.5219210
							EA	.0010	5.5016740
							EE	-.0001	5.5013900
							EE*	.0019	5.5019000
3	1	2	←	2	0	2	AA	.0005	5.6901240
							EA	.0045	5.7002040
5	3	3	←	5	2	3	AA	.0061	5.8832890
							EA	.0116	5.6361620
							EE	-.0043	5.6342290
							EE*	-.0002	5.6380330
11	2	9	←	11	1	10	AA	.0036	5.9067320
2	2	1	←	1	1	0	AA	.0024	6.3052990
5	0	5	←	4	0	4	AA	-.0021	6.3118920
							EA	-.0068	6.3110750
							EE	.0008	6.3110750
							EE*	-.0008	6.3110750
6	2	4	←	6	1	6	AA	-.0028	6.4497060
							EA	-.0064	6.4720170
							EE	-.0100	6.4721600
							EE*	-.0072	6.4717940
2	2	1	←	1	1	1	AA	.0051	6.4662220
6	3	3	←	6	2	5	AA	.0075	6.5870710
							EA	-.0136	6.7853400
							EE	-.0059	6.7870050
							EE*	.0069	6.7836590
7	3	5	←	7	2	6	AA	-.0040	6.7070660
							EA	.0056	6.5759720
							EE	-.0014	6.5747280
							EE*	-.0103	6.5771400
7	3	4	←	7	2	6	AA	.0038	6.8914280
							EA	-.0049	7.0408600
							EE	.0092	7.0422830
							EE*	.0188	7.0394230
4	1	3	←	3	0	3	AA	-.0072	7.3562280
3	2	1	←	2	1	1	AA	-.0006	7.5380720
							EA	.0229	7.6349480
							EE	.0152	7.6357540
							EE*	-.0086	7.6340700
6	2	5	←	5	2	4	AA	-.0040	7.8339840
							EA	.0018	7.8490190
							EE	.0050	7.8492270
							EE*	.0050	7.8487970
6	2	5	←	6	1	5	AA	-.0087	2.2186310
							EA	-.0025	2.2035450
							EE	-.0041	2.2032080
							EE*	.0008	2.2038820
3	0	3	←	2	1	1	AA	-.0010	2.3832880
2	1	2	←	1	1	1	AA	.0001	2.4734900
							EE*	-.0036	2.4898120
6	2	4	←	6	1	5	AA	-.0039	3.1464120
							EA	.0030	3.1739010
							EE	.0030	3.1739950
							EE*	.0017	3.1737860
7	3	4	←	7	2	6	AA	.0048	6.8914290
7	2	6	←	7	1	7	AA	.0051	6.1189030
							EA	.0057	6.1050660
							EE	-.0012	6.1048900

							EE*	.0076	6.1051670
3	2	1	←	2	1	1	AA	-.0006	7.5380720
							EA	.0009	7.6349260
							EE	.0182	7.6357570
							EE*	-.0036	7.6340750
4	3	1	←	4	2	2	AA	.0049	6.0850650
							EA	-.0153	6.2264580
							EE	-.0076	6.2271850
							EE*	-.0075	6.2257090
5	3	3	←	5	2	4	AA	.0018	6.3803750
							EA	-.0008	6.2090480
							EE	-.0022	6.2080090
							EE*	.0013	6.2100480
8	3	5	←	8	2	6	AA	.0008	5.0693090
							EA	-.0006	5.1522820
							EE	.0081	5.1532380
							EE*	.0101	5.1513310
4	3	2	←	4	2	3	AA	.0097	6.3018990
							EA	.0007	6.1531650
							EE	-.0013	6.1524270
							EE*	.0041	6.1538670
3	3	1	←	3	2	1	AA	.0030	6.1849700
3	3	1	←	3	2	2	AA	.0036	6.2614590
							EA	-.0008	6.1513810
							EE	.0033	6.1508350
							EE*	.0013	6.1518950
6	3	4	←	6	2	5	AA	-.0116	6.5110350
							EA	.0029	6.3467640
							EE	-.0045	6.3455280
							EE*	-.0154	6.3479290
4	3	2	←	4	2	2	AA	.0053	6.0785450
7	2	6	←	6	3	3	AA	.0086	2.5148070
								RMS	9.085 kHz

Table C.5: *Measured rotational transitions (ν_{obs}) and the residuals ($\nu_{\mathrm{obs}} - \nu_{\mathrm{calc}}$) for the pulegone conformer Chair 2, as obtained after the fit with the programm XIAM.*

J'	K'_a	K'_c	$\leftarrow$	J''	K''_a	K''_c		$\nu_{\mathrm{obs}} - \nu_{\mathrm{calc}}$ (MHz)	ν_{obs}(GHz)
5	0	5	$\leftarrow$	4	1	4	AA	-.0036	6.4423540
							AE	.0020	6.4373490
							EE	.0063	6.4372370
							EE*	-.0026	6.4374490
5	1	5	$\leftarrow$	4	0	4	AA	.0100	7.1816710
							AE	.0013	7.1857990
							EE	-.0003	7.1858990
							EE*	.0004	7.1856930
4	1	4	$\leftarrow$	3	0	3	AA	-.0010	6.0570500
							AE	-.0021	6.0587500
							EE	-.0001	6.0588370
							EE*	-.0001	6.0586620
4	0	4	$\leftarrow$	3	1	3	AA	-.0081	4.9585120
							AE	-.0008	4.9558870
							EE	-.0054	4.9557620
							EE*	.0018	4.9560000
3	2	1	$\leftarrow$	2	1	1	AA	.0050	7.4787750
3	2	2	$\leftarrow$	2	1	1	AA	-.0187	7.3692370
							AE	.0083	7.2550500
							EE	-.0044	7.2557750
							EE*	-.0040	7.2542750
6	4	2	$\leftarrow$	6	3	3	AA	.0015	7.4732930
3	2	1	$\leftarrow$	2	1	1	AA	.0000	7.4787700
5	4	1	$\leftarrow$	5	3	2	AA	-.0051	7.5654440
5	4	2	$\leftarrow$	5	3	3	AA	-.0109	7.6118690
7	4	4	$\leftarrow$	7	3	5	AA	.0071	7.6173530
6	0	6	$\leftarrow$	5	1	5	AA	.0095	7.8660220
							AE	-.0033	7.8578320
							EE	-.0005	7.8576750
							EE*	.0023	7.8579850
6	4	3	$\leftarrow$	6	3	3	AA	.0172	7.4683420
2	2	0	$\leftarrow$	1	1	1	AA	.0090	6.3006750
9	2	8	$\leftarrow$	8	3	6	AA	-.0069	6.2494180
6	3	4	$\leftarrow$	6	2	5	AA	-.0109	5.8303260
3	3	0	$\leftarrow$	3	2	1	AA	.0047	5.3755960
5	3	2	$\leftarrow$	5	2	3	AA	.0066	5.0130850
3	1	3	$\leftarrow$	2	0	2	AA	.0047	4.9188800
5	2	4	$\leftarrow$	5	1	5	AA	.0034	4.7068180
3	0	3	$\leftarrow$	2	1	2	AA	-.0065	3.4265040
3	1	3	$\leftarrow$	2	1	2	AA	-.0048	4.0739530
8	3	6	$\leftarrow$	7	4	3	AA	.0042	4.0870020
11	5	6	$\leftarrow$	10	6	5	AA	-.0026	4.4085380
10	4	7	$\leftarrow$	9	5	5	AA	.0010	5.0637860
4	3	1	$\leftarrow$	4	2	2	AA	.0036	5.2378960

3	3	1	←	3	2	2	AA	-.0065	5.4833600
9	4	5	←	9	3	6	AA	-.0035	6.6932890
8	5	4	←	9	2	7	AA	-.0029	7.1452000
15	5	10	←	15	4	11	AA	.0004	7.2464410
4	4	1	←	4	3	2	AA	-.0021	7.6225570
11	2	10	←	10	3	8	AA	.0009	7.8613150
								RMS	6.936 kHz

Table C.6: *Measured rotational transitions (ν_{obs}) and the residuals ($\nu_{\mathrm{obs}} - \nu_{\mathrm{calc}}$) for the pulegone conformer Chair 1 with one water molecule (Chair 1-water a), as obtained after the fit with the programm XIAM.*

J'	K'_a	K'_c	$\leftarrow$	J''	K''_a	K''_c		$\nu_{\mathrm{obs}} - \nu_{\mathrm{calc}}$ (MHz)	ν_{obs}(GHz)
2	0	2	$\leftarrow$	1	0	1	A	-.0085	2.0562620
3	0	3	$\leftarrow$	2	0	2	A	-.0032	3.0616000
							E	.0054	3.0589130
3	1	2	$\leftarrow$	2	1	1	A	-.0009	3.2397000
							E	.0092	3.2375130
4	0	4	$\leftarrow$	3	1	3	A	-.0037	3.5232620
							E	.0270	3.5167190
4	1	4	$\leftarrow$	3	1	3	A	-.0037	3.9175000
							E	-.0118	3.9182080
4	0	4	$\leftarrow$	3	0	3	A	.0082	4.0425000
							E	-.0099	4.0399700
4	2	3	$\leftarrow$	3	2	2	A	-.0002	4.1239120
4	3	1	$\leftarrow$	3	3	0	A	.0097	4.1516250
4	2	2	$\leftarrow$	3	2	1	A	-.0010	4.2126000
4	1	3	$\leftarrow$	3	1	2	A	.0086	4.3073500
							E	-.0054	4.3042730
2	2	1	$\leftarrow$	1	1	0	A	-.0044	4.3370750
4	1	4	$\leftarrow$	3	0	3	A	.0072	4.4367370
2	2	0	$\leftarrow$	1	1	1	A	-.0059	4.4447000
5	0	5	$\leftarrow$	4	1	4	A	-.0102	4.6039750
5	1	5	$\leftarrow$	4	1	4	A	-.0055	4.8828120
							E	-.0018	4.8844570
5	0	5	$\leftarrow$	4	0	4	A	.0019	4.9982250
							E	-.0043	4.9952300
5	2	4	$\leftarrow$	4	2	3	A	.0063	5.1432500
5	3	2	$\leftarrow$	4	3	1	A	.0064	5.2021120
3	2	2	$\leftarrow$	2	1	1	A	.0051	5.2715870
5	1	5	$\leftarrow$	4	0	4	A	.0066	5.2770620
							E	-.0046	5.2859820
5	2	3	$\leftarrow$	4	2	2	A	-.0020	5.3088000
5	1	4	$\leftarrow$	4	1	3	A	.0018	5.3627870
							E	-.0062	5.3581800
5	4	1	$\leftarrow$	5	3	2	A	-.0017	5.3784000
3	2	1	$\leftarrow$	2	1	2	A	.0072	5.6126000
6	1	6	$\leftarrow$	5	1	5	A	.0071	5.8412500
							E	.0062	5.8454060
6	0	6	$\leftarrow$	5	0	5	A	.0058	5.9348370
							E	-.0046	5.9296700
7	1	6	$\leftarrow$	6	2	5	A	.0076	6.0338500
							E	-.0392	6.0288450
6	1	6	$\leftarrow$	5	0	5	A	.0118	6.1200870
6	2	5	$\leftarrow$	5	2	4	A	.0065	6.1550080
4	2	3	$\leftarrow$	3	1	2	E	-.0062	6.1557870
6	4	3	$\leftarrow$	5	4	2	A	.0008	6.2281370
6	4	2	$\leftarrow$	5	4	1	A	-.0070	6.2291120
6	3	4	$\leftarrow$	5	3	3	A	.0032	6.2339500
6	3	3	$\leftarrow$	5	3	2	A	.0065	6.2638870
4	2	2	$\leftarrow$	3	1	2	A	-.0028	6.2906250
6	1	5	$\leftarrow$	5	1	4	A	-.0027	6.4010620
							A	-.0046	6.3955550
6	2	4	$\leftarrow$	5	2	3	E	-.0007	6.4159750
7	1	7	$\leftarrow$	6	1	6	A	-.0229	6.7933250
							A	.0118	6.8018900
7	0	7	$\leftarrow$	6	0	6	E	-.0019	6.8616120
							A	-.0011	6.8521500
4	2	2	$\leftarrow$	3	1	3	E	-.0039	6.8798000
3	3	0	$\leftarrow$	2	2	0	A	.0040	6.9629370
7	1	7	$\leftarrow$	6	0	6	A	-.0069	6.9785850
5	2	4	$\leftarrow$	4	1	3	A	.0045	6.9917000
7	2	6	$\leftarrow$	6	2	5	A	.0054	7.1580120

7	4	4	←	6	4	3	A	-.0011	7.2747250
7	3	5	←	6	3	4	A	-.0091	7.2765460
7	4	3	←	6	4	2	A	-.0029	7.2779620
8	1	7	←	7	2	6	A	.0020	7.2809120
							A	.0208	7.2702230
5	2	3	←	4	1	3	E	.0115	7.2921000
7	3	4	←	6	3	3	A	-.0007	7.3412250
7	1	6	←	6	1	5	A	-.0005	7.4166890
							A	-.0062	7.4113610
7	2	5	←	6	2	4	E	.0036	7.5227250
8	0	8	←	7	1	7	A	.0019	7.6691000
8	1	8	←	7	1	7	A	-.0176	7.7401200
							A	.0244	7.7533370
6	2	5	←	5	1	4	E	.0002	7.7839120
8	0	8	←	7	0	7	A	-.0012	7.7860750
							A	.0062	7.7718680
8	1	8	←	7	0	7	E	-.0037	7.8571120
7	0	7	←	6	1	6	A	.0051	6.6763750
7	1	7	←	6	0	6	A	-.0049	6.9785870
							E	-.0056	7.0083500
5	1	5	←	4	0	4	A	.0066	5.2770620
							E	-.0116	5.2859750
3	2	2	←	2	1	1	A	-.0069	5.2715750
							E	-.0042	5.2200000
								RMS	9.829 kHz

D

Conformational analysis and internal dynamics of menthyl acetate

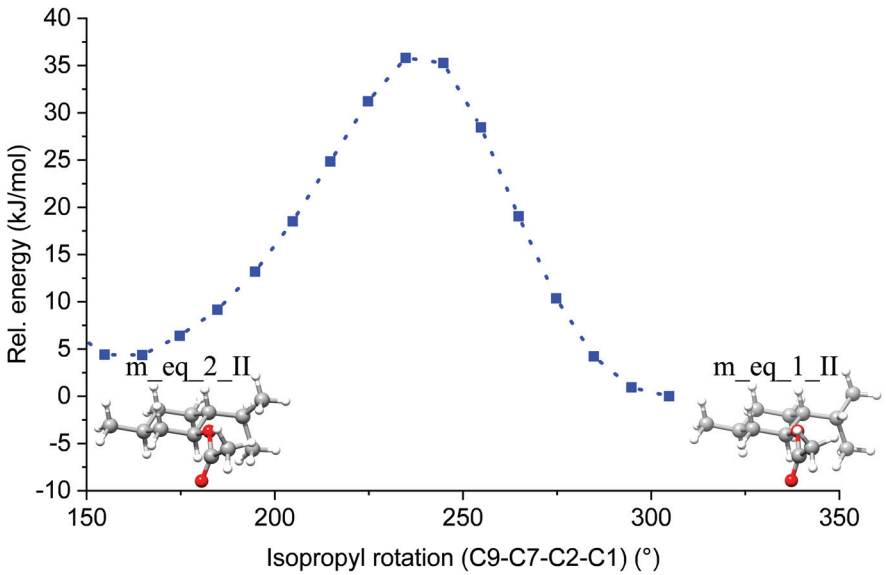

Figure D.1: *Interconversion barrier between the two lowest energy conformers of menthyl acetate as obtained by scanning the dihedral angle involving the isopropyl group (see Figure 7.1 for labelling). Calculations were done at the B3LYP-D3BJ/6-311++G(d,p) level of theory.*

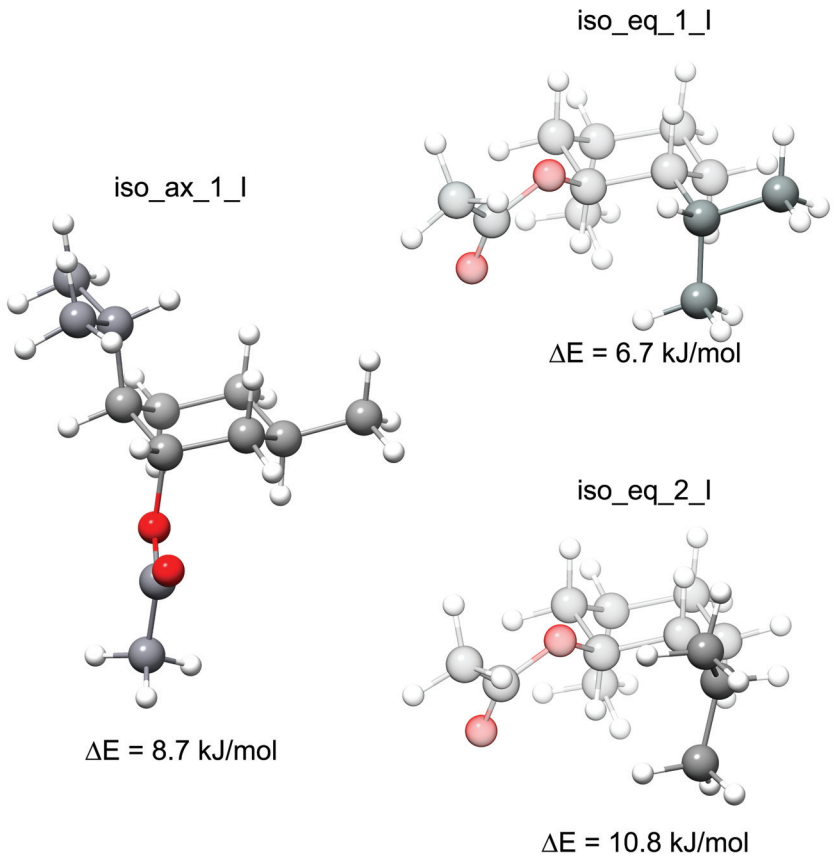

Figure D.2: *Lowest energy conformers of isomenthyl acetate, as listed in Table 7.1. For better visibility, only the differences in the orientation of the respective substituents of iso_eq_1_I and iso_eq_2_I are highlighted, while the rest of the structures is kept transparent. Zero-point corrected relative energies are given.*

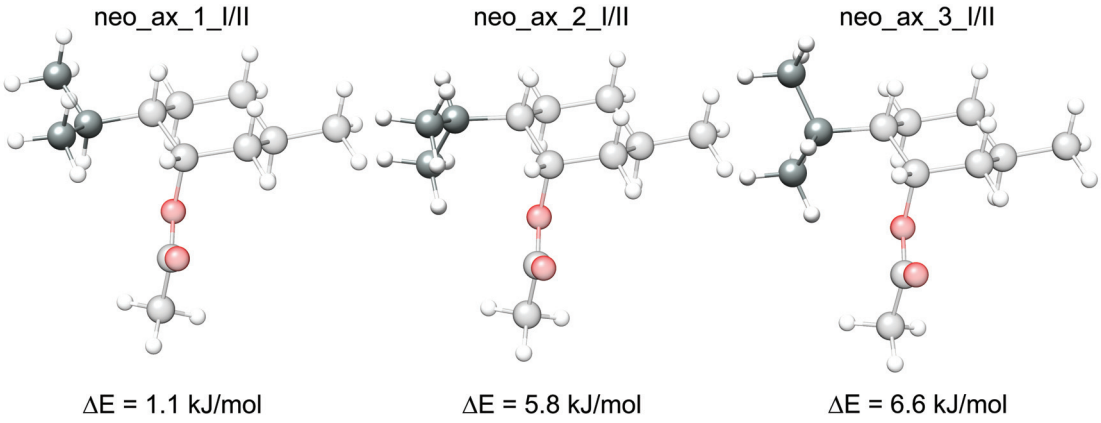

Figure D.3: *Lowest energy conformers of neomenthyl acetate, as listed in Table 7.1. For better visibility, only the differences in the orientation of the respective substituents are highlighted, while the rest of the structures is kept transparent. Zero-point corrected relative energies are given.*

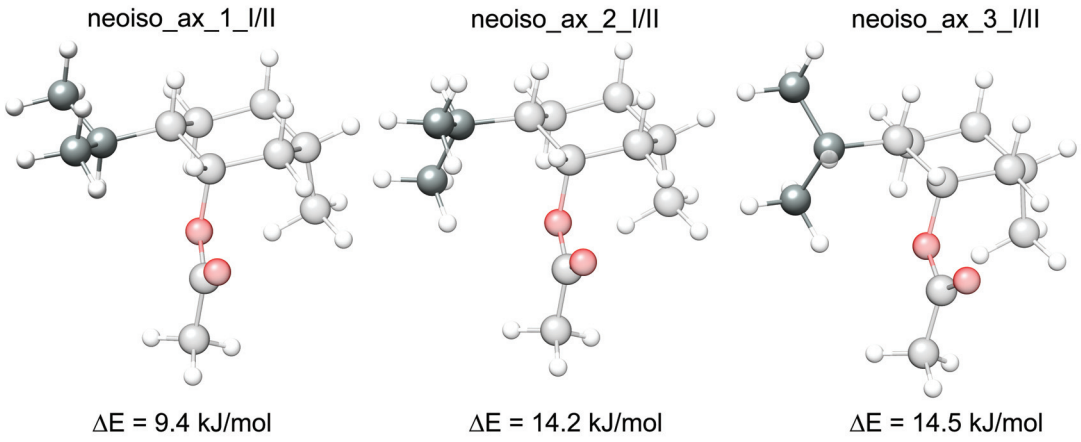

Figure D.4: *Lowest energy conformers of neoisomenthyl acetate, as listed in Table 7.1. For better visibility, only the differences in the orientation of the respective substituents are highlighted, while the rest of the structures is kept transparent. Zero-point corrected relative energies are given.*

Table D.1: *Measured rotational transitions ($\nu_{\rm obs}$) for m_eq_1_II, and the residuals ($\nu_{\rm obs} - \nu_{\rm calc}$) for the fit reported in Table 7.2.*

J'	K'_a	K'_c	$\leftarrow$	J''	K''_a	K''_c	$\nu_{\rm obs}$(GHz)	$\nu_{\rm obs} - \nu_{\rm calc}$ (MHz)
5	4	2	←	4	3	1	6.0383032	-0.0032
5	3	2	←	4	2	2	6.0528161	-0.0059
5	2	3	←	4	1	3	6.1564153	0.0036
5	1	4	←	4	0	4	6.2454882	0.0004
5	4	1	←	4	3	1	6.2475429	0.0021
5	2	4	←	4	1	4	6.2530387	-0.0032
5	3	3	←	4	2	3	6.2623159	-0.0002
6	3	3	←	5	3	2	6.2779052	-0.0092
7	2	5	←	6	3	4	6.3340865	-0.0041
7	3	5	←	6	3	4	6.3427025	-0.0006
6	4	2	←	5	4	1	6.3642258	-0.0042
7	2	5	←	6	2	4	6.3740762	0.0017
7	3	5	←	6	2	4	6.3826890	0.0021
5	4	2	←	4	3	2	6.3954104	0.0044
5	4	1	←	4	3	2	6.6046486	0.0082
6	4	3	←	5	3	2	6.6440848	-0.0083
5	5	1	←	4	4	0	6.6624452	0.0116
5	5	1	←	4	4	1	6.6935581	0.0144
5	5	0	←	4	4	1	6.7054488	0.0120
7	4	4	←	6	4	3	6.7925255	-0.0104
7	5	3	←	6	5	2	7.0167614	-0.0039
7	6	2	←	6	6	1	7.0197699	0.0112
7	3	4	←	6	3	3	7.0277873	-0.0089
8	2	6	←	7	3	5	7.0637284	-0.0006
7	6	1	←	6	6	0	7.0613343	0.0123
8	3	6	←	7	3	5	7.0653381	-0.0032
8	2	6	←	7	2	5	7.0723379	-0.0035
8	3	6	←	7	2	5	7.0739559	0.0021
7	4	4	←	6	3	3	7.1587166	0.0019
6	4	2	←	5	3	2	7.2910998	-0.0055
6	3	3	←	5	2	3	7.3101938	-0.0009
7	5	2	←	6	5	1	7.3291580	-0.0232
6	2	4	←	5	1	4	7.4572140	0.0000
6	3	4	←	5	2	4	7.4886630	0.0025
6	1	5	←	5	0	5	7.5042850	0.0053
6	2	5	←	5	1	5	7.5056447	0.0035
6	5	2	←	5	4	1	7.5171136	0.0047
8	3	5	←	7	4	4	7.5452366	-0.0211
8	4	5	←	7	4	4	7.5800004	-0.0097
6	5	1	←	5	4	1	7.6214267	-0.0042
8	3	5	←	7	3	4	7.6761685	-0.0076
8	4	5	←	7	3	4	7.7109189	-0.0096
6	5	2	←	5	4	2	7.7263533	0.0100
9	2	7	←	8	3	6	7.7803533	-0.0026
9	3	7	←	8	3	6	7.7806294	-0.0012
9	2	7	←	8	2	6	7.7819663	-0.0019
9	3	7	←	8	2	6	7.7822414	-0.0015
6	5	1	←	5	4	2	7.8306732	0.0079
5	4	2	←	4	2	3	7.8651974	-0.0026
5	4	2	←	4	1	3	7.9063223	-0.0105
8	5	4	←	7	5	3	7.9510899	-0.0155
7	5	3	←	7	4	4	2.0241329	0.0125
2	1	1	←	1	1	0	2.0888452	-0.0003
7	5	3	←	7	3	4	2.1550660	0.0272
7	3	4	←	7	2	5	2.2616023	-0.0124
6	2	4	←	6	1	5	2.3560903	-0.0055
7	4	4	←	7	3	5	2.3839189	-0.0017
7	4	4	←	7	2	5	2.3925344	0.0012
3	0	3	←	2	1	2	2.3943135	0.0048
6	3	4	←	6	2	5	2.3945773	-0.0003
8	5	4	←	8	4	5	2.3952208	0.0051

3	1	3	←	2	1	2	2.4005220	0.0038
5	1	4	←	5	0	5	2.4031633	0.0018
5	2	4	←	5	1	5	2.4115617	0.0033
2	1	1	←	1	0	1	2.4192806	0.0014
2	2	1	←	1	1	0	2.4201035	-0.0081
3	0	3	←	2	0	2	2.4265919	0.0020
3	1	3	←	2	0	2	2.4327999	0.0006
2	2	0	←	1	1	0	2.5619739	-0.0064
2	2	1	←	1	1	1	2.6401158	-0.0063
3	2	2	←	2	2	1	2.8032602	0.0089
8	3	5	←	8	2	6	2.8654379	-0.0114
8	4	5	←	8	3	6	2.8985847	-0.0047
8	4	5	←	8	2	6	2.9001956	-0.0061
7	2	5	←	7	1	6	2.9184759	-0.0103
7	3	5	←	7	2	6	2.9268599	0.0000
3	1	2	←	2	1	1	2.9879106	0.0031
4	0	4	←	3	1	3	3.1241495	0.0037
4	1	4	←	3	1	3	3.1251327	0.0038
4	0	4	←	3	0	3	3.1303589	0.0036
4	1	4	←	3	0	3	3.1313421	0.0037
3	2	2	←	2	1	1	3.1345170	-0.0004
3	2	1	←	2	2	0	3.1799244	0.0100
4	1	3	←	3	2	2	3.5741136	0.0102
4	2	3	←	3	2	2	3.6152425	0.0063
3	2	1	←	2	1	1	3.6530507	0.0014
3	1	2	←	2	0	2	3.6802273	0.0073
4	1	3	←	3	1	2	3.7207126	-0.0007
4	2	3	←	3	1	2	3.7618409	-0.0052
3	2	2	←	2	1	2	3.7945486	-0.0002
3	3	1	←	2	2	0	3.8362157	-0.0113
5	0	5	←	4	1	4	3.8413445	0.0012
5	1	5	←	4	1	4	3.8414849	0.0013
5	0	5	←	4	0	4	3.8423283	0.0020
5	1	5	←	4	0	4	3.8424692	0.0025
3	3	0	←	2	2	0	3.9088627	-0.0064
4	3	2	←	3	3	1	3.9102001	0.0143
3	3	1	←	2	2	1	3.9780910	-0.0047
3	3	0	←	2	2	1	4.0507357	-0.0021
4	2	2	←	3	2	1	4.1914511	0.0097
4	3	1	←	3	3	0	4.1946608	0.0176
5	2	3	←	4	3	1	4.2883859	0.0007
5	1	4	←	4	2	3	4.3603701	0.0033
5	2	4	←	4	2	3	4.3688982	-0.0057
5	1	4	←	4	1	3	4.4014988	-0.0007
5	2	4	←	4	1	3	4.4100389	0.0021
4	3	2	←	3	2	1	4.5664912	-0.0071
5	2	3	←	4	3	2	4.6454952	0.0104
5	3	3	←	4	3	2	4.7925305	0.0084
4	2	2	←	3	1	2	4.8565923	0.0090
4	3	1	←	3	2	1	4.9235976	-0.0003
4	1	3	←	3	0	3	4.9743501	0.0066
5	4	2	←	4	4	1	4.9752671	0.0086
4	2	3	←	3	1	3	5.0092799	0.0130
5	2	3	←	4	2	2	5.0205391	-0.0026
4	3	2	←	3	2	2	5.0850268	-0.0034
6	1	5	←	5	2	4	5.0925851	0.0042
6	2	5	←	5	2	4	5.0940864	0.0036
6	1	5	←	5	1	4	5.1011203	0.0021
6	2	5	←	5	1	4	5.1026221	0.0020
5	4	1	←	4	4	0	5.1533970	0.0143
5	3	3	←	4	2	2	5.1675714	-0.0076
4	4	1	←	3	3	0	5.2576887	-0.0024
4	4	0	←	3	3	0	5.2887978	-0.0034
5	3	2	←	4	3	1	5.3206678	0.0023
4	4	1	←	3	3	1	5.3303410	0.0077
4	4	0	←	3	3	1	5.3614437	0.0003
4	3	1	←	3	2	2	5.4421344	0.0045
6	2	4	←	5	3	3	5.5552643	-0.0001
6	3	3	←	5	4	2	5.5602744	0.0008
4	3	1	←	3	1	2	5.5887407	0.0008

6	3	4	←	5	3	3	5.5952502	0.0019
6	2	4	←	5	2	3	5.7023004	-0.0014
6	3	4	←	5	2	3	5.7422783	-0.0072
7	1	6	←	6	2	5	5.8101768	-0.0053
7	2	6	←	6	2	5	5.8104145	-0.0063
7	1	6	←	6	1	5	5.8116799	-0.0041
7	2	6	←	6	1	5	5.8119165	-0.0062
6	4	3	←	5	4	2	5.9264591	0.0068
6	5	2	←	5	5	1	6.0080741	0.0161
9	5	5	←	9	4	6	2.8713151	-0.0088
9	3	6	←	9	2	7	3.4295867	-0.0091
							RMS	7.458 kHz

Table D.2: *Measured rotational transitions ($\nu_{\rm obs}$) for m_eq_2_II, and the residuals ($\nu_{\rm obs} - \nu_{\rm calc}$) for the fit reported in Table 7.2.*

J'	K'_a	K'_c	$\leftarrow$	J''	K''_a	K''_c	$\nu_{\rm obs}$(GHz)	$\nu_{\rm obs} - \nu_{\rm calc}$ (MHz)
6	0	6	←	5	1	5	4.7496585	0.0094
6	1	6	←	5	0	5	4.7592570	0.0101
5	2	4	←	4	1	3	4.7937009	0.0082
4	2	2	←	3	1	2	4.8299538	-0.0005
6	1	5	←	5	2	4	5.1811776	-0.0014
4	2	3	←	3	1	3	5.1828316	0.0043
4	3	2	←	3	2	1	5.2285375	0.0049
4	3	1	←	3	2	1	5.3222939	-0.0007
8	4	4	←	7	5	3	5.3965686	-0.0231
6	2	5	←	5	1	4	5.4196738	0.0071
4	3	2	←	3	2	2	5.4935043	0.0051
7	0	7	←	6	1	6	5.5002354	0.0063
7	1	7	←	6	0	6	5.5030899	0.0098
4	3	1	←	3	2	2	5.5872579	-0.0033
5	3	3	←	4	2	2	5.9111002	0.0010
5	2	3	←	4	1	3	5.9916911	-0.0029
7	1	6	←	6	2	5	5.9989067	-0.0072
4	4	0	←	3	3	0	6.0559870	-0.0047
4	4	1	←	3	3	0	6.0530891	-0.0072
4	4	1	←	3	3	1	6.0677037	-0.0113
4	4	0	←	3	3	1	6.0706143	0.0038
5	3	2	←	4	2	2	6.2268463	0.0017
5	3	3	←	4	2	3	6.5608434	0.0016
8	3	5	←	7	4	4	6.6766386	0.0065
8	1	7	←	7	2	6	6.7742392	-0.0030
8	2	7	←	7	1	6	6.8081753	0.0016
5	4	2	←	4	3	1	6.9346400	0.0064
5	4	1	←	4	3	1	6.9592522	-0.0004
9	0	9	←	8	1	8	6.9962823	-0.0076
9	1	9	←	8	0	8	6.9965123	-0.0016
5	4	2	←	4	3	2	7.0283956	0.0000
7	3	5	←	6	2	4	7.0300248	0.0083
5	4	1	←	4	3	2	7.0530195	0.0047
4	3	1	←	3	0	3	7.2144445	-0.0117
6	3	3	←	5	2	3	7.2258257	-0.0098
9	1	8	←	8	2	7	7.5313342	-0.0179
8	3	6	←	7	2	5	7.5797026	0.0001
5	5	0	←	4	4	0	7.6592204	-0.0158
5	5	1	←	4	4	0	7.6587053	-0.0144
5	5	1	←	4	4	1	7.6616070	-0.0081
5	5	0	←	4	4	1	7.6621248	-0.0067
6	3	4	←	5	2	4	7.6939396	0.0183
6	4	2	←	5	3	2	7.8193998	-0.0031
3	1	3	←	2	0	2	2.6106965	0.0093
7	4	4	←	7	3	5	2.6296610	0.0007
2	2	0	←	1	1	0	2.8315980	-0.0040
9	3	6	←	9	2	7	2.8598724	0.0051
2	2	1	←	1	1	1	2.9405333	-0.0030
4	0	4	←	3	1	3	3.2166195	0.0033
4	1	4	←	3	1	3	3.2395945	0.0082
4	1	4	←	3	0	3	3.3034981	0.0071
3	1	2	←	2	0	2	3.6133058	0.0030
4	2	3	←	3	2	2	3.6195519	0.0148
11	6	6	←	11	5	7	3.6363251	0.0182
3	2	1	←	2	1	1	3.7834690	-0.0039
5	0	5	←	4	1	4	3.9922947	0.0069
5	1	5	←	4	0	4	4.0226494	0.0095
3	2	2	←	2	1	2	4.0271164	-0.0071
4	2	3	←	3	1	2	4.1802190	0.0072
5	1	4	←	4	2	3	4.2832552	0.0027
3	3	1	←	2	2	0	4.4263163	-0.0019

3	3	0	←	2	2	0	4.4409347	-0.0022
3	3	1	←	2	2	1	4.4869224	-0.0006
3	3	0	←	2	2	1	4.5015391	-0.0026
6	0	6	←	5	1	5	4.7496585	0.0094
4	1	3	←	3	0	3	4.9051188	-0.0004
5	3	2	←	4	3	1	4.9088780	0.0150
7	2	5	←	7	1	7	5.9646896	0.0137
7	2	6	←	6	2	5	6.0242897	-0.0196
7	2	6	←	6	1	5	6.0939697	0.0002
8	0	8	←	7	1	7	6.2485969	0.0077
5	3	2	←	4	2	3	6.8765916	0.0044
6	2	4	←	5	1	4	7.2768257	-0.0023
							RMS	8.412 kHz

Table D.3: *Measured rotational transitions (ν_{obs}) and the residuals ($\nu_{\mathrm{obs}} - \nu_{\mathrm{calc}}$) for the menthyl acetate conformer m_eq_1_II, as obtained after the fit with the programm XIAM.*

J'	K'_a	K'_c	$\leftarrow$	J''	K''_a	K''_c		$\nu_{\mathrm{obs}} - \nu_{\mathrm{calc}}$ (MHz)	ν_{obs}(GHz)
6	2	5	$\leftarrow$	5	1	5	E	-.0012	7.4976750
6	1	5	$\leftarrow$	5	0	5	E	.0011	7.5009673
6	2	4	$\leftarrow$	5	1	4	E	-.0072	7.4699625
6	3	4	$\leftarrow$	5	2	4	E	.0063	7.4631345
6	4	3	$\leftarrow$	5	3	3	E	.0125	7.4037250
6	5	3	$\leftarrow$	5	4	3	E	-.0105	7.3926750
5	3	2	$\leftarrow$	4	2	2	E	-.0092	6.1147875
5	4	2	$\leftarrow$	4	3	2	E	.0083	6.2171350
5	3	3	$\leftarrow$	4	2	3	E	.0114	6.1960625
5	2	4	$\leftarrow$	4	1	4	E	-.0039	6.2416750
5	1	4	$\leftarrow$	4	0	4	E	-.0035	6.2456375
5	5	0	$\leftarrow$	4	4	0	E	-.0016	6.8034875
5	2	3	$\leftarrow$	4	1	3	E	.0009	6.1981625
4	2	3	$\leftarrow$	3	1	3	E	.0119	4.9827550
4	1	3	$\leftarrow$	3	0	3	E	.0054	4.9877000
4	0	4	$\leftarrow$	3	1	3	E	.0167	2.8499997
4	4	1	$\leftarrow$	3	3	1	E	-.0058	5.1749750
4	4	0	$\leftarrow$	3	3	0	E	-.0106	5.4294500
3	1	2	$\leftarrow$	2	0	2	E	.0043	3.7185401
3	2	2	$\leftarrow$	2	1	2	E	.0085	3.7239025
3	3	1	$\leftarrow$	2	2	1	E	-.0074	3.8215875
3	3	0	$\leftarrow$	2	2	0	E	-.0021	4.0546875
2	2	0	$\leftarrow$	1	1	0	E	-.0034	2.6801875
2	1	1	$\leftarrow$	1	0	1	E	.0076	2.4529375
4	0	4	$\leftarrow$	3	1	3	A	.0048	3.1241495
4	1	4	$\leftarrow$	3	1	3	A	.0050	3.1251328
4	0	4	$\leftarrow$	3	0	3	A	.0047	3.1303589
4	1	4	$\leftarrow$	3	0	3	A	.0048	3.1313421
3	2	2	$\leftarrow$	2	1	1	A	-.0012	3.1345167
							E	.0176	3.0952600
9	3	6	$\leftarrow$	9	3	7	A	-.0123	3.4293100
9	3	6	$\leftarrow$	9	2	7	A	-.0104	3.4295867
9	4	6	$\leftarrow$	9	3	7	A	-.0086	3.4369649
9	4	6	$\leftarrow$	9	2	7	A	-.0080	3.4372402
8	2	6	$\leftarrow$	8	1	7	A	-.0052	3.4657281
8	3	6	$\leftarrow$	8	2	7	A	.0002	3.4673105
4	1	3	$\leftarrow$	3	2	2	A	.0108	3.5741136
4	2	3	$\leftarrow$	3	2	2	A	.0067	3.6152425
3	2	1	$\leftarrow$	2	1	1	A	.0002	3.6530507
							E	-.0045	3.7119032
3	1	2	$\leftarrow$	2	0	2	A	.0060	3.6802273
4	1	3	$\leftarrow$	3	1	2	A	-.0005	3.7207126
4	2	3	$\leftarrow$	3	1	2	A	-.0052	3.7618409
3	2	2	$\leftarrow$	2	1	2	A	-.0017	3.7945486
3	3	1	$\leftarrow$	2	2	0	A	-.0121	3.8362157
							E	-.0115	3.3399070
5	0	5	$\leftarrow$	4	1	4	A	.0027	3.8413445
5	1	5	$\leftarrow$	4	1	4	A	.0029	3.8414850
5	0	5	$\leftarrow$	4	0	4	A	.0137	3.8423386
5	1	5	$\leftarrow$	4	0	4	A	.0040	3.8424692
3	3	0	$\leftarrow$	2	2	0	A	-.0074	3.9088627
3	3	1	$\leftarrow$	2	2	1	A	-.0058	3.9780910
9	3	7	$\leftarrow$	9	2	8	A	-.0100	4.0088048
9	3	7	$\leftarrow$	9	1	8	A	-.0150	4.0088048
9	2	7	$\leftarrow$	9	1	8	A	.0010	4.0085460
9	2	7	$\leftarrow$	9	2	8	A	.0060	4.0085460
3	3	0	$\leftarrow$	2	2	1	A	-.0034	4.0507357
4	2	2	$\leftarrow$	3	2	1	A	.0091	4.1914509
5	2	3	$\leftarrow$	4	3	1	A	.0023	4.2883863
5	1	4	$\leftarrow$	4	2	3	A	.0043	4.3603701
5	2	4	$\leftarrow$	4	2	3	A	-.0047	4.3688984
5	1	4	$\leftarrow$	4	1	3	A	.0000	4.4014988

5	2	4	←	4	1	3	A	.0028	4.4100389
6	1	6	←	5	0	5	A	-.0013	4.5562878
							E	-.0119	4.1176301
4	3	2	←	3	2	1	A	-.0077	4.5664912
							E	-.0059	4.3389523
9	2	8	←	9	1	9	A	.0021	4.5690986
9	1	8	←	9	0	9	A	.0071	4.5690986
9	2	8	←	9	0	9	A	.0021	4.5690986
9	1	8	←	9	1	9	A	.0071	4.5690986
5	2	3	←	4	3	2	A	.0110	4.6454954
5	3	3	←	4	3	2	A	.0087	4.7925305
4	2	2	←	3	1	2	A	.0074	4.8565922
							E	.0002	4.9070747
4	3	1	←	3	2	1	A	-.0016	4.9235976
							E	-.0074	5.0350742
4	1	3	←	3	0	3	A	.0050	4.9743501
							E	.0011	4.9876957
5	2	3	←	4	2	2	A	-.0024	5.0205391
4	2	3	←	3	1	3	A	.0112	5.0092798
4	3	2	←	3	2	2	A	-.0048	5.0850268
							E	.0015	4.9556250
11	3	9	←	11	2	1	A	-.0040	5.0906437
11	2	9	←	11	1	1	A	.0025	5.0906437
11	3	9	←	11	1	1	A	-.0041	5.0906437
11	2	9	←	11	2	1	A	.0026	5.0906437
6	1	5	←	5	2	4	A	.0055	5.0925851
6	2	5	←	5	2	4	A	.0049	5.0940864
6	1	5	←	5	1	4	A	.0034	5.1011203
6	2	5	←	5	1	4	A	.0033	5.1026221
10	2	9	←	10	1	1	A	.0002	5.1087508
10	1	9	←	10	0	1	A	.0009	5.1087508
10	2	9	←	10	0	1	A	.0002	5.1087508
10	1	9	←	10	1	1	A	.0009	5.1087508
5	3	3	←	4	2	2	A	-.0074	5.1675715
4	4	1	←	3	3	0	A	-.0021	5.2576887
7	0	7	←	6	0	6	A	-.0113	5.2705629
7	1	7	←	6	1	6	A	.0051	5.2705629
7	1	7	←	6	0	6	A	-.0137	5.2705629
7	0	7	←	6	1	6	A	.0075	5.2705629
4	4	0	←	3	3	0	A	-.0033	5.2887978
5	3	2	←	4	3	1	A	.0016	5.3206678
4	4	1	←	3	3	1	A	.0079	5.3303410
6	3	3	←	5	4	1	A	-.0064	5.3510327
4	4	0	←	3	3	1	A	.0003	5.3614437
4	3	1	←	3	2	2	A	.0023	5.4421342
6	2	4	←	5	3	3	A	.0009	5.5552643
6	3	3	←	5	4	2	A	.0000	5.5602744
4	3	1	←	3	1	2	A	-.0015	5.5887407
6	3	4	←	5	3	3	A	.0029	5.5952502
6	3	4	←	5	2	3	A	-.0048	5.7422800
11	2 1	0	←	11	1	1	A	.0007	5.6483063
11	1 1	0	←	11	0	1	A	.0008	5.6483063
11	2 1	0	←	11	0	1	A	.0007	5.6483063
11	1 1	0	←	11	1	1	A	.0008	5.6483063
7	1	6	←	6	2	5	A	-.0035	5.8101768
7	2	6	←	6	2	5	A	-.0046	5.8104145
7	1	6	←	6	1	5	A	-.0024	5.8116799
7	2	6	←	6	1	5	A	-.0045	5.8119165
6	4	3	←	5	4	2	A	.0073	5.9264595
8	0	8	←	7	0	7	A	.0024	5.9849471
8	1	8	←	7	1	7	A	.0045	5.9849471
8	1	8	←	7	0	7	A	.0021	5.9849471
8	0	8	←	7	1	7	A	.0048	5.9849471
6	5	2	←	5	5	1	A	.0149	6.0080744
7	3	4	←	6	4	2	A	-.0044	6.0145979
5	4	2	←	4	3	1	A	-.0028	6.0383032
5	3	2	←	4	2	2	A	-.0075	6.0528161
6	5	1	←	5	5	0	A	.0161	6.1005055
5	2	3	←	4	1	3	A	.0021	6.1564153
5	1	4	←	4	0	4	A	-.0015	6.2454882

5	4	1	←	4	3	1	A	.0017	6.2475429
							E	.0097	6.4066064
5	2	4	←	4	1	4	A	-.0052	6.2530387
5	3	3	←	4	2	3	A	-.0018	6.2623159
6	3	3	←	5	3	2	A	-.0090	6.2779052
7	2	5	←	6	3	4	A	-.0025	6.3340865
7	3	5	←	6	3	4	A	.0010	6.3427025
6	4	2	←	5	4	1	A	-.0055	6.3642258
7	2	5	←	6	2	4	A	.0034	6.3740762
7	3	5	←	6	2	4	A	.0036	6.3826890
5	4	2	←	4	3	2	A	.0041	6.3954104
8	1	7	←	7	2	6	A	.0070	6.5248632
8	2	7	←	7	1	6	A	.0003	6.5251306
5	4	1	←	4	3	2	A	.0071	6.6046486
6	4	3	←	5	3	2	A	-.0072	6.6440848
7	3	4	←	6	4	3	A	-.0164	6.6616003
5	5	1	←	4	4	0	A	.0147	6.6624452
5	5	0	←	4	4	0	A	.0157	6.6743394
5	5	1	←	4	4	1	A	.0173	6.6935581
9	0	9	←	8	0	8	A	-.0033	6.6993285
9	1	9	←	8	1	8	A	-.0030	6.6993285
9	1	9	←	8	0	8	A	-.0033	6.6993285
9	0	9	←	8	1	8	A	-.0030	6.6993285
5	5	0	←	4	4	1	A	.0148	6.7054488
14	2	12	←	14	1	13	A	.0014	6.7110488
7	4	4	←	6	4	3	A	-.0092	6.7925255
7	5	3	←	6	5	2	A	-.0044	7.0167614
7	6	2	←	6	6	1	A	.0084	7.0197699
7	3	4	←	6	3	3	A	-.0072	7.0277873
7	6	1	←	6	6	0	A	.0089	7.0613344
8	2	6	←	7	3	5	A	.0017	7.0637284
8	3	6	←	7	3	5	A	-.0010	7.0653381
8	2	6	←	7	2	5	A	-.0014	7.0723379
8	3	6	←	7	2	5	A	.0043	7.0739559
5	3	2	←	4	2	3	A	-.0003	7.1475620
7	4	4	←	6	3	3	A	.0040	7.1587166
6	4	2	←	5	3	2	A	-.0066	7.2910998
							E	-.0056	7.3926799
6	3	3	←	5	2	3	A	-.0025	7.3101938
							E	-.0164	7.3737716
10	0	10		9	0	9	A	-.0076	7.4137176
6	2	4	←	5	1	4	A	-.0013	7.4572140
6	3	4	←	5	2	4	A	.0012	7.4886630
6	1	5	←	5	0	5	A	.0033	7.5042850
6	2	5	←	5	1	5	A	.0014	7.5056447
6	5	2	←	5	4	1	A	.0077	7.5171136
6	4	3	←	5	3	3	A	-.0028	7.5293338
8	3	5	←	7	4	4	A	-.0186	7.5452367
8	4	5	←	7	4	4	A	-.0074	7.5800003
6	5	1	←	5	4	1	A	-.0022	7.6214267
							E	.0141	7.7881247
8	3	5	←	7	3	4	A	-.0049	7.6761685
8	4	5	←	7	3	4	A	-.0069	7.7109189
6	5	2	←	5	4	2	A	.0121	7.7263533
12	4	8	←	11	5	6	A	-.0064	7.7392287
9	2	7	←	8	3	6	A	.0003	7.7803533
9	3	7	←	8	3	6	A	.0018	7.7806295
9	2	7	←	8	2	6	A	.0010	7.7819663
9	3	7	←	8	2	6	A	.0013	7.7822414
6	5	1	←	5	4	2	A	.0091	7.8306732
5	4	2	←	4	2	3	A	-.0045	7.8651976
5	4	2	←	4	1	3	A	-.0125	7.9063226
10	1	9	←	9	1	8	A	-.0070	7.9533765
8	5	4	←	7	5	3	A	-.0142	7.9510899
								RMS	7.319 kHz

E

State-Specific Enrichment of Chiral Conformers with Microwave Spectroscopy

Table E.1: *Measured rotational transitions (ν_{obs}) for cyclohexylmethanol, and the residuals ($\nu_{\mathrm{obs}} - \nu_{\mathrm{calc}}$) for the fit reported in Table 9.1.*

J'	K_a'	K_c'	$\leftarrow$	J''	K_a''	K_c''	ν_{obs}(GHz)	$\nu_{\mathrm{obs}} - \nu_{\mathrm{calc}}$ (MHz)
3	1	3	$\leftarrow$	3	0	3	2017.5087	0.0031
2	0	2	$\leftarrow$	1	1	1	2144.9500	-0.0002
2	1	2	$\leftarrow$	2	0	2	2338.7330	0.0022
1	0	1	$\leftarrow$	0	0	0	2369.0077	-0.0006
4	1	3	$\leftarrow$	3	2	1	2501.7785	-0.0009
1	1	1	$\leftarrow$	1	0	1	2575.1422	0.0004
4	1	3	$\leftarrow$	3	2	2	2590.8092	-0.0014
6	1	6	$\leftarrow$	5	2	3	2655.3675	0.0105
1	1	0	$\leftarrow$	1	0	1	2829.4763	0.0001
2	1	1	$\leftarrow$	2	0	2	3101.7375	0.0041
6	1	6	$\leftarrow$	5	2	4	3252.6164	0.0009
9	2	8	$\leftarrow$	9	1	8	3313.7031	0.0071
3	1	2	$\leftarrow$	3	0	3	3542.7197	0.0029
3	0	3	$\leftarrow$	2	1	1	3934.1738	-0.0041
8	2	7	$\leftarrow$	8	1	7	4085.7353	-0.0007
4	1	3	$\leftarrow$	4	0	4	4187.1726	0.0062
2	1	2	$\leftarrow$	1	1	1	4483.6836	0.0025
7	2	5	$\leftarrow$	6	3	3	4499.8911	0.0104
7	2	5	$\leftarrow$	6	3	4	4565.2040	-0.0035
7	1	7	$\leftarrow$	6	2	5	4621.7249	-0.0052
3	0	3	$\leftarrow$	2	1	2	4697.1778	-0.0026
2	0	2	$\leftarrow$	1	0	1	4720.0924	0.0004
7	2	6	$\leftarrow$	7	1	6	4862.5842	-0.0046
1	1	1	$\leftarrow$	0	0	0	4944.1587	0.0086
2	1	1	$\leftarrow$	1	1	0	4992.3522	0.0030
5	1	4	$\leftarrow$	5	0	5	5070.3672	0.0033
1	1	0	$\leftarrow$	0	0	0	5198.4756	-0.0088
5	1	4	$\leftarrow$	4	2	2	5259.4689	-0.0012
5	1	4	$\leftarrow$	4	2	3	5522.5812	0.0000
6	2	5	$\leftarrow$	6	1	5	5605.3692	-0.0041
4	0	4	$\leftarrow$	3	1	2	5759.1936	0.0004
8	1	8	$\leftarrow$	7	2	6	5840.2959	-0.0092
6	1	5	$\leftarrow$	6	0	6	6215.3957	-0.0047
5	2	4	$\leftarrow$	5	1	4	6282.6191	0.0006
3	1	3	$\leftarrow$	2	1	2	6714.6851	-0.0009

6	2	4	←	6	1	5	6749.7514	-0.0069
4	2	3	←	4	1	3	6871.2559	0.0058
5	2	3	←	5	1	4	6879.8789	0.0020
9	1	9	←	8	2	7	6915.8217	0.0034
3	0	3	←	2	0	2	7035.9116	0.0003
2	1	2	←	1	0	1	7058.8263	0.0035
3	2	2	←	2	2	1	7107.0151	-0.0034
4	2	2	←	4	1	3	7134.3634	0.0023
3	2	1	←	2	2	0	7178.1243	-0.0021
4	0	4	←	3	1	3	7284.4056	0.0012
5	0	5	←	4	1	3	7323.4682	0.0008
3	2	2	←	3	1	2	7355.5511	0.0020
3	2	1	←	3	1	2	7444.5781	-0.0021
3	1	2	←	2	1	1	7476.8925	-0.0022
2	2	1	←	2	1	1	7725.4224	-0.0027
2	2	0	←	2	1	1	7743.3466	-0.0018
2	1	1	←	1	0	1	7821.8289	0.0036
6	1	5	←	5	2	3	7930.9919	-0.0022
							RMS	4.183 kHz